DEVELOPMENT OF THERMALLY STABLE AEROGELS FOR AEROSPACE APPLICATIONS

BY

NATHANIEL SCOTT OLSON

DISSERTATION

Submitted in partial fulfillment of the requirements
for the degree of Doctor of Philosophy in Materials Science and Engineering
in the Graduate College of the
University of Illinois Urbana-Champaign, 2023

Urbana, Illinois

Doctoral Committee:

Associate Professor Jessica A. Krogstad, Chair
Professor Catherine J. Murphy
Dr. Frances I. Hurwitz, NASA Glenn Research Center
Assistant Professor Nicola H. Perry
Associate Professor Daniel P. Shoemaker

ABSTRACT

The extreme environments of space exploration have pushed scientists to create revolutionary materials that have filtered back to terrestrial life. A key challenge is lightweight insulation to replace dense ceramics for aerospace applications, where every kilogram is worth \$5,000 to \$20,000 to just reach low Earth orbit [1]. A promising form of insulation is aerogels. The high porosities and low densities of ceramic aerogels offer outstanding insulative performance in applications where weight is a critical factor. The high surface-to-volume ratios and specific surface areas provide extremely low thermal conductivity, but also contribute to rapid densification of the pore structure at elevated temperatures. This densification diminishes their favorable properties and inhibits use of aerogels in high temperature applications. The purpose of this work was the establishment of a design framework for thermally stable, highly porous materials. Design considerations including composition, synthetic parameters, and post-synthetic modification were evaluated via sol-gel synthesis and characterization of metal oxide aerogels.

Zirconia aerogels doped with varying concentrations of yttrium, ytterbium, gadolinium, cerium, and calcium were studied to 1200 °C. For yttria-stabilized zirconia (YSZ) aerogels, increased yttria content was associated with increased thermal stability and retention of porosity to 1200 °C. The improvements in thermal stability with increased yttria content are hypothesized to be the result of a reduction in surface energy and cation diffusivity, thereby reducing the driving force for densification and slowing transport processes that result in densification, respectively.

When the broader set of dopants were analyzed, increased dopant concentration was found to reduce rate of densification for all materials. Gadolinium and yttrium were the most effective dopants for improving thermal stability. Evaluation of material property – thermal stability relationships was challenging because of a lack of material property data for the compositions

studied. A material property database for the aerogels studied would serve as a useful tool for future analysis of design considerations for thermally stable aerogels and furthering the understanding of properties and mechanisms controlling the densification of highly porous structures.

The synthetic parameters of solids loading and water content were used to modify the starting structure of the aerogel, including its specific surface area, mesopore volume, and mesopore size. The structural evolution of these materials was studied at elevated temperatures. The differences in starting structure had negligible impact on the thermal stability of the aerogel. This result serves as an important control for the study of composition, where choice of dopant and dopant concentration influence both starting structure and thermal stability.

Post-synthetic modification of YSZ aerogels with coatings of silica was performed in an effort to further improve thermal stability. Silica coatings significantly improved thermal stability to 1000 °C but underwent rapid densification beyond this temperature, which was attributed to viscous sintering of silica. This result points towards a strong motivation to study YSZ aerogels with coatings of zirconia, titania, and alumina to identify a coating that offers improved thermal stability to temperatures beyond 1000 °C by avoidance of viscous sintering.

The colloidal stability of yttria was evaluated in an effort to develop a colloidal synthesis for YSZ aerogels. The development of a colloidal synthesis for YSZ aerogels will enable the study of aerogel thermal stability in context of structural motifs and how these motifs are assembled. Ultrasonication of yttria colloids in aqueous citric acid solutions or in ethanol were found to reduce the particle size and improve colloidal stability, an important first step in developing a colloidal YSZ synthesis. The colloidal synthesis of alumina-zirconia as an alternative composition to YSZ was also proposed and preliminary work identified precursors and possible synthetic routes.

Overall, important design considerations were identified for thermally stable metal oxide aerogels, including surface energy and cation diffusivity. Surface energy is expected to be especially important, given the extremely high specific surface energies of aerogels. There are certainly more design rules and considerations to be identified. This work suggests promising future routes of study including the establishment of material property databases in conjunction with thermal stability measurements, the use of non-densifying coatings, and the development of novel colloidal syntheses for thermally stable aerogel compositions.

Thermally stable aerogels can be implemented into flexible reinforcements such as metal oxide felts, papers, and weaves to form composite insulation. The addition of aerogel will reduce the thermal conductivity and permeability of the composite, permitting higher operating temperatures and pressures while avoiding the transport of heat and gas through the insulation. This work identified metal oxide aerogels, including zirconia doped with yttrium or gadolinium as well as silica coated aerogels, that offer promise as components in insulative composites for aerospace thermal protection systems.

ACKNOWLEDGMENTS

I would like to express my gratitude to Professor Jessica Krogstad for her continual support and mentorship through the ups and downs of this project. Her push to think deeply about the science and ask the right questions made the present work much more impactful and are lessons I will carry with me through my career. I am extremely grateful to have had the opportunity be mentored by Dr. Frances Hurwitz the past six years, starting with my internship at NASA Glenn Research Center in 2017, which completely changed the trajectory of my career, introducing me to aerogels and aerospace thermal protection systems. Dr. Hurwitz tirelessly advocated for me and provided every opportunity for growth as a researcher and professional.

My sincere thanks to Dr. Haiquan Guo for spending hours in lab showing me the art of aerogel synthesis and providing valuable inputs to this work. Special thanks to Dr. Jamesa Stokes for her mentorship and support of this project, always offering unique and valuable insights that greatly informed the work on dopants and coatings. I am also thankful for Dr. Vadim Lvovich, Dr. Richard Rogers, Ms. Jessica Cashman, Mr. Daniel Scheiman, and Dr. Rocco Viggiano at NASA Glenn Research Center for their support of this project and investment in my own professional development over the past six years.

I am also grateful to Professor Catherine Murphy, Professor Nicola Perry, and Professor Daniel Shoemaker for serving as my thesis committee and providing valuable inputs, feedback, and support. I would like to thank Jordan Meyer for his significant contributions to this work, especially on the synthetic parameter study. His questions and curiosity always made me think deeply about the work we were doing. I am also thankful for Krogstad group members past and present, especially Dr. Charles Smith and Dr. Nathan Madden for mentoring me as a young graduate student.

I could not have embarked on this journey without the mentorship of Professor Nicholas Brunelli and the members of the Catalytic Material Design Group at The Ohio State University, especially Dr. Nitish Deshpande, Dr. Aamena Parulkar, and Dr. Mariah Whitaker. Professor Brunelli demonstrated extraordinary patience and mentoring capability in taking a very inexperienced first-year student and showing him the ways of science and research. I cannot overstate the importance of what I learned through my time in his group.

Many thanks to my mentors at NASA Johnson Space Center: Dr. Adam Sidor, Mr. Stanley Bouslog, Mr. Ronald Lewis, and Mr. Scott Coughlin, who all have allowed me to be a part of an extraordinarily exciting project. Dr. Sidor has been immensely generous with his time, and I am forever grateful for his mentorship. Many thanks to Stan for sharing his vast knowledge of TPS and always involving me in opportunities for growth and exciting new ideas. I am extremely grateful for Ron and Scott's support of my professional development and career goals. I am excited to see what the future holds as I continue under their mentorship and leadership.

My time at Tinora High School was formative in my interest in math and science. Many thanks to Mrs. Jean Meyer for instilling an understanding and passion for math and her support of the science club, Mrs. Elizabeth Maurer for enabling my journey in developing a passion for chemistry, Mrs. Jenifer McConaughy for advising science club and supporting my participation in a multitude of science competitions and fairs, and Mr. Josh Clark for pushing forward my reading, writing, and critical thinking skills.

I also must thank the Illini Motorsports Formula SAE team for the opportunity to test, tune, and race their ever-improving cars the past 5 years. My time spent with the team has provided me with a wealth of memories and has made my experience at UIUC intensely richer. The drive and dedication of the team always inspired to push harder in my academic pursuits.

My deepest and most sincere appreciation goes to my parents, Scott and Dana Olson. I cannot adequately express what they have done to get me here: working tirelessly to support their children, instilling a strong work ethic in me, and always fostering an environment where curiosity and learning were valued. The rest of my family, especially my sister Marisa and grandparents, Web and Gail Olson and Mike and Judy Norden, have always been my biggest supporters and for that I am extremely grateful.

Finally, this endeavor would not have been possible without the support and love of my wife, Aliki Kolliopoulos. Apart from you, no one understands what it took to get here, and I am extremely grateful we had each other's encouragement and support through this journey. Our time together at UIUC will always remain a fond memory and I could not imagine this life without you.

To my parents Scott & Dana,

for your unwavering support of my every endeavor

And to my wife Aliki,

for the endless love and boundless joy you bring to my life

TABLE OF CONTENTS

CHAPTER 1: INTRODUCTION

A significant challenge in the field of aerospace materials is the development of lightweight, highly insulating materials that can maintain high performance in extreme environments. Materials with reduced thermal conductivity permit higher operating temperatures and improved insulative performance. Reduced weight mitigates cost and improves payload capacity. Take for example NASA's cost estimates from the Space Shuttle program: assuming a cost of $5000 per kilogram to launch into low Earth orbit, a 10% reduction in the mass of the Space Shuttle's thermal protection system would save $4.3M per launch [1,2]. A promising class of lightweight, low thermal conductivity materials are aerogels. Aerogels are highly porous, extremely lightweight (densities can be under 0.05 g/cm^3), and display extraordinarily low thermal conductivity (as low as 0.009 W/(m•K) in atmosphere and 0.003 W/(m•K) under vacuum) [3].

The same highly porous structure that makes aerogel an excellent insulator is also the source of a critical engineering challenge: thermal stability. Upon thermal exposure, the aerogel's highly porous structure collapses, and the favorable properties of low thermal conductivity and low density are lost. Aerogels with improved thermal stability must be developed to enable the use of aerogels as insulation in extreme environments and temperatures to 1200 °C. A successful aerogel system must be able to suppress both densification and phase transformations to maintain sufficiently low thermal conductivity and mechanical integrity across the full range of relevant extreme operating conditions.

The goal of the project was to develop an understanding of the structural and thermal properties of doped zirconia aerogels for use in thermal protection systems for aerospace applications. Relevant background to the project is provided in Chapter 2. Chapter 3 describes the methods employed to characterize the structure and properties of aerogels and understand how these materials evolve at high temperatures.

Formulations and synthetic approaches for high temperature aerogels were developed through iterative synthesis and characterization of zirconia aerogels. Chapter 4 describes the improvement in thermal stability realized by doping zirconia aerogels with high concentrations of yttria and presents hypotheses on property-stability relationships. The study of composition and material properties was expanded to encompass zirconia doped with yttrium, ytterbium, gadolinium, cerium, and calcium and this work is included in Chapter 5. Dopant and material properties were related to the thermal evolution of the aerogel structure to provide a thermodynamically and kinetically informed study of aerogel thermal stability. Relationships between synthetic parameters and the as dried structure and the as dried structure and thermal stability were studied and are shown in Chapter 6.

Chapter 7 expands the work on structure-stability relationships by characterizing the evolution with temperature of aerogels post-synthetically modified with various metal alkoxides. Efforts were made to develop synthetic routes to doped zirconia aerogels via colloidal precursors and these efforts are detailed in Chapter 8. By evaluating novel methods of forming aerogel structures, relationships between structure and thermal stability can be drawn. Chapter 9 summarizes the work conducted within this project and suggests routes for future study of thermally stable ceramic aerogels.

CHAPTER 2: BACKGROUND

2.1 Spacecraft thermal protection systems

Spacecraft encounter extreme environments in all phases of their operation, including ascent, on-orbit, and atmospheric entry. The systems and components of the vehicles are subjected to extremes of temperature, aerodynamic forces, and vibrational loads. The materials employed in such components must demonstrate resilience to these extremes. Thermal protection materials employed in thermal protection systems (TPS) that protect the spacecraft from high temperatures are mission critical and often mission limiting. In the most extreme cases of heating, the only current viable material option are carbon-based composites that ablate and pyrolyze upon atmospheric entry, absorbing and carrying away the heat at the material is consumed. Such ablative heat shields are employed on Earth re-entry capsules, including the Apollo, Dragon, and Orion spacecraft.

Under milder conditions, in the context of spaceflight, reusable TPS become feasible. The most famous example being the lightweight ceramic tiles that covered much of the Space Shuttle Orbiter. These tiles, consisting primarily of silica fibers, enabled the Shuttle to reenter Earth's atmosphere up to temperatures of 1200 °C and heat loads of 77 kJ/cm^2. Thermal conductivity of the tiles ranged from 0.05 to 0.126 W/m·K [2,4,5]. The tiles were categorized by their density (LI-900, LI-2200, AETB-8) and their surface coating (HRSI or LRSI).

Densities of LI-900, LI-2200, and AETB-8 were 9, 22, and 8 lb/ft^3, respectively (0.14, 0.35, and 0.13 g/cm^3) . High temperature reusable surface insulation (HRSI) used a black borosilicate reaction cured glass (RCG) coating with high emissivity to reject heat and were applied in areas where temperatures reached 1260 °C, covering much of the underside of the vehicle. Low temperature reusable surface insulation (LRSI) used a white coating that more effectively reflected sunlight to maintain proper on-orbit temperatures and were rated to 649 °C. Further improvements were made to the tiles used in the Orbiter throughout the Space Shuttle program, culminating in the replacement of some HRSI with Fibrous Refractory Composite Insulation (FRCI) and Alumina Enhanced Thermal Barrier (AETB) tiles, both of which offer reduced weight and improved toughness to orbital debris impacts.

Perhaps less well known, yet covering almost a third of the Shuttle Orbiter, were flexible insulation blankets (FIB) and felt reusable surface insulation (FRSI) blankets. Lightweight and flexible, the FIB and FRSI were employed where temperatures were below 649 and 371 °C, respectively [2,6]. Flexible materials referred to as thermal barriers were also used to prevent superheated air from flowing through penetrations on the vehicle, such as where the RCC met the wingtip (shown in Figure 2.1), the landing gear door, and the crew hatch [5]. The thermal barriers consisted of a tubular Inconel 750 wire mesh filled with Saffil (aluminosilicate) fibrous insulation wrapped with a ceramic sleeving and a Nextel AB312 alumina-borosilicate ceramic fiber outer cover. Exposed surfaces had applied a high emissivity ceramic coating and the entire barrier was attached using a room temperature vulcanizing (RTV) silicone. The materials developed in this work are candidate component materials for use in flexible insulation such as the aforementioned blankets and thermal barriers. The overall layout of the TPS on the Space Shuttle orbiter is shown in Figure 2.2 [6].

Developing TPS capable of withstanding higher temperatures and insulating the spacecraft structure enable new mission architectures and make spaceflight safer and more affordable. Take the Space Shuttle Orbiter for example. At an estimated cost of $5,000 per kg to launch into low Earth orbit (LEO) and Orbiter’s total TPS weight of 8,574 kg, a 10% reduction in TPS weight would result in $4.3 million reduction in cost per launch or equivalently 857 kg of extra science payload [1,2]. This reduction can be achieved via materials with lower density and lower thermal conductivity than existing alternatives.

2.2 Aerogels

2.2.1 History of aerogel

An aerogel is an extremely porous, lightweight material that is derived from the sol-gel process. Aerogels can vary widely in their composition, including metals, ceramics, polymers, carbon, and more. The liquid phase of the gel is replaced with a gas, leading to a material with extraordinarily low density and low thermal conductivity and surface areas upwards of 1000 m^2/g. Steven Kistler is credited with the development of aerogels while at the College of the Pacific in Stockton, California, with the first report published in Nature in 1931 [7]. The legend is that he and a friend made a bet as to who could remove the liquid from a "jelly" and replace it with a gas without shrinkage. Kistler won the bet and made the first aerogel via supercritical drying, where the solvent (generally methanol) was brought to its supercritical state. At this point, the surface tension goes to zero and the fluid can be extracted while maintaining the porous structure by avoiding the capillary stress associated with a liquid-vapor interface in small pores. Unfortunately, his process took weeks to prepare a single sample due to a tedious synthesis from sodium silicate with hydrochloric acid, which was slowly saturated with methanol via solvent exchange. Kistler came to University of Illinois shortly after his invention of the aerogel and published foundational papers on the low thermal conductivity of silica aerogels and the promise of high catalytic activity for metal oxide aerogels. The Monsanto Corporation licensed the technology from Kistler and began commercial production around 1942. Through 1970, Monsanto produced silica aerogels for use as a thickening agent for paints and makeup, cigarette filters, and as insulation in freezers [8].

In the 1970s, the French government renewed interest in aerogels using a silicon alkoxide, tetramethoxysilane (TMOS) with alcohol, water, and a catalyst. This alkoxide-based synthesis is the basis of silica aerogel production to this day [9]. Eliminating the methanol solvent exchange reduced the synthesis time from weeks to hours. The Lund group in Sweden pioneered the commercial production of aerogels using the new synthesis, but continued to use alcohol-based supercritical drying [10]. This process involved taking the methanol solvent, which contained the synthesized gels, to its supercritical point (240 °C, 80 atm). This process came under scrutiny after a gasket failure led to the explosion of 3000 liter autoclave full of methanol, destroying the entire facility [10].

Dr. Arlon Hunt's group at Lawrence Berkeley National Laboratory developed a supercritical drying process that replaced with alcohol with liquid CO_2, which has a much lower supercritical point (50 °C, 80 atm) and is not flammable [11]. This vastly increased the safety of aerogel production, both at laboratory and commercial scales.

The advancements in aerogel synthesis and supercritical drying gave rise to new and interesting applications. Physicists at CERN used aerogels as a detector for Cherenkov radiation, where pions, muons, and protons moving near the speed of light would leave an electromagnetic shock front through the aerogel, which could be detected by the light this process emits [12]. Aerogel is perhaps most famous for its spacefaring applications. NASA utilized aerogel to protect the electronics on the Mars rover, Sojourner, in 1997. The aerogel's great success led to the implementation of aerogel as insulation on both Mars Exploration rovers Spirt and Opportunity in 2003, where aerogel protected the battery, electronics, and computers. A fascinating application of aerogel as a cometary particle collector on the NASA Stardust mission, which operated from 1999 to 2006. The goal was to approach a comet, collect particles ejected from the comet, and return the particles to Earth to study the composition of comets, which would lend information on the origins of the early solar system. The mission was a complete success, as the aerogel first collected particles as they collided with the aerogel and embedded themselves within. The probe survived reentry in 2006 and the particles were able to be analyzed, with a special issue of Science devoted to the mission and its discoveries [13].

2.2.2 Aerogel structure & properties

The IUPAC defines an aerogel as a "gel comprised of a microporous solid in which the dispersed phase is a gas" [14]. This definition has come under some scrutiny, as it would also include materials such as zeolites, but also excludes many materials considered to be aerogels that have pores on the mesoscale. A more encompassing definition of an aerogel is a highly porous, three-dimensional structure where the liquid phase has been replaced with air, leading to a structure with porosity over 90% and pores smaller than 100 nm. Pores smaller than this size are required for the low thermal conductivity of aerogels and their ability to significantly reduce heat transfer via both conduction and convection. Highly porous materials with a majority of pores greater than 100 nm are often referred to as foams.

Aerogels are an extraordinarily diverse group of materials, encompassing gels based on metal oxides, metals, carbon, polyimides, polyurethanes, phenolics, cellulose, rubbers, biopolymers, and more. Obviously, the differences synthesis, structure, properties, and performance between these classes are huge, let alone the differences that can exist within a class. In this thesis, the discussion will focus on metal oxide aerogels, as these are best suited for the high temperature insulative applications that are the focus of this work.

Metal oxide aerogels are generally comprised of interconnected polymeric or colloidal primary particles that are on the order of 10 nm in size, forming a monolithic structure with most pores from 2 to 100 nm in size, with some macroporosity also present [15]. Porosities exceed 90%, leading to densities as low as 0.03 g/cm^3 and specific surface areas (SSA) from 250 to over 1000 m^2/g [16]. The properties of pore size, porosity, bulk density, SSA, and pore volume are generally the most important and relevant values to fully characterize the texture of an aerogel.

One of the most remarkable properties of aerogels are their extremely low thermal conductivities. For silica aerogels, thermal conductivity is generally near 0.015 W/(m•K). This is lower than the thermal conductivity of air, also an extraordinary insulator, at the same conditions: 0.025 W/(m•K). How can the thermal conductivity of a solid be lower than that of air at similar conditions? First, the highly porous, loosely interconnected network of small solid particles creates a very tortuous path for heat transfer via conduction. Heat must transverse a random path, traveling along the fractal-like solid structure. The ability for the aerogel to conduct heat can also be further reduced by selecting a solid material with low thermal conductivity. Second, and most critically, the mesoscale pores (2 to 100 nm) block heat transfer via convection. The mean free path of gas molecules, even at ambient conditions, is on the order of 66 nm, similar in scale and often larger than the pore size within the aerogel. Therefore, the air molecules struggle to move through the small, random pore structure of the aerogel, leading to minimal heat transfer via convection. The mean free path of particles in a gas grows linearly with temperature, so heat transfer via convection becomes even more tenuous at the high temperatures experienced in aerospace applications.

With such high specific surface area, the surface chemistry of aerogels plays an important role in their properties and potential applications. Most synthesis methods for metal oxide aerogels lead to a structure than contains unreacted surface hydroxyl groups, contributing to high hydrophilicity. Often, care must be taken to avoid adsorption of water vapor onto the vast surface area of the aerogel, which can impede catalytic activity and influence the structural evolution at high temperatures.

The unreacted surface groups also present an opportunity for functionalization of the surface. Hydrophobic groups, such as $\equiv Si–(CH_2)_xCH_3$, can be introduced either during gel synthesis or after supercritical drying, to reduce the affinity for metal oxide aerogels to take up water. Surface groups tailored for catalysis of specific chemical reactions can also be attached to the surface. The flexibility of surface functionality and the massive surface area available for reaction make aerogels of much interest to the catalytic community.

2.2.3 Sintering & densification of aerogels

With porosities in excess of 90% and primary particle sizes on the order of 10 nm, aerogels are comprised nearly entirely of free surfaces and interfaces. Free surfaces exist where the vapor phase is in contact with the solid and interfaces exist between the primary particles that make up the solid network of the aerogel. The high specific surface area of aerogels generates a large thermodynamic driving force for sintering and densification of the mesoporous structure, reducing surface area and therefore the total surface energy of the system. In a solid, the surface energy (γ) can be thought of as the work (w) required to increase the surface by a unit area (A), or the excess energy of the surface per unit area compared to the bulk material. Since the surface is associated with excess energy, the driving force of surface energy favors the elimination of surface area.

$$\gamma = \frac{dw}{dA} \qquad \textbf{Equation 2.1}$$

The source of surface energy is the disruption of intermolecular bonds at a surface. The atoms on a surface do not have a full coordination number’s worth of neighbors. The bonds will either be broken or distorted, leading to an excess energy at the surface. The value of surface energy in solids depends on numerous factors, including material composition, crystallographic face, and adsorption of surface-active species. Outside of vacuum, adsorbed species play an important role in the surface science of solid materials. In any case, the high specific surface area comes with high total surface energies, leading to instability of the mesoporous structure at high temperatures. Ceramics, both highly porous varieties as well as dense, polycrystalline materials, undergo a combination of sintering, coarsening, and densification at high temperatures to minimize the energy associated with free surfaces and interfaces.

Sintering requires the diffusion of atoms through the material. This diffusion is driven by a gradient of chemical potential. In the case of surfaces, the surface energy creates a pressure difference across curved surfaces. Since surfaces have excess energy, a curved surface seeks to become flat to minimize its energy. In turn, the pressure difference across a curved surface leads to a difference in solubility and/or vapor pressure relative to a flat surface. This increases the chemical potential of the material under a curved surface, generating a chemical potential gradient that drives diffusion when the material is heated. An additional source of sintering in aerogels is the condensation of surface hydroxyl groups. As shown in a simplified depiction in Figure 2.4, pore collapse can be driven by the condensation reaction of adjacent hydroxyl groups.

Sintering and densification in mesoporous aerogels are not well understood. The small scales involved, with pores on the scale of 2 to 100 nm and primary particles on a similar scale, make imaging of the structural evolution extremely difficult, therefore most work in this aerogel utilizes simulation to understand the structural evolution [17–21]. The validity of models is evaluated via comparison of macroscopic properties obtained in experimental work including thermal conductivity and density [22]. Experimental studies of aerogel sintering were largely conducted in the 1990s and early 2000s and were further limited by availability of high resolution microscopy [21,23–26]. Most work in this field leverages small-angle x-ray scattering (SAXS) to infer the structure of the two-phase system comprised of solid backbone and void space [27,23,28–36]. Though the nanoscale of the particles and pores involved preclude a complete understanding of the sintering mechanisms involved in aerogel densification, an understanding of traditional ceramic sintering processes informs design efforts for metal oxide aerogels.

The six mechanisms of sintering between two particles are shown in Figure 2.5. Mechanisms 1 to 3 are non-densifying, meaning they do not contribute to shrinkage or loss of porosity. Mechanisms 4 through 6 are densifying, meaning they move atoms from the bulk or grain boundaries to surfaces, reducing the total amount of porosity and shrinking the material. All six mechanisms are important to consider in the context of aerogel structural evolution. Mechanisms 1 through 3 will lead to particle growth, reduction of specific surface area, and loss of mesoporosity. Although these non-densifying mechanisms do not reduce *total* porosity, they do lead to the coalescence of pores into larger voids while maintaining constant pore volume. Loss of mesoporosity and formation of macroporosity increases the thermal conductivity of the aerogel. Mechanisms 4 through 6 can be catastrophic to an aerogel. Loss of total porosity of course increases density and thermal conductivity. Furthermore, the fragile solid network of a mesoporous aerogel cannot often survive the shrinkage associated with densification, leading to cracking and failure of the material.

Viscous flow is a process of coalescence of particles driven by surface tension and is an important mechanism in the early stages of aerogel sintering and densification. Most aerogels are amorphous as prepared and viscous flow can be a dominant mechanism in amorphous materials. The rate of sintering via viscous flow is given by Equation 2.2, where ρ is the bulk density, η is viscosity, and γ_{sv} is the surface tension, which is closely related to the surface energy.

$$\frac{1}{\rho}\frac{d\rho}{dt} = \frac{3}{4}\frac{(1-\rho)}{\rho\eta}\frac{2\gamma_{sv}}{r}$$ **Equation 2.2**

The rate of viscous flow, and therefore the rate of growth for bulk density, can be slowed by reducing the surface tension or increasing the viscosity. Therefore, reduction of surface tension is one possible route to improving the thermal stability of aerogels prone to densification and sintering via viscous flow.

Once the aerogel has crystallized, surface energy continues to be a critical factor in sintering and densification. Material continues to be transported to reduce total energy via densifying and non-densifying mechanisms. There are now added complications due to the anisotropy in surface energies and the balance between free surface energy and interfacial grain boundary energy. Anisotropy in surface energies arises due to different crystallographic faces of a material having different surface energies, owing to differences in atomic packing and bonding. This can lead to anisotropic crystallite growth, coarsening, and sintering. The balance between free surface energy and interfacial grain boundary energy must also be considered. The change in energy during sintering can be approximated as shown in Equation 2.3, with a change in free surface area (A_{sv}) leading to a change in grain boundary area (A_{gb}), each having their own energy per unit area (γ_{sv}, γ_{gb}). Generally, γ_{gb} is lower than γ_{sv}, but the magnitude of the difference is an important consideration in sintering, coarsening, and grain growth.

$$\Delta E = \Delta A_{sv} * \gamma_{sv} + \Delta A_{gb} * \gamma_{gb} \qquad \textbf{Equation 2.3}$$

In Figure 2.5, if one imagines the particles densifying, with matter transported from a free surface to the grain boundary between particles, the total free surface area will decrease, but the total grain boundary interfacial area will increase. Therefore, there will be a reduction in surface energy, but an increase in grain boundary energy. Prof. Ricardo Castro *et al.* provides excellent work on the concept of metastability in nanocrystalline ceramic systems, a field with much to offer the pursuit of thermally stable aerogels [37–40]. The general strategy employed in this work is leveraging a balance between free surface energies and grain boundary energies to achieve thermodynamic metastability of nanocrystalline ceramics. The particulars depend on the material system under study, but generally increasing γ_{gb} relative to γ_{sv}, will make densifying mechanisms less energetically favorable, as turning free surface area into grain boundary interfacial area does not reduce the total energy of the system as dramatically.

Most of the discussion thus far has focused on the thermodynamics of sintering and densification, *i.e.*, the driving forces behind these phenomena. These changes to the material require transport of matter and this of course has a kinetic perspective as well. The rates of sintering, coarsening, and densification are controlled by diffusivity, of which there are different values for the different species and for different routes, such as through the bulk, along a free surface, and along a grain boundary. Reducing the rate at which matter can be transported will in turn reduce how quickly the material can densify. This presents a set of parameters (bulk, surface, and grain boundary diffusivity) to minimize by choice of material (with or without additives or dopants) in order to improve thermal stability. There are also extrinsic methods to reducing mass transport, such as organic coatings to hinder mass transport in nucleated clusters or segregated impurities that exert a “solute drag” on boundaries and free surfaces [41,42]. Whether intrinsic or extrinsic, slowing mass transport in aerogels will extend the time and increase the temperature to which the mesoporous structure will remain stable.

In summary, a review of aerogel sintering and densification points to three possible parameters or strategies to employ to reduce rate of densification and improve thermal stability: reduce surface energy, increase γ_{gb} relative to γ_{sv}, and inhibit diffusion (via reduced diffusivity or pinning mechanisms). Identification of routes to achieve these changes and assessing the magnitude of their effects are important steps in achieving thermally stable aerogels for use in extreme environments.

2.2.4 Thermal stability of existing aerogels

Polymeric aerogels, which demonstrate excellent mechanical properties, are limited to temperatures below 500 °C due to the polymer network's decomposition [43,44]. Silica aerogels, perhaps the most studied and well-known, undergo significant sintering and densification above 700 °C [23,45,46]. Exploration of various metal oxides have led to mixed results. Zirconia aerogels lose much of their specific surface area (SSA) upon heating, from 282 m^2/g as dried to 92 m^2/g after two hours at 500 °C [47]. Similar reductions in SSA are observed for many lanthanide oxides by 650 °C [48]. Alumina aerogels demonstrate improved resistance to densification to 750 °C, but undergo significant sintering beyond 1000 °C upon forming α-alumina [49,50]. Doping alumina with yttria slightly improves the sintering resistance to 1100 °C [49]. The most significant improvement in thermal stability of alumina-based aerogels is realized by introduction of silica and use of a crystalline boehmite precursor [50]. In this case, a SSA of 266 m^2/g is maintained to 1100 °C with a reduction to 33 m^2/g at 1300 °C. In all cases, the extremely high specific surface areas of aerogels result in large driving forces for sintering and densification, which occur rapidly upon heating.

Beyond reductions in SSA and porosity, deleterious phase transformations contribute to shrinkage and cracking of the aerogel [51]. Silica and zirconia undergo multiple phase transformations between room temperature and targeted operating temperatures of 1200 °C. The introduction of silica into alumina aerogels inhibited phase transformations and improved thermal stability [50].

2.3 Sol-gel synthesis

The sol-gel process involves the preparation of a sol followed by transformation into a semi-rigid gel. The precursors used in the sol can be colloidal nanoparticles, metal alkoxides, or metal salts. Preparation of the sol from colloidal precursors involves stabilization of a colloid through steric, electrostatic, or electrosteric means. The sol forms a gel network by attractive surface forces between particles. For metal salts or alkoxides, the precursors must be hydrolyzed with water to form reactive hydroxyl (-OH) groups. The sol condenses and polymerizes into a gel network by condensation and polymerization of precursor species.

For any precursor, the pH must be carefully controlled to stabilize the sol and form the gel under controlled circumstances. While in solution, the precursors form polymeric or hydrated species dependent upon the precursor type, pH, and valence of metal cation. If careful control is not exerted over the reaction conditions, precipitation of insoluble species, such as the corresponding metal oxide, can occur prior to gel formation. This must be avoided to enable the formation of extended gel network. In some cases, catalysts may be necessary to initiate or accelerate the gelation process.

Once the gel is formed, it must be dried into its final form, which depends on the application. The sol-gel process provides great flexibility in the final material morphology obtained from the gel. It may be deposited on a substrate to form a film, ambiently dried to produce a powder or dense ceramic, supercritically dried to produce an aerogel, or spun into ceramic fibers [42]. The focus of this work is on supercritical drying to form the highly porous aerogel structure.

What follows is a discussion of each step in the sol-gel process, including hydrolysis, condensation, aging, and drying. The process is presented for the general case of silica sol-gel synthesis from tetraethyl orthosilicate (TEOS). This was selected as the process is well understood and serves as a baseline case to compare other sol-gel synthetic routes. Each stage in the process must be understood to exert control over the structure and properties of the final aerogel.

Once the general case is related, specific routes from metal salts via the Gash process and colloidal syntheses are described as these techniques were the primary routes used in this work.

2.3.1 Hydrolysis

Metal alkoxides are the most used precursor in the preparation of sol-gel derived materials. Most popular is the use of tetraethyl orthosilicate (TEOS) [$Si(OC_2H_5)_4$] as a precursor to silica materials. This process is referred to as the Stöber Process, its namesake from its inventor, Werner Stöber, whose group first published on the process in 1968 [52]. The precursors hydrolyze and polymerize to form small particles, these particles grow by continued condensation, and eventually the particles link into chains to form the extended gel network.

In general, the first step is the dissolution of the metal alkoxide in its corresponding alcohol. Water is then added in sufficient concentration to hydrolyze the alkoxide as follows in Scheme 2.1 The ratio of water to metal decides the particle size and crosslinking within the network [46].

$$\mathrm{M(OR)_z + xH_2O \rightarrow M(OR)_{z-x}(OH)_x + xROH} \qquad \textbf{Scheme 2.1}$$

The hydrolysis mechanism of silica species depends on the pH of the solution. Below in Scheme 2.2 is the acid catalyzed hydrolysis and Scheme 2.3 is the base catalyzed hydrolysis, courtesy of Danks *et al.* [53].

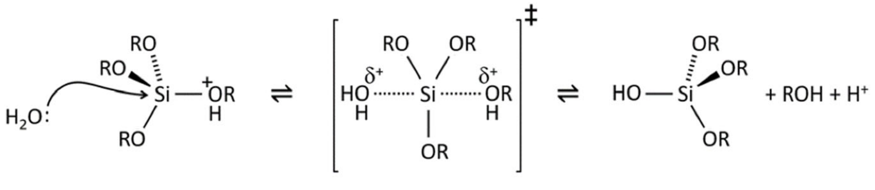

Scheme 2.2

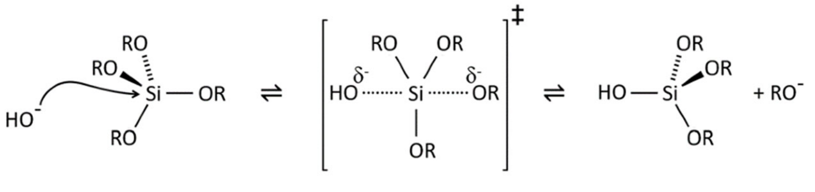

Scheme 2.3

In acid catalyzed conditions ($2 < pH < 7$), the hydrolysis occurs through nucleophilic attack of silicon by a water molecule. The alcohol acts as the leaving group, leaving behind a reactive hydroxyl group for condensation. In base catalyzed conditions ($pH > 7$), hydrolysis once again occurs by nucleophilic attack. In this case, the free hydroxyl (OH^-) group can directly attack the silicon with its negative charge. The alcohol (unprotonated) acts as the leaving group. As seen above, the final product is the same, though the rate and its dependence on reaction progress varies. The rate is a function of the stability of the transition state, which depends on the relative electron withdrawing or donating power of the -OH versus -OR group. In the case of Si-OR, an increase in length or branching of the R group decreases the rate of reaction. In Scheme 2.4 below, the relative electron density at Si is given in decreasing order for various coordination environments [54].

$$\equiv \mathrm{Si} - \mathrm{R} > \equiv \mathrm{Si} - \mathrm{OR} > \equiv \mathrm{Si} - \mathrm{OH} > \equiv \mathrm{Si} - \mathrm{O} - \mathrm{Si} \qquad \textbf{Scheme 2.4}$$

Therefore, as hydrolysis proceeds, the silicon becomes increasingly electrophilic (electron rich). In the acid catalyzed mechanism, the hydrolyzed species therefore become more stable (balance of electron rich Si and partial positive charges) and successive hydrolysis steps get progressively slower. The opposite is true in base catalyzed systems using the same line of reasoning [53,54]. This is important to consider in context of the final gel structure and connectivity as to be seen in the next section and Figure 2.7.

2.3.2 Condensation

Condensation is the reaction between alkoxy-alkoxy, hydroxyl-alkoxy, or hydroxyl-hydroxyl groups to release water and form an M-O-M bridge. The hydroxyl (-OH) group provides a reactive site for condensation and polymerization reactions to occur between species. The condensation mechanism depends on the pH of the solution. In Scheme 2.5 is the acid catalyzed condensation and Scheme 2.6 is the base catalyzed condensation, courtesy of Danks *et al.* [53].

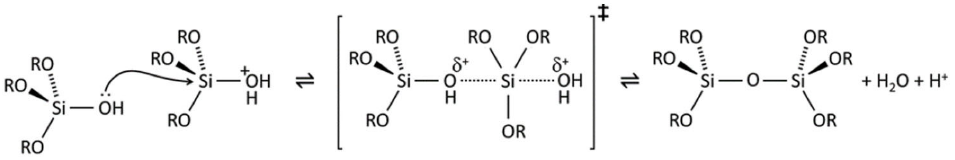

Scheme 2.5

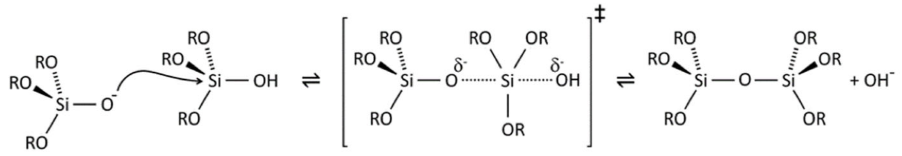

Scheme 2.6

The differences between the two mechanisms are analogous to the hydrolysis step. In acid catalyzed conditions, the neutral -OH group attacks a silicon that has a protonated group leading to a transition state with partial positive charges. In base catalyzed conditions, the negatively charged -O$^-$ directly attacks the silicon leading to a transition state with partial negative charges. The hydrolysis and condensation mechanisms have impacts on the structure of the gel. Under acid catalyzed conditions, the rate of polymerization is faster than the rate of hydrolysis. Therefore, there may only be one or two reactive -OH groups for condensation on any given silicon. This leads to long, polymeric chains with branching between chains. Under base catalyzed conditions, the rate of hydrolysis is faster than condensation. Therefore, base catalysis forms fully hydrolyzed species with four sites for reaction. Such species form highly condensed particles go on to connect, leading to strongly branched, interconnected structures as seen in Figure 2.7 [53].

These mechanisms can be extended to other metal alkoxides such as zirconium, titanium, and aluminum alkoxides. These species have lower electronegativities relative to silicon and therefore the details of partial charges, stability as a function of pH, and rates of reaction change significantly [7]. For example, the lower electronegativity results in the metal alkoxide being more prone to nucleophilic attack by water. Significant increases in the rates of hydrolysis result for Zr, Ti, and Al alkoxides, often so high that atmospheric water will hydrolyze the precursor uncontrollably, leading to insoluble precipitates that cannot condense into a gel. Such alkoxides must then be handled under inert atmospheres and carefully controlled conditions. Therefore, it would be beneficial to find alternative precursors for metals apart from silicon that can be used to form extended gel networks. To this end, researchers developed methods that utilize widely available, stable, and inexpensive metal salts, to be discussed in Section 2.3.5.

2.3.3 Aging

After formation of a solid gel with an entrapped liquid in its pores, the gel is kept in its pore liquid for a number of days. Though this may sound like a static process without any interesting characteristics, it is actually highly dynamic and leads to significant changes to the gel's properties and structure. In particular, polycondensation reactions, syneresis, and coarsening can occur while the gel ages in its solvent [46]. In particular for silica gels, the number of bridging O-Si-O bonds increases, and the number of free hydroxyls decrease. Syneresis refers to the shrinkage of the gel and subsequent pushing out of liquid of the pores. Typically, this is caused by the aforementioned polycondensation reactions, which increase the number of bridges and contracts the network. Others have suggested the driving force may be the reduction of solid-liquid interfacial area in the gel [46,55]. Coarsening, also known as Ostwald ripening, is the dissolution of the gel into a solvent in which it is soluble. The dissolved gel will then redeposit into areas of negative curvature, leading to an increase in pore size and reduction of surface area [55].

2.3.4 Drying

There are multiple routes to drying of gel materials that a number of different materials with entirely unique properties. The typical approach is conventional drying, that is elevated temperature or decreased pressure. This approach is well understood and can be divided into three stages [55,56]. First, the liquid evaporates, with the volume of liquid evaporated equal to the subsequent shrinkage of the gel. This stage results in the biggest change in mass, density, and structure. Second, the gel shrinks to a point where the strength of the solid network is enough to prevent further shrinkage caused by capillary pressure. Maximum capillary pressure results as the contact angle approaches zero and the radius of the meniscus approaches the radius of the pore, as seen in Equation 2.3 where P is capillary pressure, σ is the liquid/vapor surface energy, θ is the contact angle, and r_p is the radius of curvature of the interface [42,57].

$$P = \frac{2\sigma cos\theta}{r_p} \qquad \textbf{Equation 2.4}$$

During this stage, the solid gel typically cracks and a liquid film forms over the pore walls, which serves as a route for liquid to flow to the surface and evaporate. Third, the continuous liquid film breaks, and any remaining liquid can only leave by evaporate and diffusion through the pores to the surface of the gel. During this process, differences in pore size leads to unequal rates of evaporation and therefore unequal stresses on the pore walls, leading to pore collapse, shrinkage, and cracking. The result of the conventional drying process is a xerogel, which are typically powders. To control shrinkage, thin films are fabricated to minimize stresses associated with conventional drying. A unique chemistry-derived solution to overcome the surface energy and associated capillary pressure is modification of the pore walls with hydrophobic groups. One of the first examples of this approach involved dip coating silica gels in trimethylchlorosilane (TMCS) to form organosilyl derivatized silica which led to materials with 98.5% porosity [58].

Perhaps the most important development in drying methods for sol-gel processing is drying with supercritical fluids, known synonymously as “supercritical drying”, “supercritical fluid extraction”, or “hypercritical drying”. The result of the supercritical drying process is an aerogel, where the pore liquid has been replaced by air. As mentioned previously, Kistler made the first aerogel in the 1920s and was the inventor of supercritical drying. He demonstrated that bringing the alcohol used as the solvent for the synthesis to a temperature and pressure within the supercritical region, the pore structure was preserved by avoiding formation of a liquid-vapor interface and the associated capillary pressure. As seen in Equation 2.4, the pressure scales inversely with pore radius. A mesoporous aerogel with $r_p < 100$ nm will generate extremely large pressures that collapse the pore structure. Dr. Arlon Hunt's group at Lawrence Berkeley National Laboratory developed a supercritical drying process that replaced with alcohol with liquid CO_2, with has a much lower supercritical point than alcohols (50 °C, 80 atm) and is not flammable, making the process much safer and less energy intensive [11].

2.3.5 From metal salts via the Gash process

The development of the Gash process allows for the synthesis of metal oxide aerogels in a wide array of compositions without the use of highly reactive and often expensive metal alkoxides [59–61]. This approach involves the hydrolysis of metal salts in ethanol, followed by gelation using an epoxide that acts as a proton scavenger. Hydrolysis of the metal salt precursor forms reactive species that can then undergo condensation reactions during gelation. Below in Scheme 2.7 is an example of the hydrolysis of metal salts:

$$MCl_n \bullet mH_2O \xrightleftharpoons{H_2O} [M(H_2O)_n]^{n+} + nCl^- \qquad \textbf{Scheme 2.7}$$

To induce gelation in metal oxide systems, a gelation agent can be added, such as an organic epoxide or citric acid [59,62–65]. In organic epoxide systems, the epoxide acts as a proton scavenger, deprotonating metal-water complexes which increases their reactivity and leads to gelation. The epoxide then undergoes nucleophilic attack from a counter-ion, such as the anion of the metal salt, which leads to irreversible ring opening displayed in Scheme 2.8. The irreversible nature of the epoxide sequence of reactions leads to a homogenous and controlled rise in pH, resulting in gelation. In citric acid systems, the citric acid acts as a chelating agent. It weakly dissociates and forms complexes with the metal precursors, forming an extended backbone that can then gel upon heating [63–65].

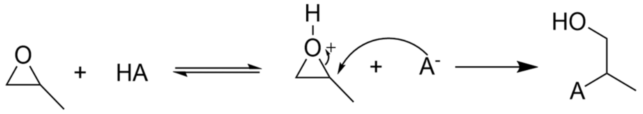

Scheme 2.8

The deprotonation of the hydrolyzed metal species by an organic epoxide is key in forming a reactive species that can undergo condensation shown in Scheme 2.9. The result of condensation is an M-O-M bond, known as an oxo bridge, and the process continues until there is an extended M-O-M network

$$[MOH_x(H_2O)_{n-x}]^{(z-x)+} \xrightarrow{[MOH_x(H_2O)_{n-x}]^{(z-x)+}} [(H_2O)_{n-x}(OH)_{x-1}M\text{-}O\text{-}M(OH)_{x-1}(H_2O)_{n-x}]^{2(z-x)+}$$

Scheme 2.9

The gels are then aged in ethanol for five to seven days and supercritically dried using carbon dioxide. The gels are washed with liquid carbon dioxide to replace ethanol in the pore structure, before bringing the carbon dioxide to its supercritical state and evacuating the fluid.

In summary, the Gash method allows for the synthesis of homogenous mixed metal oxide aerogels. In the context of the present study, this enables the study of a vast array of doped zirconia aerogels for any dopant where hydrated metal salts are readily available.

2.3.6 From colloidal precursors

In contrast to the above sol-gel syntheses from metal alkoxides and salts in solution, there is another class of sol-gel synthesis that utilizes colloidally dispersed metal oxides or hydroxides as the precursor [50,66–69]. The choice of precursor has a significant impact on the structure, as demonstrated in Figure 2.9 [53]. Gels derived from colloids (top) have particles connected by van der Waals forces, hydrogen bonding, or in some cases chemical bonding. Gels derived from hydrolysis and condensation reactions (e.g., from metal alkoxides or salts in solution) have structures resembling inorganic polymers (bottom) interconnected via covalent or ionic bonding.

The change in structure has a significant impact on the properties of the gel and the materials derived from the gel. For example, the use of aluminum chloride as a precursor favored the formation of an amorphous network of Al-O-Al tetrahedral bonding, whereas use of a crystalline boehmite precursor resulted in a gel that maintained the AlO_6 octahedral structure of the boehmite precursor [50,70,71]. This demonstrates the crystallinity of precursors can in fact be maintained into the final gel structure, which is in contrast to the standard view of a gel as an amorphous, glass-like state.

Work in this realm is not nearly as developed as sol-gel chemistry from metal salts and alkoxides. The amount of literature pales in comparison, which also means the depth of understanding of mechanisms, tunable parameters, and control over the final structure is not well understood. The nature of electrolytes in solution as well as the concentration of the colloidal precursor has a significant effect on the gel point. Furthermore, only over certain pH values will gelation occur in these systems [67]. The impacts of these various parameters are heavily dependent on the metal oxide used.

The ideas of electrostatic, steric, and electrosteric stabilization can be considered in formation of colloidal gels. Steric and electrosteric stabilization methods are not preferable in sol-gel chemistry as the bulky polymer groups prevent the necessary intermolecular interactions between metal oxide or hydroxide species. One, the steric interactions keep particles far away from one another. Two (and most important), the surface hydroxyls on the particles are blocked when polymers are functionalized or adsorbed onto the surface. Therefore, the hydroxyls cannot form strong hydrogen bonds, or in some cases covalent or ionic bonds, between the metal oxide particles. With this in mind, electrostatic interactions are the best option for synthesis of a gel from a colloidal precursor. pH and ionic strength must be carefully adjusted to (1) enable the formation of a stable colloidal suspension and then (2) slowly and controllably shift the colloid into a region of instability to flocculate the particles in a gel-like network [66,68].

2.4 Prospects for high temperature aerogels

The extremely low thermal conductivity of aerogels coupled with their low density, both enabled by a highly porous structure comprised of mesopores on the scale of 2 to 100 nm, make this class of materials promising candidates for lightweight insulation in the extreme environments of aerospace applications. The fractal solid network of interconnected nanoparticles makes for a tortuous path for heat transfer. The mesoscale pores are on the order of the mean free path of gas, even at room temperature, strongly inhibit heat transfer via convection. Their extraordinary ability to insulate have led to their use as insulation on multiple Mars rovers, but in relatively benign environments.

At high temperatures experienced during spaceflight, protection and insulation of the spacecraft structure is of paramount importance. Use of aerogels as insulation in thermal protection systems (TPS), with their low thermal conductivity and density compared to existing alternatives, would reduce TPS mass and increase operating temperature limits. Unfortunately, the highly porous nature of an aerogel is not immutable. At elevated temperatures, the vast surface area provides a large thermodynamic driving force for sintering of the solid particles and densification of the mesoporous structure. The same properties that make aerogel an extraordinary insulator also contribute to its demise at high temperatures.

To enable the use of metal oxide aerogels in the extreme environments of spaceflight, routes must be developed to stabilize the mesoporous structure at temperatures beyond 1000 °C. The development of thermally stable aerogels requires an understanding of the interplay between composition, structure, properties, and performance. This work seeks to contribute to a design framework that views aerogel thermal stability through the lens of structure and the thermodynamic and kinetic properties resulting from composition. Through the controlled synthesis of novel aerogel compositions and architectures, extensive characterization of the structure and properties of the synthesized aerogel and its evolution at high temperatures, and connection to material properties, the opportunity exists to improve metal oxide aerogel thermal stability and inform future material design efforts in the field.

2.5 Figures

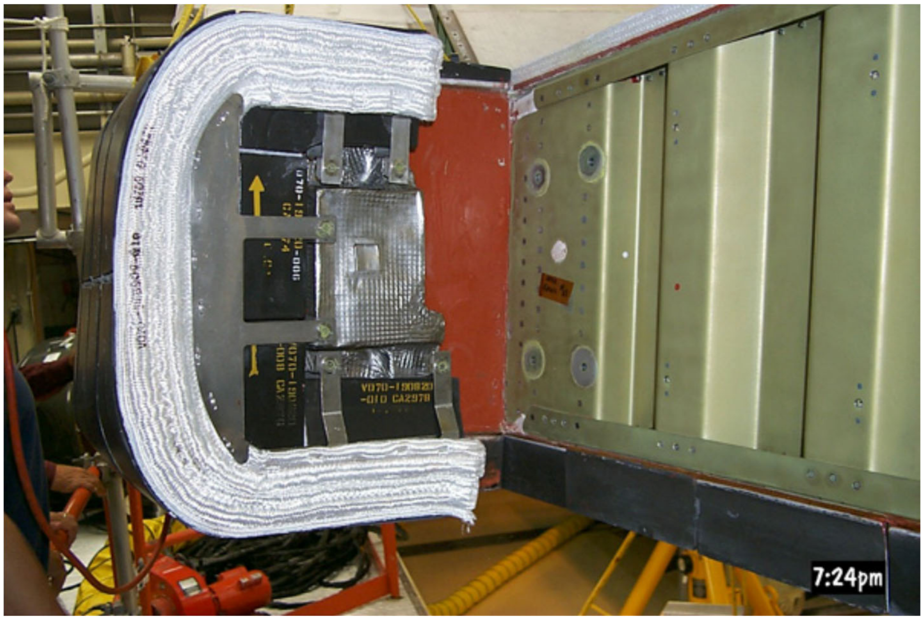

Figure 2.1: An example of a flexible thermal barrier used to seal between an RCC panel and the wingtip. The thermal barriers on the Orbiter were rated to 1093 °C. The use of aerogels in such forms of conformal insulation would afford lower thermal conductivities and lower gas permeabilities, permitting operation in more extreme environments. Image courtesy of NASA.

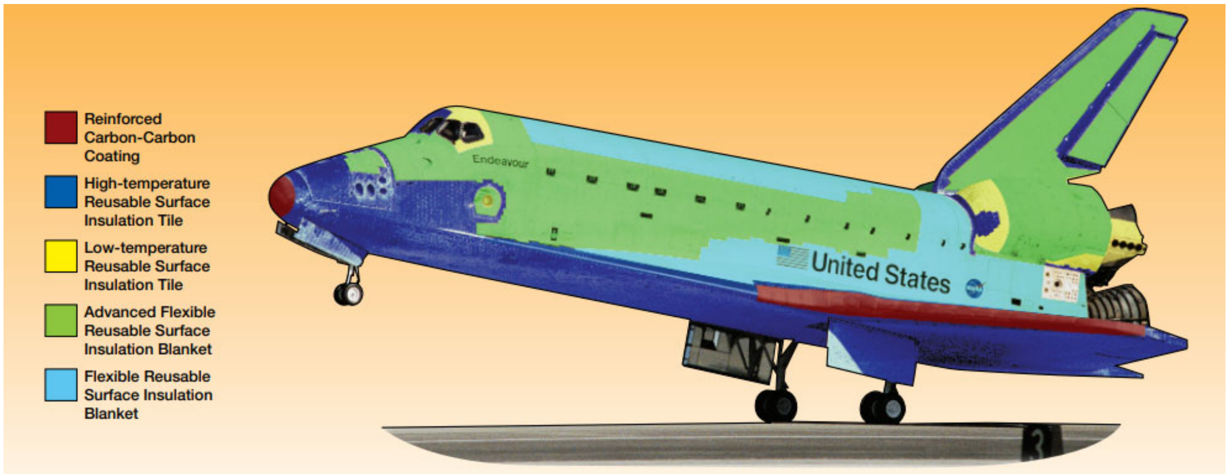

Figure 2.2: The use of TPS on the Space Shuttle orbiter varied across the vehicle depending on the heating and aerodynamic conditions. Much of the orbiter was covered in various forms of lightweight insulation, including reusable tiles and blankets, with flexible thermal barriers used in gaps between critical panels and components. Aerogels can be used in composite materials for flexible blankets and thermal barriers. Image courtesy of NASA.

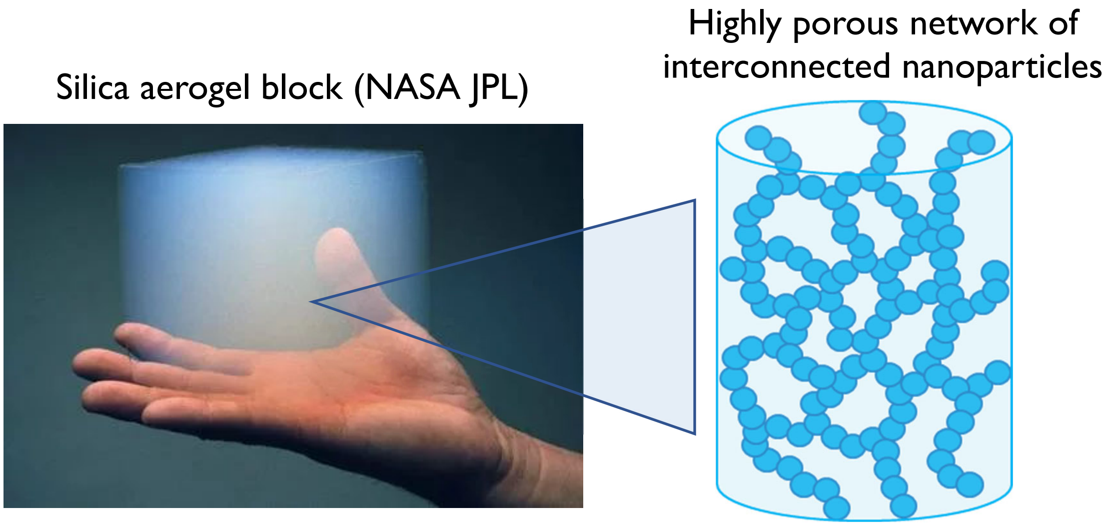

Figure 2.3: Aerogel is a highly porous (>90%), monolithic material comprised of a random network of interconnected nanoparticles. The high porosity of the aerogel contributes to extremely low thermal conductivities. The low density of the solid network creates a tortuous path for heat transfer and the small pore sizes, on the scale or even smaller than the mean free path of gas at room temperature, prevents heat transfer via convection. The aerogel image on the left is courtesy of NASA.

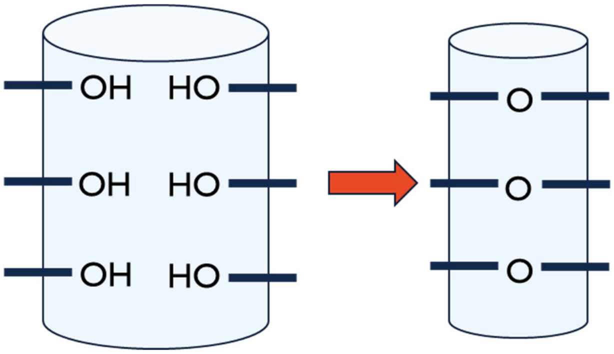

Figure 2.4: Surface hydroxyls in close proximity can condense upon heating to further drive pore collapse in metal oxide aerogels. This is one mechanism that is particularly important at low to intermediate temperatures (up to 500 °C) and can be avoid via capping of the hydroxyl groups.

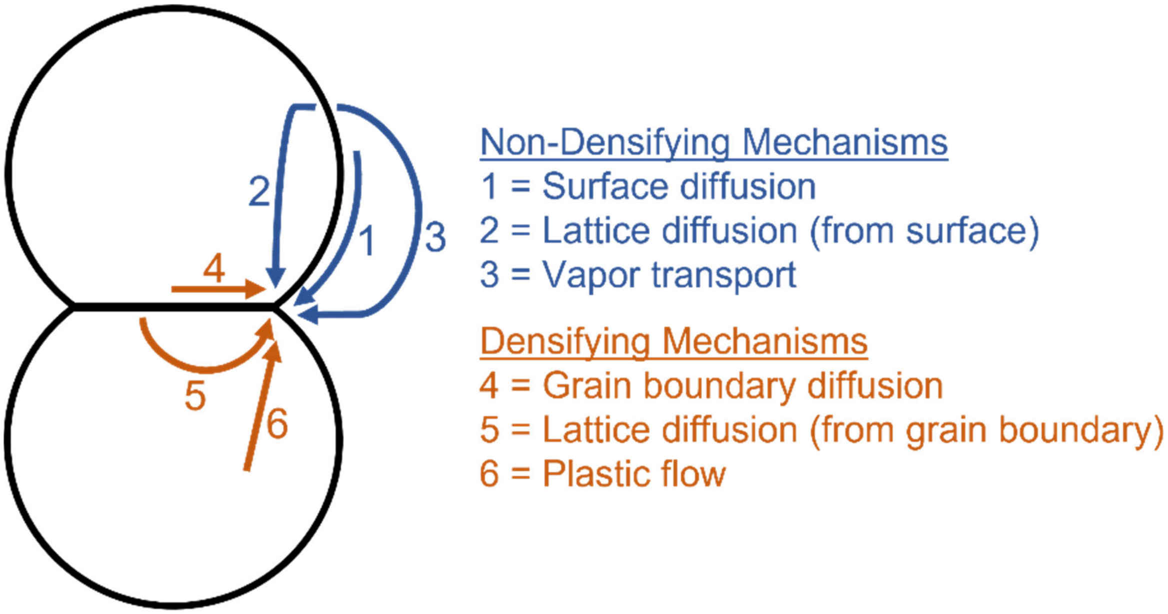

Figure 2.5: The six common mechanism of sintering for ceramics. All play a role in aerogel thermal stability, as 1 through 3 contribute to particle growth and loss of mesoporosity and 4 through 6 contribute to shrinkage and loss of overall porosity. Copyright 2003 From "Ceramic Processing and Sintering" by Mohamed Rahaman. Reproduced by permission of Taylor and Francis Group, LLC, a division of Informa plc. [72].

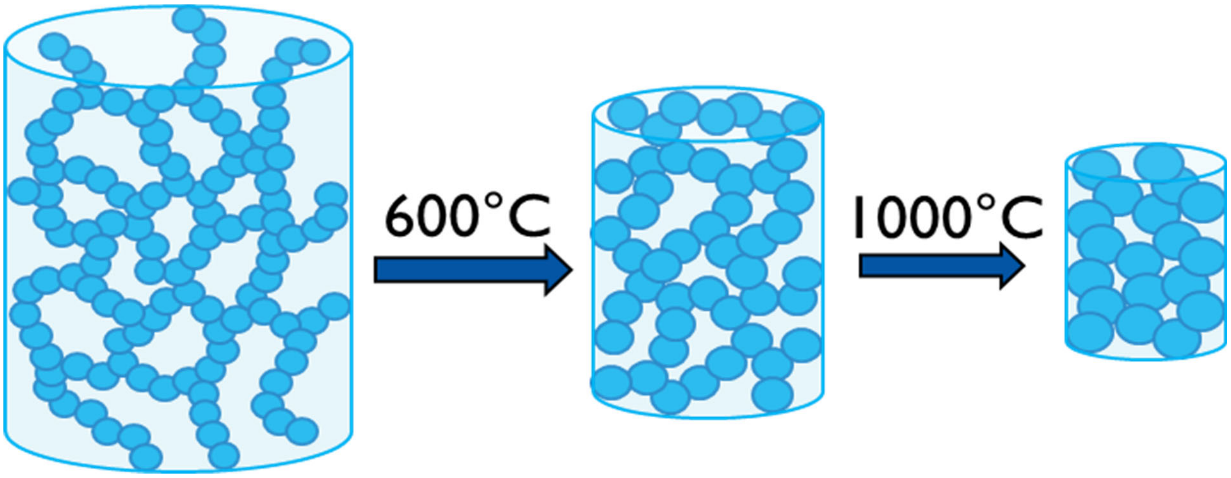

Figure 2.6: When exposed to high temperatures, the high specific surface area of aerogel provides a large driving force for sintering and densification. The particles making up the aerogel structure coalesce, grow, and begin to sinter together, eliminating the mesoporous structure. This leads to an increase in density and thermal conductivity of the aerogel as well as significant shrinkage and cracking that can lead to failure of the material.

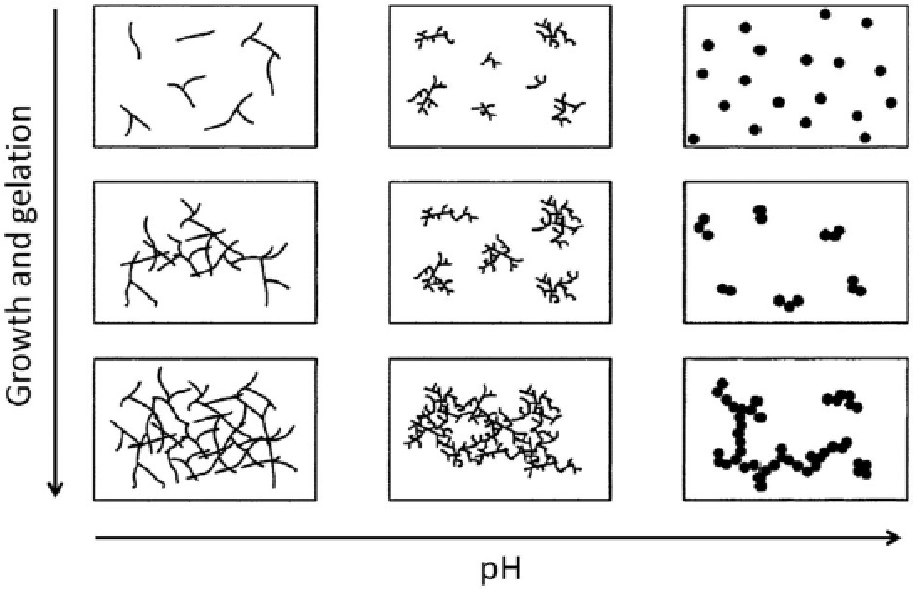

Figure 2.7: The change in gel network morphology as a function of pH and time. Low pH generally forms polymeric-like structures with weakly branched chains. Higher pH increases branching and connectivity to the point of forming a backbone that resembles spherical particles. The figure is from Danks *et al*. under a Creative Commons Attribution 3.0 Unported License [53].

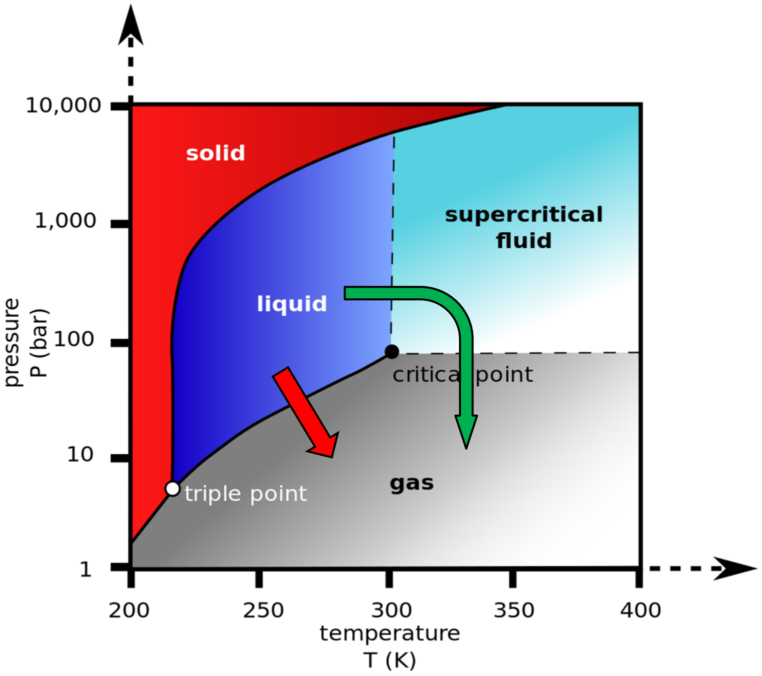

Figure 2.8: Pictured is the phase diagram for CO_2. By forming a supercritical fluid from liquid CO_2 in the pores of the aerogel and evacuating this fluid (green path), the high capillary stress and associated pore collapse resulting from a liquid-gas interface (red path) can be avoided. Image courtesy of Ben Finney and Mark Jacobs under CC0 license. (https://commons.wikimedia.org/wiki/File:Carbon_dioxide_pressure-temperature_phase_diagram.svg)

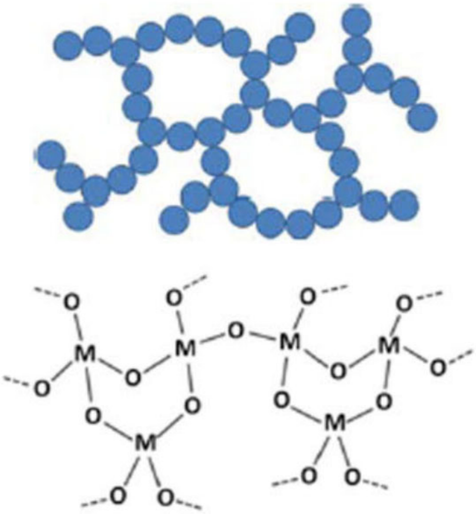

Figure 2.9: Gel network derived from colloidal precursors (top) and metal salt/alkoxide (bottom). Previous work has shown gels derived from colloidal precursors have improved thermal stability compared to their metal salt/alkoxide-derived counterparts. The figure is from Danks *et al*. under a Creative Commons Attribution 3.0 Unported License [53].

CHAPTER 3: CHARACTERIZATION OF AEROGEL STRUCTURE

3.1 Defining thermal stability

The highly porous structure of an aerogel provides extremely low thermal conductivities and densities. As described in Chapter 2, exposure to high temperatures induces rapid sintering, densification, and pore structure collapse. The high specific surface areas and the associated high total surface energy, coupled with a fragile solid network, make an aerogel prone to near total pore structure collapse at even moderate temperatures for spaceflight (600 to 1000 °C). With pore structure collapse comes an increase in thermal conductivity and density, the two parameters most relevant for aerospace TPS insulation. Therefore, in this context, aerogel thermal stability can be defined as maintaining a highly porous structure at high temperatures.

The properties selected to quantify the aerogel pore structure are specific surface area (SSA), cumulative mesopore volume (V_{BJH}), and average mesopore size (D_{BJH}), all measured via nitrogen physisorption. More detail on nitrogen physisorption and measurement of these properties is provided in 3.2. It is important to note V_{BJH} and D_{BJH} only account for pores from 2 to approximately 150 nm. Pores larger than this size are not accounted for in the pore volume or average size measurements for reasons discussed in Section 3.2.

With the properties identified, the evolution of these values with temperature defines thermal stability. Simply put, all three properties should remain as close as possible to their starting, as dried values. As dried (AD) refers to the aerogel samples following synthesis and supercritical drying, prior to any heat treatment. Maintaining a high SSA and V_{BJH} implies a highly porous structure is preserved. High SSA and V_{BJH} are correlated with low thermal conductivity and low density. Maintaining a constant D_{BJH} implies the pore structure is undergoing minimal evolution. With a constant D_{BJH}, properties such as permeability and gas convection through the material should remain constant. Properties such as bulk density and bulk shrinkage are of course relevant to thermal stability but are challenging to apply in practice because of the cracking and fracturing into irregular shapes that occur during heating.

In this work, three methods are proposed and applied to quantify differences in thermal stability between materials: absolute, relative stability (percent change), and relative stability (slope). Absolute stability is the simplest: the value of SSA, V_{BJH}, D_{BJH}, and crystallite size at a given temperature are compared for multiple samples. The higher the SSA and V_{BJH}, the higher the thermal stability at a given temperature. This analysis is useful if evaluating a material for a given application and expected environment. The second method is relative stability (percent change): the percent change of SSA, V_{BJH}, and D_{BJH} are computed over a given temperature range normalized to the starting value. This analysis normalizes the thermal stability to the starting value, which can have a strong effect on subsequent comparison at higher temperatures. It is most useful when comparing the evolution of different materials with the goal of extracting stability-property relationships to inform future design, where x represents a property.

$$Percent\ Change\ = \frac{x_{Final} - x_{Initial}}{x_{Initial}} \times 100\% \qquad \textbf{Equation 3.1}$$

The third method is relative stability (slope): the change of SSA, V_{BJH}, D_{BJH}, and crystallite size are computed over a given temperature range and divided by the change in temperature. This provides a rate (per degree) at which the structure is evolving. This analysis is useful if evaluating material performance if your desired application has a range of operating conditions where the TPS must perform. All three methods prove useful in holistically evaluating the thermal stability of aerogels for high temperature applications.

$$Slope\ = \frac{x_{Final} - x_{Initial}}{T_{Final} - T_{Initial}} \qquad \textbf{Equation 3.2}$$

The crystal structure of the aerogel also plays an important role in thermal stability. Phase transformations are associated with deleterious shrinkage and cracking of the aerogel [51]. Therefore, phase stability over expected operating temperatures and times is desirable. Small crystallite size is also essential for maintaining the highly porous structure made up of thin solid struts. If crystallites tend to grow rapidly a material, these solid struts will coalesce, and the mesoporous structure will be eliminated. Therefore, minimized crystallite growth over expected operating temperatures and times is also desirable.

3.2 Nitrogen physisorption

3.2.1 Purpose

Surface area and porosity are two of the most important properties needed to quantify and describe an aerogel's structure. The extremely high surface area and high surface-to-volume ratio of aerogels results in a tortuous path for conductive heat transfer. The small pores in many aerogels are on the scale or smaller than the mean free path of gas at room temperature and pressure of 68 nm. It is important to note at the elevated temperatures and reduced pressures associated with spaceflight, this mean free path grows significantly. The metal oxide aerogels under study in this work have pores from 10 to 150 nm and can generally be described as mesoporous. Nitrogen physisorption provides information on the pore structure near the mesopore range, generally limited to measuring pores from 2 nm to around 150 nm. Therefore, this technique is well-suited to describing the properties relevant to the use of aerogels as high-performance insulation in extreme environments.

Nitrogen physisorption is performed to provide three values: specific surface area (SSA), cumulative mesopore volume (V_{BJH}), and average mesopore size (D_{BJH}). SSA is reported in m^2/g and calculated via application of the method of Brunauer, Emmett, and Teller (BET) [73].

Cumulative mesopore volume captures pores from 2 nm to 150 nm and is reported in cm^3/g. Average mesopore size is reported in nm. Pore volume and pore size are calculated via application of the method of Barrett, Joyner, and Halenda [74]. A description of the process of adsorption and a brief overview of these calculation techniques follows.

Physisorption is a specific type of adsorption where the adsorbable gas (adsorptive) is attracted to the surface of a solid (adsorbent) via physical forces without the formation of chemical bonds. These forces are generally the family of van der Waals forces, including London dispersion, Debye, and Keesom forces [75]. For these forces to not be overcome by thermal fluctuations, the analysis must be performed at low temperatures. Nitrogen is often used as an adsorbent as it is inert, relatively inexpensive, has a well-known molecular size, and can also be used in its liquid form ($T_{bp} = 77$ K) to reduce the temperature of the sample. Physisorption of nitrogen onto the solid surface takes place in two general stages and a third stage for mesoporous materials. First, a monolayer of nitrogen adsorbs to the surface. Calculation of the amount of nitrogen required to form this monolayer is the basis of BET theory for determination of SSA [73]. Second, nitrogen adsorbs to itself to form multilayers. Third, in the case of mesoporous materials, capillary condensation of nitrogen takes place, where the gas condenses into a liquid in a pore at a pressure less than the saturation pressure of the bulk liquid. This behavior allows for determination of mesopore volume and size via BJH theory [74].

During a physisorption experiment, the amount of gas adsorbed (generally reported in mol adsorbent per g adsorbate) is tracked as a function of relative pressure p/p^o, where p is the pressure in the test vessel and p^o is the saturation pressure of the adsorbent at the test temperature. The experiment is performed as pressure is increased from zero to p^o and back from p^o to zero. The plot of amount of gas adsorbed as a function of relative pressure, at constant temperature, is called an isotherm. Isotherms are grouped into categories based on appearance according to guidelines set by the International Union of Pure and Applied Chemistry (IUPAC) shown in Figure 3.1 [75]. These isotherm shapes have been shown to be closely related to specific pore structures and was most recently updated in 2015 with an expansion from six to eight unique classifications.

In this work, samples analyzed provided Type IV(a) isotherms. Type IV are given by mesoporous materials where the dominant interactions are adsorbent-adsorbate (initial rise and plateau) and adsorbent-adsorbent within mesopores (second rise and plateau). Type IV(a) isotherms arise when capillary condensation is accompanied by hystersis. For nitrogen at 77 K, hysteresis occurs when pores larger than 4 nm are present. The adsorption branch requires nucleation of the liquid phase to begin capillary condensation and is not in thermodynamic equilibrium. The desorption stage is equivalent to a reversible liquid-vapor transition and equilibirum is established.

Hystersis can also result from network effects and pore blocking in more complex pore structures. The IUPAC provides six unique classifications of hystersis loops based upon their shapes [75]. Four of these classifications are shown in Figure 3.2 with schmatics of the pores that produce these unique loop shapes [76]. Materials under study here generally resemble H1, indicitative of a narrow range of uniform mesopores, or H2(b), indicative of more complex pore structures with network effects where the distribution of pore neck widths are quite large. Overall, important information on the structure of the porosity in an aerogel can be gleaned from the appearance of the isotherm and hysteresis loop.

Application of the BET method for SSA and BJH method for D_{BJH} and V_{BJH} provides a quantitative evaluation of the mesopore structure. For the BET method, the specific amount adsorbed (n) at relative pressure (p/p^o) is used in the following form given in Equation 3.3, where the left-hand side of the equation is plotted as a function of p/p^o. n_m is the specific monolayer capacity and C is the "BET parameter," which is exponentially related to the energy of monolayer adsorption.

$$\frac{p/p^o}{n(1-p/p^o)} = \frac{1}{n_m C} + \frac{C-1}{n_m C}(p/p^o) \qquad \textbf{Equation 3.3}$$

Data from the adsorption branch is used from p/p^o of 0.05 to 0.3. Over this range, the BET equation is linear and the slope, $(C-1)/(n_mC)$, and intercept, $1/(n_mC)$, can be calculated. These two values and equations can be used to compute C and n_m. The monolayer capacity (n_m) can then be applied in Equation 3.4 to find the BET specific surface area (a_s in m^2/g) from the molecular cross-sectional area (σ_m), Avogadro's number (L), molar volume of the gas (M_v), and mass of the adsorbent (m).

$$a_s = \frac{n_m L \sigma_m}{m M_v} \qquad \textbf{Equation 3.4}$$

Methods to assess mesoporosity in terms of pore volume and pore size distributions are based upon the Kelvin equation shown in Equation 3.5. This equation relates the change in vapor pressure (p) due to a curved liquid-vapor interface, such as the inside of a cylindrical pore, via the surface tension (γ) of the bulk fluid, the radius of the pore (r), adsorbed multilayer film thickness (t_c) and the molar liquid volume (V_m). R is the ideal gas constant and T is the temperature.

$$\ln\left(\frac{p}{p^o}\right) = -2\gamma V_m/RT(r - t_c) \qquad \textbf{Equation 3.5}$$

The method of Barrett, Joyner, and Halenda uses a modified version of the Kelvin equation applied to the isotherm data to compute pore volume and pore size distributions [74]. Care should be taken when applying the BJH method and other methods that employ the Kelvin equation to materials with pores smaller than 10 nm, at which point macroscopic theories no longer apply. If pores below 10 nm are present and of interest, recently developed methods employing densify functional theory (DFT) should be used [75].

3.2.2 Methodology

Aerogel samples used in nitrogen physisorption were both ground and unground. Initial analyses used aerogels ground in a mortar and pestle, though later studies proved this step was unnecessary and did not change the resulting pore structure properties. The mass of the sample was determined as the mass to give less than 2% instrument error in BET SSA value. The equation provided by Micromeritics to calculate the percent error in SSA (y) is the following, where x is the total area analyzed in m^2.

$$y = 0.38x^{-1} \qquad \textbf{Equation 3.6}$$

This technique requires an estimate of the SSA of the sample in m^2/g. Estimates used were generally 400 m^2/g (as dried), 150 m^2/g (600 °C, 20 min), 50 m^2/g (1000 °C, 20 min), and 20 m^2/g (1200 °C, 20 min). As a rule of thumb, 20 m^2 of surface area in the tube was targeted which provides 1.9% instrument error. Using excess sample can lead to program failure due to the amount of nitrogen required to adsorb onto the available surface area. A more in-depth analysis of error present in nitrogen physisorption methods is covered in the following Section 3.2.3, but it is prudent to note that this target of less than 2% error covers just instrument error and not error and variability resulting from mass measurements and sample inhomogeneity.

The mass of the empty tube, filler rod, and seal was obtained, the sample was added, and the mass of the tube, rod, seal, and sample was then collected. The samples were degassed on a Micromeritics Smart VacPrep under vacuum at 80 °C for 6 h. The mass of the tube, rod, seal, and sample was collected again. This measurement was used to calculate the final mass of the sample being analyzed. Analysis was performed on a Micromeritics 3Flex Adsorption Analyzer. The sample tubes were insulated with isothermal jackets, installed on the instrument, and submerged in a bath of liquid nitrogen. A 40-point sorption/desorption program was used to quantify the mesopore structure of the sample. The relative pressure ranges (p/p^o) and their corresponding pressure increments were 0.000 to 0.050 at 0.0375, 0.050 to 0.300 at 0.0500, 0.300 to 0.997 at 0.0150, and 0.997 to 0.300 at 0.0150.

From the reports generated via the Micromeritics software, the BET SSA, V_{BJH}, and D_{BJH} were obtained. For SSA, the BET report was evaluated to ensure a reasonable range of p/p^o was selected, generally between 0.05 and 0.3. Furthermore, the data as described in Equation 3.3 were ensured to be linear over this region. The single point desorption total pore volume of pores below a given size and a given pressure (generally for $2 \text{ nm} < D < 193 \text{ nm}$ and $p/p^o = 0.99$) was reported as V_{BJH} (in cm^3/g). The pore size distribution was also obtained from the BJH Desorption dV/dlog(D) pore volume with the Harkins and Jura Faas Correction. The distributions were plotted with dV/dlog(D) in cm^3/g as a function of pore diameter (nm). D_{BJH} (in nm) was provided via the BJH Desorption average pore width (4V/A).

3.2.3 Study of error

As described previously, instrument error in SSA can be estimated via a simple relationship requiring only the total area being analyzed to be known. This does not consider error arising from the two measurements of mass used to find the mass of the sample and possible inhomogeneities within the sample. Aerogel samples prepared in different synthesis, but identical parameters and conditions, were used. Four conditions were selected for the aerogel samples: as dried and after heat treatments at 600 °C, 1000 °C, and 1200 °C (each ramped at 600 °C/h with a 20 min hold). It is important to note this analysis was performed prior to the decision to use 20 m^2 of area in each analysis and ultimately was used to inform this decision. In many cases, less than 20 m^2 of area was analyzed and the instrument error was likely high in these cases. In Table 3.1, the average value and standard deviation of BET SSA, V_{BJH}, and D_{BJH} is included, along with the percent deviation for each of these properties.

Percent deviations were generally less than 10%, apart from samples heat treated at 1200 °C. To better understand the magnitude of these errors, it can be compared to instrument error from Equation 3.6. The average value of instrument error and measured percent deviation are compared for each condition in Table 3.2.

For as dried and 600 °C samples, the measured deviation exceeded the instrument error. This suggests that this error stems from variations between synthetic batches. As the samples are heat treated to higher temperatures, the instrument error in this study exceeded the measured percent deviation. The high instrument error at 1000 and 1200 °C, 8.7% and 17.0%, respectively, motivated the use of additional sample for materials heat treated to these temperatures.

The appearance of pore size distributions was used to compare samples throughout this work. To this end, comparing the variability in pore size distributions within the error study was important to evaluate the usefulness of such comparisons. Figure 3.3(a-d) compares the pore size distributions for as dried, 600 °C, 1000 °C, and 1200 °C samples. Most variability is seen in the as dried pore size distributions, which again suggests there is some degree of variability between synthetic batches. Figure 3.3(a) also includes the as dried pore size distribution for an aerogel with a different composition (15 mol% $YO_{1.5}$ in ZrO_2, whereas all other samples are 30 mol% $YO_{1.5}$). This shows the clear difference between compositional variants, suggesting the error does not diminish the ability to leverage pore size distributions to understand the impact of composition, synthetic parameters, and synthetic approach on mesopore structure.

3.3 Scanning electron microscopy (SEM)

3.3.1 Purpose

Aerogel morphology is influenced by synthetic approach, synthetic parameters, composition, and heat treatment. These influences span multiple length scales, from the primary particles, mesoporous structure (2 to 50 nm), macroporous structure (>50 nm), and macroscale texture. Scanning electron microscopy (SEM) is well-suited to evaluate the macroporous structure and the morphology of the aerogel backbone, which can be made up of spherical particles, fibers, or platelets. In the as dried state, the primary mesoporous structure is too small to be resolved by SEM and the focus is on the morphology of the macroporous structure and overall aerogel solid network. As the materials are heat treated, the pores coarsen, and particles grow. SEM is able to capture this evolution and can even be used to estimate macropore size and grain size in samples that have densified significantly. The qualitative information provided by SEM changes depending on the state of the material (as dried versus heat treated) and provides complementary analysis to the quantitative pore structure data provided by nitrogen physisorption, which is limited to 2 to 150 nm.

3.3.2 Methodology

Metal oxide aerogels are prone to strong charging with SEM if not properly mounted and imaged under the correct conditions. A small amount of aerogel is crushed and applied to carbon tape on the SEM stub. Minimal sample should be used to allow for efficient charge transfer from the sample to the carbon tape. Low accelerating voltage and current minimize the charging effect. The working distance should be minimized, which improves image resolution given the low accelerating voltage. In this work, aerogels were primarily imaged using a Hitachi S4800 at 2 kV accelerating voltage, 10 μA current, and 5 mm working distance. The mixed (M) detector setting was found to offer the best image quality for most aerogel samples. Images are collected at 45kx, 60kx, and 80kx. At a working distance of 5 mm, these magnifications maximize the available resolution on the microscope given the operating conditions. If larger features are identified in a sample, images are also collected at lower magnifications.

No coating was applied to the samples. Previous work has demonstrated coating mesoporous samples prior to SEM results in false morphology and the coating structure to be the focus of the image rather than the aerogel structure [77].

3.4 X-ray diffraction (XRD)

3.4.1 Purpose

X-ray diffraction (XRD) provides insight to the crystalline structure of a material. In the context of aerogels, the most pertinent abilities of XRD are identification of any crystalline phases present and a measure of the average crystallite size. In most aerogels, the as dried material is x-ray amorphous, so XRD is employed following heat treatments. Identification of crystalline phases can suggest if the synthesis employed was successful and achieved the target composition. Phase formation, or lack thereof, can also identify segregation of components within a material. There are situations where phase formation is a convolution of composition and particle size, as is the case with zirconia [78]. Therefore, care should be taken when using phase formation to infer chemical composition.

Lattice parameters are related to the phase and its chemical composition, among other parameters. In doped zirconias, lattice parameters shift as a function of dopant identity and amount so the lattice parameter can also be used to estimate the chemical composition. Overall, the crystalline phase influences a broad range of properties, including diffusivities, interfacial energies, kinetics of crystallite growth, mechanical properties, and more. These properties are intimately intertwined with aerogel structural evolution and thermal stability. The identity of phase(s) present and their evolution are key properties to know as part of a holistic understanding of aerogel structure and evolution.

As discussed in Section 3.1, crystallite size is an important parameter for aerogel thermal stability. If crystallites grow rapidly and to sizes larger than 100 nm, it is highly unlikely that a fine mesoporous structure of pores 2 nm to 100 nm is being maintained. The breadth of XRD peaks is related to the crystallite size via the Scherrer equation shown below in Equation 3.7. D is the crystallite size (nm), C is the Scherrer constant (typically taken as 0.9), λ is the x-ray wavelength (nm), β is the peak width at half the maximum intensity (radians), and θ is the Bragg angle.

$$D = C\lambda/\beta cos\theta \qquad \textbf{Equation 3.7}$$

This equation can be applied directly to fits of the peaks to provide crystallite size as to be discussed in Section 3.4.3. Alternatively, full pattern fitting methods such as Rietveld refinement can be employed to provide crystallite size as to be discussed in Section 3.4.4.

3.4.2 Methodology

Samples for XRD were crushed with a mortar and pestle. The powders were deposited via suspension in 200 proof ethanol onto low background holders. XRD was performed using Cu Kα radiation on a Bruker D8 Advance XRD. Scanning conditions were 10 to 100° 2θ, 0.02 degrees per step, and 0.25 seconds per step. Parallel beam geometry was used with a 0.2 mm divergence slit and a panoramic Soller slit. The goniometer had a radius of 280 mm.

3.4.3 Crystal structure via peak fitting

Individual peak fitting is one method to quantify crystallite size from XRD data via application of the Scherrer equation (Equation 3.7). Once values of crystallite size are computed for individual peaks, there are several methods available to determine a final crystallite size, including use of single peaks, average of all peaks, and several weighted methods [79]. In this work, OriginPro® (v. 9.6.0.172) was used to fit the XRD data and provide peak positions and peak widths assuming Gaussian peak shapes. The Scherrer equation was applied to each peak to calculate D/C. This does not provide an absolute measurement of crystallite size but does allow for comparison between samples. An average value was obtained by averaging the D/C value of each peak.

For single phase systems with simple XRD patterns, a combination of peak positions and a visual inspection can be adequate to identify the phase present via comparison with known patterns. Bragg's law shown in Equation 3.8 is used to find the grating constant (d) from the diffraction order (n), peak position (θ), and x-ray wavelength (λ).

$$n\lambda = 2dsin\theta \qquad \textbf{Equation 3.8}$$

For cubic systems, which were the focus of study when this methodology was employed, the lattice parameter (a) can be obtained via the following relationship in Equation 3.9 where h, k, and l are the Miller indices of the Bragg plane. For the cubic YSZ system, the lattice parameter (a) was taken as the average of *a* for the (111), (200), (220), and (311) planes.

$$a = d\sqrt{h^2 + k^2 + l^2} \qquad \textbf{Equation 3.9}$$

3.4.4 Crystal structure via Rietveld refinement

Whole pattern fitting, such as the Rietveld refinement, uses the XRD pattern to provide many properties of the material's structure. From peak position, unit cell parameters are calculated. From peak intensity, atomic parameters and preferred orientation may be inferred. Peak shape provides a measure of crystallite size and/or strain. These properties and more can be provided via a non-linear least squares method [80]. For this work, the majority of Rietveld refinements were performed in GSAS II (v. 4783) to identify crystalline phase, calculate lattice parameter(s), and calculate crystallite size using structural data from the Crystallography Open Database (http://www.crystallography.net/cod/) [81]. Rietveld refinement as implemented in the JADE (Materials Data, Inc.) software package was also used in conjunction with the International Center for Diffraction Data (ICDD) crystallographic database for some analysis.

3.5 Fourier transform infrared spectroscopy (FTIR)

3.5.1 Purpose

Fourier transform infrared spectroscopy (FTIR) is a technique used to obtain information on the bonds and surface groups within an aerogel. For mixed metal oxide aerogels, it can be used to provide information on the bonding between and within the metal oxides used in the material. FTIR can also be used to estimate the degree to which residual carbon (from the synthetic precursors) is incorporated to the structure and the relative amount of surface hydroxyl groups. The bonding and surface chemistry of the aerogel will change as a function of synthetic route and the degree of heat treatment. In this work, the primary purpose of FTIR was to understand the structure and evolution of post-synthetically applied metal oxide layers on the aerogel free surfaces via a liquid alkoxide deposition method. FTIR was also used in efforts to measure the degree of functionalization for yttria nanoparticles with surfactants for colloidal stabilization.

3.5.2 Methodology

During the following steps, extreme care must be taken to avoid any source of contamination. All equipment and material that encounters the sample should be thoroughly cleaned and completely dried before use. For each measurement, approximately 25 mg of sample was required to ensure extra sample remained for repeat runs. The samples were lightly ground in a clean mortar and pestle. The powders were added to open-top vials and dried at 80 °C in air for 24 h. A small portion of the sample was then added to KBr which was ground together and pressed into a pellet. The ratio of sample to KBr is dependent on the absorption characteristics of the specific sample and therefore had to be adjusted following the first round of data collection. If absorption reaches 100% at any point in the spectrum, a lower ratio of sample to KBr is required. On the other hand, if absorption is low and noise dominates the spectrum, a higher ratio of sample to KBr is required. The pellet was loaded into the instrument. The Nicolet Nexus 670 FTIR was used in this work and collected data in transmission mode from 4000 to 800 cm^{-1}.

By identifying the functional group and/or bond corresponding to a given peak from literature or reference material, the magnitude and shape of the peak could be compared between samples to identify the presence of a given bonding motif and its relative amount.

3.6 Colloidal characterization

3.6.1 Purpose

As described in Section 2.3.6, the use of colloidal precursors for synthesis of aerogels offers the potential for improved thermal stability. To the author's knowledge, there is no existing synthetic route to mesoporous stabilized zirconia aerogels from colloidal precursors of zirconia and/or the stabilizing metal oxide (yttria, ytterbia, gadolinia, etc.). It was therefore sought to develop such a synthesis, and this requires the preparation and characterization of a stable colloid of zirconia and/or yttria precursors. The two properties of interest are particle size and colloidal stability. Particle size must be small enough to form a mesoporous structure with pores between 2 and 100 nm. Particles beyond 100 nm will not be conducive to forming such a structure. Colloidal stability refers to the tendency of particles to flocculate as well as settle. Flocculation will lead to increase in particle size and settling will lead to inhomogeneities in the final gel. Therefore, high colloidal stability, at least over time scales of hours to days, is desired. In this work, a Malvern

Zetasizer Nano ZS, which operates on the principles of Dynamic Light Scattering (DLS), was used to measure particle size distributions and zeta potential for zirconia and yttria colloids.

3.6.2 Sample guidelines

Sample preparation has strong influences over the properties measured with the Zetasizer. In particular, concentration of particles in solution can influence the measurement and, if not chosen carefully, lead to wildly inaccurate results. With regards to developing guidelines for preparing samples in this work, I would like to give my sincere thanks to Prof. Dr. rer. nat. Michael Bredol at FH Münster for his advice on colloid ball milling and target sample concentrations for yttria colloids based upon his work on yttria colloids [82].

Target sample concentrations for the yttria system, the primary focus of this work, were on the order of 0.1 g/L. The optical measurement system on the Malvern Zetasizer provides nonphysical results if the colloid being analyzed is too concentrated or strongly absorbing. Choosing the proper concentration is not enough to achieve consistent, repeatable results. This also requires dispersing the particles well. For most metal oxide systems, the metal oxide powder will need dispersed via some energetic method prior to measurement. In this work, the methods used were bath sonication, ultrasonication, and colloidal ball milling. Following dispersion, time must be tracked as the powders often have the tendency to settle quickly. Time after dispersion is a key parameter that ultimately must be studied to provide a measure of colloidal stability. Generally, Zetasizer measurements were taken as soon as possible following dispersion.

3.6.3 Particle size and zeta potential measurements

Colloids were prepared by adding the desired powder into DI water or 200 proof ethanol. Typical target solids loadings were 10 to 20 wt. %. The powder was then further dispersed via bath sonication, ultrasonication, or ball milling. Immediately following dispersion, a small amount of the colloid was removed and diluted with additional DI water or ethanol to 0.1 g/L. This diluted colloid was added to a Malvern Folded Capillary Zeta Cell (Malvern Panalytical #DTS1070). The cell was held upside down and the colloid was injected to the halfway point of the channel using a syringe, at which point the cell was flipped right-side up and the channel was filled to the full mark. This procedure ensured no air bubbles were trapped. At this point, the cell could be loaded into the instrument for both size distribution and Zeta potential measurements.

The Malvern Zetasizer used in this work is capable of measuring particles in the range of 0.6 nm to 6 μm. The included software provides an indication of "data quality" that is generally reliable. If data quality was "Good", the test should be rerun a minimum of three times to ensure a constant size distribution. In Figure 3.4, (a) shows a stable colloid with high quality data, evidenced by the constant size distribution, whereas (b) shows either an unstable colloid or unreliable data. The drift towards larger particle size suggests the particles are flocculating. A similar method was used for measuring Zeta potential, with any sample of "Good" data quality run a total of three times as a measure of stability.

3.7 Figures and tables

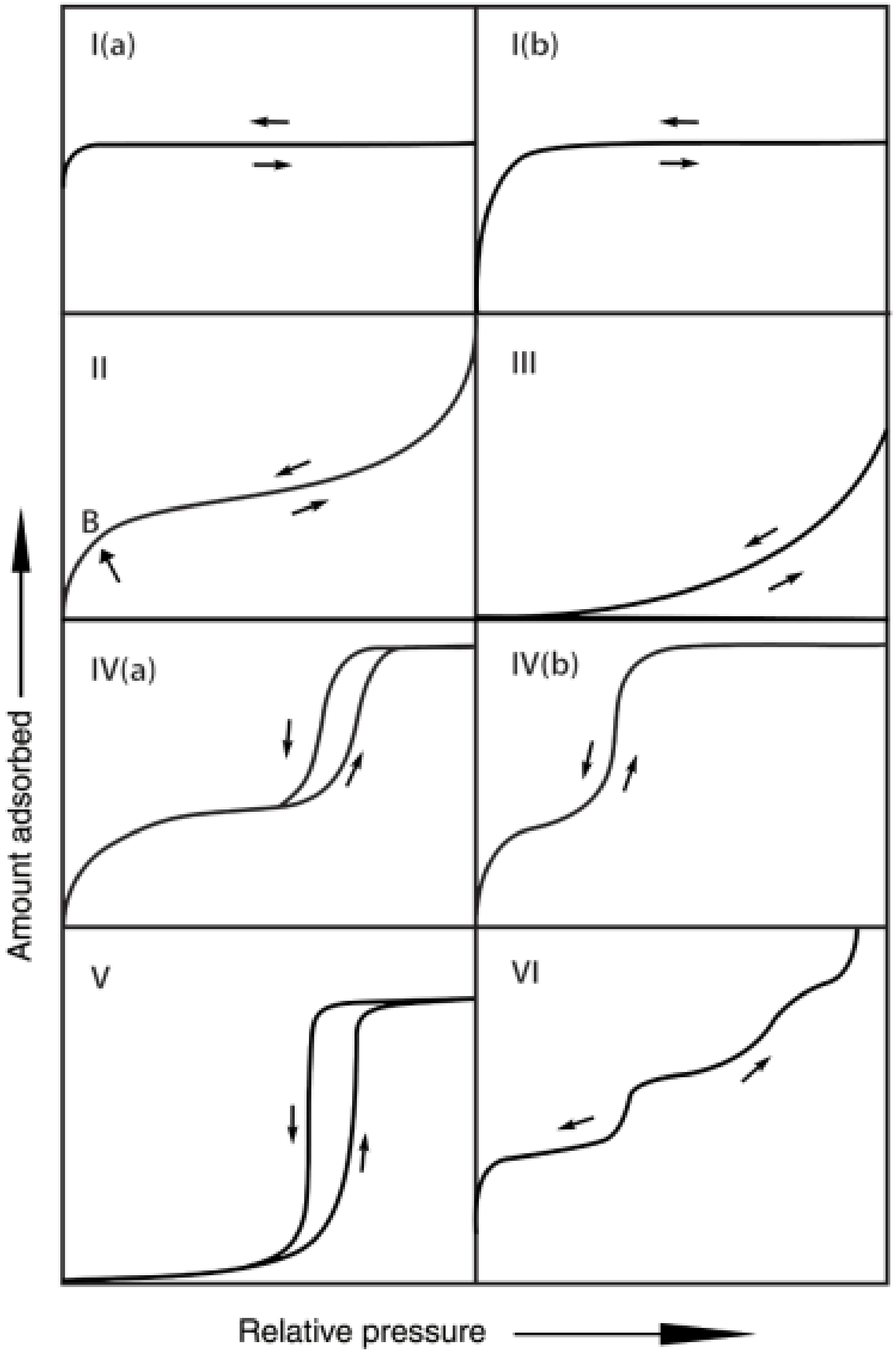

Figure 3.1: The eight isotherm classifications according to the 2015 IUPAC report on nitrogen physisorption. Most materials in this study are Type IV(a), indicating the material is mesoporous. The figure is courtesy of Thommes *et al.* [75].

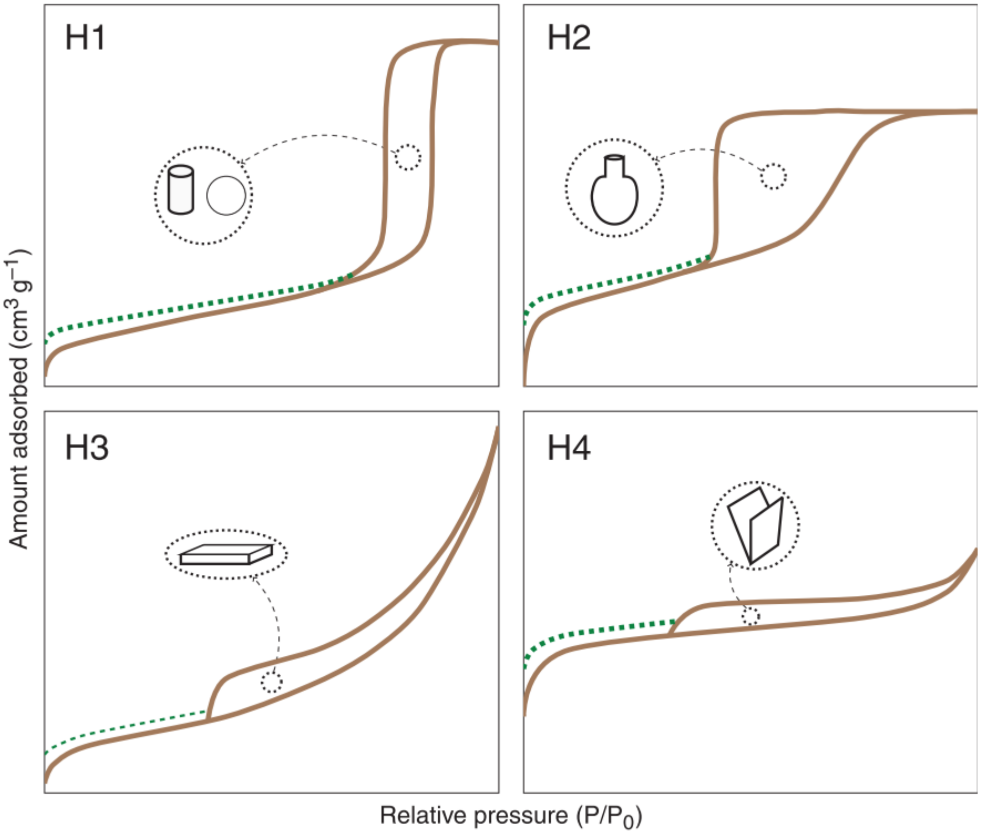

Figure 3.2: Four of the six classifications of hysteresis loops with schematics of the pore shape that produces a given hysteresis loop. In this work, the hysteresis loops resemble H1, indicative of cylindrical mesopores with a narrow size distribution. The figure is used with permission from Bardestani *et al*. [76].

Table 3.1: Mean and standard deviation (μ ± σ) for each property reported from nitrogen physisorption along with percent deviation in parentheses. The sample size was 5 for as dried, 600, and 1000 °C and 4 for 1200 °C.

Condition	**SSA (m^2/g)**	**V_{BJH} (cm^3/g)**	**D_{BJH} (nm)**
As Dried	489 ± 46 (9.3%)	2.92 ± 0.20 (6.8%)	25.8 ± 1.3 (4.9%)
600 °C	151 ± 9 (6.2%)	1.08 ± 0.03 (3.1%)	25.5 ± 0.6 (2.5%)
1000 °C	47.0 ± 3.4 (7.3%)	0.50 ± 0.01 (2.0%)	36.5 ± 2.6 (7.2%)
1200 °C	18 ± 2 (10.2%)	0.20 ± 0.02 (10.9%)	48.2 ± 5.7 (11.9%)

Table 3.2: The average area analyzed for each condition was obtained by multiplying the measured SSA by the mass of the sample. The calculated instrument error is the result of using this value in Equation 3.6. The measured percent deviation was lower than the expected instrument error for 1000 and 1200 °C.

Condition	Average Area Analyzed (m^2)	Calculated Instrument Error (%)	Measured Percent Deviation (%)
As Dried	39	1.0	9.3
600 °C	15	2.8	6.2
1000 °C	4.8	8.7	7.3
1200 °C	2.3	17.0	10.2

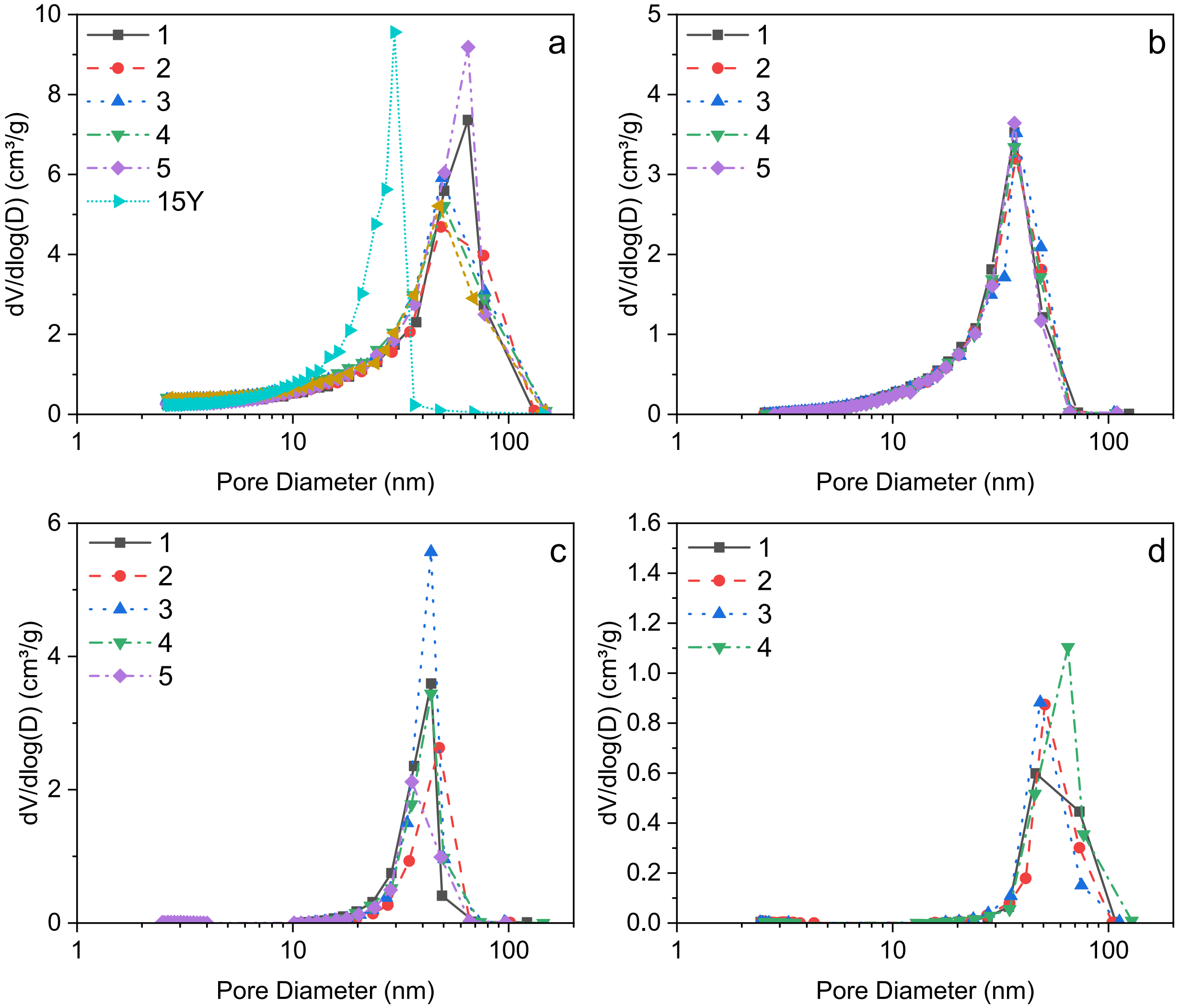

Figure 3.3(a-d): BJH desorption pore size distributions for repeats at (a) as dried, (b) 600 °C, (c) 1000 °C, and (d) 1200 °C. A different compositional variant (15Y) is included in (a) to demonstrate the greater difference in pore size distribution between unique samples compared to repeats of an identical variant.

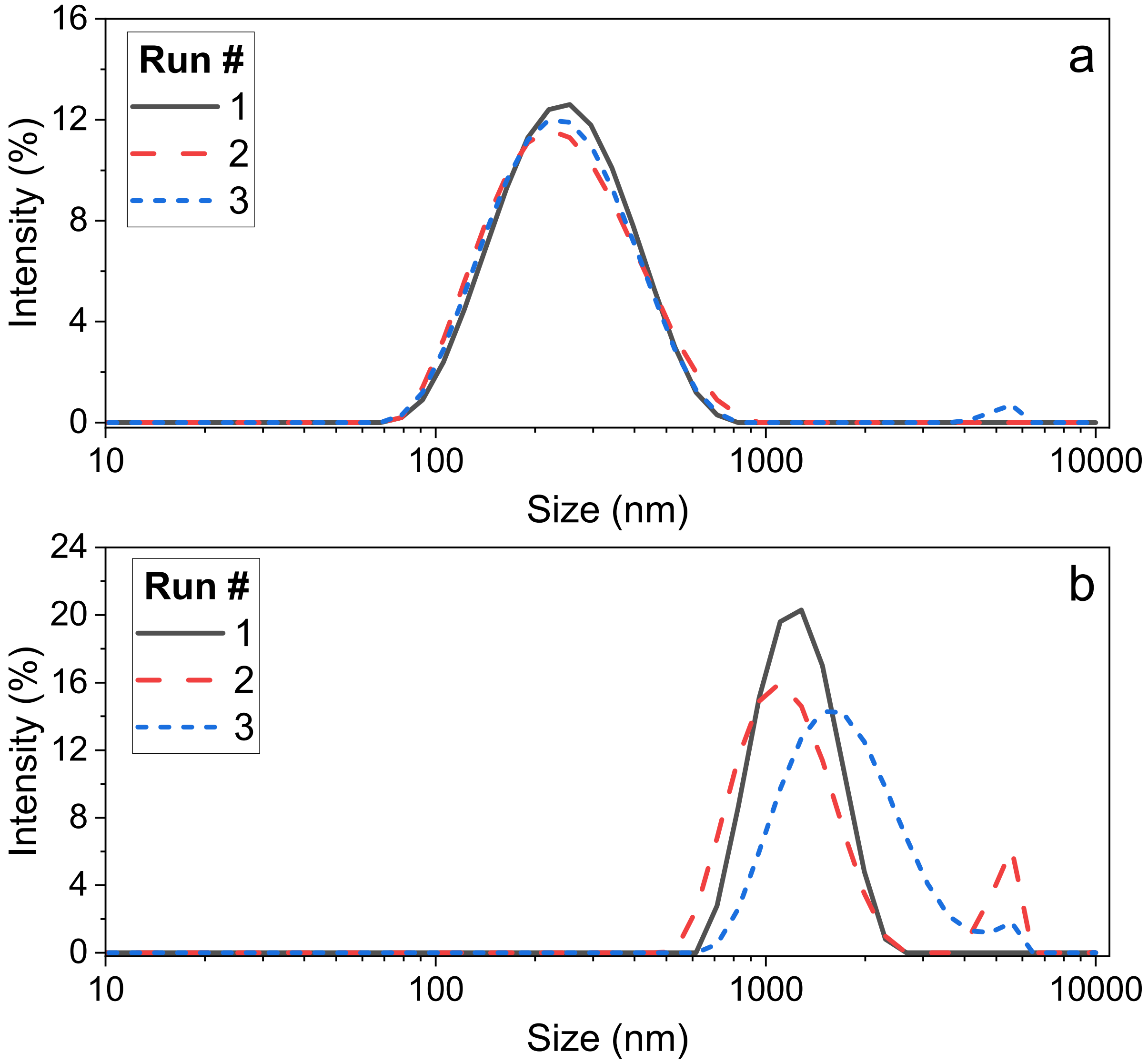

Figure 3.4(a-b): Particle size distribution by intensity for two yttria colloids obtained with a Malvern Zetasizer. In (a), the colloid appears stable as the distribution does not change significantly over three separate measurements. In (b), the colloid is unstable as the distribution is changing significantly over the course of three measurements. From Run 1 to 3, the particles appear to be flocculating and increasing in size.

CHAPTER 4: EFFECT OF YTTRIA CONTENT ON THERMAL STABILITY OF YTTRIA STABILIZED ZIRCONIA AEROGELS

4.1 Introduction

A successful aerogel material system must be able to suppress both densification and phase transformations to maintain sufficiently low thermal conductivity and mechanical integrity across the full range of relevant extreme operating conditions. A promising material system to achieve such aims is yttria-stabilized zirconia (YSZ), which can maintain a cubic crystal structure from room temperature to over 2600 °C if properly stabilized [83]. Tetragonal YSZ has been extensively studied as a thermal barrier coating (TBC) on the basis of suitable phase stability, low thermal conductivity, and toughness [84–91]. YSZ TBCs are applied in turbine engines and can withstand multiple cycles to 1150°C [92,93]. Given this practical, industrial experience, it follows that an YSZ-based aerogel could be an effective, lightweight insulator that does not undergo phase transformation at elevated temperatures.

While the tetragonal phase of YSZ has been the primary focus of TBC work, the cubic phase has attributes that may prove promising for insulative aerogels. First, the thermal conductivity of YSZ is further reduced from the tetragonal to the cubic phase. Increased yttria content reduces the thermal conductivity because of higher oxygen vacancy concentration and subsequent phonon scattering [94]. The thermal conductivity of cubic YSZ is also lower than many previously studied aerogel compositions, such as silica, aluminosilicate, and zirconia [95–99]. Second, stabilization of the cubic phase avoids phase transformations that can occur at lower yttria content [83]. Overall, a cubic YSZ aerogel could exhibit all three properties of a good insulator, with low thermal conductivity, low weight, and thermal stability at high temperatures.

YSZ aerogels have been studied previously. Synthetic procedures have been developed utilizing propylene oxide [61,100] as well as citric acid [65], though these studies are restricted to a limited compositional space and focused on synthesis over microstructural evolution at high temperatures. The stabilizing effect of yttria in YSZ aerogels was demonstrated in studies utilizing up to 8.7 mol% $YO_{1.5}$ [101] and 15 mol% $YO_{1.5}$ [102]. Prior work on yttria- and ytterbia-stabilized zirconia in the range of 0 to 15 mol% $MO_{1.5}$ demonstrated improvements to the thermal stability upon doping of zirconia aerogels to 1000 °C [103]. In all works, higher dopant levels maintained higher surface areas and smaller particle sizes, though still shy of acceptable values for use as effective insulation. Beyond these studies, there remains much to be understood in terms of the thermodynamic and kinetic contributions to the microstructural evolution of porous structures. A thorough study of the microstructural evolution of YSZ aerogels is warranted to improve the understanding of how yttria stabilizes the pore structure of high surface area materials.

The factors central to a thermodynamically and kinetically informed aerogel design process include surface energy, cation diffusivity, and nucleation kinetics, all of which are a function of Y-concentration in fully stabilized zirconia [104–107]. As such, systematic investigation of cubic YSZ aerogels (beyond 15 mol% $YO_{1.5}$) is a highly promising route to improving pore stability and the associated thermal conductivity. Increased yttria content reduces the surface energy in YSZ, with significant reductions from the monoclinic to tetragonal and tetragonal to cubic phase [104]. Such a reduction in surface energy reduces the driving force for sintering and densification, a reduction that is of utmost importance in a material as porous as an aerogel. From a kinetic perspective, increased yttria content decreases cation diffusivity, especially between 14.8 to 48.4 mol% $YO_{1.5}$ [105,106]. Cation diffusivity controls mass transport in the YSZ system and a reduction in mass transport with increased yttria content is expected to lessen sintering, densification, and crystallite/grain growth. Cubic YSZ maintained smaller crystallites and lowered relative density compared to tetragonal YSZ and monoclinic zirconia to temperatures of 1200 °C and exposure of fewer than two hours [108–110]. As this work is focused on aerospace applications such as atmospheric re-entry, exposure times at maximum temperature are expected to be brief and the use of cubic YSZ is justified.

In the present work, YSZ aerogels in the range of 0 to 50 mol% $YO_{1.5}$ are prepared to evaluate the stability of cubic YSZ aerogels and the effects of dopant level within a single phase. The thermal stability is evaluated through characterization of the microstructural evolution and crystalline phase development. Thermal stability is assessed on the basis of constant pore size distribution, high SSA, and minimal crystallite growth. Overall, this study establishes the foundation for a thermodynamically and kinetically informed aerogel design strategy that incorporates the evolution of the structure and thermal properties, thereby enabling eventual use of robust aerogels in the extreme environments of aerospace applications.

4.2 Materials & methods

4.2.1 YSZ aerogel synthesis

YSZ aerogels of 0, 15, 30, and 50 mol% $YO_{1.5}$ were prepared using a sol-gel process adapted from previous work [59]. Zirconyl chloride octahydrate ($ZrOCl_2{\cdot}8H_2O$, Alfa Aesar 99.9%) and yttrium trichloride hexahydrate ($YCl_3{\cdot}6H_2O$, Acros Organics 99.9%), were first dissolved in 200 proof ethanol (Decon Labs) in separate containers. The standard solids loading was 1.263 mmol metal per mL of ethanol. DI water was added in six times the stoichiometric amount for each metal precursor (e.g., 24 moles water per mole of Zr, 18 moles of water per mole of Y). The precursors were stirred separately for 60 minutes for hydrolysis. The precursors were then combined and stirred for 15 minutes. The solution was placed in an ice bath and propylene oxide

(PO) (CH_3CHCH_2O, Sigma Aldrich) was added dropwise at a ratio of 2.342 mole PO per mole of metal. The solution was stirred for 5 minutes and then transferred to molds made from polyethylene syringes (24 mL) with the tip cut off. The plunger was placed at 20 mL and the mold was filled to the 10 mL mark. Gelation occurred within 10 to 30 minutes. The gels were held in the mold for 24 hours, extracted into room temperature 200 proof ethanol, and aged for 5 to 7 days. The gels were then supercritically dried using carbon dioxide [111]. The process used four washes in liquid carbon dioxide to replace ethanol in the pore structure, before bringing the carbon dioxide to its supercritical state and evacuating the fluid.

4.2.2 Heat treatments

For all heat treatments, aerogels were placed into high purity alumina crucibles. Heat treatments at 600 °C were performed in a box furnace under air with a temperature ramp of 20 °C/min. The aerogels were heated to 1000 and 1200 °C in a tube furnace under a flowing argon atmosphere and a ramp of 5 °C/min. The maximum temperature was held for 18 minutes, and the aerogels were cooled to room temperature within the furnace.

4.2.3 Material characterization

The supercritically dried aerogels underwent physical measurement to characterize shrinkage and bulk density. The length and diameter of cylindrical aerogel monoliths were measured and used to calculate bulk density and shrinkage relative to the diameter of the mold. Scanning electron microscopy (SEM) was performed on a Hitachi S4700 SEM to characterize pore morphology. Samples were crushed onto carbon tape and imaged uncoated at 2 kV.

Nitrogen adsorption/desorption experiments were conducted on Micromeritics ASAP 2020 (NASA Glenn Research Center) and Micromeritics TriStar 3020 (Aerogel Technologies) to measure the specific surface area via the method of Brunauer-Emmett-Teller (BET) and porosity via the method of Barret-Joyner-Halenda (BJH). Prior to adsorption/desorption, samples were degassed under vacuum and heated at 5 °C/min to 80 °C with an 8-hour hold. Average pore size and cumulative pore volume were calculated using the BJH desorption method.

Powder x-ray diffraction (XRD) was used to determine the crystalline phase and the crystallite size via the Scherrer equation. Samples for XRD were crushed with a mortar and pestle. The powders were deposited via suspension in 200 proof ethanol onto low background holders. XRD was performed using Cu Kα radiation on a Bruker D8 Advance XRD. Scanning conditions were 10 to 100° 2θ, 0.02 degrees per step, and 0.25 seconds per step. Parallel beam geometry was used with a 0.2 mm divergence slit and a panoramic Soller slit. OriginPro® (v. 9.6.0.172) was used to fit the XRD data and provide peak positions and peak widths assuming Gaussian peak shapes. Metallic elemental composition was quantified using inductively coupled plasma optical emission spectroscopy (ICP-OES) and halide content using Ion Selective Electrodes (ISE).

The *in-situ* Ion Irradiation TEM (I^3TEM) facility at Sandia National Lab was utilized to study crystallization kinetics of yttria stabilized zirconia aerogels. The I^3TEM facility is a combination of a modified JEOL 2100 TEM that was operated at 200 kV and a 6 MeV Tandem ion accelerator, although no irradiation was performed in this study. The in-situ heat treatments were conducted while using traditional bright-field TEM imaging modes. The samples were heated using the Gatan double tilt heating holder, model 652. Each sample was ramped to 800 °C at a 10 °C/min heating rate with a 5-minute hold at the final temperature. While ramping to 800 °C, a 4-minute hold was employed every 100 °C for taking dark field images and electron diffraction patterns. The image analysis was conducted using open-source software called ImageJ, utilizing a specific distribution of the software called FIJI [112]. FIJI was used for the segmentation of the images and to identify specific features within the image. This segmentation was done using a plugin associated with FIJI called Trainable Weka Segmentation; details of the plugin can be found elsewhere [113]. The thresholding of the segmented images was used to determine the size analysis of crystallites.

4.3 Results

4.3.1 As dried aerogels

The composition as measured by inductively coupled plasma optical emission spectroscopy (ICP-OES), physical properties, measurements of specific surface area (SSA), and porosity are included in Table 4.1 for aerogels of 0, 15, 30, and 50 mol% $YO_{1.5}$ prepared by the sol-gel route and supercritically dried. Hereafter, the samples are referred to as xYSZ, where x is mol% $YO_{1.5}$. Shrinkage and bulk density measurements were not obtained for 50YSZ as all samples broke during supercritical drying.

The formulated and measured compositions agree within 2 mol% $YO_{1.5}$ in all cases, suggesting both metal salts were sufficiently hydrolyzed and incorporated into the structure at similar rates and selectivities. Shrinkages were obtained by the dried aerogel's diameter relative to the mold and varied from -13.2% to -25.6%. Measured bulk densities ranged from 0.193 to 0.292 g/cm^3. Increased yttria content decreased density and shrinkage. Furthermore, undoped-zirconia aerogels were observed to be translucent and increased yttria content increased opacity of the aerogel. Qualitatively, yttria content improved the structural coherency and strength of the aerogel monoliths to 30YSZ. 50YSZ samples were fragile and easily broke into powdery fragments after supercritical drying. SSAs and pore size distributions of the aerogels were measured with nitrogen physisorption experiments. SSAs ranged from 301 to 456 m^2/g. Figure 4.1(a-b) depicts the adsorption/desorption isotherms and the pore size distributions for the four levels of yttria dopant. All isotherms in Figure 4.1(a) exhibited hysteresis loops characteristic of mesoporosity. The average pore size (BJH desorption method) shifted to larger values with introduction of yttria, from 7.5 nm for 0YSZ (undoped zirconia) to between 10 and 14 nm after doping with yttria (Figure 4.1(b)). A notable change in the shape of the pore size distribution was observed as the yttria content increases from 15 to 30 mol% $YO_{1.5}$. 0YSZ and 15 YSZ have monodisperse distributions with an abrupt decrease after its peak. In stark contrast are 30YSZ and 50YSZ, which have very broad distributions that extend to much larger pore sizes.

The morphologies of the as dried aerogels were observed with SEM as shown in Figure 4.2(a-d). Overall, SEM corroborated the results of nitrogen physisorption. Very fine pores were observed in the undoped zirconia aerogels, with appearance of additional larger pores in the YSZ samples with higher yttria content. For 30 and 50YSZ (Figures 4.2(c-d)), an increasingly hierarchical pore structure formed which contained both meso- and macroporosity. The macroporosity became most evident for 50YSZ. The increase in dispersity of the pore structure with increased yttria content can explain the decrease in SSA and shift to a larger peak pore size. Images of the wet gels are inlaid in Figure 4.2 to demonstrate increased in opacity with increased yttria content. Overall, yttria content's strong effect on as dried zirconia aerogel structure was demonstrated through nitrogen physisorption, SEM, and measurement of physical properties.

4.3.2 Pore Structure and Thermal Stability

The evolution of the pore structure in the YSZ aerogels after heat treatment at 600, 1000, and 1200 °C was characterized using the same methods described previously for the as dried aerogels. The pore morphology evaluated with SEM is presented in Figure 4.3(a-h). Not included are materials at 600 °C as they exhibited little visual change in pore morphology. After heating at 1000 °C for 18 minutes, 0YSZ developed into a network of spherical particles with notable necking visible in Figure 4.3(a). By 1200 °C, 0YSZ had densified with no evidence of the mesoporous structure remaining as shown in Figure 4.3(e). 15YSZ maintained its porosity to 1000 °C but formed a network of spherical grains with loss of most mesoporosity at 1200 °C. In stark contrast, 30YSZ and 50YSZ clearly maintained mesoporosity characteristic of an aerogel to 1200 °C (Figure 4.3(g-h)).

Nitrogen physisorption was used to quantify the structural evolution of the YSZ aerogels after heat treatment. Pore size distributions are shown in Figure 4.4(a-d) of the four compositions as dried and after heat treatment at 600, 1000, and 1200 °C. Pores smaller than 100 nm were eliminated entirely by 1000 °C for 0YSZ and 1200 °C for 15YSZ. Measurable mesoporosity remained in 30 and 50YSZ to 1200 °C. The distribution for 30YSZ in Figure 4.4(c) reveals notable thermal stability of the pore distribution up to 1000 °C, with a nearly constant pore size distribution centered about 22 nm. The pore size distribution does change below 1000ºC for 50YSZ, but a remarkably consistent distribution is maintained from 1000 to 1200 °C. While both the 30 and 50YSZ samples maintained mesoporosity to 1200 °C, the evolution of the pore size distributions follows different pathways. Figure 4.5 depicts the evolution of SSA, average pore size, and cumulative pore volume of the four samples upon heating. All materials experienced significant loss of SSA, with 0 and 15YSZ having the largest percent reduction. By 1200 °C, both 0 and 15YSZ had no measurable surface area. Doping with yttria maintained porosity to 1200 °C in 30YSZ (22 m^2/g, 0.157 cm^3/g) and 50YSZ (44 m^2/g, 0.390 cm^3/g). The introduction of yttria mitigated densification and coarsening of zirconia aerogels according to the results of nitrogen physisorption and SEM.

4.3.3 Evolution of Crystal Structure

All materials were amorphous following supercritical drying. Powder XRD patterns of the aerogels after heat treatment are shown in Figure 4.6(a-d). No unexpected phase transformations or segregations were observed [83]. 0YSZ predominantly crystallized into the monoclinic phase and 30YSZ and 50YSZ into the cubic phase, as expected. 15YSZ crystallized into either the cubic or tetragonal phase, with higher temperatures favoring the formation of the cubic phase as observed previously [103]. Given the very small crystallite size, it was impossible to definitively distinguish between the cubic and tetragonal phases of YSZ using lab-scale XRD, although, based upon the diffraction profile and phase diagram, 30 and 50YSZ are expected to be cubic and 15YSZ lies near the phase boundary. The phase behavior of 15YSZ did not have a significant impact on the evolution of the pore structure, as most porosity was eliminated by 1000 °C.

It was observed that increased yttria doping broadened peaks, which can be evidence of smaller crystallite size. As determination of absolute crystallite size would introduce unnecessary uncertainty, D/C values from the Scherrer equation were calculated according to Equation 4.1 to compare between samples and are shown in Figure 4.7. D is the crystallite size (nm), C the Scherrer constant, λ the x-ray wavelength (nm), β the full width at half maximum (rad.), and θ the peak position (rad.).

$$\frac{D}{C} = \frac{\lambda}{\beta cos(\theta)} \qquad \textbf{Equation 4.1}$$

The full width at half maximum (FWHM) values and peak positions were obtained via multiple Gaussian peak fitting in OriginPro®. In general, doping with yttria increased FWHM at 600 and 1000 °C. At 1200 °C, 50YSZ maintained a small crystallite size relative to the other materials. The observed temperature required for the onset of rapid crystallite growth increased with increased yttria content. The scatter in the 15YSZ at 1200 °C is attributed to the development of a bimodal particle size distribution as observed with SEM in Figure 4.3(f).

To further explore yttria's effect on crystallite size, dark field imaging via *in situ* TEM was utilized. Darkfield images were produced by selecting a representative spot on each electron diffraction pattern on the first bright ring. An example diffraction pattern and its corresponding dark field image are presented in Figure 4.8(a). Image processing of the dark field images produced average crystallite sizes for each composition. Crystallite size distributions at 800 °C are shown in Figure 4.8(b). Observed differences in average crystallite size between 0 and 15YSZ, 0 and 30YSZ, and 0 and 50YSZ were significantly different ($\alpha = 0.05$). Outliers were included in the calculation of the mean crystallite sizes and tests for statistical significance. Increased yttria content suppressed crystallite growth as evidenced by both XRD and dark field TEM.

Lattice parameters were calculated for 15YSZ, 30YSZ, and 50YSZ heat-treated at 1000 and 1200 °C. The (111), (200), (220), and (311) reflections were selected for calculations from the XRD patterns assuming a cubic structure. The lattice parameters are included in Table 4.2. Lattice parameters increased as the yttria content increased as expected [114].

4.4 Discussion

4.4.1 Effect of composition on as dried aerogels

The SSA of the YSZ aerogels peaked for 15YSZ, with decreasing SSA for 30YSZ and 50YSZ. This result can be understood by evaluating the materials' pore size distributions in Figure 4.4(a-d). The lower SSAs of 30YSZ and 50YSZ result from a much wider distribution encompassing larger pore sizes. The narrow distribution and small average pore size of 0YSZ and 15YSZ contribute to much larger SSAs.

Increased yttria content widened the pore size distribution and increased the average pore size. Qualitatively, the microstructure shifts from a highly homogenous distribution of mesopores in the case of pure zirconia to a more heterogenous pore structure of meso- and macropores in 30 and 50YSZ. Two proposed mechanisms that explain this shift follow.

One, the change in structure is hypothesized to be the result of increased chloride ion content. Because of the nature of the precursors, $ZrOCl_2 \bullet xH_2O$ and $YCl_3 \bullet xH_2O$, increased yttria content increases the chloride concentration in the reaction solution. According to the mechanisms proposed for the synthesis method utilized in this work [59], the chloride ion performs a nucleophilic attack on the propylene oxide, resulting in irreversible ring opening, consumption of a proton, and subsequent increase in pH. Increasing the chloride ion concentration is expected to increase the reaction rate for this process. As the reaction rate increases, the resulting structure is anticipated to resemble an agglomerated network of nanoparticles with more dispersed pore sizes as the process leans towards precipitation rather than gelation. Slow reaction rates will lead to more homogeneous rises in pH throughout the solution, increasing the homogeneity of the gel structures and pore size distributions. Previous work on the effect of propylene oxide to metal (PO/M) ratios in aluminosilicate aerogels demonstrated narrower pore size distributions at lower PO/M ratios (slower reaction rate) and broader pore size distributions at higher PO/M ratios (faster reaction rate) [50]. Similar effects are observed in the SEM micrographs and pore size distributions of the YSZ aerogels; 0 and 15YSZ have homogeneous pore size distributions whereas 30 and 50YSZ display more dispersity in their pore sizes and structures that increasingly resemble agglomerated nanoparticles, but still maintain mesoporosity.

The second proposed mechanism arises from potential effects from the differing behavior of Zr^{4+} and Y^{3+} in solution. This mechanism was proposed following the work described in Chapter 5 and will be covered in greater detail in the coming chapter. The acidity of the hydrated metal cation $[M(H_2O)_x]^{x+}$ increases with increasing oxidation state and decreasing cation radius [115]. As the acidity increases, the rate of reaction increases. Thus, higher oxidation states will make hydrolysis occur more quickly. In this work, increasing the concentration of $YO_{1.5}$ reduces the average oxidation state and increases the cation radius in solution, both resulting in reduced reaction rate and increased gel time [116].

A study on mixed metal-silicon oxide aerogels (Al, Cr, Zr, Hf, Nb, Ta, W, and more) by Clapsaddle et al. evaluated the structure of aerogels prepared from hydrated metal salts and propylene oxide [60]. In this work, gel times decreased as coordination number increased, owing to increased acidity and reactivity of the water in the hydrated metal complexes. With shorter gel times, observed shrinkages were higher and the average pore sizes were lower. Longer gel times were generally associated with large particle sizes and coarser pore structures. The authors proposed that with longer gel times, there was more time for nucleation and growth of particles in the sol prior to gelation. Larger particles cannot pack as closely together, leading to reduced shrinkage and larger pore size. This interpretation also is sensible given the evidence for YSZ, where increased $YO_{1.5}$ content reduces reaction rate and increases gel time, resulting in larger particles and larger pore sizes as observed in SEM and quantified with nitrogen physisorption.

Notably, the two proposed mechanisms differ in their hypotheses of how yttria content influences gelation time. The first mechanism suggests a reduction in gel time based upon changing chloride content, resulting in a structure that resembles agglomerated precipitates rather than a homogeneous gel network. The second mechanism suggests an increase in gel time based upon changing yttrium ion content in solution, resulting in increased time for nucleation and growth of particles and a population of larger particles that cannot pack as efficiently. Experimentally, no major differences were noted between the four samples in gel time. Future studies utilizing nitrate precursors to adjust the nucleophilicity of the counterion and other cations to adjust acidity may be useful in elucidating the connection between the choice of precursor, reaction rate, and gel structure.

The increase in breadth of the pore size distribution changes the appearance and mechanical robustness of the material. 0YSZ was completely transparent, whereas 15, 30, and 50YSZ were opaque and increasingly so with higher yttria content. This implies that the broader pore size distribution leads to increased light scattering and opaqueness. Qualitatively, the mechanical integrity of the aerogel increased with increased yttria content to 30 mol% $YO_{1.5}$. 50YSZ was the only material that did not remain monolithic after supercritical drying, which suggests that as the pore size distribution widens, ultimately there is a tradeoff between mechanical integrity and thermal stability.

4.4.2 Effect of composition on structural evolution

This work set out to improve the thermal stability of aerogels for use as insulation in the extreme environments associated with aerospace applications. To assess thermal stability, several indicators were monitored. These include maintenance of a high surface area, constant pore size distributions, limited phase transitions, and minimal shrinkage and cracking over the temperature regimes of interest (600 to 1200 °C). High surface area implies a highly porous material, which is associated with very low thermal conductivities. Constant pore size distributions contribute to invariant transport properties through the insulation. Limiting the phase transitions, shrinkage, and cracking will ensure structural integrity of the insulation in maintained.

The crystallite and grain growth behavior of nanocrystalline YSZ at varying yttria doping levels have previously been studied. Yttria doping suppressed crystallite growth at 500 °C, but heating to 1400 °C resulted in cubic YSZ having larger grains than both undoped zirconia and tetragonal YSZ [117]. It was further revealed that the relative sizes and growth rates of crystallites in cubic and tetragonal YSZ are a strong function of temperature and time [108–110]. To temperatures of 1000 °C, crystallites in cubic YSZ are smaller than in tetragonal YSZ. The growth rate of cubic crystallites begins to exceed that of tetragonal crystallites at about 1200 °C and over an hour of exposure [109]. This presents an upper limit to the use of cubic YSZ aerogels in applications involving long-term thermal exposure. In the present work, the addition of sufficient yttria to stabilize the cubic phase also significantly suppressed the growth of crystallites to 1200 °C. We observed significant growth of crystallites in 15 and 30YSZ between 1000 and 1200 °C, consistent with the temperature at which the growth rate of cubic crystallites is expected to increase. Interestingly, 50YSZ exhibited very little crystallite growth to 1200 °C despite being identified as cubic like the 15 and 30YSZ. The increased yttria content in 50YSZ and decreased grain boundary energy or diffusivity may play a role in this behavior as discussed later. The prevention of rapid crystallite growth at higher yttria content is promising for maintenance of the highly porous structures to 1200 °C and exposure times of less than 30 minutes.

The extent of yttria doping in YSZ has a significant effect on the key kinetic and thermodynamic parameters responsible for driving structural evolution. Take, for example, the surface energy, which has been measured as a function of mol% $YO_{1.5}$ for anhydrous YSZ from 0 to 33 mol% $YO_{1.5}$ [104]. The surface energy decreased significantly from monoclinic zirconia (1.9278 ± 0.1543 J/m^2) to cubic YSZ (0.9601 ± 0.0283 J/m^2) and within cubic YSZ, the surface energy decreased with increased yttria content [104]. The decreased surface energy of YSZ with increased yttria content may explain the reduction in densification of 30 and 50YSZ. In materials with very large specific surface areas such as the presently studied aerogels, reductions in surface energy will significantly reduce driving forces for densification.

In YSZ, slow cation diffusion controls mass transport and therefore densification and crystallite growth. Previous work [105–107] measured bulk cation diffusivity in YSZ from 14.8 to 48 mol% $YO_{1.5}$. Decreased yttrium and zirconium bulk diffusion coefficients with increased yttria content were reported. Though surface diffusion is expected to occur as a result of high surface-to-volume ratios in aerogels, surface diffusion is a non-densifying mechanism and only contributes to neck growth. The reduced diffusivity with increased yttria content may be partially responsible for the reduced densification and crystallite growth in 30 and 50YSZ relative to 0 and 15YSZ. Reduced mass transport will reduce sintering and densification of highly porous structures up to the temperature where the activation energy barrier is surmounted, and rapid crystallite growth occurs. Rapid crystallite growth is observed to occur between 600 and 1000 °C for 0YSZ, 1000 and 1200 °C for 15YSZ and 30YSZ, and beyond 1200 °C for 50YSZ, as evident in Figure 4.7.

Grain boundary energy and its relative value to surface energy are expected to play an important role in crystallite and grain growth behavior [37]. To date there are only a limited number of systematic efforts that attempt to quantify or understand the complete impact of aliovalent doping on these key parameters in zirconia-based ceramics. Molecular dynamics simulations of YSZ grain boundaries in model bicrystals did not reveal a clear relationship between yttria content, grain boundary energy, or grain boundary diffusivity [118]. Experimental measurement of grain boundary energy with microcalorimetry suggests reducing YSZ grain boundary energy with increased levels of gadolinium doping [38] and lanthanum doping [39]. Despite this apparent discord in the YSZ system, studies on densification and grain growth in a broader range of nanocrystalline ceramics consistently point towards doping as an effective route to microstructural stabilization [40].

Ultimately, the nucleation and growth behavior of crystallites is affected by changes in surface energy and diffusivity as a function of yttria content. With increased yttria content, the relative difference in surface energy between the amorphous and crystalline state is reduced [104], thereby decreasing the critical size for nucleation. The trends in crystallite size as a function of yttria content presented herein are consistent with this expectation. It is proposed that the diminishing barrier to nucleation with increased yttria doping will form smaller crystallites at higher yttria content and the reduced diffusivity will prevent their growth resulting in high specific surface areas with exceptional thermal stability.

In this work, the distribution of yttrium is unknown and the small scale of the aerogel structure limits such characterization. Previous work has demonstrated the ability of dopants and defects to segregate to grain boundaries and free surfaces, imparting a drag or space charge effect that inhibits sintering and grain growth [38,119–122]. These effects cannot be ruled out in this work given the lack of data on the distribution of yttrium in the material. It is safe to assume the high surface area, relative to grain boundary area, will make dopant segregation to surfaces the most important parameter in this context. Looking forward, high resolution chemical mapping techniques would be beneficial, especially for high dopant concentrations, to establish the distribution of dopants in zirconia in the as dried material and following heat treatments.

4.4.3 Connection of properties, behavior, and thermal stability

The starting structure appears to have little bearing on the thermal stability of the pore structure. In all cases, mesoporous materials with average pore sizes of 6.4 to 13.9 nm were synthesized and supercritically dried. The level of yttria dopant appreciably changed the structural evolution and thermal stability of the pore structure in YSZ aerogels. Generally, it is accepted that suppressed crystallite growth leads to faster densification because (1) the diffusion distances for densification decrease with crystallite/grain size and (2) driving forces increase with increased interfacial area. This effect has been observed experimentally [123,124]. The rate of densification for intermediate and final state sintering has been shown to be inversely proportional to the grain size raised to an exponent that is dependent on the diffusion mechanism [125]. Though in this work, both suppressed crystallite growth and slower densification are observed. This contradiction may be explained by the combination of lowered surface energy and cation diffusivity with increased yttria content. These two trends reduce driving forces and mobility for densification and crystallite growth, leading to a highly porous aerogel structure with improved thermal stability in 30 and 50YSZ. Though this work demonstrated increasing the yttria doping in YSZ aerogels is an effective way of improving the thermal stability, the materials still undergo significant shrinkage, cracking, and loss of specific surface area. These issues must be overcome for use in composite materials and aerospace applications, though shrinkage and cracking in aerogel monoliths may be mitigated by use of the aerogel as a matrix in composites. Work focused on simultaneously improving the mechanical properties and thermal stability of the pore structure are underway utilizing crystalline precursors, surface modification, and other dopant schemes.

4.5 Summary

YSZ aerogels of 0 to 50 mol% $YO_{1.5}$ were prepared using a sol-gel technique and supercritical drying. Increased yttria doping formed structures with larger pores and more dispersity in pore size. Increasing yttria content to 30 and 50 mol% $YO_{1.5}$ is closely correlated with improved thermal stability. The pore size distribution for 30YSZ remained remarkably self-similar to 1000 °C, though with reduced specific surface area and pore volume. While 15, 30, and 50YSZ all were identified to crystallize in the cubic phase, their micro/meso-structures evolved in unique ways. 15 and 30YSZ experienced rapid crystallite growth between 1000 and 1200 °C, while 50YSZ underwent little crystallite growth to 1200 °C. 30 and 50YSZ displayed improved resistance to densification and maintained a mesoporous structure to 1200 °C, evidenced by SEM and nitrogen physisorption measurements. It is expected that a reduction of both surface energy and cation diffusivity contribute to improved thermal stability with increased yttria content. By improving the thermodynamic stability and reducing the rate of mass transport in the material, thermally stable mesoporous aerogel structures are formed from doped metal oxide systems, with thermally stable aerogels being defined as those capable of maintaining high SSAs, constant pore size distributions, and minimal crystallite growth to temperatures of 1200 °C. Consideration of other dopants and metal oxide systems remain of interest to further elucidate the importance of a thermodynamically and kinetically driven design process for improved thermal stability of highly porous structures.

4.6 Figures and tables

Table 4.1: Physical and textural properties of YSZ aerogels. Yttria was incorporated near target levels according to ICP. Pore size increases and density decreases with increasing yttria content.

mol % $YO_{1.5}$	Actual mol% $YO_{1.5}$ (ICP)	SSA (m^2/g)	V_{BJH} (cm^3/g)	D_{BJH} (nm)	D_{peak} (nm)	S (%)	ρ_b (g/cm^3)
0	0.0	419	0.986	6.4	7.5	-25.6	0.292
15	14.3	456	1.950	13.9	22.9	-21.1	0.250
30	28.2	407	1.190	10.1	22.8	-13.2	0.193
50	48.0	301	0.997	10.8	28.5	-	-

SSA = BET specific surface area
V_{BJH} = BJH desorption cumulative pore volume
D_{BJH} = BJH desorption average pore diameter
D_{peak} = peak diameter in pore size distribution
S = as dried shrinkage (diameter)
ρ_b = bulk density

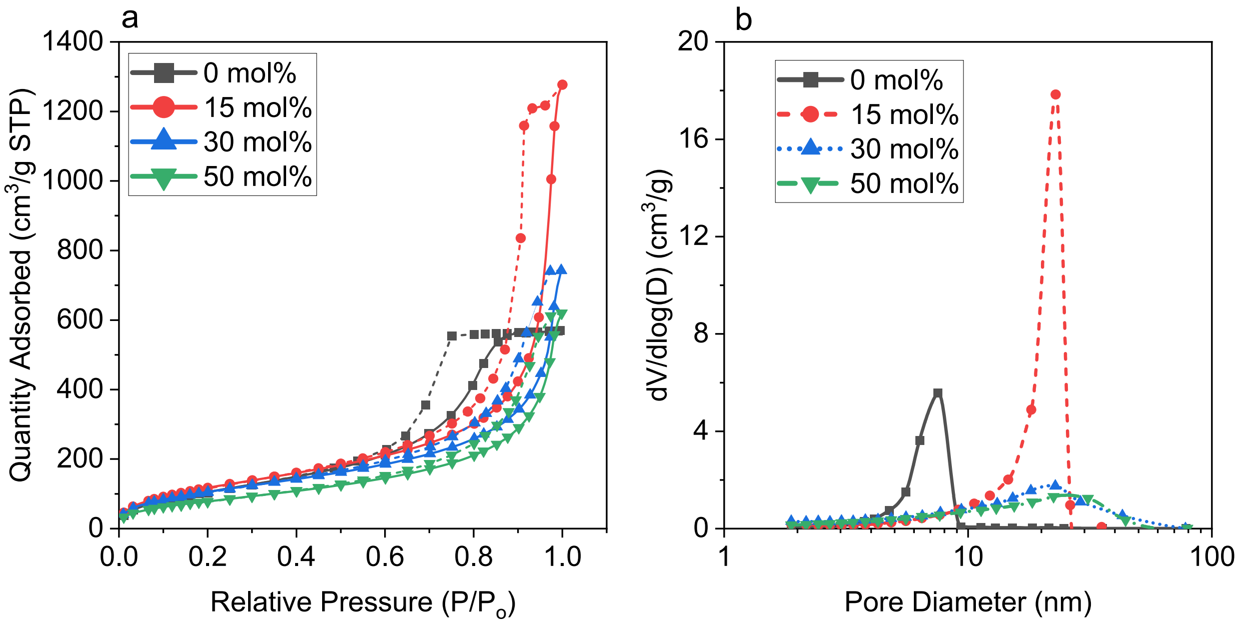

Figure 4.1(a-b): (a) adsorption (solid) and desorption (dashed) isotherms for the as dried 0, 15, 30, and 50YSZ and (b) the associated pore size distributions which become notably broad for 30 and 50YSZ as dried.

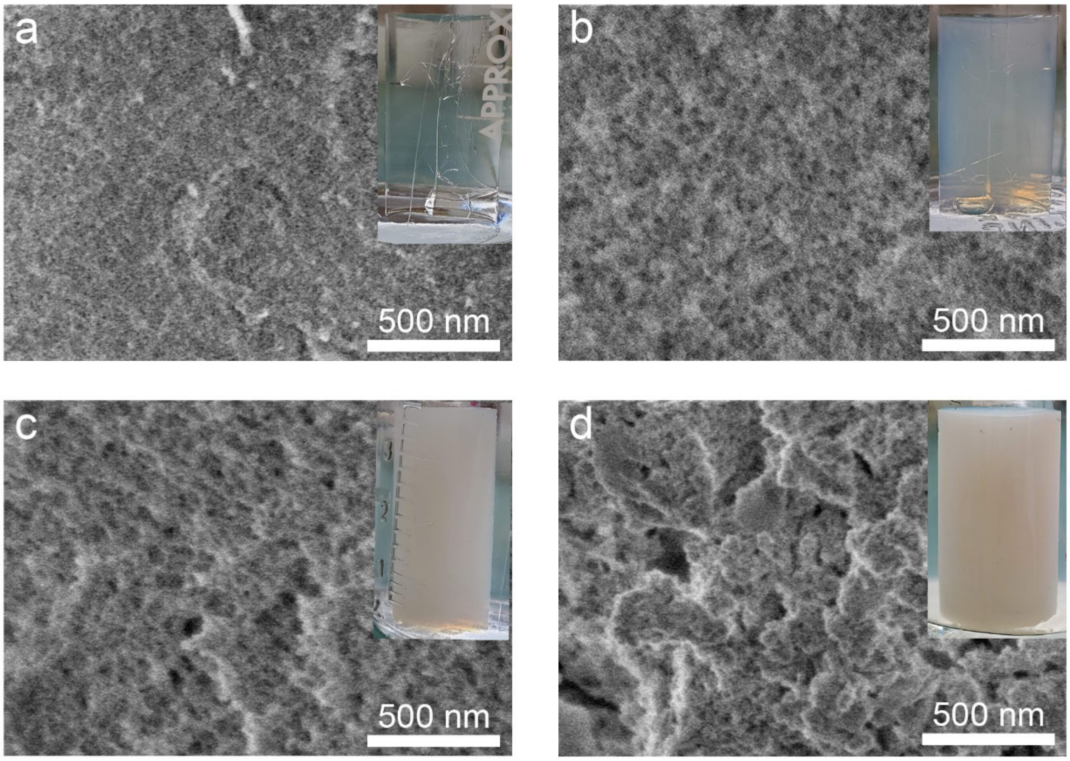

Figure 4.2(a-d): SEM images of 0, 15, 30, and 50YSZ in (a) through (d), respectively. The pore distribution becomes increasingly heterogeneous with increased yttria content for the as dried aerogels. The inlaid images of the gels show the increase in opacity with increased yttria content.

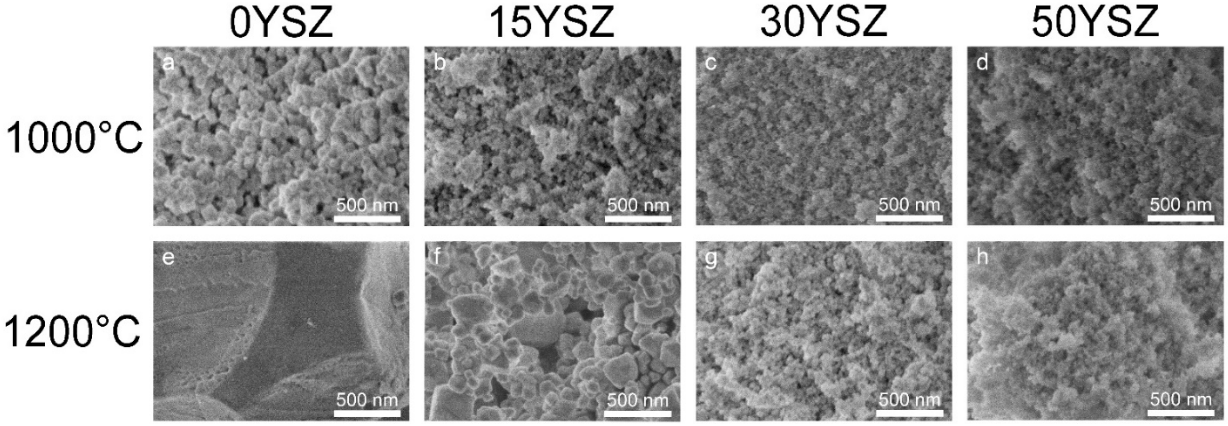

Figure 4.3(a-h): SEM images of pore structure of YSZ aerogels after heat treatment at 1000 °C (a-d) and 1200 °C (e-h). Necking between particles (a) and significant densification (e) observed in 0YSZ. Mesoporous structure maintained to 1200 °C in 30YSZ (g) and 50YSZ (h).

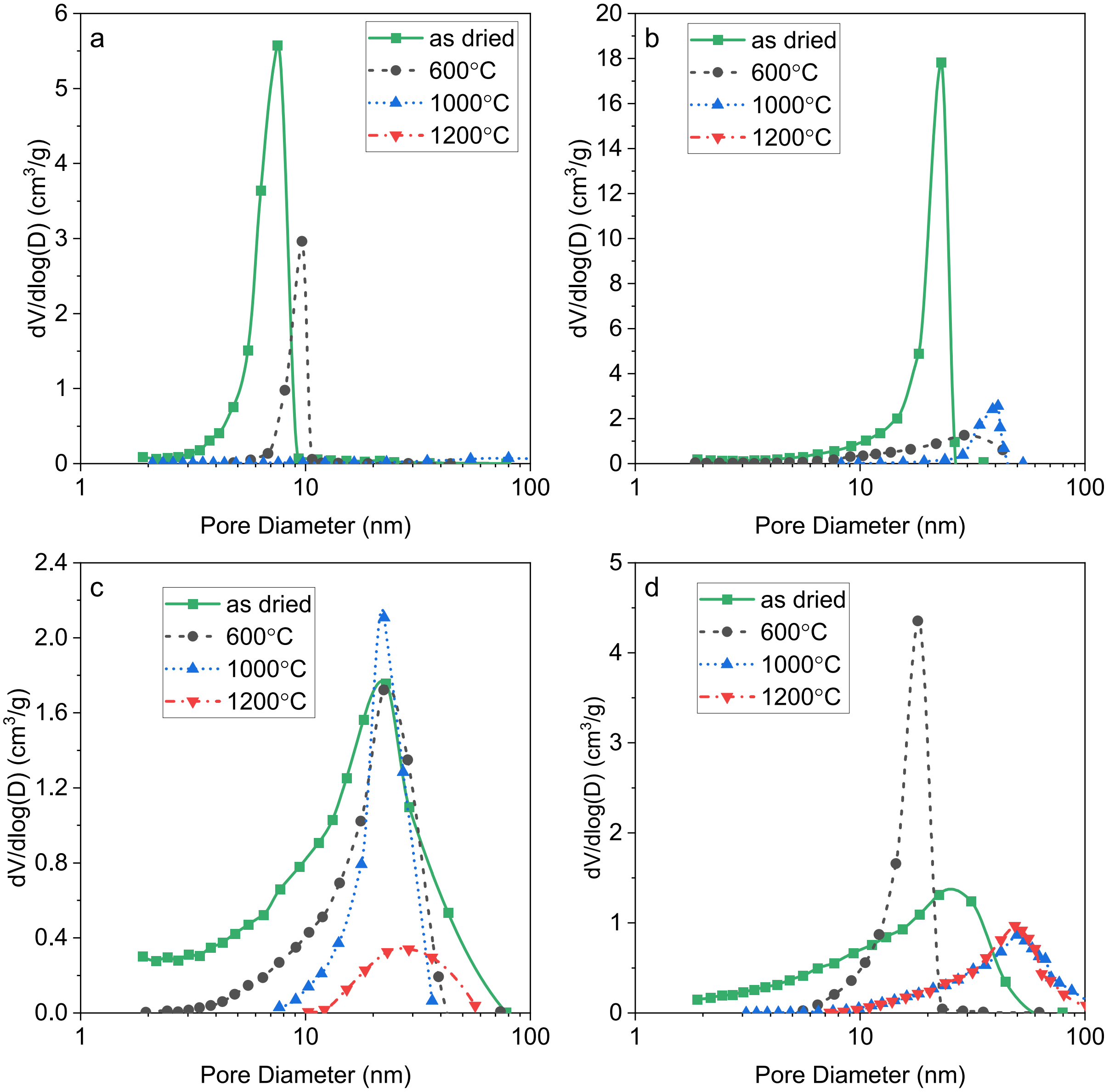

Figure 4.4(a-d): Evolution of BJH pore size distributions for 0YSZ (a), 15YSZ (b), 30YSZ (c), and 50YSZ (d). Significant elimination of pore volume in 0 and 15YSZ by 1000 °C. 30YSZ maintains a self-similar pore size distribution to 1000 °C. Porosity persists in both 30YSZ and 50YSZ to 1200 °C.

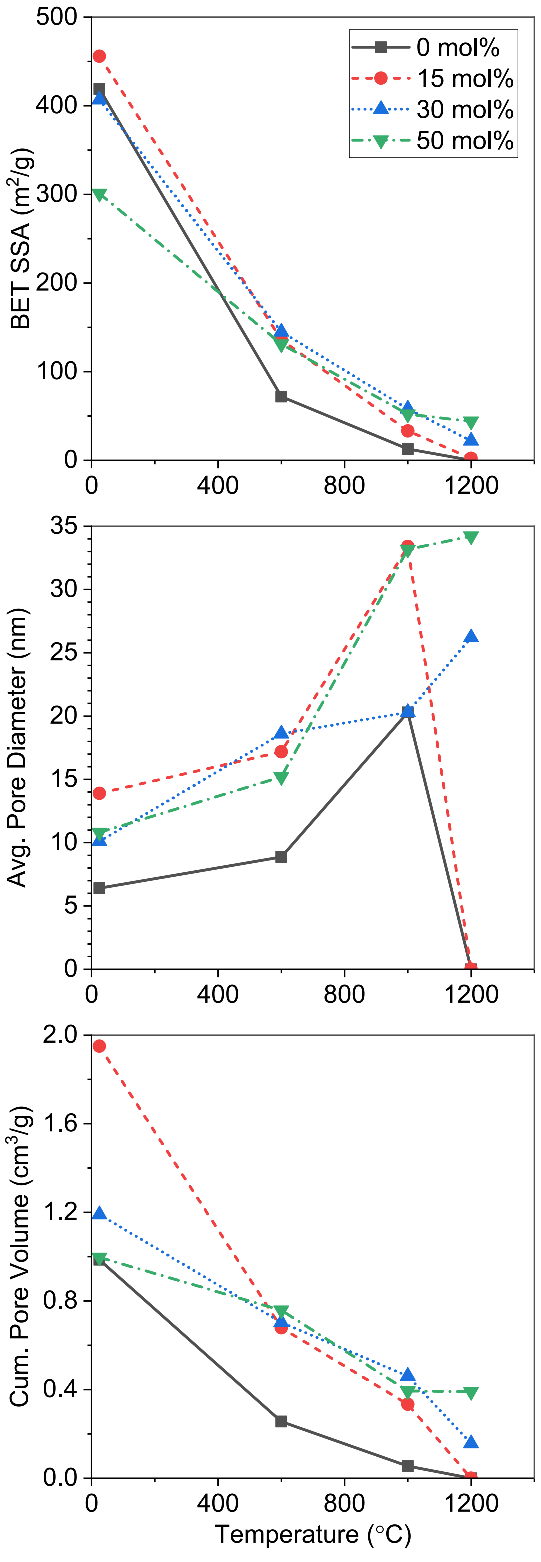

Figure 4.5: The evolution of BET SSA, BJH desorption average pore size, and cumulative pore volume for YSZ aerogels to 1200 °C. All aerogels suffer from reduction in SSA and pore volume, but largest percentage losses occur in 0 and 15YSZ. Only 30 and 50YSZ maintain measurable porosity to 1200 °C.

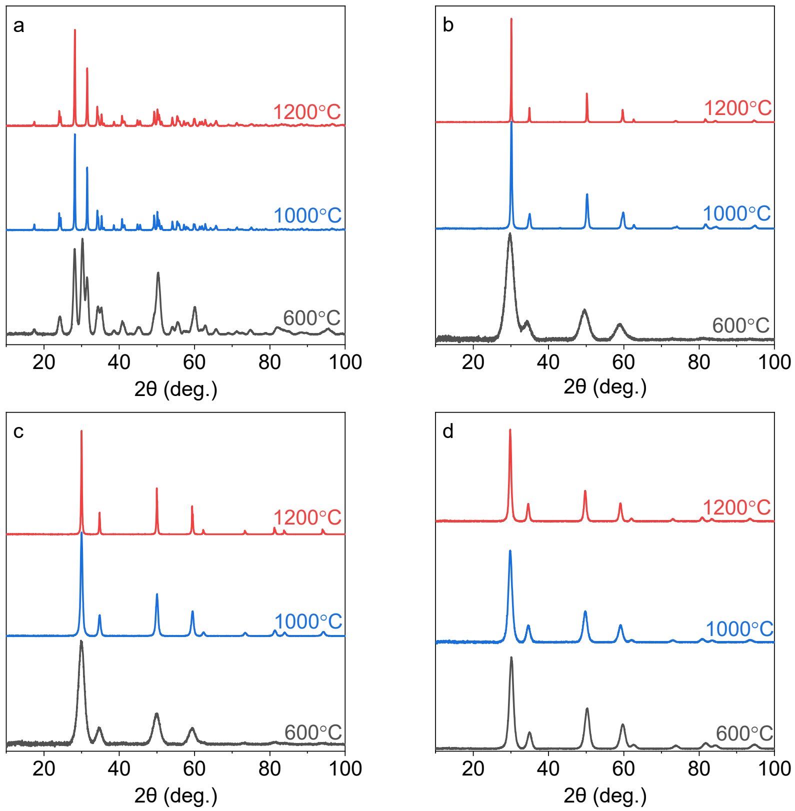

Figure 4.6(a-d): Powder XRD patterns for heat treated YSZ aerogels. 0YSZ (a) crystalizes into the monoclinic phase. 15YSZ (b), 30YSZ (c), and 50YSZ (d) crystallize into the cubic phase. At 1200 °C, peaks were observed to be significantly broader in 50YSZ.

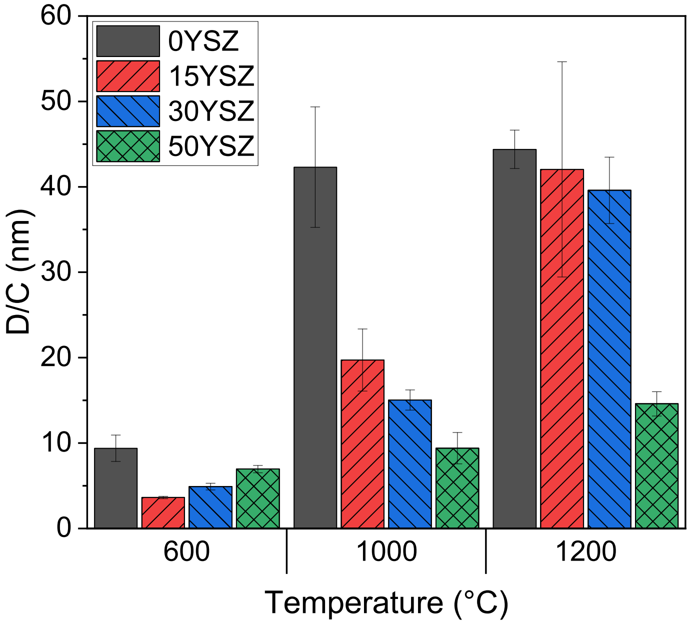

Figure 4.7: Calculated crystallite sizes (normalized) via the Scherrer equation. Significant crystallite growth in 0YSZ from 600 to 1000 °C and in 15YSZ and 30YSZ from 1000 to 1200 °C. 50YSZ undergoes little crystallite growth to 1200 °C.

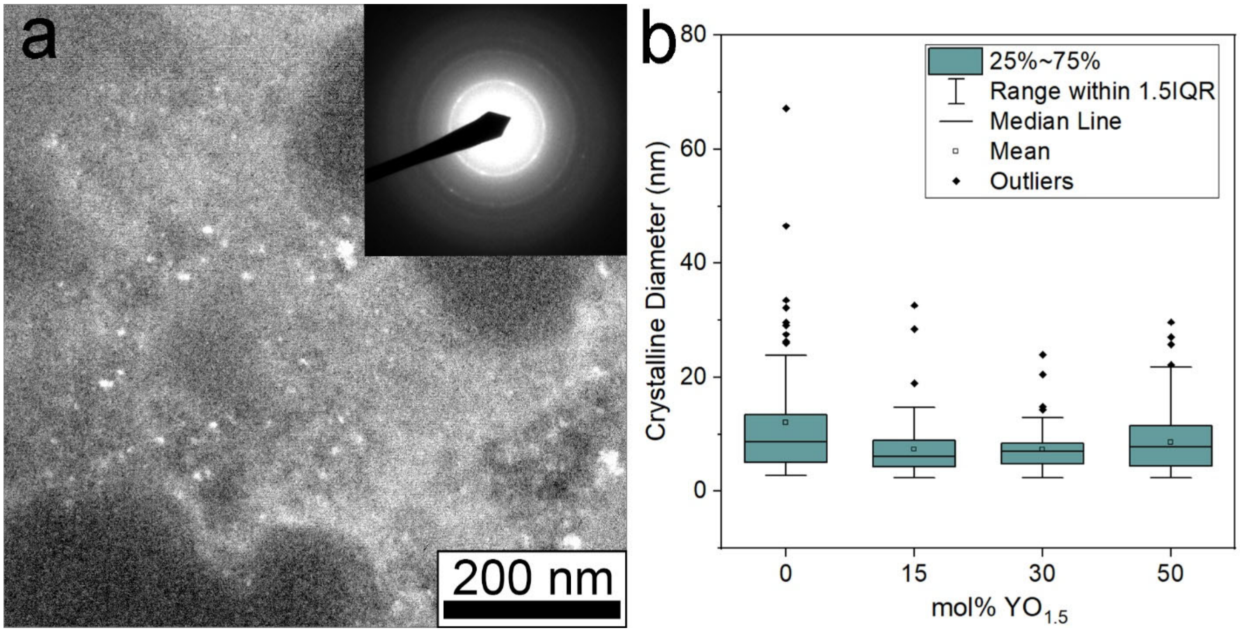

Figure 4.8(a-b): (a) Electron diffraction pattern (inset) for 15YSZ at 800 °C and the corresponding dark field image. In dark field, light spots are crystallites contributing to a selected feature on the diffraction pattern. (b) Box-and-whisker plot of calculated crystallite sizes at 800 °C from dark field images using image analysis. Crystallite growth suppressed with increased yttria content. The 0YSZ/15YSZ, 0YSZ/30YSZ, and 0YSZ/50YSZ crystallite sizes were significantly different at α = 0.05.

Table 4.2: Lattice parameters for cubic YSZ aerogels (15, 30, 50YSZ). 15YSZ at 1000 °C is mixture of tetragonal and cubic. Lattice parameters increase with increased yttria content and increase slightly from 1000 to 1200 °C.

	a (Å)	
mol % $YO_{1.5}$	**1000 °C**	**1200 °C**
15	-	5.138 ± 0.001
30	5.158 ± 0.002	5.159 ± 0.001
50	5.183 ± 0.002	5.185 ± 0.002

CHAPTER 5: EVALUATION OF RARE EARTH DOPANTS IN ZIRCONIA AEROGELS

5.1 Introduction

A study on doping of yttria and ytterbia into zirconia aerogels up to 15 mol% $MO_{1.5}$ improved the thermal stability and the work described in Chapter 4 demonstrated yttria doping beyond 30 mol% $YO_{1.5}$ proved to be an even more effective means of improving the thermal stability of the pore structure [103,126]. The latter work hypothesized that a reduction in surface energy (driving force for densification) and cation diffusivity (rate of densification) with higher yttria content contributed to the improvement in thermal stability.

To further evaluate the effect of composition and material properties on zirconia aerogel thermal stability, the study of other dopants, including ytterbium, gadolinium, cerium, and calcium, is warranted. Work in doped zirconias in the field of thermal barrier coatings (TBCs) have demonstrated the influence of dopants on the structure, properties, and structural evolution of the material. For TBCs, materials are sought with low thermal conductivity, high phase stability, high erosion resistance, and ease of processability. Modifying the dopant identity and concentration has been linked to changes in thermal conductivity and is established as a means of enabling advanced TBC material design [84,88,90,91,127,128]. A variety of rare earth dopant systems have been studied in the context of nanocrystalline zirconias, again with dopant identity and concentration changing the sintering and coarsening behavior of the materials [37,39,129–132]. Obtaining an understanding of how relevant kinetic and thermodynamic material properties, including surface energy, cation diffusivity, surface and grain boundary diffusivity, thermal conductivity and more, in doped zirconia influence thermal stability will contribute to the development and understanding of thermally stable aerogels.

In this work, zirconia aerogels doped with 15 or 30 mol% M/(M+Zr) where M = Y, Yb, Gd, Ce, Ca are prepared to study the evolution of the aerogel structure as a function of composition to temperatures of 1200 °C. The evolution of the microstructure, porosity, and crystal structure are characterized to assess thermal stability. Materials with improved thermal stability are expected to exhibit higher SSAs, constant pore size distributions, minimal crystallite growth, and maintenance of a single crystal phase. This study demonstrates again the impact of dopants on improving the thermal stability of zirconia aerogels but suggests limitations on the magnitude of thermal stability improvement achievable by tuning composition.

5.2 Materials & methods

5.2.1 Synthesis

Doped zirconia aerogels were prepared using a sol-gel synthesis adapted from previous work [59]. Metal salts utilized in this work were zirconyl chloride octahydrate ($ZrOCl_2·8H_2O$, Alfa Aesar 99.9%), yttrium(III) chloride hexahydrate ($YCl_3·6H_2O$, Acros Organics 99.9%), ytterbium(III) chloride hexahydrate ($YbCl_3·6H_2O$, Sigma Aldrich 99.9%), gadolinium(III) chloride hexahydrate ($GdCl_3·6H_2O$, Sigma Aldrich 99.9%), cerium(III) chloride heptahydrate ($CeCl_3·7H_2O$, Sigma Aldrich 99.9%), and calcium(II) nitrate tetrahydrate ($Ca(NO_3)_2·4H_2O$, Sigma-Aldrich 99.9%). Zirconyl chloride octahydrate and the dopant metal salt were dissolved in 200 proof ethanol (Decon Labs) in separate jars at a ratio of 1.263 mmol metal per mL ethanol. After 30 minutes of stirring, DI water was added at six times the stoichiometric amount needed to fully hydrolyze the metal salt. As an example, for each mole of Zr^{4+}, 24 moles of water were added. The precursor solutions were hydrolyzed under stirring for 60 minutes and were then combined and stirred for 15 minutes. The combined solution was placed in an ice bath to slow down the gelation reaction and propylene oxide (PO) (CH_3CHCH_2O, Sigma Aldrich) was added dropwise at a ratio of 2.342 mol PO per mole of metal. The solution was stirred for 5 minutes and transferred to molds made from polyethylene syringes (24 mL) with the top cut off. For consistency, the plunger was placed at 20 mL and the mold filled to the 10 mL mark. Gelation was generally complete within 30 min. Parafilm was used to seal the mold and gels were held in the mold for 24 hours. Gels were then extracted into 200 proof ethanol and aged for 5 to 7 days. The aged gels were then supercritically dried using carbon dioxide, featuring four washes in liquid carbon dioxide before bringing the carbon dioxide to its supercritical state and evacuating the fluid.

5.2.2 Heat treatments

Aerogels were heated treated in high purity alumina crucibles. Heat treatments were performed in a box furnace under air with a temperature ramp of 10 °C/min to 600, 1000, or 1200 °C, each with a 20-minute hold at the maximum temperature. Aerogels were cooled to room temperature within the furnace.

5.2.3 Characterization

The diameter and length of supercritically dried (as dried) aerogel monoliths were measured to characterize bulk density and shrinkage relative to the mold. Nitrogen physisorption measurements were performed using a Micromeritics 3Flex to measure specific surface area via the method of Brunauer-Emmett-Teller (BET) and pore volume and size via the method of Barret-Joyner-Halenda (BJH). Prior to physisorption analysis, samples were degassed under vacuum at 80 °C with a heating rate of 5 °C/min and a hold of 8 hours. Scanning electron microscopy (SEM) was conducted on a Hitachi S4800 SEM to characterize pore morphology and microstructure. Samples were crushed onto carbon tape and imaged uncoated at 2 kV, 10 μA, and a working distance of 5 mm. Powder x-ray diffraction (XRD) was used to identify the crystalline phase and calculate the crystallite size via the Scherrer equation. To prepare samples for XRD, powders were crushed in a mortar and pestle with a small amount of 200 proof ethanol. The suspension was dropped via pipette onto low background holders. XRD was performed on a Bruker D8 Advance (Cu Kα, 1.5406 Å) from 10 to 100° 2θ, 0.02 degrees per step, and 0.25 seconds per step. Parallel beam geometry was used with a 0.2 mm divergence slit and a panoramic Soller slit. Rietveld refinements were performed in GSAS II (v. 4783) to identify crystalline phase and calculate crystallite size.[133] Peak positions and widths were exported and the Scherrer equation was applied to each. The reported crystallite size was obtained by taking the average of all peaks.

5.2.4 Statistical analysis

Statistical tests were conducted in OriginPro 2021b (v. 9.8.5.212). For all statistical tests, a significance level (α) was selected of 0.05. Two-way ANOVAs were first applied with dopant and concentration as the two factors. For significant factor-response pairs, Tukey tests were employed to determine which levels of the factor had a significant effect on the response.

5.3 Results

5.3.1 As dried aerogels

Zirconia (ZrO_2) aerogels were prepared at 15 and 30 mol% MO_x for M = Y, Yb, Gd, Ca, and Ce. The properties of these dopants are summarized in Table 5.1. Dopants were selected to vary charge, radius, and mass to explore the relationship between composition and thermal stability. From here, samples will be referred to as 15M or 30M (*e.g.*, 15Y, 30Y, 15Yb, etc.). Aerogels of all compositions successfully gelled and remained monolithic following supercritical drying. Qualitatively, the Y, Yb, and Gd were white and more opaque with increased dopant concentration. Ca-doped aerogels were also opaque but were markedly glassier and more brittle. Ce-doped aerogels appeared yellow with some signs of white streaking through the material.

The mass, diameter, and length of the aerogel monoliths were measured and averaged to obtain percent shrinkage and bulk density measurements. Nitrogen physisorption isotherms were used to calculate BET specific surface areas (SSA), BJH desorption cumulative pore volume (V_{BJH}), and BJH desorption average pore diameter (D_{BJH}). The summary of these results is tabulated in Table 5.2, with SSAs between 400 and 550 m^2/g and D_{BJH} from 14 to 27 nm. Increased dopant level was correlated with statistically significantly reduced shrinkage, from -21.9% for 15 mol% and -15.2% for 30 mol% ($p=0.012$). The dopant identity did not have a bearing on shrinkage or density. The dopant level modified all aspects of the pore structure with increased dopant concentration leading to lower SSA ($p=0.046$), higher V_{BJH} ($p=0.016$), and higher D_{BJH} ($p=0.022$). The dopant identity only influenced SSA ($p=0.042$). A Tukey test indicated Gd (average SSA of 500 m^2/g) and Ce (average SSA of 428 m^2/g) were significantly different, with the other dopants lying between these extremes with no statistically significant difference.

Evaluation of BJH pore size distributions (PSD) in Figure 5.1 provided additional insight to the pore structures of the doped zirconia aerogels. Increased dopant level increased the average pore size and the PSD breadth for all dopants. The PSDs appeared remarkably similar at the same dopant level, regardless of dopant identity. 30 mol% MO_x consistently formed more disperse pore structures with a larger average pore size. Scanning electron microscopy (SEM) provided a qualitative look at the as dried pore structure as a function of dopant identity and level in Figure 5.2. In general, the pores appeared larger with more dispersity in size at higher dopant level, consistent with the BJH desorption pore sizes and distributions.

5.3.2 Pore structure evolution with heat treatment

Nitrogen physisorption was performed on materials subjected to heat treatments of 600, 1000, and 1200 °C. Thermal stability is defined as maximum SSA, maximum V_{BJH}, and minimum change in D_{BJH} following heat treatment. Figure 5.3(a-c) displays the change in SSA, V_{BJH}, and D_{BJH} for each composition as a function of temperature. At 600 °C, 30Y and 30Gd performed the best, maintaining SSAs of 166 and 140 m^2/g, respectively. At 1000 °C, 30Y and 30Gd again maintained the highest SSAs of 47 and 50 m^2/g, respectively, with 30Ce also exhibiting notable stability with 49 m^2/g. Both Ce-doped samples are remarkably stable from 600 to 1200 °C, as visible in the reduced slope of the SSA between these two temperatures. All samples underwent significant densification and loss of porosity by 1200 °C with SSA generally reduced by an order of magnitude compared to 1000 °C and two orders of magnitude compared to the as dried structure. Yet again, 30Y (16 m^2/g) and 30Gd (15 m^2/g) maintained over double the average SSA of all materials at 1200 °C (7 m^2/g). Similar trends were observed in pore volume, with 30Y and 30Gd exhibiting the greatest pore volume at each temperature. In Section 5.4.2, the evolution of these structures will be evaluated in a relative sense.

From statistical analysis, dopant level consistently had a significant effect on SSA, V_{BJH}, and D_{BJH} at all temperatures, with p-values for (SSA | V_{BJH} | D_{BJH}) of (600 °C: p=0.027, 0.005, 0.003 | 1000 °C: p=0.018, 0.001, 0.004 | 1200 °C: p=0.017, 0.005, 0.014). 30 mol% M consistently gave rise to higher SSA, V_{BJH}, and D_{BJH}. Dopant identity had a statistically significant effect on SSA at 600 (p=0.010) and 1000 °C (p=0.019), despite having no statistically measurable effect in the as dried structure. No significance was detected at 1200 °C. At 600 °C, Y (15%: 125 m^2/g | 30%: 166 m^2/g) and Gd (15%: 127 m^2/g | 30%: 140 m^2/g) were significantly different than Ce (15%: 72 m^2/g | 30%: 85 m^2/g) according to a Tukey test. At 1000 °C, Gd (15%: 40 m^2/g | 30%: 50 m^2/g) and Ce (15%: 41 m^2/g | 30%: 49 m^2/g) were significantly different than Yb (15%: 22 m^2/g | 30%: 28 m^2/g).

The evolution of D_{BJH} was found to depend on dopant level, but not identity. Figure 5.3(c) demonstrates 30 mol% M had a larger average pore size at all temperatures regardless of dopant. Of note is the pore size evolution of the trivalent dopants: Y, Yb, Gd. At 30 mol%, the structures gradually coarsen with increasing temperature, before experiencing a large increase in D_{BJH} from 1000 to 1200 °C. At 15 mol%, the structures also coarsen, but only to 1000 °C, beyond which D_{BJH} drops precipitously. This behavior is remarkably consistent among the trivalent dopants, which appear to display the same trend, only shifted in absolute value. 15Ca and 15Ce behave similarly to their trivalent counterparts at 15 mol%, but D_{BJH} for 30Ca and 30Ce remains stable from 1000 to 1200 °C.

BJH desorption PSDs provided a deeper look at the pore structure as a function of composition and temperature. Figure 5.4(a-f) includes the PSD of all 10 samples at 600, 1000, and 1200 °C. At 600 °C, the PSD for 15 mol% M samples exhibited a high degree of similarity, with sharp distributions set at smaller pore sizes. The trivalent dopants (Y, Yb, Gd) PSDs nearly overlapped at 30 mol%. The area under the PSD is proportional to the total pore volume. By 1000 °C, it became evident that 30 mol% M samples maintained more porosity than their 15 mol% counterparts for all dopants. This was even more obvious at 1200 °C, where all 15 mol% distributions were essentially flat, except for 15Gd. Of the 30 mol% samples, 30Y and 30Gd maintained the most porosity made evident by their larger PSD.

SEM images were also taken for all samples at each temperature and are included in Figure 5.5(a-c) at 600, 100, and 1200 °C. At 600 °C, there was little change from the as dried structure in Figure 5.2. Only at 1000 °C did it become apparent that composition influenced densification behavior. 15Y, 15Yb, and 15Ca exhibited increased particle growth and coarsening. The other samples maintained their mesoporous structure. At 1200 °C, all samples underwent significant particle growth and sintering. In general, 30 mol% M samples maintained smaller particle sizes and some semblance of a porous structure. 15Yb and 15Ce underwent notable sintering by 1200 °C, with little mesoporosity visible.

Overall, 30Y and 30Gd displayed the most promising evolution in context of thermal stability. The results thus far evaluated thermal stability in an absolute sense, that is, which samples maintained the highest SSA and V_{BJH} while maintaining a constant D_{BJH}. In Section 5.4.2, thermal stability will be further evaluated in a relative sense by calculating the percent change or slope of a given property over a selected temperature range. Taking these results together in the context of material properties, a deeper insight may be gained into the thermal stability of highly porous structures at elevated temperatures.

5.3.3 Evolution of the crystal structure

In addition to pore structure, the evolution of the crystal structure is an important factor when considering the thermal stability of a highly porous material. Deleterious phase transformations can weaken the structure and rapid crystallite growth may contribute to significant sintering and densification of the fine mesoporous structure. All aerogels were x-ray amorphous as dried. Figure 5.6(a-j) shows the XRD patterns for all samples after heat treatments at 600, 1000, and 1200 °C and Table 5.3 includes the phases identified in all materials upon heat treatment. In general, the trivalent dopants crystallized into the cubic (c) structure. 15Ca and 15Ce exhibited a mix of tetragonal (t) and monoclinic (m) phases. 30Ca was consistently cubic and 30Ce tetragonal. In 30Ce, the tetragonal phase is known to be kinetically stabilized and in this work does not appear thermodynamically equilibrated after heat treatments at 1200 °C, where a mixture of cubic and tetragonal is expected to exist [134,135].

The XRD patterns were fit in GSASII [133]. The peak widths were used in the Scherrer equation and an average was computed from all peaks to provide a single value of crystallite size (L). The crystallite sizes measured in this work, all under 100 nm, are well within the range of relevance for this technique [136]. The results are summarized in Figure 5.7 by dopant, dopant level, and temperature. The trivalent dopants shared similar behavior, with higher dopant level suppressing crystallite growth to 1000 °C. In general, Gd maintained the smallest crystallites, followed by Y, and finally Yb. From 1000 to 1200 °C, the 30 mol% samples underwent significant crystallite growth. The 30Ca aerogel displayed similar behavior and crystallite sizes to the 30 mol% trivalent dopants. The 30Ce aerogel exhibited the most promising behavior as it maintained a single phase and much smaller crystallites than all other samples. At 1200 °C, the crystallites for 30Ce were less than half the size of any trivalent dopant. The crystallite growth behavior is markedly more complex in the Ca- and Ce-doped aerogels at 15 mol% M. In these cases, the formation of secondary monoclinic phases modifies the crystallite growth behavior. The tetragonal crystallites in these samples continued to grow, albeit at a reduced rate once the monoclinic phase was detected. The monoclinic phase, once formed, exhibited a drop in crystallite size from 1000 to 1200 °C.

5.4 Discussion

5.4.1 Effect of dopant level and concentration on the as dried structure

Increased dopant concentration from 15 to 30 mol% $MO_{1.5}$ formed coarser pore structures with lower SSA, larger pore volume, larger average pore size, and more disperse pore size distributions. This trend held true for all dopants. This presents a challenge to a hypothesis proposed in our previous work on YSZ aerogels from 0 to 50 mol% $YO_{1.5}$, described in Chapter 4, where a similar trend was observed of coarser pore structures with increasing yttria content [126].

We hypothesized that with increasing yttria content, the concentration of nucleophile (Cl^-) for epoxide ring opening is higher as YCl_3•xH_2O provides more chloride than $ZrOCl_2$•xH_2O. This in turn increases the rate of gelation and results in structures that resemble agglomerated networks of precipitates rather than homogenous gels. The challenge arises for Ca-doped ZrO_2, which should not exhibit this behavior according to our previous hypothesis as $Ca(NO_3)_2$•xH_2O does not provide additional nucleophile compared to $ZrOCl_2$•xH_2O. Despite providing the same amount of nucleophile, 30 mol% CaO formed a coarser pore structure much like the other dopants in the study that do increase nucleophile concentration. To examine this effect and re-evaluate our hypothesis, previous work on epoxide-assisted sol-gel chemistry is informative [60,62]. Beyond concentration of nucleophiles for the ring opening reaction, the nucleophilicity of chloride compared to the nitrate anion as well as the charge of the metal ions must be considered.

First, it is important to recognize that the calcium precursor is the only nitrate salt used in this study. The hydrated calcium chloride salt is prohibitively expensive if these aerogels are to be used in insulative applications. Previous work by Gash et al. on iron oxide aerogels prepared from chloride and nitrate precursors evaluated the structure of the aerogel as a function of salt anion and solvent [62]. In ethanol, the rate of gel formation was found to be faster for the nitrate salt compared to the chloride salt, despite the nitrate anion being the weaker nucleophile. SSA, pore volume, and pore size were higher for the chloride salt. In the presently studied Ca-doped ZrO_2 aerogels, the pore size was larger at higher mol% CaO, despite the share of nitrate anions increasing, which would be expected to decrease pore size according to the results from Gash. Thus, the difference between chloride and nitrate does not explain the behavior observed in the present work.

The charge of metal ions influences the acidity of hydrated metal cation species, $[M(H_2O)_x]^{x+}$, in solution. As water coordinates to the metal center during hydrolysis, a higher metal coordination number makes the water molecules more acidic. Thus, higher oxidation states will make hydrolysis occur more quickly [115]. A study on mixed metal-silicon oxide aerogels (Al, Cr, Zr, Hf, Nb, Ta, W, and more) by Clapsaddle et al. evaluated the structure of aerogels prepared from hydrated metal salts and propylene oxide [60]. In this work, gel times decreased as coordination number increased, owing to increased acidity and reactivity of the water in the hydrated metal complexes. With shorter gel times, observed shrinkages were higher and the average pore sizes were lower. Longer gel times were generally associated with large particle sizes and coarser pore structures. The authors proposed that with longer gel times, there was more time for nucleation and growth of particles in the sol prior to gelation. Larger particles cannot pack as closely together, leading to reduced shrinkage and larger pore size.

This observation can be applied to the present work to understand the change in structure with increased dopant level. For Y^{3+}, Yb^{3+}, Gd^{3+}, and Ce^{3+}, adding more dopant relative to Zr^{4+} reduces the average oxidation state and acidity of hydrated metal complexes, thereby reducing the reaction rate. Reducing the reaction rate generates coarser structures by allowing more time for nucleation and growth of particles in the sol prior to gelation. The same is true for Ca^{2+}, which again lowers the average oxidation state of metal ions in solution. Although the ratio of nitrate to chloride is increased at higher mol% CaO, it is evident the effect of metal oxidation state is greater than that of changing nucleophile. That said, if the shrinkage and pore size of the Ca-doped aerogels are compared to other dopants, the aerogels did experience more shrinkage and have slightly smaller pore sizes which is consistent with previous work on aerogels derived from nitrate salts, which reduce the gel time and therefore the time for nucleation and growth of particles.

In summary, as the level of dopant is increased from 15 to 30 mol%, a metal with a +4 oxidation state (Zr^{4+}) is being replaced by metals of +2 or +3 oxidation states (Y^{3+}, Yb^{3+}, Gd^{3+}, Ce^{3+}, Ca^{2+}) This reduces the reaction rate by reducing the acidity of water in the hydrated metal complexes, allowing for more nucleation and growth in the sol prior to gelation. This results in coarser structures composed of larger particles that exhibit lower shrinkages and broader pore size distributions.

5.4.2 Evaluation of thermal stability

It is prudent to first define by what metrics thermal stability may be evaluated in the context of aerogels. The most relevant assessment of thermal stability is maintaining a highly porous structure conducive to low thermal conductivity. The loss of porosity should be minimized by maximizing SSA and pore volume. By minimizing change in pore size, thermal conductivity and other transport properties can be maintained at a similar value through the operating temperature range of the material. Limiting phase transformations and crystallite growth will ensure structural integrity of the aerogel. All the metrics can be evaluated in an absolute sense, that is directly comparing the SSA or any other property of one formulation to another at a given temperature. This is the simplest method by which thermal stability can be evaluated.

As covered in the Results, increased dopant concentration lends improved thermal stability, with select dopants outperforming the rest. At 1000 °C, 30 mol% Ce, Gd, and Y maintain the highest SSA and pore volume. At 1200 °C, 30 mol% Gd and Y perform the best It is important to note increased dopant concentration also changed the as dried structure, forming coarser structures with larger initial pore sizes. The coarser structure with higher dopant concentration should reduce the driving force for sintering and densification, improving thermal stability. The effect of starting structure on thermal stability was evaluated in Section 6.4.3. The analysis therein suggests the differences in as dried structure between 15 and 30 mol% dopant should not have a significant effect on thermal stability. Therefore, the effect is believed to be the result of the increased dopant concentration and not the change in the as dried structure.

It is also possible to evaluate relative stability, which looks at how a property changes over a selected temperature range. This method of evaluation can give insight to what degree a material's structure changes over a given operating range of temperatures. Information on the evolution of the materials may be gleaned by calculating the percent change (Equation 5.1) or slope (Equation 5.2) of a property over a temperature interval. X represents a structural property, such as SSA, V_{BJH}, or D_{BJH} and T is temperature in degrees Celsius. In this work, all materials are highly porous as dried, and it is ultimately the ability to minimize the change in structure that will prove advantageous when applied as insulation. For SSA, pore size, and pore volume, calculation of percent change will be applied to evaluate relative stability, with lower percent change reflecting higher thermal stability. For crystallite size, calculation of slope will be applied to evaluate relative stability. Since the crystallite size is effectively zero in the initial as dried, x-ray amorphous state, the initial value of crystallite size upon crystallization can undesirably affect the comparison of thermal stability when percent change is applied. It allows for the comparison of the responses of materials that have different starting structures.

$$Percent\ Change\ = \frac{X_{Final} - X_{Initial}}{X_{Initial}} \times 100\% \qquad \textbf{Equation 5.1}$$

$$Slope\ = \frac{X_{Final} - X_{Initial}}{T_{Final} - T_{Initial}} \qquad \textbf{Equation 5.2}$$

Relative stability may be evaluated over the entire temperature range or select temperature ranges. Comparison of materials over different temperature ranges is useful for potential applications and their unique operating temperature ranges. Figure 5.8 displays the percent change of SSA, pore volume, and pore size over three temperature ranges: as dried to 600 °C, 600 to 1000

°C, and 1000 to 1200 °C. Figure 5.9 shows the slope of crystallite size from 600 to 1000 °C and 1000 to 1200 °C.

For analysis within this study, the change from the as dried structure to 1000 °C was selected for SSA, pore size, and pore volume and change from 600 to 1200 °C for crystallite size. The values of percent change and slope are included in Table 5.4. Dopant identity ($p=0.016$) and concentration ($p=0.010$) had significant effects on the percent change of SSA from as dried to 1000 °C, with 30 mol% dopant retaining more SSA. From a Tukey test, there were three different groups of dopants for retention of SSA, listed here in descending order of stability: Ce/Gd/Y, Gd/Y/Ca, Y/Ca/Yb. Though 30 mol% Ce performed the best in terms of relative stability to 1000 °C, this composition rapidly densified from 1000 to 1200 °C. This demonstrates the importance of considering both relative and absolute stability, as well as considering different temperatures and ranges depending on the application.

Dopant identity had a significant effect ($p=0.013$) on crystallite growth, but the concentration did not ($p=0.384$). There were two significantly different groups of dopants: Y/Yb/Gd/Ca and Ca/Ce. Yb, Y, and Gd experienced the most crystallite growth, but were also the most phase stable. Within the series of trivalent dopants, smaller ionic radius was associated with increased crystallite growth. Despite minimizing crystallite growth, phase stability may be a disadvantage with Ce and Ca. The exception is 30 mol% Ce, which maintained a single tetragonal phase and the least crystallite growth. This composition also maintained a stable pore structure to 1000 °C, but densified rapidly upon exposure to 1200 °C.

5.4.3 Towards a design framework for thermally stable aerogels

Evaluation of thermal stability in context of material properties will contribute towards a design framework to enable the intentional exploration of thermally stable aerogels. Previous work did this for YSZ aerogels: lower cation diffusivity and lower surface energy were identified as potential markers for improved thermal stability [104,106,126]. To further evaluate these hypotheses, study of a wider range of dopants and concentrations is necessary. In the present work, many dopants were evaluated, but material properties are not readily available for the entire range of materials studied. Cation properties, such as radius, mass, and charge, may serve as useful proxies for other material properties. The properties can be weighted by cation composition to reveal the effect of changing radius, mass, and charge. This is demonstrated in Equation 5.3, where x_M is the mole fraction MO_y and P_M is the property of dopant M^{2y+}. The weighted properties were then scaled on [0, 1] to allow for comparison between radius, mass, and charge on the same plot.

$$Weighted\ Property = x_{Zr}P_{Zr} + x_M P_M \qquad \textbf{Equation 5.3}$$

The thermal stability as a function of the weighted property can be evaluated in an absolute or relative sense. For absolute stability, the SSA, pore volume, pore size, and crystallite size were taken at 1000 °C and plotted as a function of the scaled and weighted cation properties in Figure 5.10(a-d), respectively. Linear regression was then performed. Cation radius and charge did influence the pore structure at 1000 °C. Increased radius was associated with higher pore volume ($p=0.04$) and larger pore size ($p<0.001$). Increased charge was associated with smaller pore size ($p<0.001$). Linear regression was similarly performed for relative stability (percent change, slope), but no statistically significant relationships were identified. The data for relative stability as a function of weighted cation properties are included in Figure 5.11(a-d).

Additional work is required to bring together property and performance measurement to improve the design of thermally stable aerogels. Despite the fact that radius, charge, and mass of the cation do not have clear effects on thermal stability, many material properties have complex relationships with these cation properties. Well-designed experiments, especially coupled with simulation, measuring material properties and thermal stability will enable design rule development.

Lastly, the magnitude of changes to thermal stability as a function of composition must be considered. Though statistically significant differences were observed in this work, none are arguably large enough to consider any of the presently studied pore structures “thermally stable”. Here, we probed the extremes of doped zirconia. Previous work studying composition’s influence on thermal stability has led to mixed results. Aerogels composed of TiO_2, Nb_2O_5, and ZrO_2 aerogels maintained SSAs that varied by a factor of 3 at 500 °C, but this same variation was observed in the as dried state [47]. Oxide aerogels of Ce, Pr, Sm, and Tb were prepared with SSAs of 250, 296, 129, and 147 m^2/g, respectively, and maintained SSAs of 60, 60, 90, and 90 m^2/g after heat treatment at 650 °C [48]. Looking at this wide range of metal oxides with varying properties and as dried SSAs, the difference in thermal stability was small. Doping alumina with yttria and zirconia with yttria and/or ytterbia improved thermal stability [49,103,126]. These doped aerogels offered improved thermal stability to 1000 °C, but any advantage was consistently eliminated beyond this temperature.

More impactful routes to thermal stability may include new synthetic techniques and post-synthetic modification of aerogels to improve the robustness of the structure towards densification. Comparing soluble precursors (metal salts) to colloidal boehmite in the preparation of aluminosilicate aerogels demonstrated the dramatic influence of synthetic route on the structure, chemistry, and thermal stability of aerogels [50]. The effect of precursor and synthetic route goes beyond simply changing the SSA and pore size for a given composition, rather emerging from the morphology of the precursor, connectivity of primary particles, and the spatial distribution of constituents in multi-oxide aerogels. The improved stability of the boehmite derived materials might be attributable to the boehmite being crystalline to start, eliminating the shrinkages associated with the crystallization of an amorphous as-dried gel. Continued work on novel colloidal syntheses of aerogels may serve as useful routes towards the development of thermally stable aerogels [137,138]. Modification of aerogel structures with post-synthetic coatings and functional groups has proven effective to have marked improvement on thermal stability [139,140]. Such approaches prevent condensation of surface hydroxyl groups by capping hydroxyl groups with non-condensable functional groups which then form secondary-phase particles that pin grain boundaries and prevent crystallite growth at higher temperatures. Overall, advances in aerogel synthesis may prove the most effective means of achieving thermal stability and enabling the use of aerogel as insulation in extreme environments. The advances must go beyond straightforward synthetic parameters and leverage novel precursors, assembly techniques, and post-synthetic modifications to enhance thermal stability.

5.5 Summary

Doped zirconia aerogels of 15 and 30 mol% M/(M+Zr) where M = Y, Yb, Gd, Ce, Ca were synthesized from metal salt precursors and supercritically dried. Higher dopant concentration formed coarser pore structures with broader pore size distributions and larger average pore sizes. This result was linked to the reduction in average metal oxidation state in solution with increased dopant level. The thermal stability as a function of composition was evaluated in absolute terms, with 30 mol% $GdO_{1.5}$ and $YO_{1.5}$ maintaining the highest SSA and pore volume to 1200 °C. In general, increased dopant concentration improved the thermal stability for all dopants at 1200 °C, which may be correlated to the initial microstructure of the as-dried aerogels. Relative stability was also used to compare thermal stabilities, again with increased dopant concentration lending improved thermal stability and Y and Gd performing the best of all dopants. Attempts to derive relationships between thermal stability and weighted cation properties (charge, mass, size) were largely unsuccessful, with only a few statistically significant relationships. Overall, the magnitude of thermal stability improvement achieved by modifying dopant identity and concentration was considered in context to other routes, including modification of synthetic techniques. This comparison points towards the fact that development of new synthetic techniques will likely offer the greatest chance at achieving the thermal stability required to use aerogels as insulation in the extreme environments of aerospace applications.

5.6 High-throughput analysis & machine learning for material discovery

5.6.1 Overview

A machine learning program was written in Python for the purposes of providing a deeper analysis of the data produced by this project. The code is available online upon request at https://colab.research.google.com/drive/1gZ8e5zyE6nRtshLqkAlmr0sl6EzwMJ3H?usp=sharing. The program requires a set of aerogel porosity data, including SSA, V_{BJH}, and D_{BJH} for the as dried material and these properties plus crystallite size after heat treatments at 600, 1000, and 1200 °C. A set of material property data for the compositions being studied is also required for the machine learning portion of the program.

The first segment of the program cleans the data and performs calculation of slopes and percent changes. Next, the program can produce visualizations of the data in an array of graphs relevant to this work. The most important part of the program employs random forest (RF) algorithms for machine learning via scikit-learn [141]. The RF algorithm is trained on the experimental data (SSA, pore size, pore volume, crystallite size as a function of temperature) and material property data for a given composition pulled from literature and various databases. The accuracy of the model is then tested on a small subset of the experimental data not used in training the algorithm. The RF employs many decision trees and averages the result of each tree to provide a prediction of a selected property at a given temperature (or the change in the property over a temperature interval). Hyperparameter tuning was conducted to maximize the accuracy of the model.

Predictions were then provided for several compositions of potential aerogels not yet synthesized. By feeding the program the material's properties, the SSA, pore volume, pore size, and crystallite size could be predicted at high temperature. In essence, we can pre-select favorable candidate compositions for synthesis rather than blindly selecting materials to test. Further work is required to improve the quality of material property data used to train the model before these predictions can be utilized.

5.6.2 Material property data used in machine learning

There are innumerable properties that change as a function of composition for the materials under study in this work. For the YSZ study, improvements in thermal stability at high yttria concentrations were attributed to (1) reduced surface energy and (2) reduced cation diffusivity with increased yttria content. Reduced surface energy will reduce driving force for densification and pore collapse. Reduced cation diffusivity will reduce rates of mass transport leading to densification and pore collapse. For the dopant study, where five dopants are studied at two concentrations each, it becomes more difficult to connect material properties to thermal stability. To aid in this effort, a key part of this project will be correlation thermal stability to several material properties obtained via literature references. The properties used, where available, were melting point, enthalpy of formation, weighted cation mass, weighted cation charge, weighted cation radius, and theta (estimate of contribution of a given cation to the specific heat capacity of the material) [116,142].

5.6.3 Machine learning with random forests

Random forests (RF) are a machine learning technique that can be used for classification or regression, among other tasks. RFs utilize many decision trees and provide the mode of the classes (in the case of classification) or the mean prediction (in the case of regression) of the individual trees. The use of many trees can overcome the primary issue of individual decision trees: a tendency to overfit data.

RFs are often used for regression problems. Regression is used on labeled data for supervised learning to provide (1) relationships between dependent and independent variables and (2) predictive models for these variables (dependent variable = response, independent = predictor). Here, the database of material properties will serve as predictors (e.g., cation radius, cation mass, melting temperature, etc.). These predictors are based upon the material's composition.

For the response, the analysis is divided into two parts. First, absolute performance where the responses will be the SSA and V_{BJH} at 600, 1000, and 1200°C. The objective is to maximize these responses. Second, rate of densification where the response will be the percent change of SSA, V_{BJH}, and D from the AD to 1000°C and the slope of crystallite size (L) from 600 to 1000°C. The objective is to minimize these responses.

In other words, a model was trained for each of these responses (6 from absolute, 4 from rate of densification). There are two important takeaways from the RF model. One will be an understanding of the relative importance of each predictor on the response. The second will be a model that will allow prediction of the performance of a material based upon its material properties. This will enable the pre-screening of candidate materials for thermally stable aerogels and targeted study of promising compositions.

5.6.4 Results from random forest models

Data was prepared by taking the necessary data from data frames into numpy arrays. Hyperparameter tuning was performed on the entire data set of SSA percent changes from AD to 1000 °C. To quantify model quality, the model mean square error (MSE) was compared to the baseline MSE, the baseline MSE being the MSE where all samples are predicted to have the overall mean percent change. First, a random grid was created of parameters. Once an area of "optimal" parameters was found, a full grid was created to decide on a single set of hyperparameters. The final set of hyperparameters used were 30 estimators/trees, 4 minimum samples for a split, 2 minimum samples per leaf, maximum features of 'sqrt', maximum depth of 50, and bootstrapping enabled.

Once hyperparameters were identified, a total of ten random forest models were trained (SSA and V_{BJH} each at 600, 1000, and 1200 °C; percent change of SSA, V_{BJH}, and D each from AD to 1000 °C; slope of L from 600 to 1000 °C). For each, the percent improvement over the baseline for that measurement was evaluated. Given the set of hyperparameters selected, seven models offered significant improvement over the baseline: SSA at 1000 °C, SSA at 1200 °C, V_{BJH} at 1200 °C, L at 600 °C, L at 1200 °C, SSA percent change from AD to 1000 °C, and V_{BJH} percent change from AD to 1000 °C. Lists of feature importance were generated for these models, and it was revealed cation radius, cation mass, enthalpy of formation, and specific heat capacity had the biggest impact on the model. This might be a hint of properties to pursue in the future. Included in Table 5.5 are the responses with RF models that outperformed the baseline MSE along with the most important factors to the model.

Finally, as a demonstration of the planned utility for the models, several compositions were proposed that have yet to be synthesized and characterized. The compositions assessed in the models were 30 mol% M_xO_y in ZrO_2 (M_xO_y = $FeO_{1.5}$, SrO, $LaO_{1.5}$, $ScO_{1.5}$, HfO_2) and 30 mol% $YO_{1.5}$ in HfO_2. Using the models that showed improvement over the baseline, predictions were generated for the structural properties & relative stability of these materials at high temperatures and are shown in Table 5.6. These predictions offer insight into promising material compositions to prepare and study in the future, but it is important to note none of the compositions assessed here outperformed the material already studied. This is due in part to a limitation of machine learning to extrapolate beyond existing data, but also points to composition being an insufficient parameter to achieve high thermal stability, indicating alternative routes including new syntheses, novel precursors, and post-synthetic surface modification are routes for future study.

There exist opportunities to improve quality of the data, especially the material property data that is fed into the model. Combing through literature, material property databases, and books for material data could prove useful. An ever-present issue in this work was overcoming different sample preparation and measurement techniques used in the literature, leading to discrepancies between materials. When possible, using fundamental material property data is ideal. Machine learning algorithms beyond random forests may also be of interest. Random forests suffer from lack of interpretability and the weights given to various factors do not have any physical meaning, making it difficult to fully understand property-stability relationships at a fundamental level.

5.7 Figures and tables

Table 5.1: Precursor and cation properties for metal oxides under study. Cation radii are listed for a coordination number of 8. The cation charges below are assumptions. For Ce, the charge was assumed to be +3 for the precursor, but +4 following aerogel heat treatment [116,143].

M	Precursor	Cation Charge	Cation Radius (Å)	Cation Mass (amu)
Zr	$ZrOCl_2 \bullet 8H_2O$	+4	0.840	91.22
Y	$YCl_3 \bullet 6H_2O$	+3	1.019	88.91
Yb	$YbCl_3 \bullet 6H_2O$	+3	0.985	173.0
Gd	$GdCl_3 \bullet 6H_2O$	+3	1.053	157.2
Ca	$Ca(NO_3)_2 \bullet 4H_2O$	+2	1.120	40.08
Ce	$CeCl_3 \bullet 7H_2O$	+3/+4	0.970	140.01

Table 5.2: Measurements of porosity and physical structure for the as dried aerogels. In general, increased dopant results in lower shrinkage and coarser pore structures with lower SSA, larger D_{BJH}, and larger V_{BJH}.

SSA = BET specific surface area
V_{BJH} = BJH desorption cumulative pore volume
D_{BJH} = BJH desorption average pore diameter
S = as dried shrinkage (diameter)
ρ_b = bulk density

M	mol % MO_x	SSA (m^2/g)	V_{BJH} (cm^3/g)	D_{BJH} (nm)	S (%)	ρ_b (g/cm^3)
Y	15	501	2.07	16.4	-21.1	0.250
	30	473	2.91	26.9	-12.5	0.186
Yb	15	463	1.98	17.8	-20.0	0.234
	30	452	2.29	19.1	-12.9	0.220
Gd	15	532	2.10	14.5	-19.6	0.230
	30	469	2.26	17.9	-12.4	0.219
Ca	15	478	1.61	14.3	-24.7	0.232
	30	463	2.43	22.6	-23.8	0.208
Ce	15	437	1.73	16.7	-24.0	0.281
	30	419	2.56	26.7	-14.3	0.202

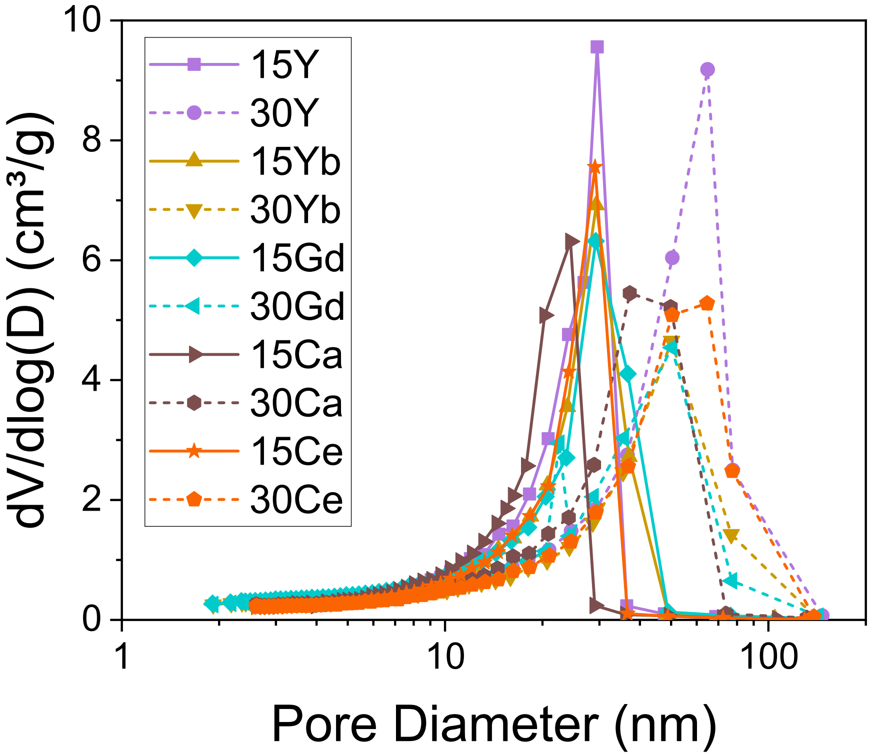

Figure 5.1: BJH desorption pore size distributions for as dried materials. For the as dried material, the distributions are grouped by dopant concentration with 15 mol% having a narrower distribution with smaller average pore size. Increased dopant concentration forms a broader distribution of larger pores.

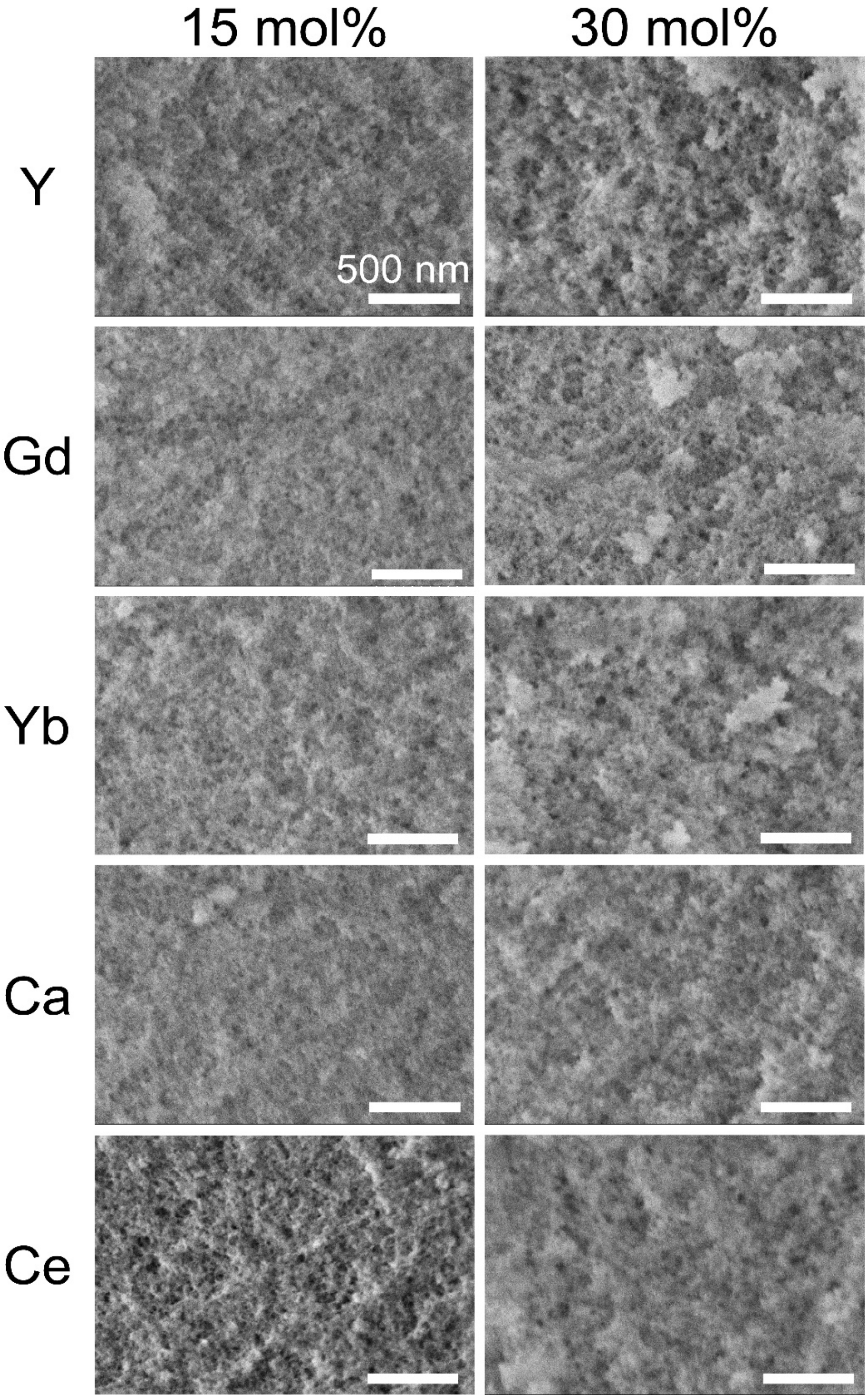

Figure 5.2: SEM images for the as dried aerogel samples. The scale bar is 500 nm in all images. In general, increased dopant concentration is associated with a more heterogenous population of pore sizes with larger pore size on average. SEM is capturing the macroporosity and does not have the resolution required to image mesoporosity directly.

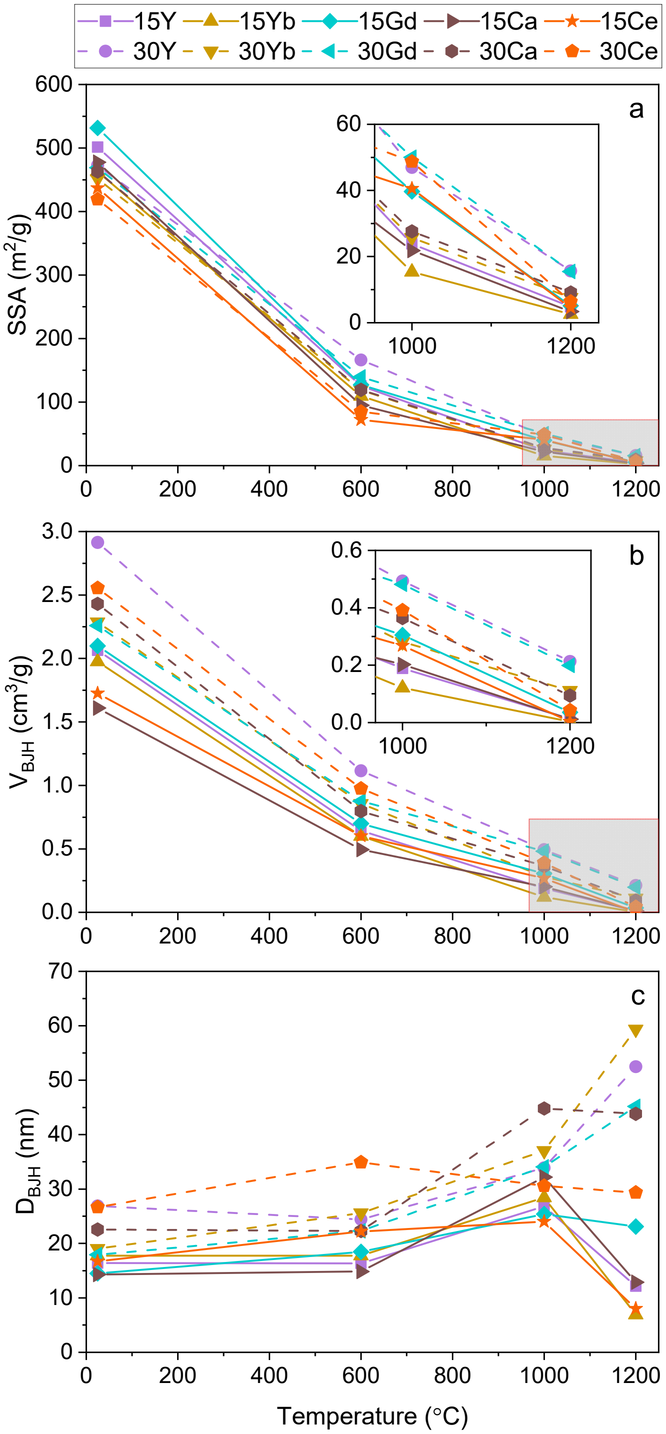

Figure 5.3(a-c): The evolution of (a) SSA, (b) V_{BJH}, and (c) D_{BJH} from as dried to 1200 °C. As seen in the inset images in (a) and (b), increased dopant concentration has improved thermal stability, retaining higher SSA and V_{BJH} at 1000 and 1200 °C. 30Y and 30Gd perform the best of all samples. The evolution of pore size has no distinct trends to 1000 °C, but from 1000 to 1200 °C, all 30 mol% trivalent dopants (Y, Yb, Gd) grow in size while the same dopants at 15 mol% shrink in size. Sufficient mass and sample area were utilized to minimize instrument error. Error bars are expected to be on the order of the marker size.

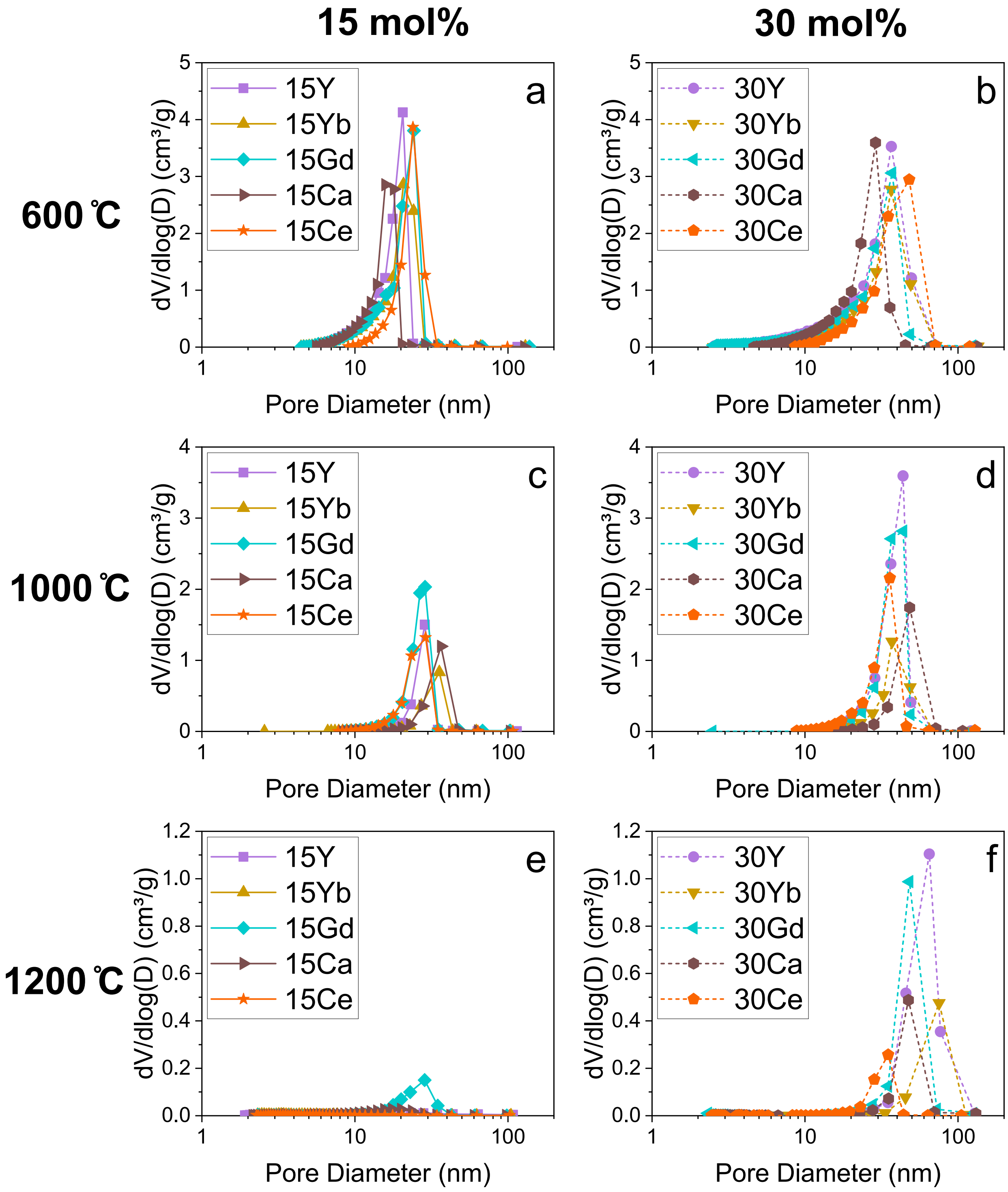

Figure 5.4(a-f): BJH pore size distributions for 15 mol% (left column) and 30 mol% (right column) as a function of temperature. As the materials are heated, 30 mol% dopant samples in (d) and (f) have increased pore volume compared to their 15 mol% counterparts in (c) and (e). At 1200°C, the only 15 mol% sample to maintain mesoporosity is 15Gd, whereas all 30 mol% samples maintain mesoporosity. Note the scale of the y-axis changes between temperatures.

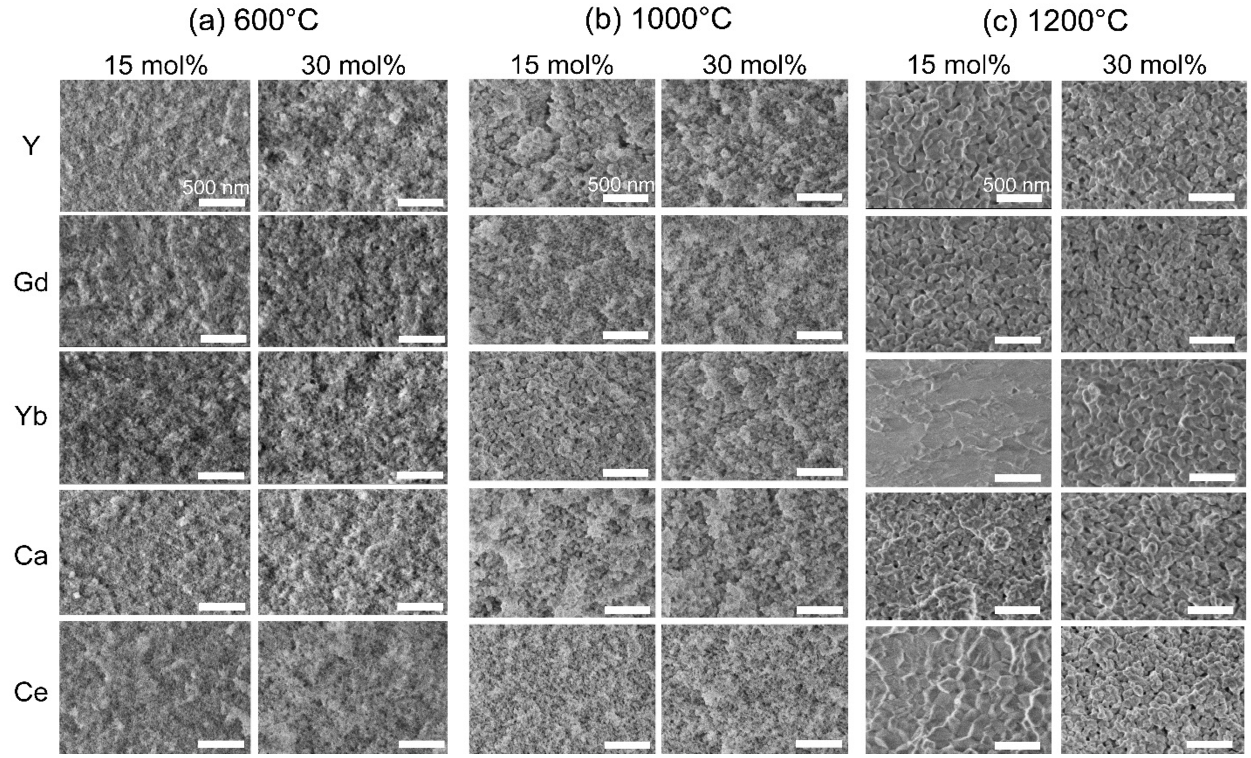

Figure 5.5(a-c): SEM images after heat treatment at (a) 600 °C, (b) 1000 °C, and (c) 1200 °C. Differences begin to appear at 1000 °C for 15Y, 15Yb, and 15Ca with increased particle growth and coarsening. At 1200 °C, all samples begin to show coarsening and loss of mesoporosity.

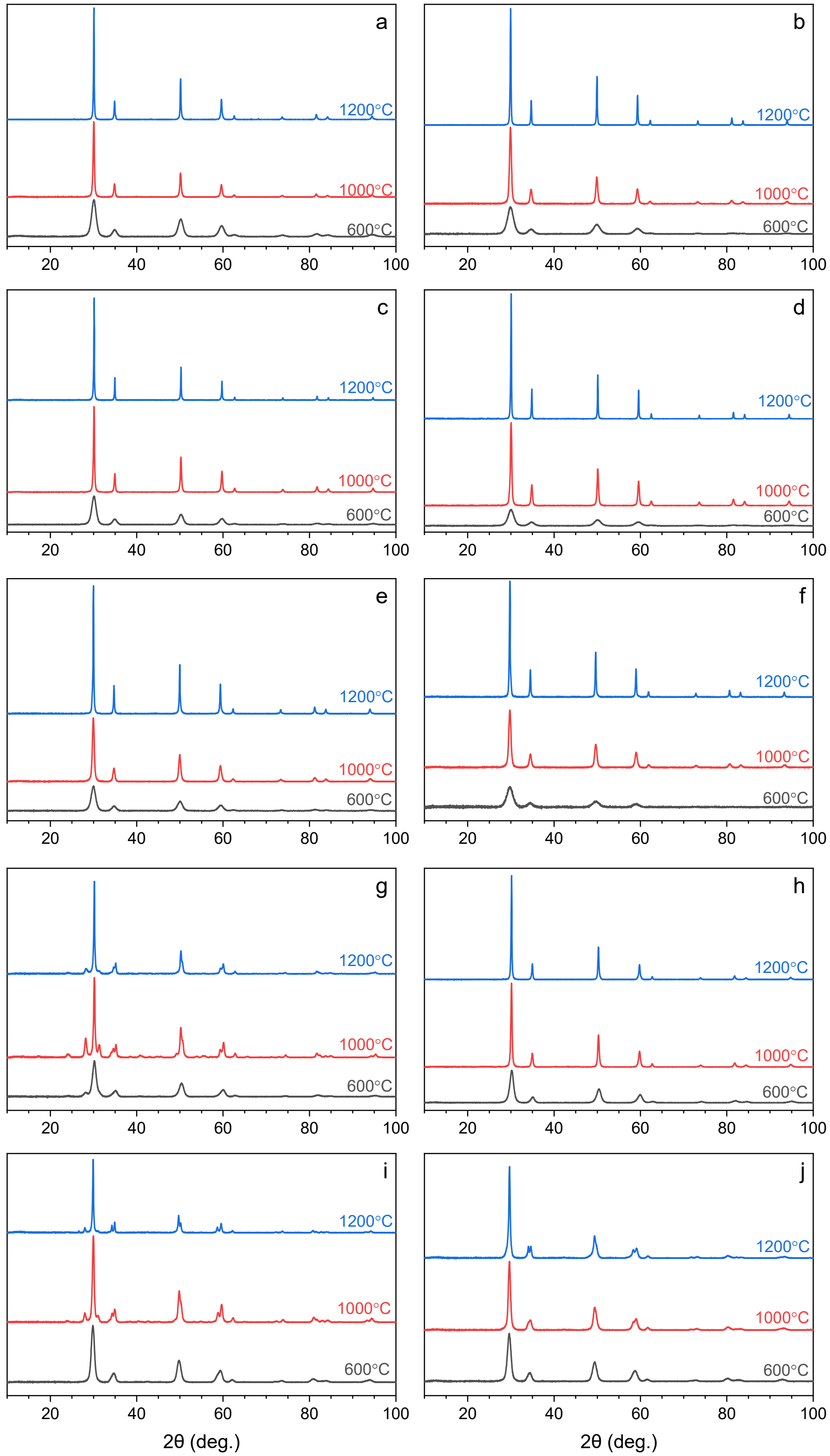

Figure 5.6(a-j): XRD patterns for (a) 15Y, (b) 30Y, (c) 15Yb, (d) 30Yb, (e) 15Gd, (f) 30Gd, (g) 15Ca, (h) 30Ca, (i) 15Ce, and (j) 30Ce. The phases identified in each sample are included in Table 5.3 and crystallite sizes in Figure 5.7.

Table 5.3: Crystalline phases identified in heat treated aerogels (c=cubic, t=tetragonal, m=monoclinic). Y, Yb, and Gd identified as cubic at all temperatures and dopant levels. 30Ca was cubic and 30Ce tetragonal. 15Ca and 15Ce both crystallized into the tetragonal phase, but the monoclinic phase was identified at 1000 and 1200 °C.

	mol % MO_x	**600 °C**	**1000 °C**	**1200 °C**
Y	15	c	c	c
	30	c	c	c
Yb	15	c	c	c
	30	c	c	c
Gd	15	c	c	c
	30	c	c	c
Ca	15	t	t, m	t, m
	30	c	c	c
Ce	15	t	t, m	t, m
	30	t	t	t

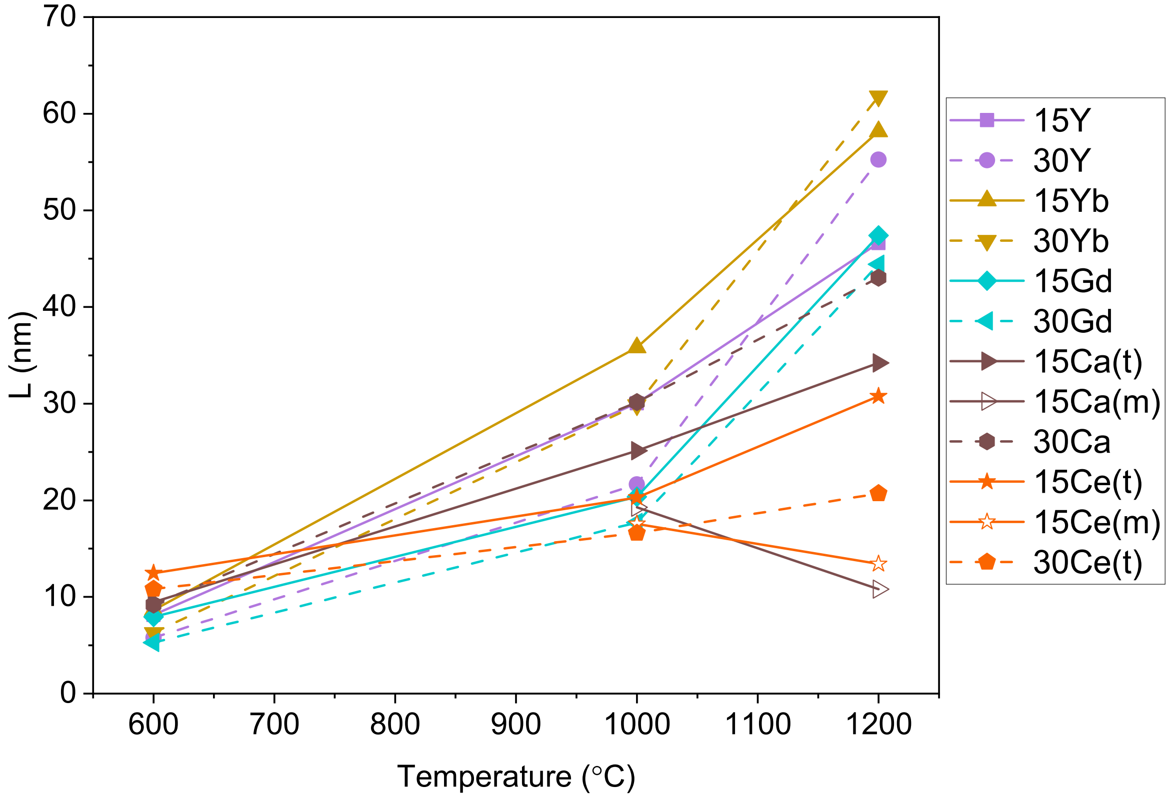

Figure 5.7: The evolution of crystallite size for all samples, including multiple phases for 15Ca and 15Ce. The trivalent dopants display similar behavior, with higher dopant levels suppressing crystallite growth to 1000 °C (Gd < Y < Yb). 30Ce maintained the smallest crystallite size at 1000 and 1200 °C for a single-phase sample. The scatter is smaller than the markers, so error bars are excluded (standard deviation generally lower than 1 nm).

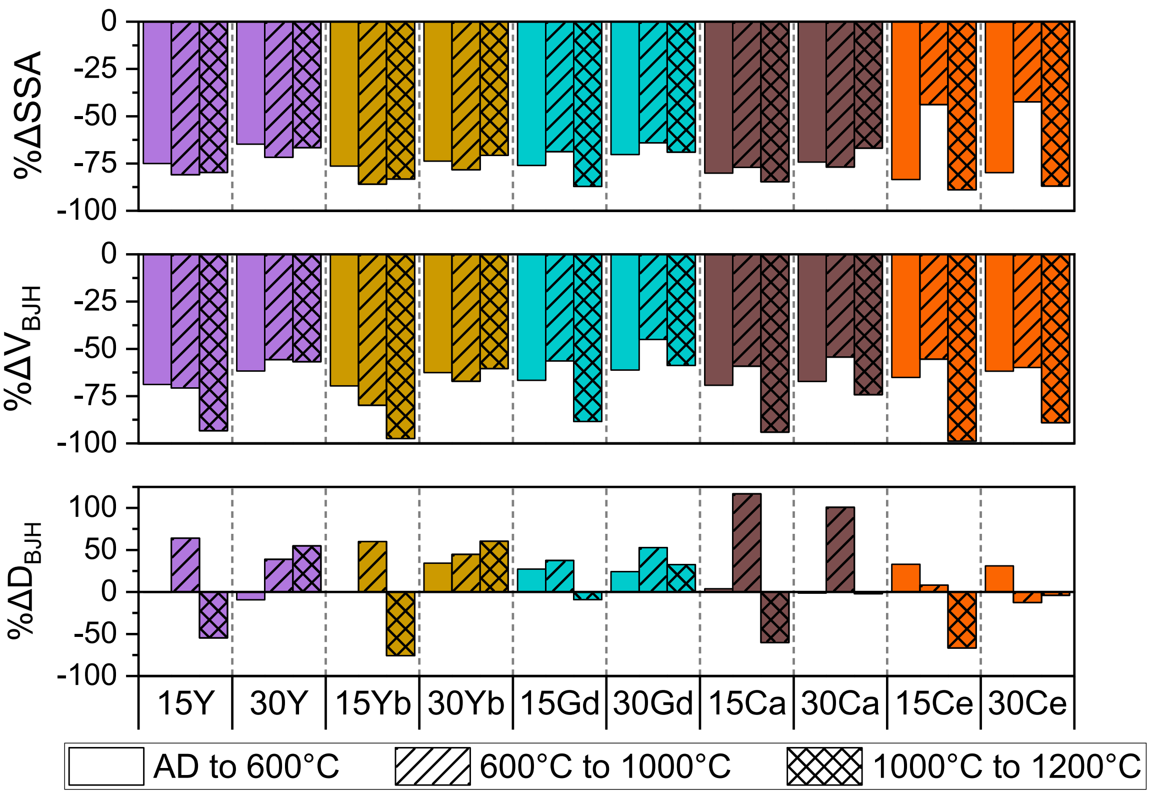

Figure 5.8: The percent change of SSA, V_{BJH}, and D_{BJH} from AD to 600 °C, 600 to 1000 °C, and 1000 to 1200 °C. The change in SSA and V_{BJH} permit stability over a given temperature range to be evaluated. As an example, doping with Ce leads to rapid loss of porosity from AD to 600 °C and 1000 to 1200 °C, but improved stability from 600 to 1000 °C.

Table 5.4: The percent change of SSA, V_{BJH}, and D_{BJH} from the as dried state to 1000 °C. The slope of L is calculated from 600 to 1200 °C. Samples with best overall thermal stability to 1000 °C are 30Y, 30Gd, and 30Ce. For all samples, increased dopant concentration reduced the amount of densification experienced.

M	**mol % MO_x**	**SSA**	**V_{BJH}**	**D_{BJH}**	**L**
Y	15	-95.2	-90.9	63.6	0.064
	30	-90.1	-83.1	26.2	0.082
Yb	15	-96.7	-93.9	60.1	0.083
	30	-94.3	-87.7	94.4	0.093
Gd	15	-92.5	-85.5	75.3	0.066
	30	-89.3	-78.7	90.1	0.065
Ca	15	-95.4	-87.4	125.1	0.041
	30	-94.0	-85.0	98.6	0.056
Ce	15	-90.7	-84.4	43.8	0.031
	30	-88.4	-84.7	14.7	0.014

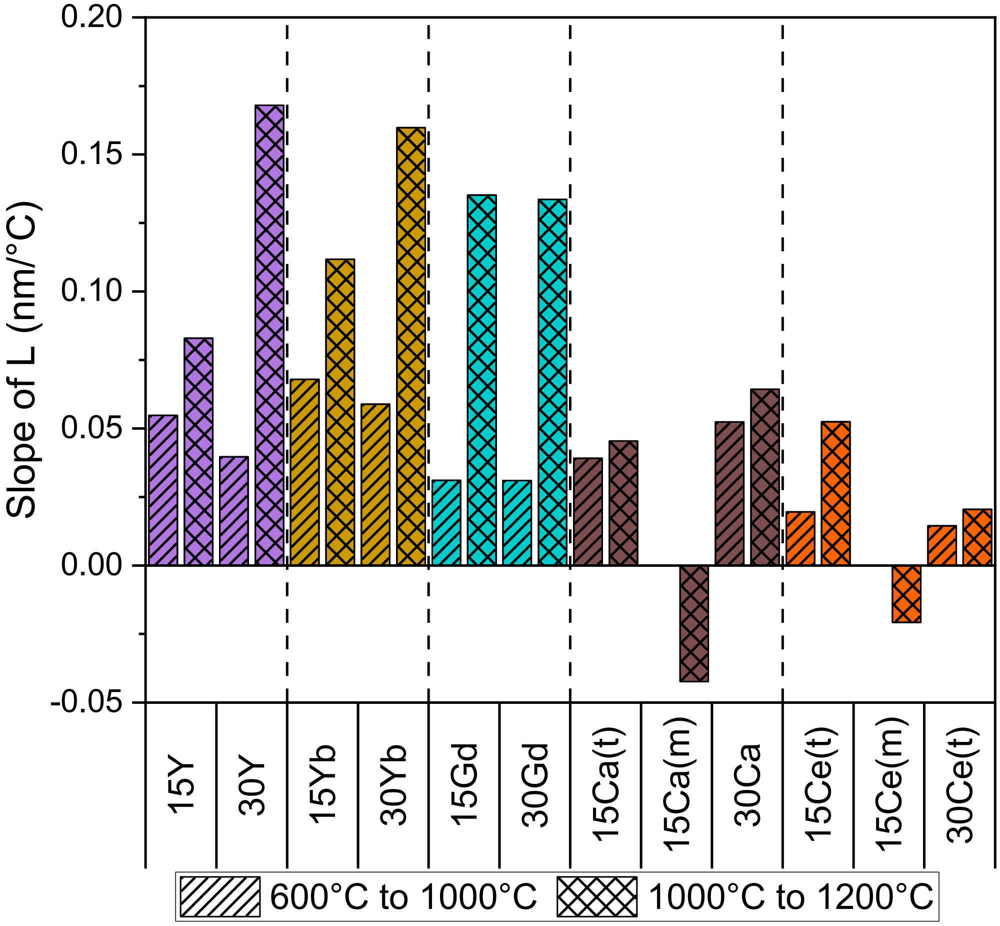

Figure 5.9: The slope of crystallite size from 600 to 1000 °C and 1000 to 1200 °C for each material and unique phase. All materials were cubic phase unless otherwise noted (t=tetragonal, m=monoclinic). For Y, Yb, and Gd, increased dopant concentration generally suppresses crystallite growth from 600 to 1000 °C, but 30 mol% samples grow rapidly from 1000 to 1200 °C. The crystallite growth of 15Ca and 15Ce is complicated by the phase changes experienced in those samples. 30Ce maintains a single phase and undergoes minimal crystallite growth relative to other samples.

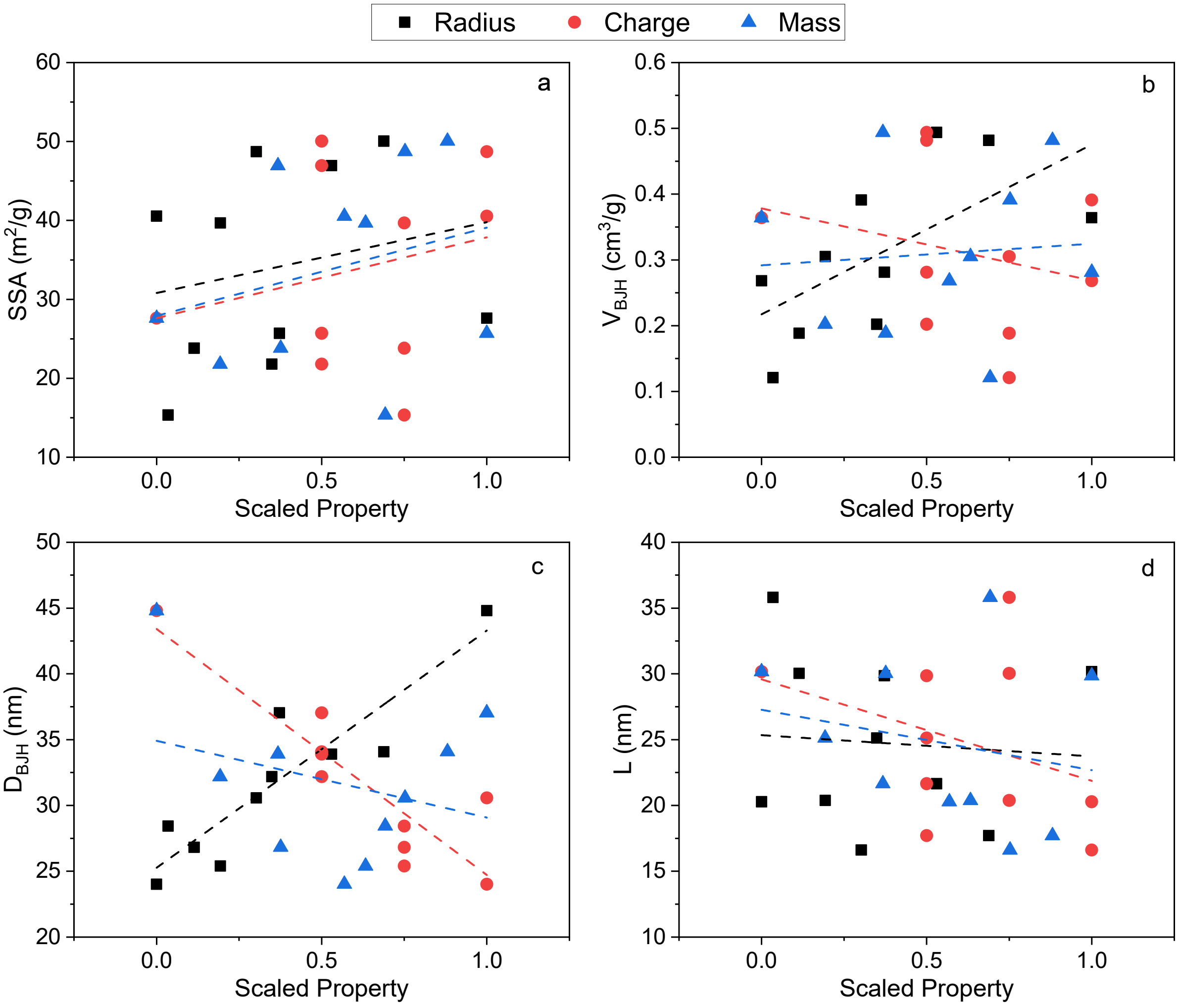

Figure 5.10(a-d): The (a) SSA, (b) V_{BJH}, (c) D_{BJH}, and (d) crystallite size, all after 1000 °C heat treatment, as a function of weighted properties of cation radius, charge, and mass. Statistical analysis was then performed to identify significant effects of weighted properties on aerogel structure. Increased radius was associated with higher pore volume ($p=0.04$) and larger pore size ($p<0.001$). Increased charge was associated with smaller pore size ($p<0.001$).

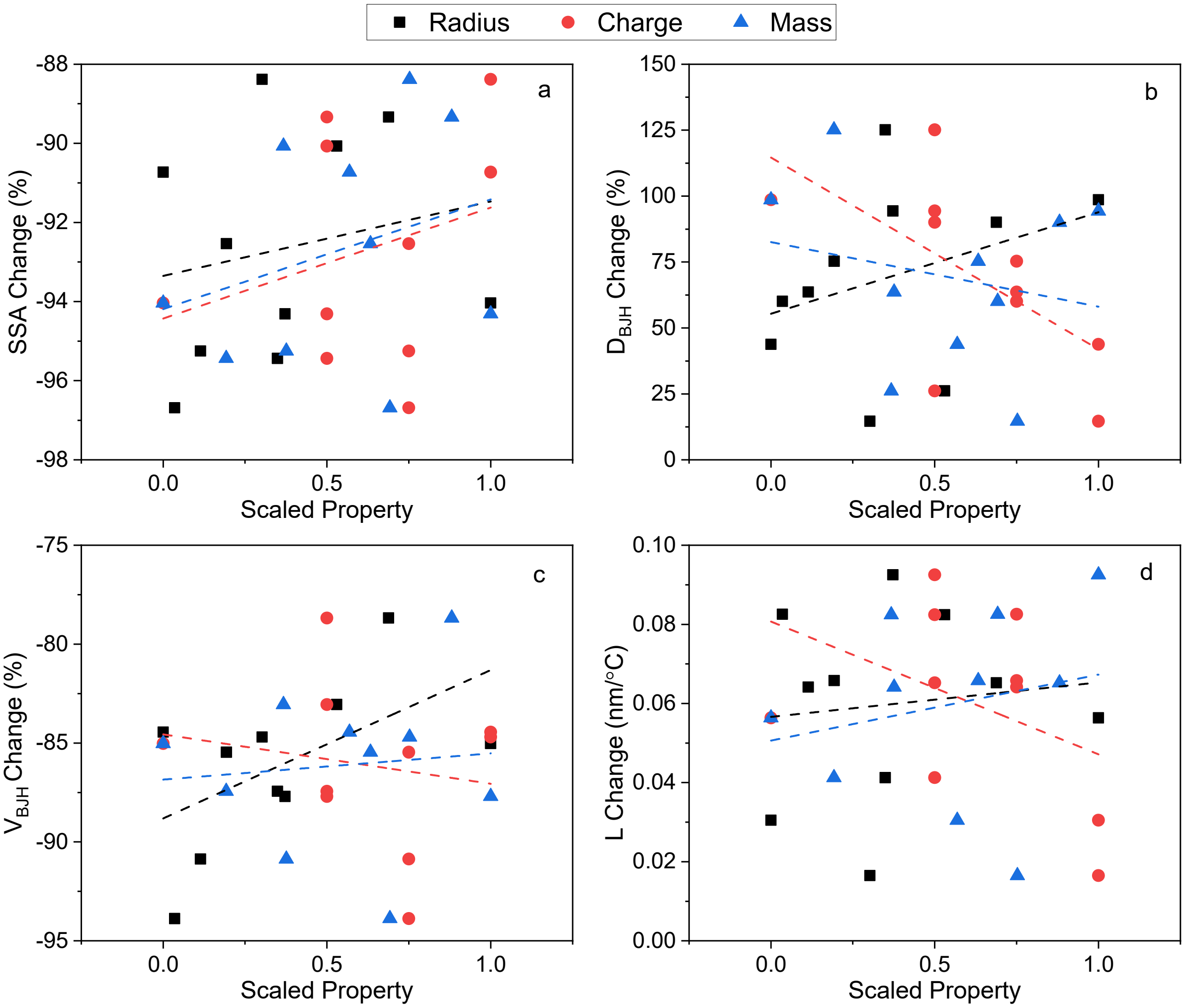

Figure 5.11(a-d): The percent change of (a) SSA, (b) V_{BJH}, (c) D_{BJH}, and (d) crystallite size from AD to 1000 °C as a function of weighted properties of cation radius, charge, and mass. No statistically significant relationships were identified in this analysis.

Table 5.5: Random forest models that achieved a significant improvement over the baseline MSE. Of note are the quality of models for SSA and V_{BJH} at 1200 °C. The most important factors for each model are listed.

Response	% Improvement	1st Factor	2nd Factor	3rd Factor
SSA at 1000°C	36%	Enthalpy	Melting Temp	Theta
SSA at 1200°C	88.5%	Cation Radius	Enthalpy	Cation Mass
V_{BJH} at 1200°C	93.1%	Enthalpy	Cation Radius	Cation Charge
L at 600°C	31.1%	Enthalpy	Cation Radius	Melting Temp
L at 1200°C	26.4%	Melting Temp	Theta	Cation Charge
SSA from AD to 1000°C	61.1%	Enthalpy	Cation Radius	Theta
V_{BJH} from AD to 1000°C	53.5%	Theta	Cation Mass	Cation Radius

Table 5.6: Predicted percent change of SSA from AD to 1000 °C and predicted SSA, V_{BJH}, and crystallite size (L) at 1200 °C. The predictions are based upon random forest models generated from material properties and thermal stability data from the experimental work on Y, Yb, Gd, Ce, and Ca in ZrO_2. The most promising materials are 30 mol% $LaO_{1.5}$ in ZrO_2 and 30 mol% $YO_{1.5}$ in HfO_2.

Material	% Change SSA AD to 1000°C	SSA (m^2/g)	V_{BJH} (cm^3/g)	L (nm)
30Fe in ZrO_2	-91.3%	11	0.07	32.9
30Sr in ZrO_2	-90.2%	15	0.11	31.4
30La in ZrO_2	-89.5%	17	0.15	33.2
30Sc in ZrO_2	-90.9%	15	0.14	44.6
30Hf in ZrO_2	-93.1%	6	0.03	42.1
30Y in HfO_2	-89.8%	16	0.14	34.1

CHAPTER 6: TUNING STRUCTURE USING SYNTHETIC PARAMETERS

6.1 Introduction

First, I want to offer my many thanks to Jordan Meyer for co-authoring the present chapter following his significant contributions to the experimental work contained herein.

Aerogel composition has been shown to impact thermal stability and the temperature at which significant densification occurs. Silica aerogels are constrained to temperatures below 700 °C and alumina aerogels to 1000 °C [45,50,144]. Several lanthanide oxide aerogels lost most of their SSA after heating to 650 °C [48]. Zirconia aerogels experienced a reduction in SSA from 282 m^2/g as dried to 92 m^2/g after two hours at 500 °C [47]. Doping has been shown to be an effective strategy to improve the thermal stability of metal oxide aerogels. Alumina doped with yttria, or silica in conjunction with a crystalline boehmite precursor, has shown sintering resistance up to 1100 °C [50,144]. Studies of yttria- and ytterbia-stabilized zirconia aerogels have been performed up to 15 mol% $MO_{1.5}$ (M = Y, Yb) with higher surface areas and smaller particles sizes observed to 1000 °C for higher dopant concentrations [103]. Further investigation of YSZ up to 50 mol% $YO_{1.5}$ demonstrated increased yttria content enhances thermal stability of the pore structure [126]. In this case, only 30 and 50 mol% $YO_{1.5}$ compositions retained mesoporous structures up to 1200 °C. Despite these findings, the gains in thermal stability from doping remain incremental, even at 50 mol% $YO_{1.5}$. New avenues must be explored in conjunction with doping to significantly improve the stability of the YSZ aerogel pore structure at high temperatures.

Modifying synthetic parameters to tune structural properties could inform new relationships between structure and thermal stability, identifying novel ways to improve aerogel thermal stability. However, the effects of synthetic parameters are usually analyzed in the context of the properties of the as dried (i.e., the structure formed following supercritical drying) material, rather than the microstructural evolution of the aerogels at high temperatures [47,145,146]. A facile synthetic procedure for YSZ and other metal oxide aerogels uses metal salt precursors and epoxides as the gelation agent, often referred to as the Gash process [59,61,62]. Previous work on this synthesis has shown changes to the metal, solvent, epoxide, ratio of water to salt, and ratio of epoxide to salt had influences on the gel formation and the as dried structure [60,62,100,147].

Furthermore, the present work can evaluate the magnitude of the effect of starting structure on thermal stability. This is especially important in studies where changing composition results in changes to both the as dried structure and the thermal stability, as was the case with YSZ [126]. Since yttria concentration was influencing both the as dried structure and thermal stability of the pore structure, it could not be definitively stated if the improvement in thermal stability was the result of changing yttria concentration and associated material properties, or the result of changing as dried structure. Evaluation of the effect of the as dried structure on thermal stability at a fixed composition could serve as a control for studies where composition influences both the as dried structure and thermal stability. The present work allows for evaluation of this effect.

Considering the capability of synthetic parameters to influence the as dried structure, a comprehensive study is warranted to understand the effects of these synthetic parameters on the as dried structure and how these effects may influence thermal stability. In this work, solids loading and water content were selected as the synthetic parameters of interest. YSZ aerogels at a fixed composition of 30 mol% $YO_{1.5}$ were prepared in a 3^2 full factorial design, with three levels of each of the two factors. Thermal stability is evaluated through characterization of the microstructural evolution and crystalline phase development. This work informs the ways in which the aerogel pore structure at high temperatures is sensitive and insensitive to the variation in synthetic parameters. Furthermore, connections were drawn between the key discoveries in this work and the change in thermal stability for doped zirconia aerogels discussed in Chapters 4 and 5. An improved understanding of the relationships between synthetic parameters, as dried structure, and thermal stability will inform future efforts in the design and synthesis of aerogels with thermal stability in extreme environments.

6.2 Materials & methods

6.2.1 Aerogel synthesis

YSZ aerogels of 30 mol% $YO_{1.5}$ were prepared with a sol-gel process from metal salts adapted from previous work [59,61]. Zirconyl chloride octahydrate ($ZrOCl_2{\cdot}8H_2O$, Alfa Aesar 99.9%) and yttrium trichloride hexahydrate ($YCl_3{\cdot}6H_2O$, Acros Organics 99.9%), were first dissolved in 200 proof ethanol (Decon Labs) in separate containers. The solids loading ratios used were 1.263 (low), 1.895 (medium), and 2.526 (high) mmol metal per mL ethanol. These containers were stirred for 30 minutes before adding DI water at six (low), eight (medium), or ten (high) times the stoichiometric amount needed to fully hydrolyze the metal salt. The stochiometric amounts of water were taken as 4 moles of water per mole of Zr^{4+} and 3 moles of water per mol of Y^{3+}. The separate containers were stirred for 60 minutes to ensure hydrolysis before combining the solutions together and stirring for 15 minutes. The combined solution was then placed in an ice bath to slow down gelation, followed by the dropwise addition of a gelation agent, propylene oxide (PO) (CH_3CHCH_2O, Sigma Aldrich), at a ratio of 2.342 mol PO per mole of metal. After stirring for 5 minutes, the solution was transferred to molds made from polyethylene syringes (24 mL) with the tops cut off. For each separate gel, the plunger was placed at 20 mL and the mold filled to the 10 mL mark. Gelation occurred within about 30 minutes. Once gelation occurred, the molds were sealed with parafilm for 24 hours. Gels were then extracted into 200 proof ethanol and aged for 5 to 7 days. To form the aerogel monoliths, aged gels were supercritically dried with carbon dioxide.

Solvent exchange occurred over four washes with liquid carbon dioxide before bringing the carbon dioxide to its supercritical state and evacuating the fluid.

6.2.2 Heat treatments

Aerogels were heated treated in high purity alumina crucibles. Heat treatments were performed in a box furnace under air with a temperature ramp of 10 °C/min to 600, 1000, or 1200 °C, each with a 20-minute hold at the maximum temperature. Aerogels were cooled to room temperature within the furnace.

6.2.3 Characterization

The diameter and length of supercritically dried (as dried) aerogel monoliths were measured to characterize bulk density and shrinkage relative to the mold. Nitrogen physisorption measurements were performed using a Micromeritics 3Flex to measure specific surface area via the method of Brunauer-Emmett-Teller (BET) and pore volume and size via the method of Barret-Joyner-Halenda (BJH). Prior to physisorption analysis, samples were degassed under vacuum at 80 °C with a heating rate of 5 °C/min and a hold of 8 hours. Scanning electron microscopy (SEM) was conducted on a Hitachi S4800 SEM to characterize pore morphology and microstructure. Samples were crushed onto carbon tape and imaged uncoated at 2 kV, 7 μA, and a working distance of 5 mm. Powder x-ray diffraction (XRD) was used to identify the crystalline phase and calculate the crystallite size via the Scherrer equation. To prepare samples for XRD, powders were crushed in a mortar and pestle with a small amount of 200 proof ethanol. The suspension was dropped via pipette onto zero background holders and the ethanol was evaporated, leaving behind a thin film of particles. XRD was performed on a Bruker D8 Advance (Cu Kα, 1.5406 Å) from 10 to 100° 2θ, 0.02 degrees per step, and 0.25 seconds per step. Parallel beam geometry was used with a 0.2 mm divergence slit and a panoramic Soller slit. The YSZ cubic phase (111), (200), (220), and (311) reflections were selected for calculations of crystallite sizes and lattice parameters. Peak positions and widths were obtained assuming a pseudo-Voight profile with an adjusted R-square greater than 0.9. Peak positions and widths were exported and the Scherrer equation was applied to each. The reported crystallite size was obtained by taking the average of all peaks.

6.2.4 Statistical analysis

Statistical tests were conducted in OriginPro 2021b (v. 9.8.5.212). For all statistical tests, a significance level (α) was selected of 0.05. Two-way ANOVAs were first applied with dopant and concentration as the two factors. For significant factor-response pairs, Tukey tests were employed to determine which levels of the factor had a significant effect on the response.

6.3 Results

6.3.1 As dried aerogels

YSZ aerogels with 30 mol% $YO_{1.5}$ were prepared with solids loading at 1.263, 1.895, or 2.526 mmol metal per mL of ethanol, and water content at six, eight, or ten times the stoichiometric amount for each metal precursor. A 3^2 full factorial experimental design was utilized, resulting in a total of nine unique combinations of solids loading and water content. From this point, samples will be referred to as XS-YW, where X represents the solids loading level and Y represents the water content as low (L), medium (M), and high (H). For example, MS-LW was synthesized at 1.895 mmol metal per mL ethanol (medium solids loading) and six times stoichiometric water (low water content).

The mass, length, and diameter of the aerogel monoliths were measured to calculate percent shrinkage and bulk density. Percent shrinkages ranged from -12.1% to -14.9%, and measured bulk densities ranged from 0.175 to 0.266 g/cm^3. Nitrogen physisorption isotherms were used to calculate BET specific surfaces areas (SSA), BJH desorption cumulative pore volumes (V_{BJH}), and

BJH desorption average pore diameter (D_{BJH}). SSAs ranged from 384 to 507 m^2/g, and D_{BJH} ranged from 19 to 27 nm. Table 6.1 summarizes the synthetic parameters used for each sample and their corresponding physical and structural properties. Increased solids loading and decreased water content increased density. Shrinkage varied parabolically with both solids loading and water content, with minimal shrinkage observed for intermediate values of both factors. Figure 6.1(a-b) depicts the sample space for density and shrinkage to illustrate the observed trends.

Statistical analysis from two-way ANOVA also showed significant effects of solids loading and water content on shrinkage ($p=0.028$ and $p=0.020$, respectively) and density ($p=0.003$ and $p=0.007$). Tukey tests were then conducted between synthetic parameter levels. For shrinkage, there was a significant difference between the low and medium solids loading samples and between the medium and high water content samples. For density, the low and medium solids loading samples were significantly different from the high solids loading samples. Low water content samples were significantly different from medium and high water content samples for density.

Two-way ANOVA on the structural data of SSA, V_{BJH}, and D_{BJH} showed solids loading and water content had only a significant effect on D_{BJH} ($p=4.28 \times 10^{-4}$ and $p=0.025$). Larger D_{BJH} was observed at decreased solids loading and increased water content. Further Tukey tests showed significant differences between low, medium, and high solids loading samples and between low and high water content samples for D_{BJH}. The as dried BJH desorption pore size distributions (PSD) in Figure 6.2(a) display clear shifts between the low (blue) and high solids (red) loading samples. The PSDs at high solids loading are narrow and similar in appearance. Decreasing to medium solids loading and greater water content increased the average pore size and the breadth of the PSDs. Low solids loading further broadened the PSD, with the medium and high water content samples containing significant proportions of macropores in the as dried state.

Scanning electron microscopy (SEM) qualitatively evaluated the as dried pore structure as a function of the synthetic parameters in Figure 6.3(a-i). Images taken across the sample space depict the mesoporosity of the as dried samples. Available resolution limits the ability to examine the change in mesopore sizes as synthetic parameters are varied. Although, open pore structures and additional macroporosity are visible at low and medium solids loading with medium and high water content, corroborating the PSDs obtained with nitrogen physisorption.

6.3.2 Pore structure evolution to 1200 ˚C

After heat treatment at 600, 1000, and 1200 °C, the materials were characterized with the same methods as for the as dried samples. SEM analysis of the pore morphology is depicted for 600 °C and 1000 °C heat treatments in Figure 6.4(a-i) and Figure 6.5(a-i), respectively. At 600 °C, the mesoporous structure is maintained for all samples. Like the as dried structure, available resolution limits the ability to evaluate differences in mesopore structure between samples. At 1000 °C, the entire sample space shows signs of densification via particle growth and visible necking. Further growth of the particles and coarsening of the structure occurred upon heat treatment to 1200 °C shown for select samples in Figure 6.6(a-d). From SEM, macroscopic sintering behavior did not depend on the variation in synthetic parameters.

Nitrogen physisorption was used to evaluate the thermal stability of the heat-treated samples at 600 and 1000 °C. Samples were not evaluated at 1200 °C as most mesoporosity was eliminated as made evident by SEM. Figure 6.7(a-c) displays the values of SSA, V_{BJH}, and D_{BJH} as a function of temperature. All samples lost the majority of SSA and V_{BJH} by 1000 °C. At 600 °C, the range of SSA was 144 to 175 m^2/g, and V_{BJH} range was 0.63 to 1.14 cm^3/g. Both the smallest SSA and smallest V_{BJH} were obtained with HS-LW. The largest SSA was obtained with MS-LW, and the largest V_{BJH} with LS-HW. The ranges of SSA and V_{BJH} values narrowed at 1000 °C, with SSA from 43 to 60 m^2/g, and V_{BJH} from 0.34 to 0.54 cm^3/g. At 1000 °C, both the smallest SSA and smallest V_{BJH} were again obtained with HS-LW. Both the largest SSA and the largest V_{BJH} were obtained with LS-HW. All samples showed increases in D_{BJH} from the as dried state to 1000 °C shown in Figure 6.7(c). This data also demonstrates the three distinct groupings of pore size by solids loading, with high solids loading having the smallest pores, followed by medium, and low solids loading with the largest pores. Figure 6.7(b) also shows clear separation between V_{BJH} values based on solids loading at each temperature, with higher solids loading leading to smaller pore volume. Although, two-way ANOVA demonstrated the effect of solids loading on V_{BJH} was significant only at 1000 °C ($p=6.95 \times 10^{-3}$). Further Tukey tests showed significant differences between low and medium, and low and high solids loading samples for V_{BJH}.

Figure 6.2(b-c) depicts the BJH desorption PSDs for samples heat treated at 600 °C and 1000 °C. At 600 °C, the PSDs shifted to smaller average pore sizes, but the relative order was preserved. Medium and low solids loading samples still possessed broader PSDs than the set of high solids loading samples. At 1000 °C, the PSDs narrowed and became similar across the sample space except for the medium and high water content samples at low solids loading. These samples continued to exhibit broader PSDs with pores 10 to 20 nm larger than the rest of the sample space. There was also still clear separation in average pore sizes between the high solids loading samples and the rest of the sample space, with a 4 to 5 nm difference in D_{BJH} which can be seen in Figure 6.7(c).

X-ray diffraction data confirmed the formation of the cubic phase in all materials upon heat treatment in Figure 6.8, consistent with expectations for 30 mol% $YO_{1.5}$ YSZ. Figure 6.9 compares crystallite size among samples from 600 to 1200 ˚C. Crystallite size was calculated via Equation 6.1, with D/C serving to compare crystallite growth between samples rather than providing an absolute measure of crystallite size where λ is the x-ray wavelength, β is the full width at half maximum, and θ is the peak position.

$$D/C = \lambda/\beta cos\theta \qquad \textbf{Equation 6.1}$$

The effect of synthetic parameters on crystallite size was minimal across the temperature range studied. Lattice parameters were also calculated from the peak positions for all samples, again with minimal effect from synthetic parameters. This data is included in Figure 6.10, and all values fall within the expected range for ZrO_2 doped with 30 mol% $YO_{1.5}$.

6.4 Discussion

6.4.1 Synthetic parameters and the as dried structure

In the as dried structures, increased densities due to increased solids loading were expected based on a study of precursor concentration in alumina aerogels [146]. A thicker solid network leads to reduced pore size and pore volume, though pore volume was not found to be significantly influenced here by solids loading. Lower solids loading can exacerbate shrinkage due to greater physical separation of precursor molecules by solvent molecules [148]. Reduced crosslinking then results in a weaker and less dense network, more prone to shrinkage during supercritical drying. The relationship with water content is more nuanced and requires the consideration of the relative values of rates for hydrolysis and condensation [53]. Although the lowest water content studied is six times the minimum to fully hydrolyze the metal salt, incomplete hydrolysis could result if condensation outpaces hydrolysis. The condensation rate should be constant due to a constant molar ratio of metal to propylene oxide, the gelation agent used in the synthesis. The increased density and shrinkage at low water content may be the result of incomplete hydrolysis and poor network formation. As mentioned previously, this type of structure is more prone to shrinking during drying. The opposite case is considered with excess water, which accelerates hydrolysis. If condensation rates are low in comparison, network formation may exhibit clustering, weak branching, and large pores. These networks also tend to exhibit large shrinkage. Figure 6.1(b) depicts a potential optimum around the intermediate solids loading and water content. Shrinkage is minimized in the middle of the sample space, which indicates the aerogel structure formed at this set of parameters is more robust towards shrinkage from drying stresses.

The significant effects of solids loading and water content on pore size confirm these two synthetic parameters can modify the as dried structure. Solids loading has a greater influence on pore size than water content, with significant differences between pore size values at each solids loading, whereas only low and high water contents were significantly different. If the aim is to control the pore size, then solids loading is also more predictable. The increase in breadth of pore size distribution with water content is most likely due to a change in the relative rates of hydrolysis and condensation. Growth of larger particles in the sol prior to gelation cannot pack as efficiently, generating a heterogeneous structure and broader pore size distribution. The significant effect of these synthetic parameters motivated the creation of a model for pore size in Equation 6.2 where SL is the solids loading in mmol metal per mL ethanol and WC is the water content in number of stoichiometric equivalents. The model generated from OriginPro is a good fit for data ($R^2 = 0.98$, Adjusted $R^2 = 0.96$), and it allows fine-tuning of the pore structure for the desired application.

$$D_{BJH}(nm) = 35.6 + 0.395WC - 13.3SL + 0.047SL \cdot WC + 2.2\,SL^2 \quad \textbf{Equation 6.2}$$

To understand the magnitude of influence the synthetic parameters have on the as dried structure, the changes in SSA, V_{BJH}, and D_{BJH} can be compared to work that modifies composition. Our previous work on YSZ aerogels from 0 to 50 mol% $YO_{1.5}$ resulted in materials exhibiting differences between maximum and minimum SSA of 155 m^2/g, V_{BJH} of 0.96 cm^3/g, and D_{BJH} of 7.5 nm [126]. For the dopant study of 15 and 30 mol% of MO_x (M = Y, Yb, Gd, Ca, Ce) described in Chapter 5, the differences were SSA of 112 m^2/g, V_{BJH} of 1.3 cm^3/g, and D_{BJH} of 12.4 nm. In this work, the differences achieved in the as dried structure were SSA of 123 m^2/g, V_{BJH} of 1.03 cm^3/g, and D_{BJH} of 8.2 nm. According to work by Clapsaddle *et al*. for twelve different lanthanide oxide aerogels, the ranges for SSA, V_{BJH}, and D_{BJH} were 130 m^2/g, 1.5 cm^3/g, and 9 nm, respectively [48]. Via the synthetic parameters of solids loading and water content, changes in SSA, V_{BJH}, and D_{BJH} of 123 m^2/g, 1.1 cm^3/g, and 8.1 nm, respectively, were achieved. Clearly, the range of as dried structural properties achieved with synthetic parameters is comparable to that of very unique compositions for a given synthetic method. The relationship between the as dried structure and thermal stability in context of the study on YSZ will be the focus of the next two sections of the discussion.

6.4.2 Thermal stability as a function of synthetic parameters

Thermal stability is defined as maintaining high SSA and V_{BJH} with minimum change in D_{BJH}. Heat treatment led to significant densification and coarsening, especially beyond 1000 °C. Despite the differences measured by nitrogen physisorption in as dried SSA and pore volume across the sample space, available SEM resolution made it difficult to distinguish these variations. At 1000 °C, the differences in pore structure remain far too subtle to determine with SEM, as shown in Figure 6.5(a-i). The XRD data showed that crystallite growth was consistent across the sample space. Rapid cubic crystallite growth was expected between 1000 °C and 1200 °C [108–110]. Variations can be accounted for by scatter and the quality of the peak-fitting procedure. The differences in crystallite growth are not expected to be the result of changes to synthetic parameters. As composition was fixed at 30 mol% $YO_{1.5}$, changes in lattice parameters were not expected due to the synthetic parameters. Only a slight decrease was observed under heat treatment, likely due to crystallization from the amorphous phase. The low crystallinity at 600 °C versus 1000 °C and 1200 °C contributed to the large scatter observed. The peak-fitting procedure was less successful at fitting the peaks at 600 °C, with R-square values closer to 0.9.

Pore size control as a function of solids loading and water content was retained through heat treatment shown in Figure 6.7(c), with distinct clusters for each solids loading at each temperature. More information on the evolution of the pore structures can be gleaned via examination of the pore size distributions as a function of synthetic parameters and temperature. From as dried to 600 °C, the HS-LW sample displays a greater decrease in average pore size relative to the other samples and this may be due to a higher proportion of smaller pores prone to densification, which can be observed in Figure 6.2(a-b). By 1000 °C, elimination of the pore size distribution tails in Figure 6.2(c) showed that most of the porosity loss during heat treatment was due to the smallest pores, with pores below 20 nm in size were likely to have coalesced or closed off during the densification. This may explain the increase in average pore size from as dried to 1000 °C for all materials as shown in Figure 6.7(c). Overall, the evolution of pore size as a function of temperature is similar for all sets of synthetic parameters, only shifted in their relative value by the solids loading, maintaining their relative positions from the as dried state.

Large decreases in surface area and pore volume under heat treatment were observed across the sample space in Figure 6.7(a-b). Solids loading and water content seem to have minimal influence on thermal stability in comparison to the compositional change observed with yttria doping from 0 to 30 mol% $YO_{1.5}$. The data shows the convergence of SSA and V_{BJH} under heat treatment from initially wide ranges in the as dried state, with the data collapsing to a common value from the as dried state to 600 °C, and from 600 °C to 1000 °C. From this data, synthetic parameters have no clear impact on the thermal stability of YSZ aerogels to 1000 °C.

An alternative method that may reveal additional insight is calculation of relative stability via percent change. Calculating the percent change in as dried quantities under heat treatment is performed with Equation 6.3, which provides a number to compare relative stabilities, with lower percent change indicative of improved thermal stability. X represents a structural property, such as SSA, V_{BJH}, or D_{BJH}. It allows for the comparison of the responses of materials that have different starting structures.

$$Percent\ Change\ = \frac{X_{Final} - X_{Initial}}{X_{Initial}} \times 100\% \qquad \textbf{Equation 6.3}$$

Table 6.2 displays the percent change from the as dried state to 1000 °C for both SSA and V_{BJH}. Only one statistically significant relationship between synthetic parameters and percent change of SSA or V_{BJH} were identified. Linear regression revealed a significant effect of water content on the percent change of V_{BJH} from the as dried state to 1000 °C ($p=0.020$). It is important to stress that this effect was very minor, a difference of a few percent at most, but significant, nonetheless.

The possibility remains that the as dried pore structure may have an influence on the thermal stability. This requires a switch of dependent variables from solids loading and water content to the as dried SSA, V_{BJH}, and D_{BJH}. Highly porous structures with high SSA and V_{BJH} have large driving forces for sintering and densification to eliminate surface area and its associated surface energy. The question remains whether the differences in structural properties achieved with the synthetic parameters used in this study are sufficient to reveal significant effects in thermal stability.

6.4.3 Quantifying the impact of starting structure on thermal stability

To evaluate the impact of the as dried structural properties on thermal stability, another statistical analysis was made with linear regression of the percent change of SSA, V_{BJH}, and D_{BJH} as a function of the as dried SSA, V_{BJH}, and D_{BJH}. From this data shown in Table 6.2, linear regression was performed, and the results are included in Table 6.3 and the fits are shown in Figure 6.11(a-c) as a guide to the eye. The significant effects of as dried SSA on the percent change of SSA and V_{BJH} were determined through linear regression ($p=0.049$ and $p=0.012$, respectively). Higher as dried SSAs experienced a greater relative loss in SSA and V_{BJH} from the as dried state to 1000 °C. Higher surface areas generated higher thermodynamic driving forces for densification. Thus, higher surface area samples experienced greater losses in porosity over a given temperature range.

The magnitude of change in thermal stability is also important to consider. The sample with the lowest as dried SSA of 384 m^2/g (LS-LW) maintained a SSA of 54 m^2/g and V_{BJH} of 0.50 cm^3/g at 1000 °C. The sample with the highest as dried SSA of 507 m^2/g (HS-MW) maintained a SSA of 49 m^2/g and V_{BJH} of 0.40 cm^3/g at 1000 °C. The improvement in thermal stability at 1000 °C is an increase in SSA of 5 m^2/g and V_{BJH} of 0.10 cm^3/g for a starting SSA lower by 123 m^2/g. This result can be related to a previous assertion that the present study may serve as a control for studies where composition influences both thermal stability and the as dried structure, such as varying $YO_{1.5}$ concentration in YSZ, where 0 mol% $YO_{1.5}$ (0YSZ) and 50 mol% $YO_{1.5}$ (50YSZ) can be compared. In this previous study, the synthetic parameters utilized were equivalent to LS-LW.

At 1000 °C, 50YSZ maintained 39 m^2/g more SSA and 0.35 cm^3/g more V_{BJH} than 0YSZ. 50YSZ also had an as dried SSA that was 118 m^2/g lower than 0YSZ. The magnitude of difference in as dried SSA is similar for synthetic parameters (123 m^2/g) and YSZ (118 m^2/g). The magnitude in improvement of thermal stability at 1000 °C achieved by changing composition is significantly greater, with a 39 m^2/g difference for YSZ and only 5 m^2/g for synthetic parameters [126]. Therefore, the present work on synthetic parameters and the influence of as dried structure on thermal stability supports the previously stated hypothesis that increased yttria content improves the thermal stability of YSZ aerogels by modifying material properties, namely via a reduction in surface energy and cation diffusivity.

6.5 Summary

A total of nine unique 30 mol% $YO_{1.5}$ YSZ aerogels were prepared in a 3^2 full factorial study of solids loading and water content. The synthetic parameters allowed for adjustment of the as dried composition at fixed composition, resulting in materials with SSAs from 384 to 507 m^2/g and D_{BJH} from 19 to 27 nm. Control over pore size was quantified via model fitting. Moving beyond the as dried structure, the thermal stability of the pore structure to 1000 °C was evaluated in both an absolute and relative sense. There were no clear connections between synthetic parameters and thermal stability. For a more informed and relevant analysis, thermal stability was assessed as a function of the as dried structural properties. Highly porous structures with higher SSA and pore volume have the tendency to collapse and densify to a greater extent as expected from the higher thermodynamic driving force for densification. The magnitude of change in thermal stability resulting from as dried structural properties is small compared to the change achieved with increased yttria content. This result allows the present work to serve as an important control for studies where composition affects both as dried structure and thermal stability.

6.6 Figures and tables

Table 6.1: Physical and textural properties of as dried YSZ aerogels with variations in solids loading and water content. Density increases with solids loading and decreases with water content. Shrinkage maximizes at intermediate levels of solids loading and water content. Significantly, pore size increases with water content and decreases with solids loading.

Sample	SSA (m^2/g)	V_{BJH} (cm^3/g)	D_{BJH} (nm)	S (%)	ρ_b (g/cm^3)
LS-LW	384	2.18	25.0	-13.4	0.205
LS-MW	467	2.77	25.6	-13.2	0.183
LS-HW	445	2.80	27.3	-14.9	0.175
MS-LW	450	2.29	21.7	-12.3	0.224
MS-MW	436	2.31	22.4	-12.1	0.204
MS-HW	469	2.49	22.6	-13.2	0.196
HS-LW	397	1.77	19.1	-13.7	0.266
HS-MW	507	2.39	19.9	-12.5	0.225
HS-HW	431	2.29	21.7	-12.1	0.216

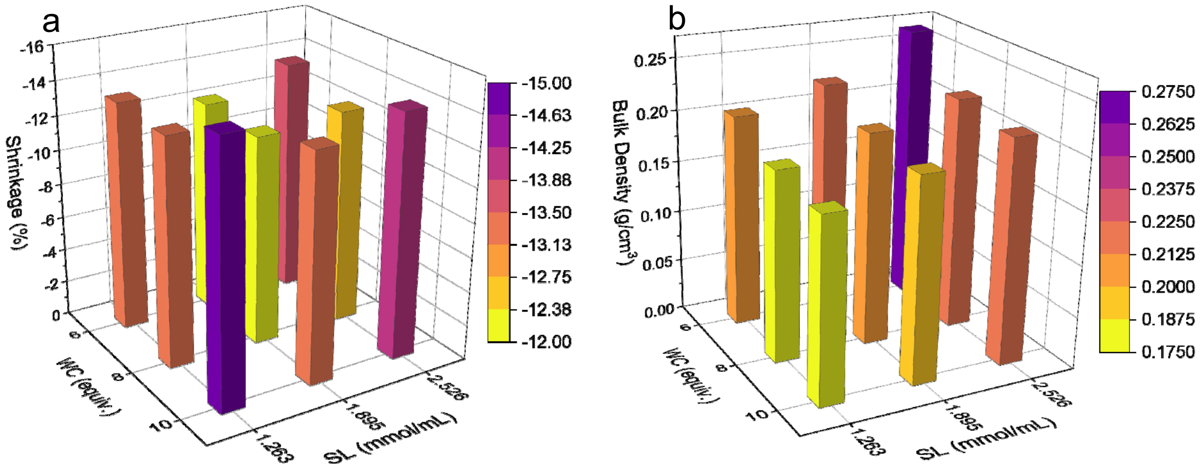

Figure 6.1(a-b): Shrinkage and bulk density of aerogels following supercritical drying as a function of water content and solids loading. Increased solids loading and decreased water content increased density. Shrinkage varied parabolically with both solids loading and water content, with minimal shrinkage observed for intermediate values of both factors.

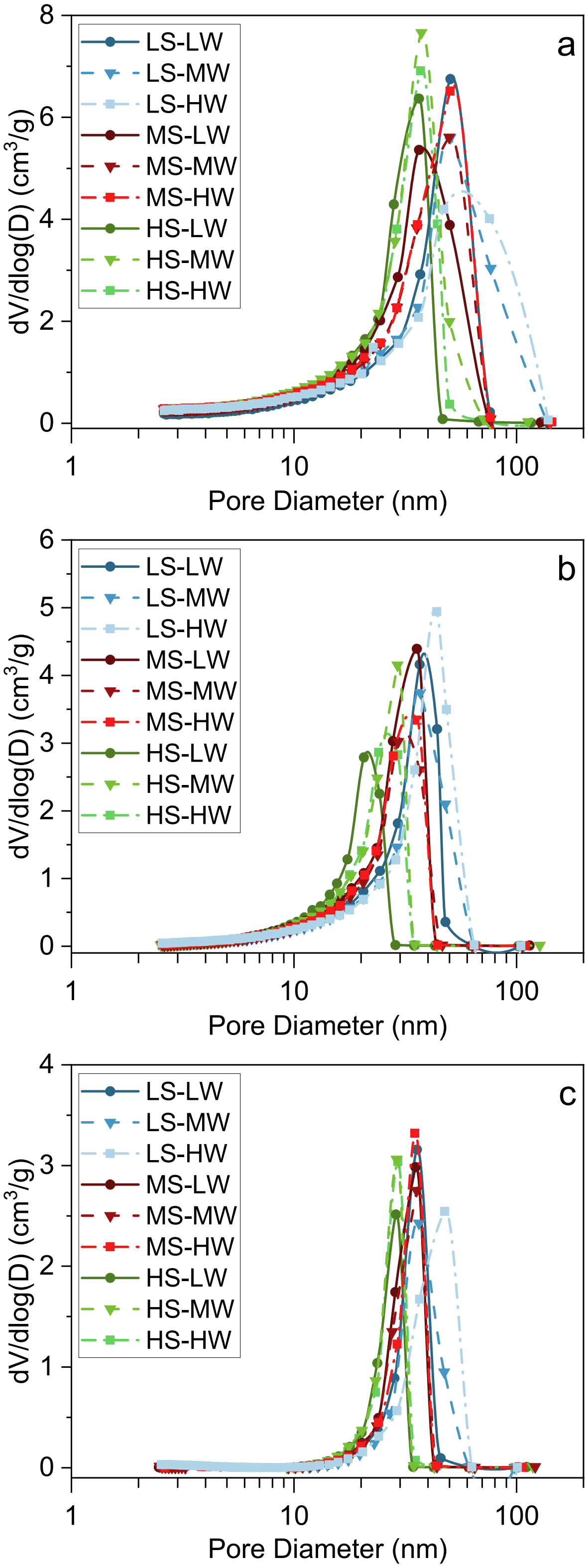

Figure 6.2(a-c): Evolution of BJH pore size distributions in (a) as dried aerogels and under heat treatment at (b) 600°C, and (c) 1000°C. Differences in pore size are distinguishable between each solids loading level, grouped by analogous colors, up to 1000˚C.

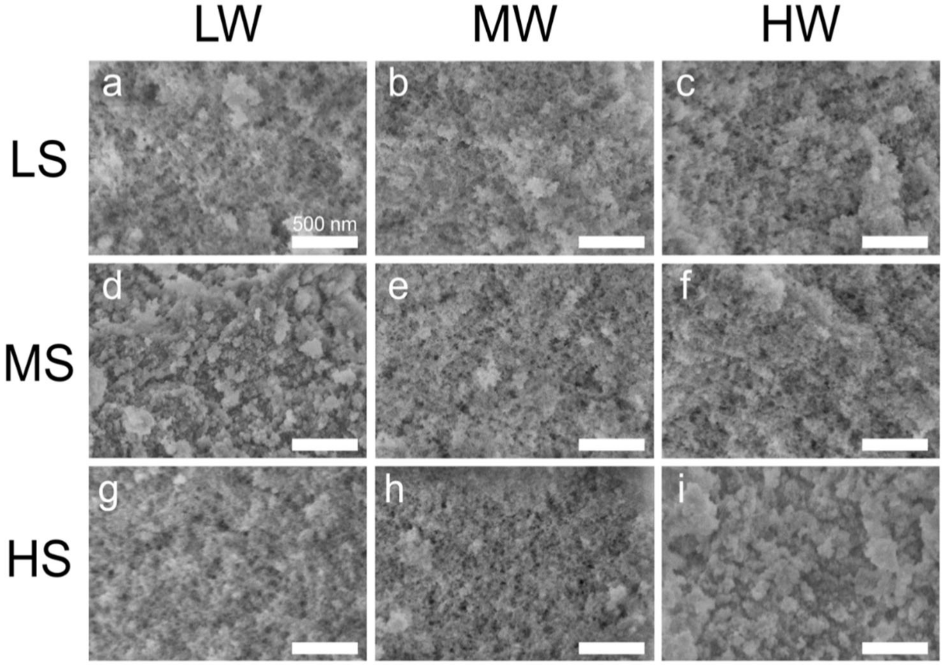

Figure 6.3(a-i): SEM images of as-dried LS-LW (a), LS-MW (b), LS-HW (c), MS-LW (d), MS-MW (e), MS-HW (f), HS-LW (g), HS-MW (h), HS-HW (i). Medium and high water content samples at low and medium solids loading display slightly larger pores and a more heterogeneous structure.

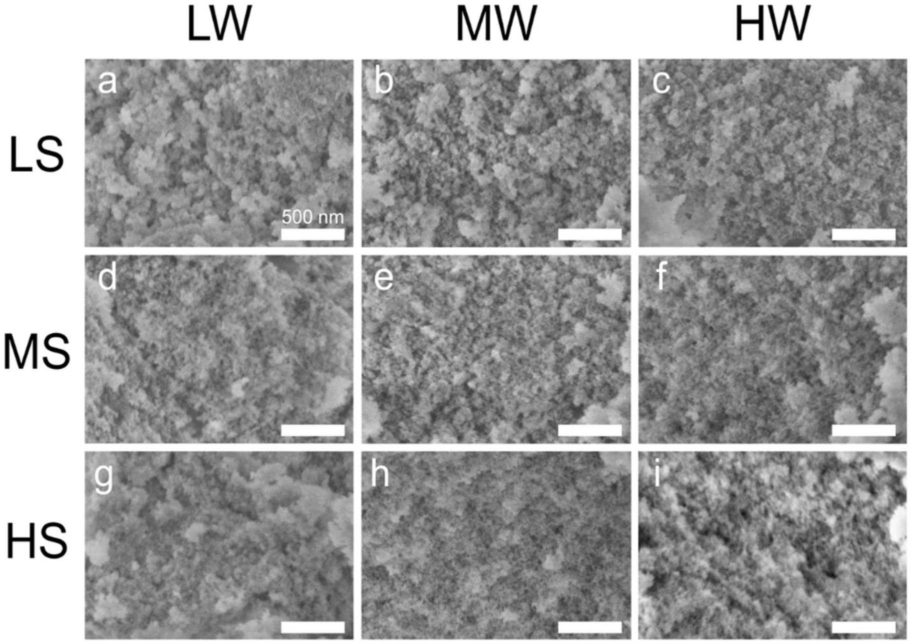

Figure 6.4(a-i): SEM images of 600°C heat-treated LS-LW (a), LS-MW (b), LS-HW (c), MS-LW (d), MS-MW (e), MS-HW (f), HS-LW (g), HS-MW (h), HS-HW (i). The mesoporous structure is maintained in all samples, but differences remain difficult to discern.

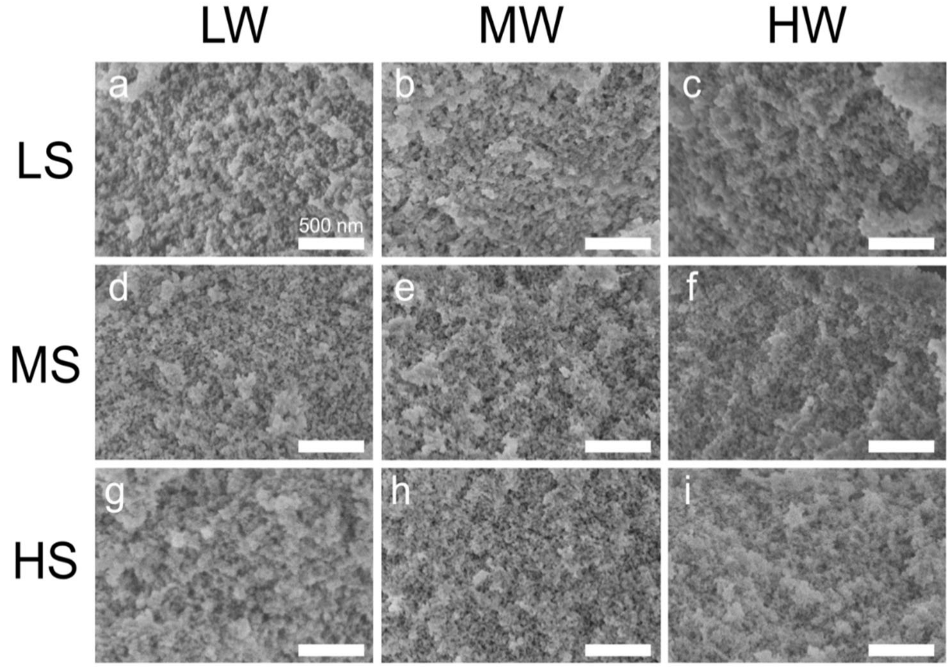

Figure 6.5(a-i): SEM of 1000°C heat-treated LS-LW (a), LS-MW (b), LS-HW (c), MS-LW (d), MS-MW (e), MS-HW (f), HS-LW (g), HS-MW (h), HS-HW (i). At 1000 °C, significant particle growth and sintering are evident, though with no clear dependence on sample identity.

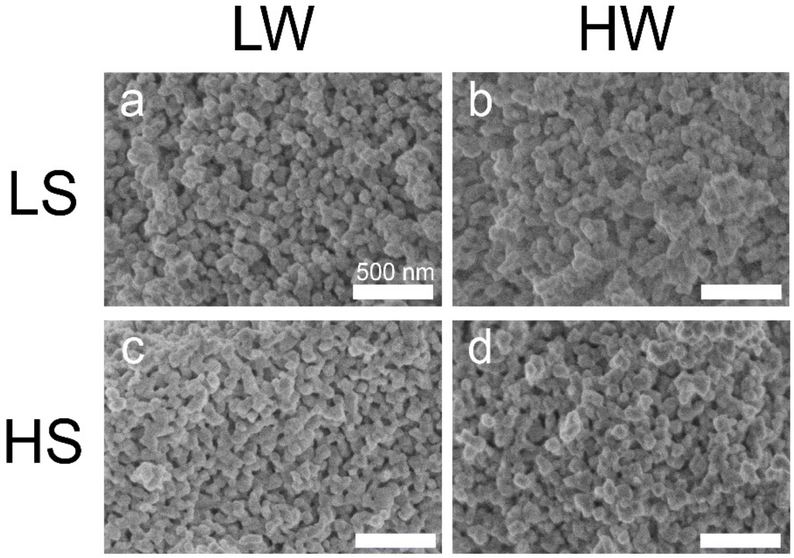

Figure 6.6(a-d): SEM images for (a) LS-LW, (b) LS-HW, (c) HS-LW, and (d) HS-HW) after heat treatment to 1200 °C. The microstructures show a significant reduction in mesoporosity and apparent particle growth and sintering between particles.

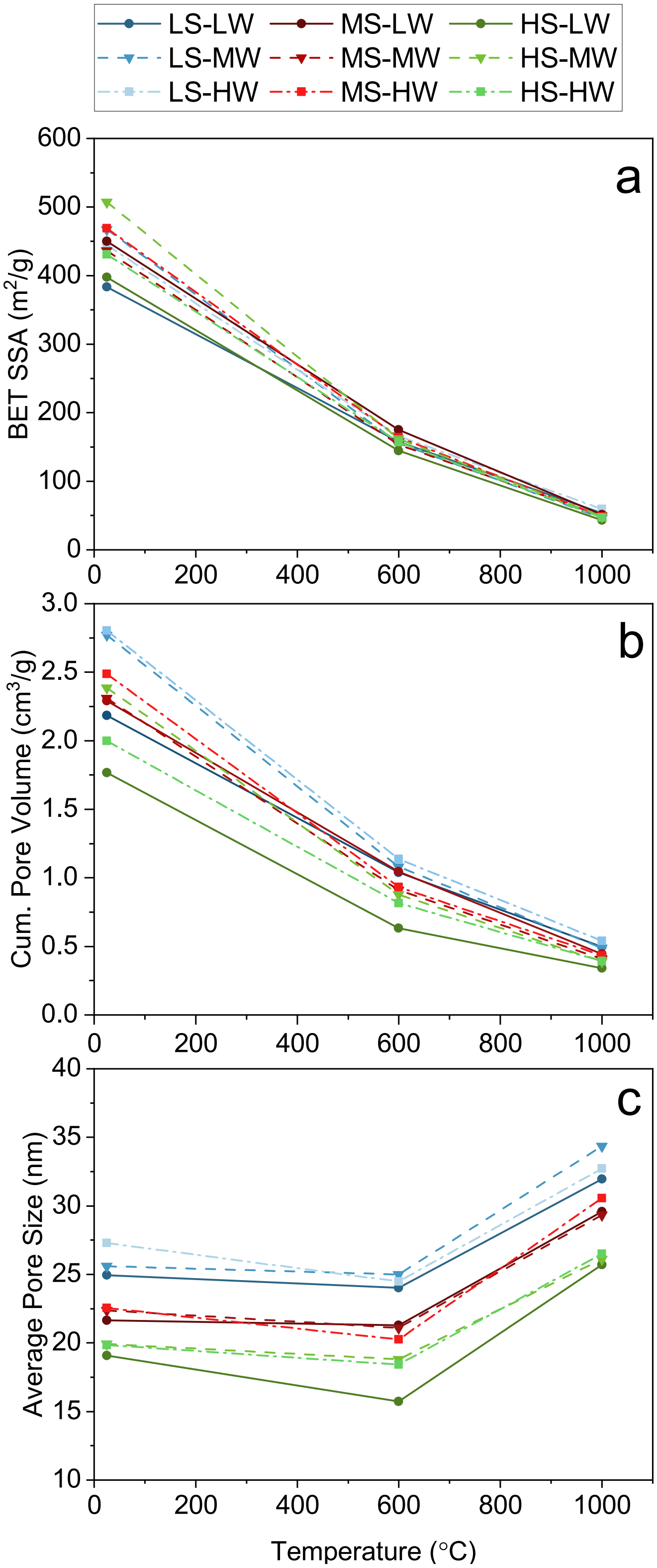

Figure 6.7(a-c): The evolution of SSA, V_{BJH}, and D_{BJH} for YSZ aerogels to 1000°C. Significant reductions in SSA and cumulative pore volume are observed across all samples. Decreases in pore size at 600˚C attributed to elimination of the smallest mesopores.

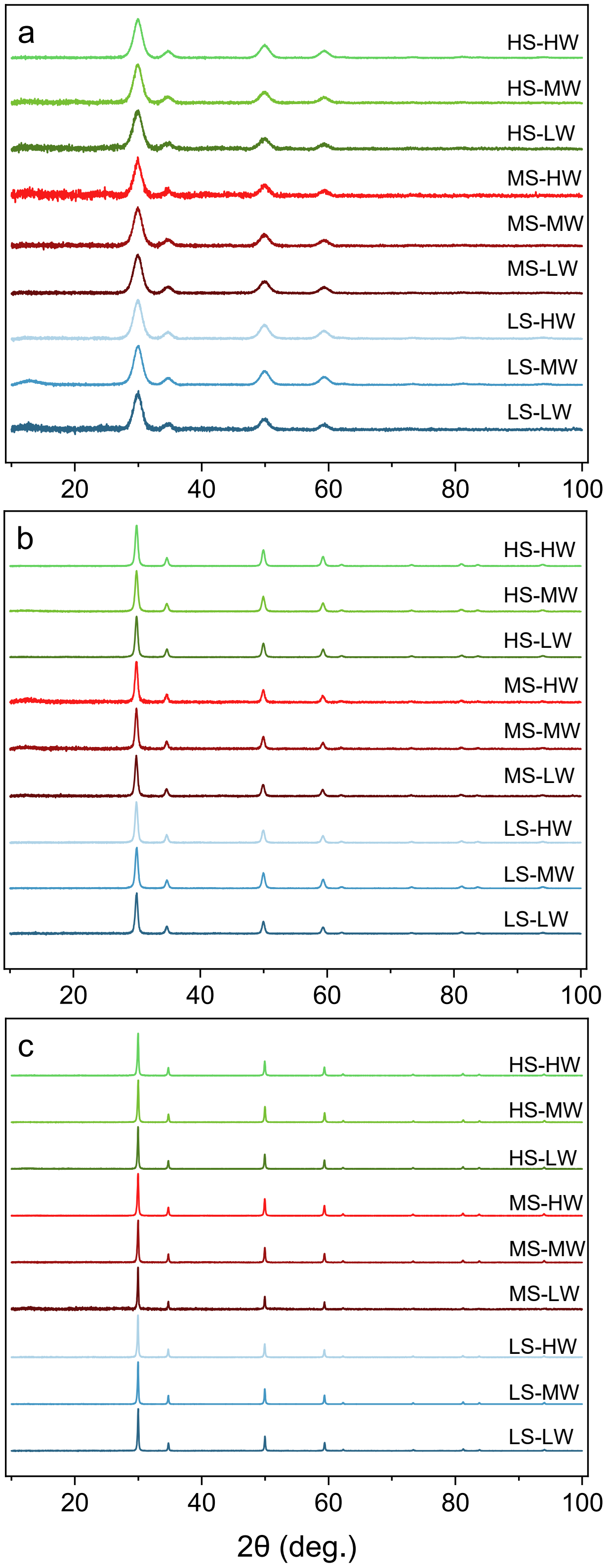

Figure 6.8(a-c): XRD patterns for samples after heat treatment at (a) 600 °C, (b) 1000 °C, and (c) 1200 °C. All samples were identified as cubic with no differences in peak position, shape, or size.

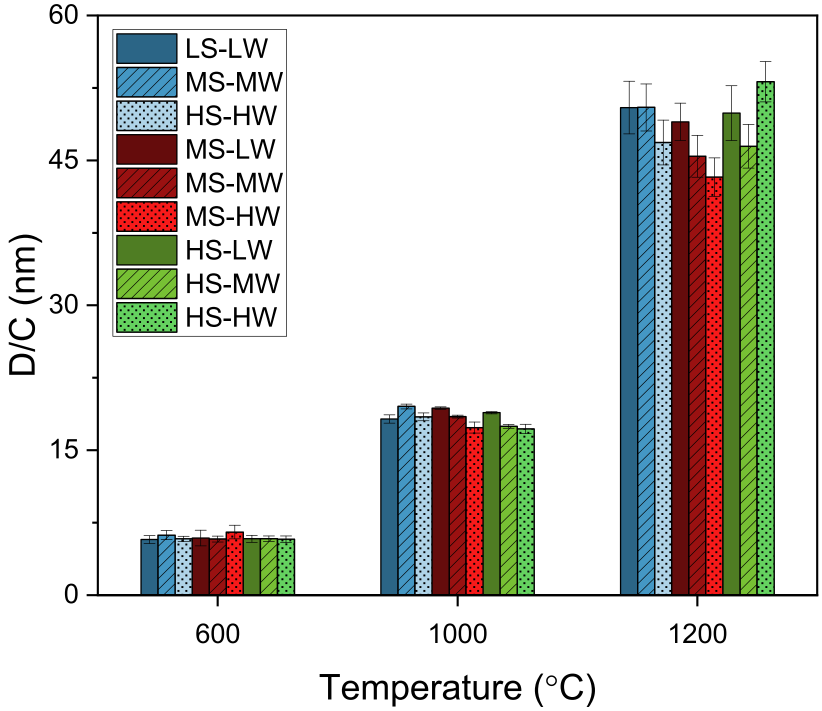

Figure 6.9: Comparison of crystallite sizes (D/C) after heat treatment to 600, 1000, or 1200 °C. In general, solids loading and water content do not influence the growth rate of crystallites.

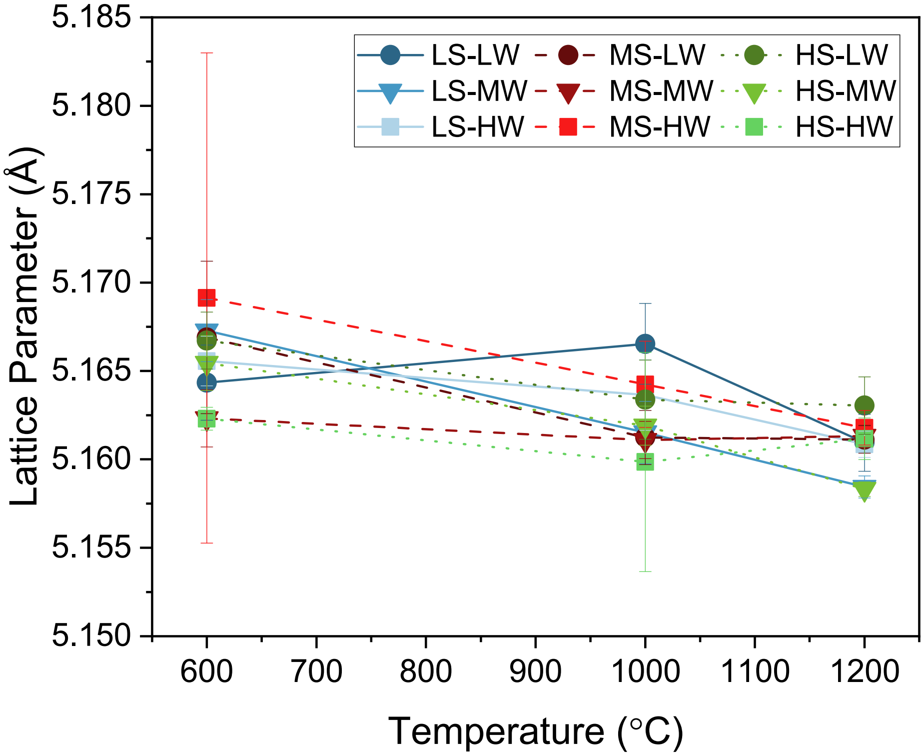

Figure 6.10: Lattice parameters for all samples as a function of temperature. All samples fall within the range expected for 30 mol% $YO_{1.5}$ in ZrO_2 [149].

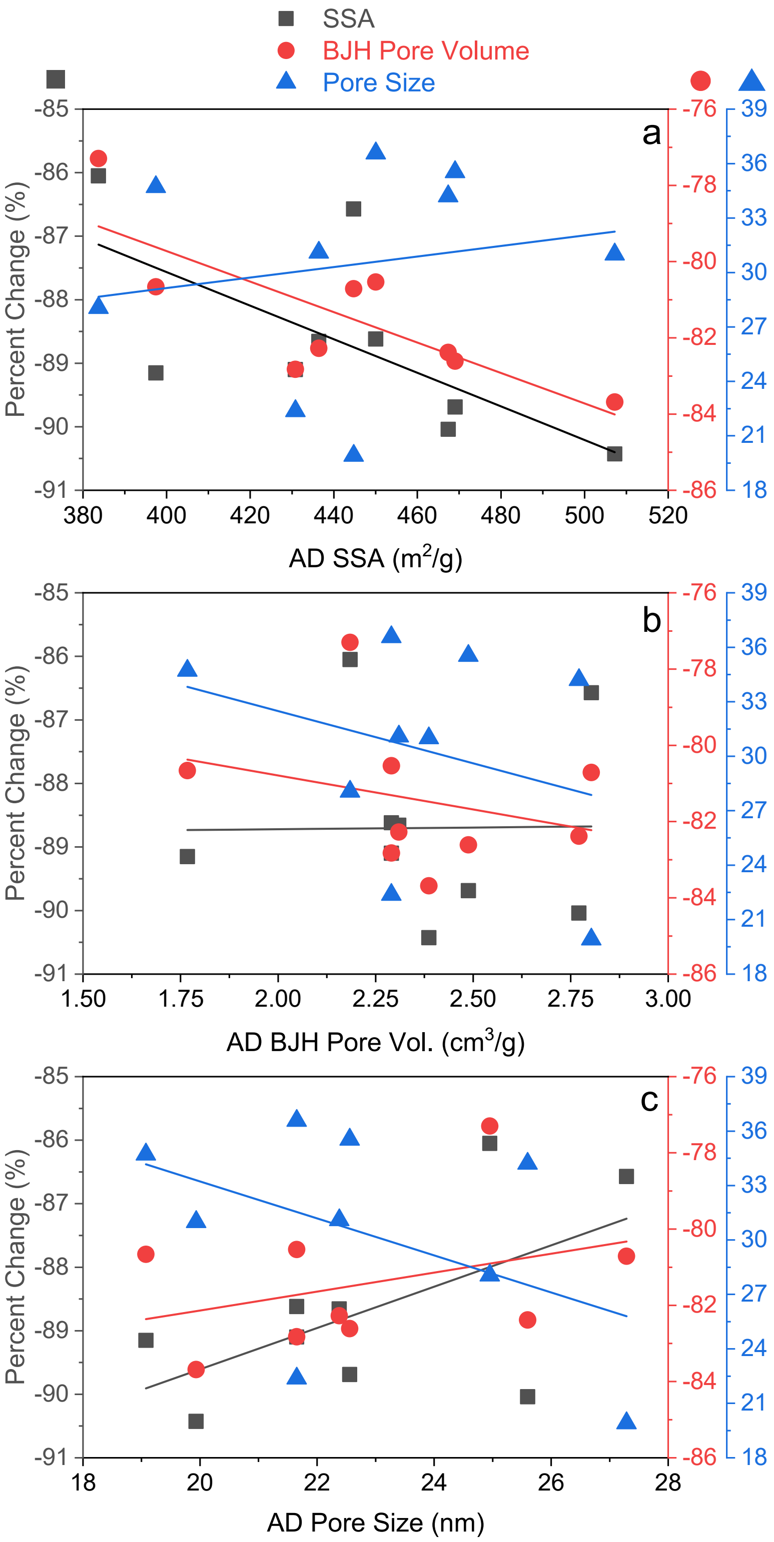

Figure 6.11(a-c): Percent change of SSA, V_{BJH}, and D_{BJH} from AD to 1000 °C as a function of (a) AD SSA, (b) AD V_{BJH}, and (C) AD D_{BJH}. The lines are the best fit and are for visualization only. The only statistically significant effects (α=0.05) are found in (a): increased AD SSA leads to a greater loss in SSA and V_{BJH} to 1000 °C.

Table 6.2: Percent change from as dried to 1000°C of both the BET specific surface area (SSA), and the cumulative pore volume. The medium water content samples display the largest percent decreases in SSA and cumulative pore volume.

Sample	% Change - AD to 1000°C SSA	% Change - AD to 1000°C V_{BJH}
LS-LW	-86.1	-77.3
LS-MW	-90.0	-82.4
LS-HW	-86.6	-80.7
MS-LW	-88.6	-80.5
MS-MW	-88.7	-82.3
MS-HW	-89.7	-82.6
HS-LW	-89.2	-80.7
HS-MW	-90.4	-83.7
HS-HW	-89.1	-82.8

Table 6.3: Linear regression data of percent change of SSA, V_{BJH}, or D_{BJH} from AD to 1000˚C as a function of AD structural properties. The only statistically significant effects (α=0.05) are that of AD SSA on the percent change of SSA and V_{BJH}, with higher AD SSA correlated with a larger reduction in SSA and V_{BJH} to 1000°C.

AD Property (x)	% Change - AD to 1000°C (y)	Slope	Intercept	p-value	R^2
SSA	SSA	-0.03	-77	0.049	0.44
SSA	V_{BJH}	-0.04	-64	0.012	0.62
SSA	D_{BJH}	0.03	18	0.635	0.03
D_{BJH}	SSA	0.33	-96	0.097	0.59
D_{BJH}	V_{BJH}	0.25	-87	0.357	0.35
D_{BJH}	D_{BJH}	-1.02	54	0.209	0.21
V_{BJH}	SSA	0.05	-89	0.977	0.01
V_{BJH}	V_{BJH}	-1.79	-77	0.446	0.09
V_{BJH}	D_{BJH}	-5.75	44	0.427	0.09

CHAPTER 7: POST-SYNTHETIC COATINGS FOR ENHANCED THERMAL STABILITY

7.1 Introduction

In the search for a thermally stable aerogel, adjusting the composition via changing dopants and dopant concentration led to improvements in thermal stability as detailed in Chapters 4 and 5. For example, ZrO_2 doped with 30 mol% $YO_{1.5}$ maintained over four times the SSA at 1000 °C compared to undoped ZrO_2 as described in Chapter 4 [126]. Although when the magnitude is considered, compared to the SSA of 407 m^2/g that 30YSZ started with in the as dried state, only 58 m^2/g remained at 1000 °C, a loss of nearly 86%. This reduction is unacceptable in applications with temperatures approaching and exceeding 1000 °C. Further advancements must be made to enhance the thermal stability at temperatures of 1000 °C and above. The lessons learned and materials identified in the work on doped zirconias are informative in selecting baseline materials to modify further in efforts to improve thermal stability. In this chapter, post-synthetic modification via alkoxide deposition, referred to herein as coating, is pursued as a potential route to stabilizing the aerogel pore structure at high temperatures, leveraging a coating procedure reported by Zu *et al*. [140].

The high surface hydroxyl content of most metal oxide aerogels provides a vast number of sites for functionalization of the surface. Numerous functional groups and other moieties can be attached to modify the properties and surface chemistry of aerogels which often proves useful in the field of catalysis, given the high surface area and high activity of aerogel-based catalysts [150–155]. Of particular relevance to this work are the capping approach [156] and coating approach [157], both of which have demonstrated improved retention of porosity at elevated temperatures.

For the capping approach, Wu *et al.* the surface hydroxyl groups (—OH) of tin(IV) oxide (SnO_2), titania (TiO_2), and zirconia (ZrO_2) aerogels were capped with hexamethyldisilane (HMDS, $[Si(CH_3)_3]_2NH$), forming non-condensable methyl siloxyl groups (—$OSi(CH_3)_3$). The metal oxide aerogels were first prepared from a sol-gel synthesis and supercritical drying. The HMDS capping treatment involved placing the aerogels in a closed container with HMDS, raising the temperature to 150 °C to vaporize the HMDS, and allowing 1 h for the HMDS to react with the hydroxyl groups to form methyl siloxyl groups. At low temperatures, the non-condensable HMDS groups covering the surface preclude the condensation of surface hydroxyls that would otherwise be a driver of pore collapse. As the capped aerogel is exposed to temperatures exceeding 350 °C, the HMDS groups decompose to form silica particles dotting the surface. These then serve as secondary phase pinning particles that prevent grain and crystal growth, further preserving the mesoporous structure of the aerogel. For example, despite starting with the same SSA, the capped SnO_2 aerogel maintained nearly twice the SSA at 300 °C and nearly thrice the SSA at 600 °C compared to its uncapped counterpart. The study did not detail evolution past 600 °C.

The coating approach involves soaking the gel in a solution containing a metal alkoxide. This could be a solution of tetraethyl orthosilicate (TEOS, $Si(OC_2H_5)_4$) in ethanol according to Wang *et al.* [157] or a solution of alkoxide, ethanol, water, and nitric acid according to Zu *et al.* [140], where the alkoxide may be TEOS, zirconium(IV) butoxide ($Zr(OC_4H_9)_4$), titanium(IV) isopropoxide ($Ti[OCH(CH_3)_2]_4$), or aluminum-tri-sec-butoxide ($Al[OCH(CH_3)C_2H_5]_3$). The work by Zu *et al.* further investigated hybrid coating approaches, where the first layer was M_xO_y (ZrO_2, TiO_2, or Al_2O_3), followed by a 50/50 mix of SiO_2 and M_xO_y, and a third layer of SiO_2 only. For alumina (Al_2O_3), the aerogel maintained an SSA of 139 m^2/g to 1300 °C. For zirconia and titania, SSAs at 1000 °C were 186 and 154 m^2/g, respectively. Furthermore, coated aerogels exhibited modified phase behavior and inhibited crystallite growth compared to uncoated materials. As an example, the uncoated zirconia aerogel crystallized into the monoclinic phase at 1000 °C, whereas the coated zirconia aerogel formed either a tetragonal or cubic phase. For alumina at 1300 °C, the uncoated aerogel forms θ-Al_2O_3 and α-Al_2O_3 whereas the coated aerogel only forms θ-Al_2O_3. In all coated aerogels, the SiO_2 phase presumably remains amorphous, though the XRD patterns do not include data below 15° 2θ where the amorphous hump should appear.

The impressive increase in thermal stability and the anomalous crystal structure evolution for coated aerogels warrants further exploration. It is suggested in the work by Zu *et al*. that the formation of silica particles on the aerogel surface prevent particle growth and phase transformation, though the mechanism is not fully understood. Furthermore, the characterization performed in this work does not provide clear evidence of silica particle formation on the aerogel surface, relying only on FTIR data to show presence of Si-O-Si bonding and EDS to indicate the presence of Si. The morphology of the SiO_2 coating is not clear, but the improvement in thermal stability to 1000 °C is remarkable.

In this work, the coating procedure by Zu *et al*. is adapted for use on highly doped (20 and 30 mol% $YO_{1.5}$) YSZ aerogels with coatings of silica, titania, zirconia, alumina, and boehmite (AlOOH). By selecting an aerogel with improved thermal stability as the core, the application of a coating will offer the potential for a highly thermally stable aerogel. Furthermore, there are critical questions that remain to be answered. How does the coating process change the structure and chemistry of the aerogel? How does the structure and chemistry of the aerogel and coating evolve at high temperatures? What are the limits of thermal stability for each coating chemistry and what are the related mechanisms of stabilization and destabilization? An improved understanding of coated aerogel structure and evolution will be an important contribution to the design framework for thermally stable aerogels.

7.2 Materials & methods

7.2.1 Aerogel synthesis

YSZ aerogels of 20 and 30 mol% $YO_{1.5}$ (20YSZ and 30YSZ, respectively) were prepared using a sol-gel process adapted from previous work [59]. Zirconyl chloride octahydrate ($ZrOCl_2{\cdot}8H_2O$, Alfa Aesar, 99.9%) and yttrium trichloride hexahydrate ($YCl_3{\cdot}6H_2O$, Acros Organics, 99.9%), were first dissolved in 200 proof ethanol (Decon Labs) in separate containers. The standard solids loading was 1.263 mmol metal per mL of ethanol. DI water was added in six times the stoichiometric amount for each metal precursor (e.g., 24 moles water per mole of Zr, 18 moles of water per mole of Y). The synthesis procedure was the same as described in Chapters 4, 5, and 6 and corresponds to LS-LW from the synthetic parameter study. The precursors were stirred separately for 60 minutes for hydrolysis. The precursors were combined and stirred for 15 minutes. The solution was placed in an ice bath and propylene oxide (PO) (CH_3CHCH_2O, Sigma Aldrich) was added dropwise at a ratio of 2.342 mole PO per mole of metal. The solution was stirred for 5 minutes and transferred to molds made from polyethylene syringes (24 mL) with the tip cut off. The plunger was placed at 20 mL and the mold was filled to the 10 mL mark. Gelation occurred within 10 to 30 minutes. All gels were held in the mold for 24 hours. Gels to remain uncoated were extracted into room temperature 200 proof ethanol and aged for 6 days. Gels to be coated according to the procedures outlined in Sections 7.2.2 and 7.2.3 were extracted into coating solutions, aged for 3 days, extracted into 200 proof ethanol, and aged for 3 days. All gels were supercritically dried using carbon dioxide [111]. The process used four washes in liquid carbon dioxide to replace ethanol in the pores, before bringing the carbon dioxide to its supercritical state and evacuating the fluid.

7.2.2 Coating with metal alkoxides

Gels were coated with alkoxides of Si, Al, Zr, and Ti. The alkoxides of Si, Al, Zr, and Ti used in this work were tetraethyl orthosilicate (TEOS, $Si(OC_2H_5)_4$, Sigma Aldrich, 98%), aluminum-tri-sec-butoxide ($Al[OCH(CH_3)C_2H_5]_3$, Sigma Aldrich 97%), zirconium(IV) butoxide ($Zr(OC_4H_9)_4$, Sigma Aldrich 80 wt.% in 1-butanol), and titanium(IV) isopropoxide ($Ti[OCH(CH_3)_2]_4$, Sigma Aldrich 97%). Molar ratios are included below in Table 7.1 and are adapted from Zu *et al.* [140]. A coating solution was prepared from the alkoxide, DI water, and nitric acid (HNO_3, Sigma Aldrich 70 wt.%) in 200 proof ethanol (Decon Labs).

For Si, Zr, and Ti, the alkoxide was added to 75% of the total amount of ethanol. The water and nitric acid were added to the remaining 25% ethanol. The two solutions were combined, and the resulting solution was mixed for 30 minutes. Coating solutions using aluminum-tri-sec-butoxide were prepared inside a glovebox filled with argon to prevent hydrolysis, condensation, and oxidation of the alkoxide. The aluminum-tri-sec-butoxide was added to 75% of the ethanol and stirred. At this point, a white precipitate forms throughout the entire solution. A second solution of DI water and nitric acid in the remaining 25% of the ethanol was prepared. The two solutions were mixed, heated to 60 °C, and stirred for 2 h. After this time, the solution was entirely clear.

After the synthesis as described in Section 7.2.1, the gels were held in the mold for 24 h, extracted into the coating solution, and aged for 3 days. Following 3 days in the coating solution, the coated gels were extracted into 200 proof ethanol and aged for 3 days to remove unreacted alkoxide. Gels prepared using this process and Zu *et al.* ratios are referred to as 20YSZ-M_xO_y and 30YSZ-M_xO_y, where $M_xO_y = SiO_2$, Al_2O_3, ZrO_2, and TiO_2.

Gels were also coated using a 25 vol.% alkoxide solution in 200 proof ethanol. Similar to above, the coating solution was mixed for 30 minutes, the gels were added and aged for 3 days in the coating solution, extracted into 200 proof ethanol and aged for 3 days, and supercritically dried. Gels prepared using 25 vol.% alkoxide solutions are referred to as 20YSZ-25%M_xO_y, where $M_xO_y = SiO_2$, ZrO_2, and TiO_2. 25 vol.% solutions of aluminum-tri-sec-butoxide were not successfully prepared due to the high reactivity of this alkoxide, even when heated for 2 h at 60 °C.

7.2.3 Coating with colloidal boehmite

As an alternative to the highly reactive aluminum-tri-sec-butoxide, stable colloids of boehmite (AlOOH) were prepared from P2W or AL25-HP. DISPERAL® P2W (Sasol) is a water-dispersible bohemite powder with average dispersed particle size of 20 nm. Coating solutions were prepared at 15 wt.% of AlOOH in DI water. The powder was slowly added to DI water under stirring. The powder was further dispersed using a Misonix 4000 ultrasonic processor (Qsonica, Newtown, CT, USA) with a 419 tip for 2 min at 60% amplitude [50]. Nyacol® AL25-HP is a colloidal dispersion of boehmite in water at 20% Al_2O_3 and dispersed particle sizes of 70 to 80 nm. This colloid was stirred for 30 minutes and used as-is to coat gels. For both P2W and AL25-HP, the gels were aged in the colloids for 3 days, extracted into 200 proof ethanol, and aged for 3 days, and finally supercritically dried. Gels prepared from P2W are referred to as 20YSZ-AlOOH-P2W and from Al25HP as 20YSZ-AlOOH-25HP.

7.2.4 Heat treatments

Aerogels were heated treated in high purity alumina crucibles. Heat treatments were performed in a box furnace under air with a temperature ramp of 10 °C/min to 600, 1000, or 1200

°C, each with a 20-minute hold at the maximum temperature. Aerogels were cooled to room temperature within the furnace. To study the crystallization of silica, heat treatments at higher temperatures and/or longer hold times were also performed, including 1200 °C at 12 h, 1400 °C for 20 min, 1400 °C for 12 h, 1500 °C for 20 min, and 1500 °C for 12 h.

7.2.5 Characterization

The as-dried aerogels underwent physical measurement to characterize shrinkage and bulk density. The length and diameter of cylindrical aerogel monoliths were measured and used to calculate bulk density and shrinkage relative to the diameter of the mold. Scanning electron microscopy (SEM) was performed on a S4800 SEM to characterize pore morphology. Samples were crushed onto carbon tape and imaged uncoated at 2 kV accelerating voltage, 10 μA current, and 5 mm working distance

Nitrogen adsorption/desorption experiments were conducted on Micromeritics 3Flex (University of Illinois at Urbana-Champaign, School of Chemical Sciences, Microanalysis Laboratory) to measure the specific surface area via the method of Brunauer-Emmett-Teller (BET) and porosity via the method of Barret-Joyner-Halenda (BJH). Prior to adsorption/desorption, samples were degassed under vacuum and heated at 5°C/min to 80°C with an 8-hour hold. Average pore size and cumulative pore volume were calculated using the BJH desorption method.

Powder x-ray diffraction (XRD) was used to identify the crystalline phase and calculate the crystallite size via the whole pattern fitting. To prepare samples for XRD, powders were crushed in a mortar and pestle with a small amount of 200 proof ethanol. The suspension was dropped via pipette onto low background holders. XRD was performed on a Bruker D8 Advance (Cu Kα, 1.5406 Å) from 10 to 100° 2θ, 0.02 degrees per step, and 0.25 seconds per step. Parallel beam geometry was used with a 0.2 mm divergence slit and a panoramic Soller slit. Rietveld refinements were performed in GSAS II (v. 4783) to identify crystalline phase and calculate crystallite size [81]. Peak positions and widths were exported and the Scherrer equation was applied to each. The reported crystallite size was obtained by taking the average of all peaks. For some samples, Rietveld refinement was performed as implemented in JADE (Materials Data, Inc.) with the International Center for Diffraction Data (ICDD) crystallographic database.

Fourier transform infrared spectroscopy (FTIR) was performed on a Nicolet Nexus 670. Aerogel powders were dried at 80 °C under vacuum overnight, ground with KBr, and pressed into transparent pellets. Data were collected in transmission mode from 4000 to 800 cm^{-1}.

Energy dispersive spectroscopy (EDS) was performed on a ThermoFisher Axia ChemiSEM. A small amount of aerogel powder was pressed onto carbon tape applied to an aluminum stub. The conditions used were high vacuum mode, accelerating voltage of 30 kV, spot size of 6, and working distance of 10 mm. An area that showed minimal charging was selected and a point analysis (60 s) was run for three points per area. This process was repeated for three areas per sample. The composition was calculated from an average of all point analyses.

Transmission electron microscopy (TEM) was performed on a JEOL 2011 LaB6 TEM. Samples were prepared via drop casting. The aerogel was ground to a fine powder with a mortar and pestle. The powder was added to 200 proof ethanol at 0.1 mg/mL and sonicated for 15 minutes in a bath sonicator. The suspension was drop cast on 200-mesh carbon-coated Cu grid and dried overnight. For *in situ* heating experiments, high temperature Mo grids were used in the same drop casting procedure. The temperature inside the TEM was ramped from room temperature to 900 °C at approximately 20 °C/min with a 30-minute hold at 900 °C. Bright field images and diffraction patterns were obtained at every 100 °C from 500 to 900 °C, every 10 minutes during the 30-minute hold at 900 °C, and after cooling to room temperature.

7.3 Results for SiO_2 coatings

7.3.1 As dried aerogels

Aerogels of 30 mol% $YO_{1.5}$ in ZrO_2 were prepared either uncoated (30YSZ) or coated (30YSZ-SiO_2). Table 7.2 summarizes the physical and textural properties of the as dried (AD) aerogels following supercritical drying. Coating the aerogel with SiO_2 increased the SSA but reduced the cumulative pore volume. Pore size was slightly reduced in the coated aerogel. Comparing the AD pore size distributions in Figure 7.2(a-b), the size distribution of 30YSZ-SiO_2 in Figure 7.2(b) is slightly broader, with an increased volume of pores from 70 to 150 nm. The SEM images of the AD structure in Figure 7.3(a) for 30YSZ and Figure 7.3(e) for 30YSZ-SiO_2 display no discernable difference. Although the shrinkage was reduced by coating, the bulk density of the aerogel was notably higher in the coated variant. Qualitatively, 30YSZ-SiO_2 was much more robust during handling.

The amount of Si deposited on the aerogel was quantified with EDS. The average atomic ratio of Zr:Y:Si in 30YSZ-SiO_2 was 1.00:0.55:3.01 with no strong dependence of composition on location. EDS mapping did not reveal any inhomogeneities in the composition of the coated aerogel, though the resolution of the Axia ChemiSEM is likely not adequate in this regard.

7.3.2 Structural evolution to 1200 °C

The structural evolution of the aerogels was studied to 1200 °C, with heat treatments of 600, 1000, and 1200 °C each performed with a hold of 20 minutes. Figure 7.1(a-c) shows the change in SSA, V_{BJH}, and D_{BJH} from AD to 1200 °C. Distinctly, 30YSZ-SiO_2 maintains a higher SSA and V_{BJH} to 1000 °C. At 600 °C, the SSA for 30YSZ-SiO_2 is 2.3 times greater than 30YSZ (378 and 166 m^2/g). At 1000 °C, the SSA for 30YSZ-SiO_2 is 3.7 times higher than 30YSZ (175 and 47 m^2/g). At 1200 °C, the SSA is similar with 21 m^2/g for 30YSZ-SiO_2 and 16 m^2/g for 30YSZ, but V_{BJH} is lower for 30YSZ-SiO_2 with just 0.088 cm^3/g compared to 30YSZ's 0.213 cm^3/g. The evolutions of pore size for the two samples are extremely similar to 1000 °C, at which point the behavior deviates, with 30YSZ increasing in average pore size and 30YSZ-SiO_2 decreasing.

The BJH desorption pore size distributions are included in Figure 7.2(a-b). The pore size distribution of 30YSZ-SiO_2 in Figure 7.2(b) is remarkably stable to 1000 °C. The size distribution of 30YSZ in Figure 7.2(a) shows stability between 600 and 1000 °C, but it does change from AD to 600 °C. Comparing the pore size distributions of 30YSZ and 30YSZ-SiO_2 at 600 and 1000 °C, the distributions for 30YSZ-SiO_2 are broader and encompass much larger pore volume being contributed by pores of 50 to 100 nm in size. From 1000 to 1200 °C, there is a significant loss of mesoporosity in both samples, but most dramatically in 30YSZ-SiO_2.

Figure 7.3(a-h) shows the SEM micrographs for 30YSZ and 30YSZ-SiO_2 from AD to 1200 °C. From AD to 1000 °C, there are no discernable differences between the coated and uncoated samples. At the resolution available with SEM, the meso- and macroporous structure of both samples are maintained. For 30YSZ at 1000 °C in Figure 7.3(c), there are the first signs of particle growth. At 1200 °C, both samples show distinct evolution in morphology. 30YSZ in Figure 7.3(d) shows significant particle growth and necking between particles. The sponge-like mesoporous network is no longer visible, replaced by large macropores between partially sintered particles. The change in morphology of 30YSZ-SiO_2 in Figure 7.3(h) is even more dramatic. Not only does it appear like particles have grown but also sintered together to a greater extent than in 30YSZ. The macropore size in 30YSZ-SiO_2 is clearly smaller than that in 30YSZ. This result harkens to the change in average mesopore size from 1000 to 1200 °C shown in Figure 7.1(c), where 30YSZ increases and 30YSZ-SiO_2 decreases in average pore size.

TEM images of 30YSZ-SiO_2 heat treated at 1000 and 1200 °C are shown in Figure 7.4(a-b), respectively. At 1000 °C, the small particle size and mesoporosity is visible. The morphology changes significantly after heat treatment at 1200 °C. The particle size is significantly larger than at 1000 °C. Furthermore, mesoporosity was no longer visible. The sample takes on the appearance of dark, spherical particles embedded in a continuous matrix. This is hypothesized to be YSZ particles contained within an amorphous SiO_2 matrix. EDS was performed by collaborators at NASA Glenn Research Center that supports this hypothesis, but the data are not included in this report. Furthermore, it is possible that at 1000 °C the same morphology of YSZ particles in a SiO_2 matrix is present but is too small to resolve.

All samples were x-ray amorphous as dried. The XRD patterns from 600 to 1200 °C are shown in Figure 7.5. The SiO_2 coating slowed crystallization of the YSZ aerogel. At 600 °C, 30YSZ crystallizes into cubic ZrO_2, whereas 30YSZ-SiO_2 remains amorphous at this temperature. The 30YSZ-SiO_2 aerogel only appeared weakly crystalline at 1000 °C. Lattice parameters and crystallite sizes obtained via refinement in GSASII are included in Table 7.3. Crystallite growth is strongly inhibited in the SiO_2 coated aerogel. At 1000 °C, the crystallite size is 3.2 nm for 30YSZ-SiO_2, compared to 21.7 nm for 30YSZ. The difference in crystallite size grows at 1200 °C, with 55.3 nm for 30YSZ and 13.9 nm for 30YSZ-SiO_2. The lattice parameter of 5.163 Å for 30YSZ aligns with expected values for 30 mol% $YO_{1.5}$ [149,158]. The lattice parameters for coated and uncoated materials are virtually identical at 1000 °C. At 1200 °C, the lattice parameter contracts slightly for 30YSZ-SiO_2.

TEM images for 30YSZ-SiO_2 at 1000 and 1200 °C were used to compare the visual YSZ particle size to the crystallite sizes calculated via Rietveld refinement of XRD data. From the TEM images, the line-intercept method was employed to estimate particle size. A line was drawn in

ImageJ and the number of particles intersecting the line were counted. The length of the line was divided by the number of particles to provide a measure for particle size. At 1000 °C, the estimated particle size was 5.2 (±0.7) nm, compared to 3.2 nm crystallite size calculated via the Scherrer method. At 1200 °C, the estimated particle size was 16.0 (±1.7) nm, compared to 13.9 nm crystallite size. The estimated values from TEM increases the confidence in the use of the Scherrer method to extract crystallite size from XRD data for these heat treated aerogels.

FTIR spectra were also obtained for 30YSZ and 30YSZ-SiO_2 as dried and following heat treatments at 600, 1000, and 1200 °C. The spectra are shown in Figure 7.6. The broad peak from 3750 to 3250 cm^{-1} is associated with hydroxyl (OH) groups. Hydroxyl content decreases in all samples upon heat treatment but most so in 30YSZ. The most notable difference between 30YSZ and 30YSZ-SiO_2 is the Si-O-Si peak at 1150 cm^{-1} [26]. Another clear peak that appears in all samples is a doublet near 1630 cm^{-1} with reduced intensity as a function of heat treatment temperature. At this time, this peak has not been assigned to any bonding motif or functional group. C=C bonds or free alcohols or water often appear in this range, but it is unlikely that such species would persist in the material to temperatures of 1200 °C [157].

7.3.3 Evolution of SiO_2 beyond 1200 °C

As noted previously and shown in Figure 7.5, 30YSZ-SiO_2 crystallizes into the cubic zirconia phase with no sign of SiO_2 crystallization to 1200 °C. The only difference in the patterns of 30YSZ and 30YSZ-SiO_2 was a broad amorphous hump at low angles, indicating the silica exists as a separate amorphous phase after heat treatment. This result was corroborated by the TEM image in Figure 7.4(b), which shows distinct crystalline particles, presumably YSZ, in a continuous non-crystalline matrix, which is presumably SiO_2. Additional chemical analysis is needed to further corroborate this distribution of YSZ and SiO_2. To further study the evolution of the SiO_2 coating, heat treatments were performed at 1200 °C with a 12 h hold, 1400 °C with a 12 h hold, and 1500 °C with either a 20 min or 12 h hold. For the samples heat treated at 1400 and 1500 °C, a clear, glassy material was adhered to the crucible and was separate from the white aerogel powder. XRD was performed on the samples and the patterns are included in Figure 7.7.

In all patterns for the extended heat treatments, the amorphous SiO_2 hump was not present. After 12 h at 1200 °C, the only phase identified was cubic zirconia, albeit with narrower peaks than after 20 min. The formation of a second phase, identified to be cristobalite, occurs in 30YSZ-SiO_2 heat treated at 1400 °C for 12 h and 1500 °C for either 20 min or 12 h. Furthermore, peaks associated with a $Y_2Si_2O_7$ phase also are present in the 30YSZ-SiO_2 heated to 1500 °C for 12 h. Whole pattern fitting estimates 64.2 wt.% crystalline SiO_2 at 1400 °C for 12 h, 56.6 wt.% at 1500 °C for 20 min, and 48.4 wt.% at 1500 °C for 12 h. The reduction in crystallite SiO_2 content with increased temperature and hold time may be the result of SiO_2 flowing and reacting with the crucible, at which point it is no longer a part of the powder sample that is analyzed in XRD.

7.4 Discussion for SiO_2 coatings

7.4.1 Change to as dried structure

The effects of coating on the structure can be inferred from the physical measurements of the aerogel, including shrinkage and density, and the measurements of the mesoporous structure with nitrogen physisorption. The change in composition following coating is measured using EDS and calculated from the phase fractions of samples following heat treatments.

There was a significant increase in density of the aerogel after coating, from 0.186 to 0.275 g/cm^3, despite a reduction in shrinkage from -12.5 to -10.7%. Considering the density and shrinkage, the changes reflect the success of the coating procedure. As the TEOS infiltrates the pore structure and reacts with surface hydroxyl groups of the YSZ aerogel, -O-Si-O- form, adding material to the structure and increasing the density. A reduction in shrinkage, all other factors equal, would typically reduce the density of an aerogel since a given mass of solution-phase precursors occupies a greater volume in the gel form. Here, this is not the case and 30YSZ-SiO_2 is of higher density despite having lower shrinkage. The reduction in shrinkage is likely a result of increased robustness of the gel towards the pressures that drive shrinkage during gelation and drying. The amount of TEOS that reacts and deposits on the gel is enough to overcome the reduction in shrinkage and result in an increase the overall density of the aerogel. Though an increase in density is not necessarily ideal for the purposes of lightweight insulation, the potential for an improvement in thermal stability at temperatures of interest may well be worth the cost.

Upon coating with SiO_2, the SSA of the aerogel increased from 473 to 599 m^2/g, but with a slight reduction in mesopore volume (2.914 to 2.842 cm^3/g) and mesopore size (26.9 to 25.1 nm). When interpreting the results of nitrogen physisorption, it is essential to keep in mind the limitations of the technique. Adsorption can occur on any free surface that is accessible to nitrogen molecules. Adsorption of nitrogen is used to calculate the SSA, so this includes both mesoporosity (2 to 100 nm) and macroporosity (> 100 nm). The BJH method for calculating cumulative pore volume, average pore size, and pore size distribution relies on the phenomenon of capillary condensation, which occurs over the mesopore range (2 to 100 nm) and up to 150 nm. Therefore, the cumulative pore volume and average pore size only represent mesopores and *not* macropores.

With this limitation of nitrogen physisorption in mind, the slight reduction in mesopore volume and size likely reflects the filling of some mesoporosity with reacted TEOS. While TEOS is reacting with free surface in the mesopore structure of the aerogel, it is also improving the resistance of the mesopore structure to shrinkage as mentioned previously, so there is a balance between reduced mesopore shrinkage during drying and reduced mesopore volume from coating for the coated aerogel. Since the change in mesopore volume and size is small in relation to the change in SSA, the significant increase of SSA is likely the result of increased macroporosity, which itself stems from reduced macroscopic shrinkage of the aerogel. Though the pore size distributions in Figure 7.2(a-b) cannot directly measure macroporosity larger than 150 nm, a possible change in macroporosity can still be gleaned when comparing the AD distributions in Figure 7.2(a) for 30YSZ and 7.2(b) for 30YSZ-SiO_2. The distribution for 30YSZ-SiO_2 indicates greater pore volume contributions from pores of 100 to 150 nm compared to 30YSZ. A shift towards larger mesopore sizes is also reported for coated aerogels by Zu *et al*. [140]. This shift, along with the reduction in macroscopic shrinkage and small change in mesopore volume, suggests that increased macroporosity is the source of increased SSA in 30YSZ-SiO_2. There also remains the possibility that the YSZ gel structure undergoes significant reconstruction while soaking in the alkoxide solution. As described in the following section, the change in composition is dramatic, and does not preclude possible dissolution and redeposition of the gel in ways not yet understood. Ostwald ripening occurs through gel aging and the effect of soaking the gel in an acidic alkoxide solution is not known.

7.4.2 Composition of coated aerogel

The atomic ratio of Zr:Y:Si obtained with EDS, averaged over multiple measurements, was 1.00:0.55:3.01. Initially, this result was treated with skepticism as it suggests the coated material exists in three times the atomic amount of the aerogel itself. To evaluate this result, calculations of possible compositions were performed based upon the coating solutions or the change in density. Each aerogel monolith was soaked in 60 mL of the Si coating solution described in Section 7.2 and detailed in Table 7.1. The amount of Zr and Y in the aerogel was calculated from the amount of Zr and Y salts used in the synthesis of the gel, assuming 100% conversion of salt into gel. The amount of Si deposited was then estimated under three different assumed values for percent of Si reacted from TEOS in 60 mL of coating solution. For 25, 50, and 100% of Si reacted, the atomic ratios of Zr:Y:Si are 1:0.42:4.89, 1:0.45:9.80, and 1:0.50:21.0. Even at just 25% of Si reacted, there would be enough Si present to exceed the ratio measured with EDS. The percent of Si reacted that gives a Zr:Si ratio of 1.00:3.01 is just 15.9%. From the amount of Si present in the coating solution, the atomic ratio obtained with EDS appeared reasonable.

The change in density can also be used to estimate the amount of SiO_2 present. Given the change in density from 0.193 to 0.275 g/cm^3 after coating and neglecting the change in shrinkage, the amount of SiO_2 deposited can be approximated as 29.8 wt.% SiO_2 to 70.2 wt.% 30YSZ. This is equivalent to an atomic ratio of 1.00:0.42:1.20 for Zr:Y:Si. The amount of Si deposited estimated by change in density is significantly lower than that measured with EDS or estimated by amount of TEOS reacted. This discrepancy may be caused in part by neglecting the change in shrinkage but may also suggest soaking the aerogel in the alkoxide solution may be doing more than simply coating on -O-Si-O- layer-by-layer. To provide another estimate of composition in an attempt to reconcile these results, XRD may prove useful.

After heat treatment for 12 h at 1400 °C, whole pattern fitting of XRD data suggested 64.2 wt.% crystalline SiO_2, with this number reduced to 56.6 and 48.4 wt.% after heating to 1500 °C for 20 min and 12 h, respectively. As noted previously, this reduction in SiO_2 content is thought to be the result of flow and subsequent reaction of SiO_2 with the alumina crucible. Taking the composition estimated at 1400 °C and 12 h, both the YSZ and SiO_2 can be expected to be fully crystalline given the lack of amorphous hump in Figure 7.7. 64.2 wt.% SiO_2 is equivalent to an atomic ratio of Zr:Si of 1.00:4.81, which is well within the bounds of the measurement with EDS and other estimations. Like these other methods, XRD points to the fact that Si exists in very high abundance in 30YSZ-SiO_2.

Overall, the significant amount of SiO_2 deposited suggests the soaking process is doing much more to the aerogel structure than simply coating several layers of SiO_2 to the YSZ aerogel structure. Subsequent evolution at elevated temperatures, including the formation of a seemingly pure 30 mol% $YO_{1.5}$ cubic ZrO_2 phase (Figure 7.5) and the appearance of YSZ particles embedded in an amorphous SiO_2 matrix (Figure 7.4(b)), suggest the SiO_2 phase is distinct from the YSZ phase, though the extent to which the YSZ aerogel structure is modified by the coating solution is unknown and warrants further study.

7.4.3 Improvement in thermal stability via SiO_2 coatings to 1000 °C

30YSZ-SiO_2 displayed significantly higher thermal stability at 600 and 1000 °C when compared to 30YSZ. At 600 °C, 30YSZ-SiO_2 maintained 2.3 times the SSA and 1.7 times the V_{BJH} relative to 30YSZ. This improvement in performance with coating grew at 1000 °C, at which point 30YSZ-SiO_2 maintained 3.7 times the SSA and 2.4 times the V_{BJH} of 30YSZ. The gap in performance is visually indicated in Figure 7.1(a-b). Crystallite growth was also strongly suppressed with the crystallite size at 1000 °C being nearly 7 times larger in 30YSZ than 30YSZ-SiO_2. Crystallite size cannot be compared at 600 °C because 30YSZ-SiO_2 remained x-ray amorphous.

As described in Chapter 4, increasing the concentration of $YO_{1.5}$ in ZrO_2 aerogel increased the SSA at 1000 °C by a factor of 4.8. This improvement was built upon by coating 30YSZ with SiO_2, with the SSA at 1000 °C increased by a further factor of 3.7 relative to 30YSZ. The improvement achieved in 30YSZ with SiO_2 coating can be compared to previous capped and coated aerogels. In the work by Wu *et al.*, SnO_2 aerogels capped with HMDS maintained 3 times the SSA at 600 °C. Without the HMDS treatment, the SnO_2 aerogel's SSA was more than halved by 400 °C, whereas the capped aerogel increased in SSA to this temperature. The ZrO_2 aerogels with ZrO_2/ZrO_2-SiO_2/SiO_2 coatings in work by Zu *et al*. had 2.4 times the SSA at 600 °C and 4 times the SSA at 1000 °C compared to their uncoated counterparts. These values are closely in agreement with the improvements achieved in this work.

This improvement in thermal stability is meaningful in the context of applications that require highly insulative mesoporous materials exposed to temperatures up to 1000 °C. To expand the impact of this improvement, a deeper understanding of the source of thermal stability for coated aerogels will prove useful in developing refined coating approaches that enhance thermal stability to an even greater degree than achieved here. To this end, several sources and mechanisms of improved thermal stability must be evaluated.

The work by Zu and Wu both tout the effect of surface SiO_2 particles to pin grain and particle boundaries, inhibiting both densification and crystallite and/or grain growth [140,156]. Formation of secondary phases and/or particles at interfaces has repeatedly been demonstrated to induce solute drag and inhibit particle, grain, and crystallite growth [37–40,108–110,119,120,159,160]. The inhibition of growth is generally achieved with small amounts of the secondary phase, often less than 10 mol%, and is the result of space charge effect, reduction in surface energy with an increase in the surface excess of the dopant, or a shift in the relative values of surface and grain boundary energies [37,40]. On the other hand, SiO_2 has also been employed as a sintering aid for ceramics, especially in cases where the concentration of SiO_2 is high, allowing the SiO_2 to form a continuous film and enable liquid phase sintering [161,162]. The pitfall of viscous sintering, which is particularly relevant given the high concentration of Si measured in the coated YSZ aerogels, will be further discussed in Section 7.4.4. Given the 3:1 ratio of Si to Zr measured in the coated aerogel, referring to the SiO_2 phase as a secondary phase or pinning phase may not be accurate. Rather, an increase in particle size and a reduction in surface energy upon SiO_2 coating are important considerations in context of improved thermal stability to 1000 °C.

The coating work by Zu *et al.* also suggests that increased size of both the particles that make up the aerogel backbone and the struts that connect them improve the robustness of the structure towards densification. This hypothesis is also supported by the fact that maximum capillary pressure is inversely related to particle size [55] and reduced capillary pressure is reduced driving force for densification and compaction upon heating. Molecular dynamics simulations of silica aerogel sintering also supports that increased primary particle size reduces the rate of densification [22]. While this mechanism remains possible, the work by Zu *et al.* does not provide data on the distribution or morphology of SiO_2 in relation to the MO_x aerogel apart from the fact that SiO_2 does not crystalize to 1000 °C for TiO_2 and ZrO_2 aerogels or 1300 °C for Al_2O_3 aerogels.

As described in Chapters 2 and 4, reduced surface energy is hypothesized to be an important factor in improving the thermal stability of highly porous, high SSA materials such as aerogels [104,126]. Considering the large amount of Si detected in the coated material, it can be assumed that 30YSZ-SiO_2 has a surface composed primary of SiO_2. The surface energy of amorphous silica is 0.259 J/m^2 if dry and 0.129 J/m^2 if fully hydrated [163]. This can be compared to that of 30 mol% $YO_{1.5}$ ZrO_2 (30YSZ), which is 0.83 J/m^2 if dry as averaged for a polycrystalline sample, with little dependence on whether the YSZ is crystalline or amorphous [104]. The aerogels are hydrophilic and likely have some degree of hydration on their surface, though the water adsorbed to the surface should be negligible at temperatures where sintering and densification occur. Therefore, it is sensible to compare the dry surface energies. Comparing these two values, the surface energy of amorphous SiO_2 (0.259 J/m^2) is significantly lower than that of 30YSZ (0.83

J/m^2). This will reduce the driving force for sintering, densification, and elimination of the surface area and associated surface energy.

As an example, one can consider the change in energy associated with surface area for a surface composed of SiO_2 compared to that of a surface composed of 30YSZ. Assuming a specific surface area of 400 m^2/g, the energy arising from the surface for SiO_2 is 104 J/g and for 30YSZ is 332 J/g – over a factor of three reduction in energy for SiO_2. In the context of a key thermodynamic driving force for sintering and densification, this reduction may prove significant and aligns with the expectations set forth in Chapter 4 for the surface energy of YSZ with changing yttria content. Frankly, there are several confounding factors in the case of SiO_2 coatings and correlation of reduced surface energy with improved thermal stability does not imply causation.

There is no evidence generated by this work to explicitly refute these hypotheses on the effect of pinning and increased particle size. Rather, the hypothesis on reduced surface energy is presented as another possible mechanism by which the process of coating or capping an aerogel improves stability of the pore structure at high temperatures. Further work characterizing the starting structure of the material, namely on how the coating solution is changing the YSZ aerogel's structure and chemistry, and the evolution of the SiO_2 in relation to the YSZ aerogel from the range of room temperature to 1000 °C is required to better understand the source of thermal stability in coated metal oxide aerogels.

7.4.4 Enhanced densification beyond 1000 °C with SiO_2 coatings

Despite a significant improvement in thermal stability of 30YSZ with an SiO_2 coating to 1000 °C, the SiO_2 coating enhances densification beyond this temperature. The slope of SSA and V_{BJH} in Figure 7.1(a-b) for 30YSZ-SiO_2 indicate a sharp decrease in the thermal stability of the coated material. The SSA for 30YSZ and 30YSZ-SiO_2 are virtually identical and the mesopore volume of 30YSZ-SiO_2 is 2.3 times *smaller* than 30YSZ, a stark change from 1000 °C, where 30YSZ-SiO_2 maintains 2.4 times the mesopore volume of 30YSZ. Despite the massive loss of SSA and V_{BJH}, the crystallite size of 30YSZ-SiO_2 remains very small, 13.9 nm, compared to 55.3 nm for 30YSZ.

Comparing the thermal stability of 30YSZ-SiO_2 to previously studied capped and coated aerogels to temperatures of 1200 °C is not possible, as Wu only measured stability to 600 °C and Zu only to 1000 °C for ZrO_2 and TiO_2 aerogels. It is important to note the work by Zu did demonstrate coated Al_2O_3 aerogels maintained good thermal stability to 1300 °C with an SSA of 139 m^2/g. The fact that ZrO_2 and TiO_2 aerogels were reported to only 1000 °C suggests these materials also densified beyond this temperature.

The SEM and TEM images of 30YSZ-SiO_2 at 1200 °C in Figures 7.3(h) and 7.4(b), respectively, show a dramatic change in morphology at multiple length scales. From SEM, the foam-like mesopore structure has disappeared. From TEM, the structure goes from a porous, web-like structure to one that appears fully dense with clearly defined spherical particles contained within a nebulous matrix. The dense appearance of the aerogel in both SEM and TEM collected after 1200 ºC heat treatments implies that SiO_2 may be flowing and enabling viscous sintering of the aerogel. Previous work has demonstrated viscous sintering is an effective means of enhancing densification and is expected to be enabled at temperatures above 1100 °C for amorphous SiO_2 [164–167]. Small particle size is expected to lower the temperature at which viscous sintering can occur in SiO_2, often from 50 to 100% of the bulk melting point of 1,710 °C [168–172]. Structural rearrangements are also expected up to and at the glass transition temperature of 1207 °C for bulk amorphous SiO_2 that would aid in the rearrangement and densification of the aerogel structure [173].

The ability of SiO_2 to hasten densification from 1000 to 1200 °C has been demonstrated in work by Fahrenholtz and Smith on diphasic aluminosilicate aerogels [174]. This concept will be discussed in greater detail in Chapter 8, but also informs the observations made in this work. Diphasic aluminosilicate aerogels are composed of Al_2O_3-rich and SiO_2-rich regions. The heterogenous nature of the structure permits amorphous SiO_2-rich regions to persist to temperatures of 1250 °C. From 1100 to 1300 °C, an extraordinarily dramatic increase in density occurs for diphasic aerogels. From these previous works, it is hypothesized viscous sintering, enabled by the presence of over 60 wt.% SiO_2 in 30YSZ-SiO_2, enhances densification, reducing the thermal stability of this material at temperatures exceeding 1000 °C.

As SiO_2 flows, it may be filling in mesopores and aiding in the rearrangement and compaction of primary particles, leading to the dramatic reduction in mesopore volume and average mesopore size observed from 1000 to 1200 °C in Figure 7.1(b-c). The slightly higher SSA of 30YSZ-SiO_2 compared to 30YSZ must be the result of greater macroporosity since the mesoporosity of 30YSZ-SiO_2 is dramatically reduced at 1200 °C. At 1200 °C, there is no sign of mesoporosity in the TEM image shown in Figure 7.4(b), which instead reveals the formation of extremely spherical YSZ particles embedded in an amorphous SiO_2 matrix. The chemical composition of these two unique areas are supported by TEM EDS data collected by collaborators and not included in the present document. This effect has been reported previously for nanocrystalline YSZ polycrystals coated with a sodium strontium silicate glass [175]. Sintering at 1400 °C for 1 h lead to highly faceted polyhedral grains for uncoated YSZ and increasingly round grains for YSZ with increasing glass content. This effect was posited by the authors to be the result of the SiO_2 coating exerting a homogenous strain across the surface of the YSZ grains but may also result from a change in the relative surface energy of crystalline facets in YSZ. The suppression of crystallite growth of YSZ with SiO_2 coatings has also been previously noted and is attributed to the SiO_2 layers serving as grain boundary pinning agents and diffusion barriers, effectively limiting the ability of adjacent YSZ particles to diffuse together [175,176].

Overall, the ability of SiO_2 to flow at temperatures exceeding 1000 °C enables viscous sintering of the aerogel. This leads to rapid densification and destabilization of the mesoporous structure from 1000 to 1200 °C. SiO_2-coated 30YSZ aerogels do not offer any improvement in thermal stability at 1200 °C and are limited to use to temperatures of 1000 °C. Despite enhancing densification of the pore structure, the SiO_2 coating continues to serve as a diffusion barrier, preventing the growth of crystallites to 1200 °C though this is not enough to prevent destabilization of the porosity.

7.4.5 Phase formation in SiO_2 coated YSZ aerogels

In the work by Zu *et al.*, the aerogels were crystalline as synthesized, owing to a different drying technique that used ethanol as the supercritical fluid at temperatures beyond 260 °C and pressures of 10 MPa [140]. Still, the effect of coating was clear, strongly reducing crystallite size at 1000 °C and also modifying the phase behavior of the ZrO_2 and Al_2O_3 aerogels. In the case of ZrO_2, the aerogel was tetragonal as synthesized, but formed a mixture of monoclinic and tetragonal phases after heat treatment at 1000 °C. Upon coating, the tetragonal phase alone persisted to 1000 °C. The uncoated Al_2O_3 aerogel transformed from boehmite as synthesized to a mixture of α- and θ-Al_2O_3 at 1300 °C, whereas the coated Al_2O_3 only formed the θ-Al_2O_3 phase after 1300 °C heat treatment. This suppression of crystallite growth and phase transformation is suggested to be the result of inhibition by the core-shell nanostructure generated by the coating procedure. The specific mechanisms that drive the inhibition are not described. In the case of ZrO_2, the formation of a pure tetragonal phase at 1000 °C may be the result of reduced crystallite size, with the tetragonal phase of ZrO_2 having a lower surface energy than the monoclinic phase. Therefore, there is a size effect where smaller particle size can stabilize the tetragonal phase [78].

The changes in phase formation observed by Zu *et al*. are noteworthy but are difficult to extrapolate to the suppression of crystallization observed in the present work. The application of SiO_2 coating to the 30YSZ aerogel not only suppressed crystallite growth, but also delayed crystallization to higher temperatures. 30YSZ-SiO_2 was x-ray amorphous at 600 °C and only weakly crystalline at 1000 °C. The cubic phase formed in both the coated and uncoated sample with similar lattice parameters at 1000 °C. There was no sign of SiO_2 apart from an amorphous hump until 1400 °C, where it crystallized into cristobalite, and 1500 °C, where it also formed a small amount of $Y_2Si_2O_7$.

Regarding the evolution of 30YSZ-SiO_2, the maintenance of an amorphous SiO_2 phase following heat treatments at 1200 °C is supported by previous work by Li *et al.* on the devitrification of silica powders [177]. Li *et al*. observed an increase in cristobalite fraction, relative to the amorphous phase, from 1300 to 1500 °C. After 90 min at 1300 °C, the powder was weakly crystalline and only the peak near 22° 2θ was visible. Given, the 20 min heat treatments applied here, the absence of cristobalite from 600 to 1200 °C is not surprising. The SiO_2 remains amorphous and does not interact with the YSZ phase until 1500 °C, at which point a small amount of $Y_2Si_2O_7$ was detected.

Therefore, interdiffusion of Zr, Y, or Si does not appear to occur at any appreciable amount, an observation supported by the literature. Work by De Souza and De Souza evaluated the effect of a silicate liquid phase on the sintering of YSZ ceramics [161]. The YSZ material was 7.0 mol% Y_2O_3 in ZrO_2 and to this was added 2.5 mol% SiO_2 plus minor amounts of Al_2O_3, TiO_2, and CaO. The material was sintered at 1610 °C for 16 h and the composition of the ceramic grains, intergranular glass phase, and expelled glass phase were analyzed, which provides insight to the amount of segregation and interdiffusion to be expected in the 30YSZ-SiO_2 aerogel. The ceramic grains were reported to be 92.3 mol% ZrO_2, 7.0 mol% Y_2O_3, and 0.5 mol% SiO_2. The intergranular glass phase was 75 mol% SiO_2, 7 mol% ZrO_2, and 5.1 mol% Y_2O_3 and the expelled glass phase 84.5 mol% SiO_2, 2.6 mol% Y_2O_3, and no detectable ZrO_2. The sintering time and temperature in the aforementioned study exceeds the conditions used for 30YSZ-SiO_2. Nonetheless, it remains informative in showing that very little Si is expected to diffuse into the YSZ aerogel, while small amounts of Zr and Y can diffuse into the glassy phase. The amount of interdiffusion in the present work appears to be low, as $ZrSiO_4$ (zircon) is never detected, and $Y_2Si_2O_7$ only forms a minority phase following 12 h at 1500 °C, well above the temperature at which this phase is anticipated to crystallize [178,179]. The slight reduction in lattice parameter at 1200 °C for 30YSZ-SiO_2 may reflect a loss of Y, though the shift in parameter is perilously close to experimental error [114].

In summary, over the primary range of interest from 600 to 1200 °C, SiO_2 coating suppresses crystallite growth and phase formation, with the SiO_2 remaining a distinct amorphous phase. Previous hypotheses put forward rooted in interface pinning may no longer be relevant given the high concentration of SiO_2 present. There are two hypotheses to put forward based upon the observations in the present work. One, if the SiO_2 coating is forming a shell that encapsulates a YSZ aerogel core, the SiO_2 coating may serve as a diffusion barrier, constraining the YSZ aerogel and preventing crystallite growth and the necessary atomic rearrangement for crystallization. Two, the coating procedure is dramatically altering the structure of the YSZ aerogel via reconstruction, Ostwald ripening, or other mechanisms. This picture becomes significantly more complex, but the initial structure of intermingled regions of YSZ and SiO_2, coupled with the low inter-diffusivity of Zr, Y, and Si, may serve as a source of “confusion” that requires significant rearrangement prior to crystallization and subsequent crystallite growth. Both cases only hold true to the point where SiO_2 begins to flow and undergo viscous sintering, observed to be between 1000 and 1200 °C, at which point the continuous liquid phase provides for enhanced densification of the pore structure.

7.5 Use of non-densifying coatings

7.5.1 Motivation

SiO_2 coatings offer a strong improvement in thermal stability to 1000 °C. Unfortunately, the amorphous nature and relatively low melting point of SiO_2 enables viscous sintering and enhanced densification beyond 1000 °C. Bulk amorphous silica has reported to have a glass transition at 1207 °C, above which SiO_2 behaves as a melt, and can occur even lower with small particle size [173]. In the work by Zu *et al.*, hybrid coatings were explored where the first layer was M_xO_y (ZrO_2, TiO_2, or Al_2O_3), followed by a 50/50 mix of SiO_2 and M_xO_y, and a third layer of SiO_2 only [140]. Precursors used for ZrO_2, TiO_2, and Al_2O_3 were zirconium(IV) butoxide, titanium(IV) isopropoxide, and aluminum-tri-sec-butoxide, respectively. This paper did not explore coatings deposited exclusively from these metal alkoxides. If the enhanced thermal stability of SiO_2 coatings to 1000 °C can be recreated with a different metal oxide, while avoiding the viscous sintering that occurs beyond this temperature, a coated aerogel with high thermal stability to temperatures exceeding 1200 °C may be achievable. The other metal oxides are expected to crystallize prior to the onset of viscous sintering and therefore improve thermal stability at temperatures beyond 1000 °C, though the amorphous nature of the SiO_2 coating and the morphology of the coating achieved with TEOS may not be replicated with the other metal alkoxides. Work must be conducted on developing procedures to prepare aerogels with coatings from alternative metal alkoxides and characterizing their structure after exposure to high temperatures to understand the phenomena behind stabilization for coated aerogels.

7.5.2 Challenges with reactive metal alkoxides of Zr, Ti, and Al

A critical challenge that must be faced to apply coatings of zirconia, titania, alumina, and other metal oxides is the high reactivity and/or prohibitive cost of their respective metal alkoxides [53,180–184]. Work on the sol-gel synthesis from alkoxides has had a near complete focus on silicon alkoxides, owing to several factors including a four-fold coordination in precursor as well as oxide, high electronegativity of Si, and small partial charge of Si [46,183]. These last two factors contribute to silicon alkoxides' low sensitivity to hydrolysis, allowing for careful control of reaction kinetics and the final gel structure. Acid or base catalysis is typically required to initiate hydrolysis and condensation in silicon alkoxide sol-gel chemistry.

On the other hand, the other metals of interest are more electropositive than silicon, making them susceptible to nucleophilic attack and rapid hydrolysis, leading to self-condensation and precipitation. As an example, both silicon and titanium have an oxidation state of +4. Because of the lower electronegativity of Ti, the hydrolysis rate of $Ti(OR)_4$ is 10^5 times faster than that of $Si(OR)_4$ for the same alkoxy group (R) [180]. Zirconium has a hydrolysis rate even faster than titanium. With such high hydrolysis rates, precipitates rapidly occur upon addition of water, and often simply via reaction with the water present in ambient air. Strategies must be employed to reduce the rate of hydrolysis, including the use of longer and/or bulkier alkoxide substituents and modification via chelation agents [53,180,185–187]. Longer and bulkier chains reduce the nucleophilicity of the metal center and therefore reduce hydrolysis rates. Chelation agents replace or block alkoxide substituents, reducing the number of sites for nucleophilic attack of the metal. In this work, long chain alkoxides were selected where available. The use of chelation agents was not explored for coating solutions but was applied for alumina-zirconia sol-gel synthesis in Chapter 8 and offers an additional parameter to tune the rate of metal alkoxide deposition.

Aluminum-tri-sec butoxide presented unique challenges, even when handled in an inert atmosphere while avoiding contact with water. Upon addition of the aluminum-tri-sec-butoxide to 200 proof ethanol in an argon-filled glovebox, precipitation occurred rapidly. This was noted even with new 200 proof ethanol, indicating it was not residual water reacting with the alkoxide. It is hypothesized that this was the result of ethanol exchanging on the alkoxide to form the much more reactive aluminum ethoxide. Work by Pérez *et al.* points to the fact that alcohols are not simply a way to solubilize metal alkoxides, but also can react with alkoxides in unexpected ways [188]. This can result in unforeseen precipitation, as observed here, or in an ill-defined mixture of alkoxides that leads to anisotropic and irregular growth in assembled structures. An Al_2O_3 sol-gel synthesis developed by Poco *et al.* notes this precipitation, but manages to restabilize an alumina sol via heating to 60 °C and stirring for 45 minutes [189]. This step was adapted here and resulted in a perfectly clear solution with no visible precipitates.

Precipitation was also commonly observed when using zirconium(IV) butoxide and titanium isopropoxide. For zirconium(IV) butoxide, the precipitate was generally white and powdery and tended to settle to the bottom of the soaking solution as well as coat the exterior of the aerogel monolith. This coating generally fell off with light handling or supercritical drying. Titanium isopropoxide solutions tended to form highly angular, star-shaped crystalline precipitates in the bottom of the soaking solution. In some cases, a crystalline, glassy shell would form around the aerogel monolith. This shell was not chemically bound to the aerogel and could be removed with tweezers. The surface of the aerogel was likely acting as a nucleation site for precipitation of the alkoxide.

As mentioned previously, the use of chelation agents to slow the reactivity of these alkoxides may prove useful. If precipitation is occurring, the metal alkoxide is not depositing on the aerogel structure as desired. The hydrolysis rate of these precursors must be slowed to allow the alkoxide sufficient time to diffuse through the mesoporous structure of the aerogel and homogeneously deposit on its surfaces.

7.6 Summary

Post-synthetic modification of aerogels with capping groups or coatings is a route to improved thermal stability through inhibition of hydroxyl condensation, coarsening of the starting structure, grain boundary pinning, or a combination of these effects. In this work, silica coatings were applied to YSZ aerogels, and their evolution was studied to 1200 °C. Silica coatings significantly improved the thermal stability to 1000 °C, hypothesized to be the result of grain boundary pinning, which reduces the rate of crystallite growth, and a strong reduction in surface energy, which reduces the thermodynamic driving force for elimination of surface area. Beyond 1000 °C, the silica coated aerogels densify rapidly and have thermal stability equivalent to, even perhaps worse than, their uncoated counterparts. This is thought to be the result of viscous sintering, where the silica flows, both filling in mesopores and enabling primary particle rearrangement into a denser configuration. Further work is required to fully characterize the structure of the SiO_2 coating in relation to the YSZ aerogel, as Si exists in over three times the abundance of Zr. Exploration of different TEOS concentrations in the coating solution is also of interest. Lower TEOS concentration may reduce the amount of Si in the final aerogel. EDS could once again be used to quantify Si, Zr, and Y content, followed by evaluation of thermal stability in relation to the amount of Si present.

The use of coatings that will not undergo viscous sintering, including zirconia, titania, alumina, and boehmite (all referred to as “non-densifying coatings”), may provide the enhancement in thermal stability to temperatures of 1200 °C and beyond. To this end, YSZ aerogels were modified with coatings from zirconium, titanium, and aluminum alkoxides and boehmite colloids. Steps had to be taken to control the high reactivity of these alkoxides. Future work encompasses the characterization of the coated materials to determine the success of the coating procedure and their structural evolution at high temperatures. Optimization of the coating procedure and exploration of capping groups may offer improved thermal stability with non-densifying coatings.

7.7 Figures and tables

Table 7.1: Molar ratios of alkoxide, 200 proof ethanol, DI water, and HNO_3 for the preparation of coating solutions according to Zu *et al.* ratios.

Metal	Alkoxide	Ethanol	Water	HNO_3
Si	1	7.7	1.5	0.01
Al	1	85	0.85	0.019
Zr	1	115	1.5	0.5
Ti	1	55	2	0.013

Table 7.2: The physical and textural properties for uncoated and SiO_2-coated 30YSZ aerogels. SSA is BET specific surface area, V_{BJH} is BJH desorption cumulative pore volume, D_{BJH} is BJH desorption average pore size, S is percent shrinkage, and ρ_b is bulk density.

Sample	SSA (m^2/g)	V_{BJH} (cm^3/g)	D_{BJH} (nm)	S (%)	ρ_b (g/cm^3)
30YSZ	473	2.914	26.9	-12.5	0.186
30YSZ-SiO_2	599	2.843	25.1	-10.7	0.275

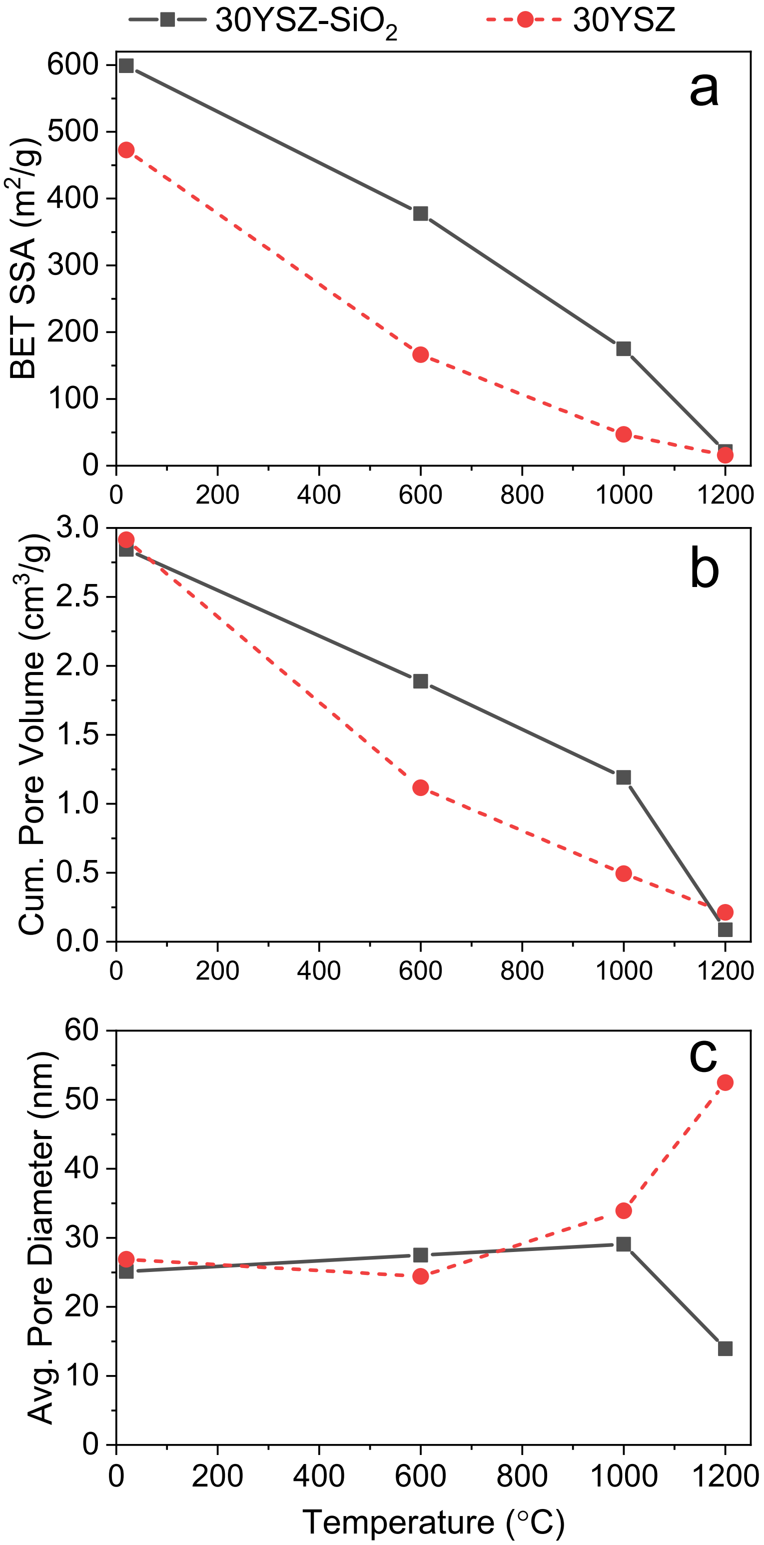

Figure 7.1(a-c): (a) BET SSA, (b) cumulative pore volume, and (c) average pore size for 30YSZ and 30YSZ-SiO_2 from AD to 1200 °C. 30YSZ-SiO_2 maintains a higher SSA and V_{BJH}, but only to 1000 °C. At 1200 °C, the SSAs are comparable and V_{BJH} is lower for 30YSZ-SiO_2.

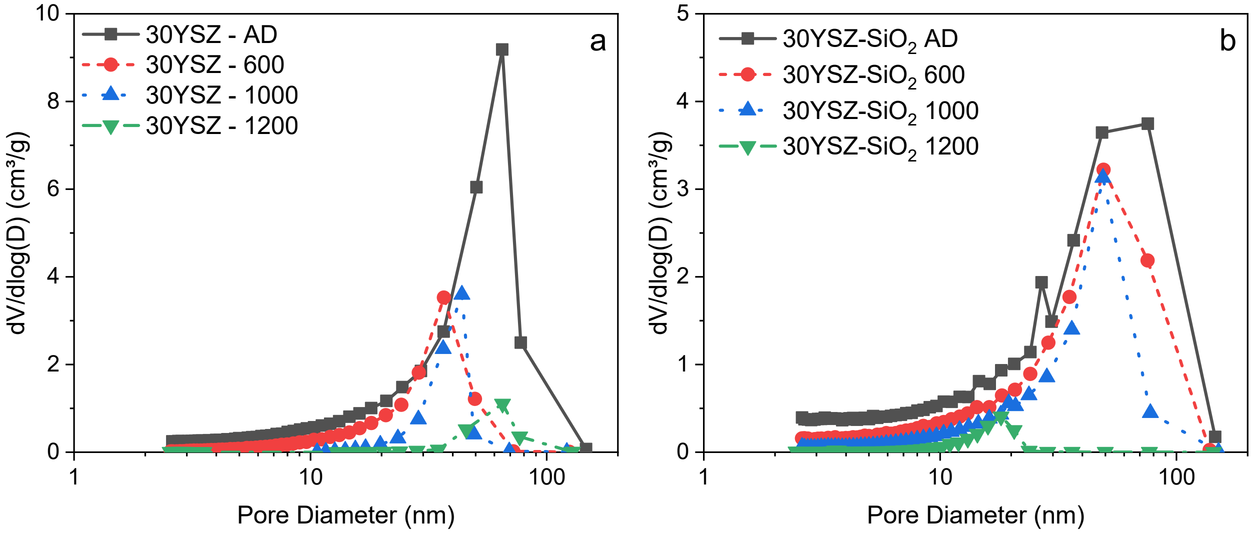

Figure 7.2(a-b): BJH desorption pore size distributions for (a) 30YSZ and (b) 30YSZ-SiO_2 from AD to 1200 °C. The distribution of pores appears more stable in 30YSZ-SiO_2 from AD to 1000 °C, but undergoes significant densification from 1000 to 1200 °C.

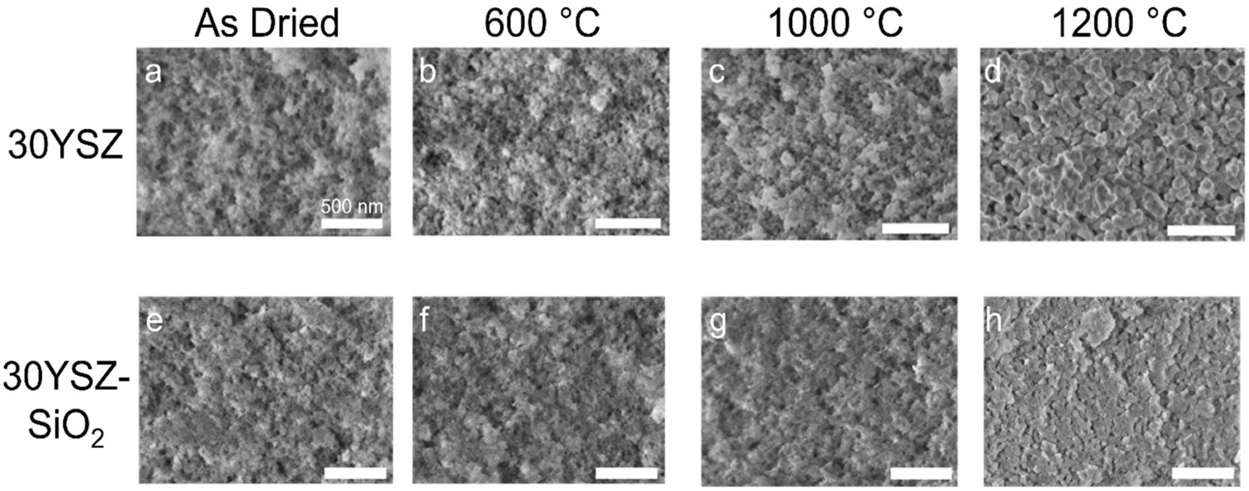

Figure 7.3(a-h): SEM micrographs of the evolution of (a-d) 30YSZ and (e-f) 30YSZ-SiO_2 from AD to 1200 °C. There is no distinct difference from AD to 1000 °C between 30YSZ and 30YSZ-SiO_2. At 1200 °C, particle growth and necking are visible in (d) 30YSZ and significant densification is visible in (h) 30YSZ-SiO_2. The scale bar in all images is 500 nm.

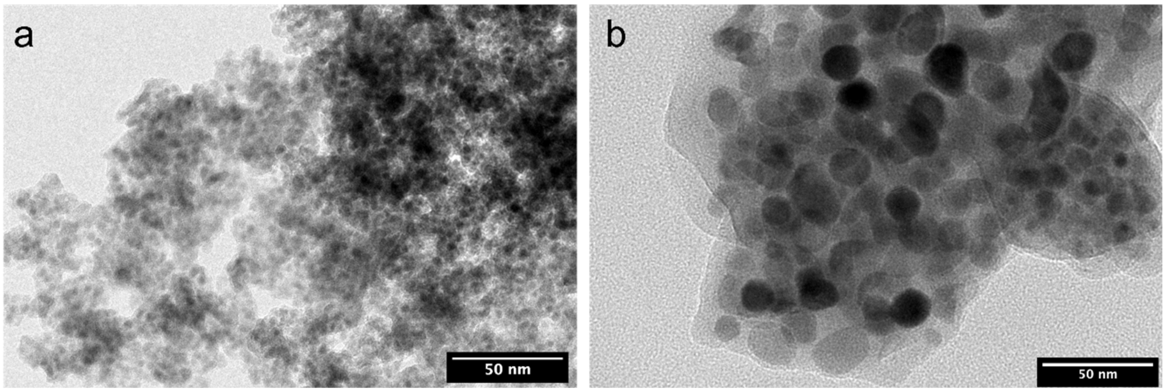

Figure 7.4(a-b): TEM images of 30YSZ-SiO_2 at (a) 1000 °C and (b) 1200 °C. At 1000 °C, mesoporosity is still visible and the particle size remains small. At 1200 °C, there is no sign of mesoporosity in the image and the particle size has increased dramatically. The dark particles are hypothesized to be YSZ which are embedded in a matrix of SiO_2, the semi-translucent material. This morphology may also be present at 1000 °C, but too small to resolve. The scale bar in both images is 50 nm.

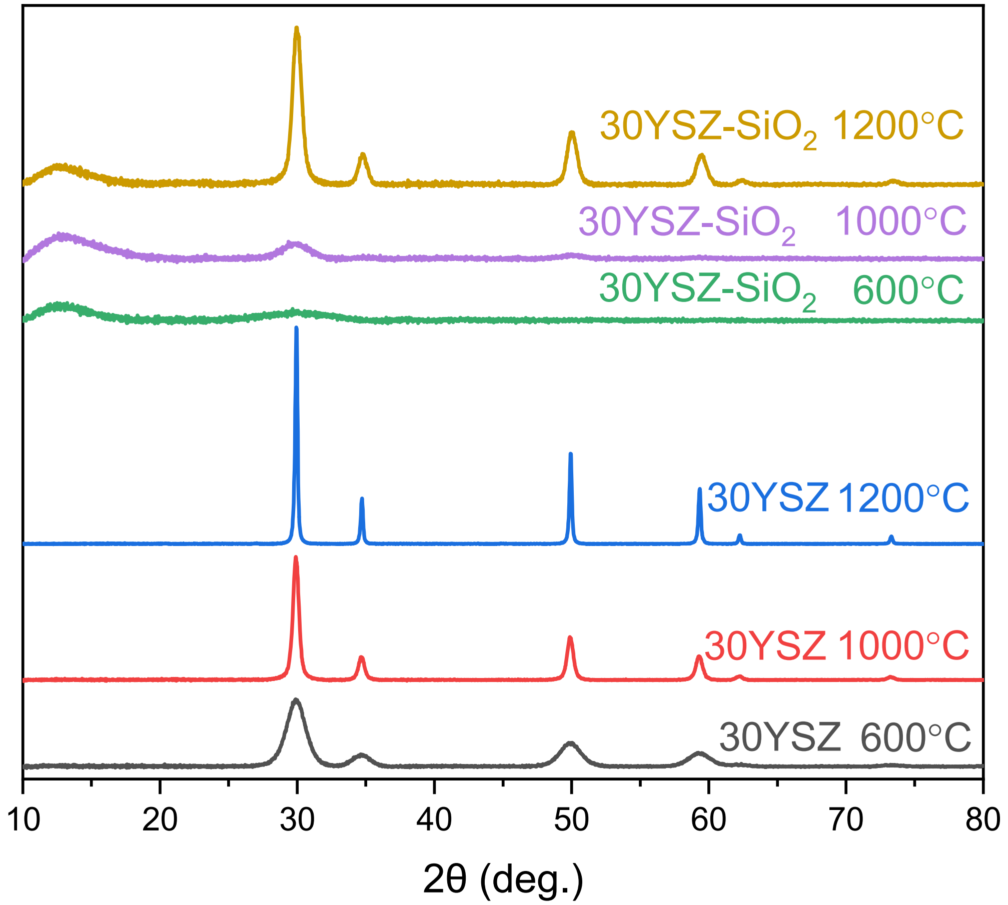

Figure 7.5: XRD patterns of 30YSZ and 30YSZ-SiO_2 at 600, 1000, and 1200 °C. Once crystallized, all materials form the cubic phase. Peaks do not appear in 30YSZ-SiO_2 until 1000 °C. Crystallinity in 30YSZ-SiO_2 is significantly lower than that of 30YSZ. An amorphous hump between 10 and 15 deg. 2θ appears in 30YSZ-SiO_2 at all temperatures.

Table 7.3: Crystallite sizes and lattice parameters (a) for 30YSZ and 30YSZ-SiO_2 at 600, 1000, and 1200 °C as calculated via refinement in GSASII. In general, crystallite sizes are significantly lower for 30YSZ-SiO_2. Lattice parameters align with expectations for 30 mol% $YO_{1.5}$, though a slight reduction in lattice parameter is observed for 30YSZ-SiO_2 at 1200 °C.

Sample	T (°C)	Crystallite Size (nm)	a (Å)
30YSZ	600	5.8	5.163
30YSZ-SiO_2	600	-	-
30YSZ	1000	21.7	5.163
30YSZ-SiO_2	1000	3.2	5.162
30YSZ	1200	55.3	5.163
30YSZ-SiO_2	1200	13.9	5.153

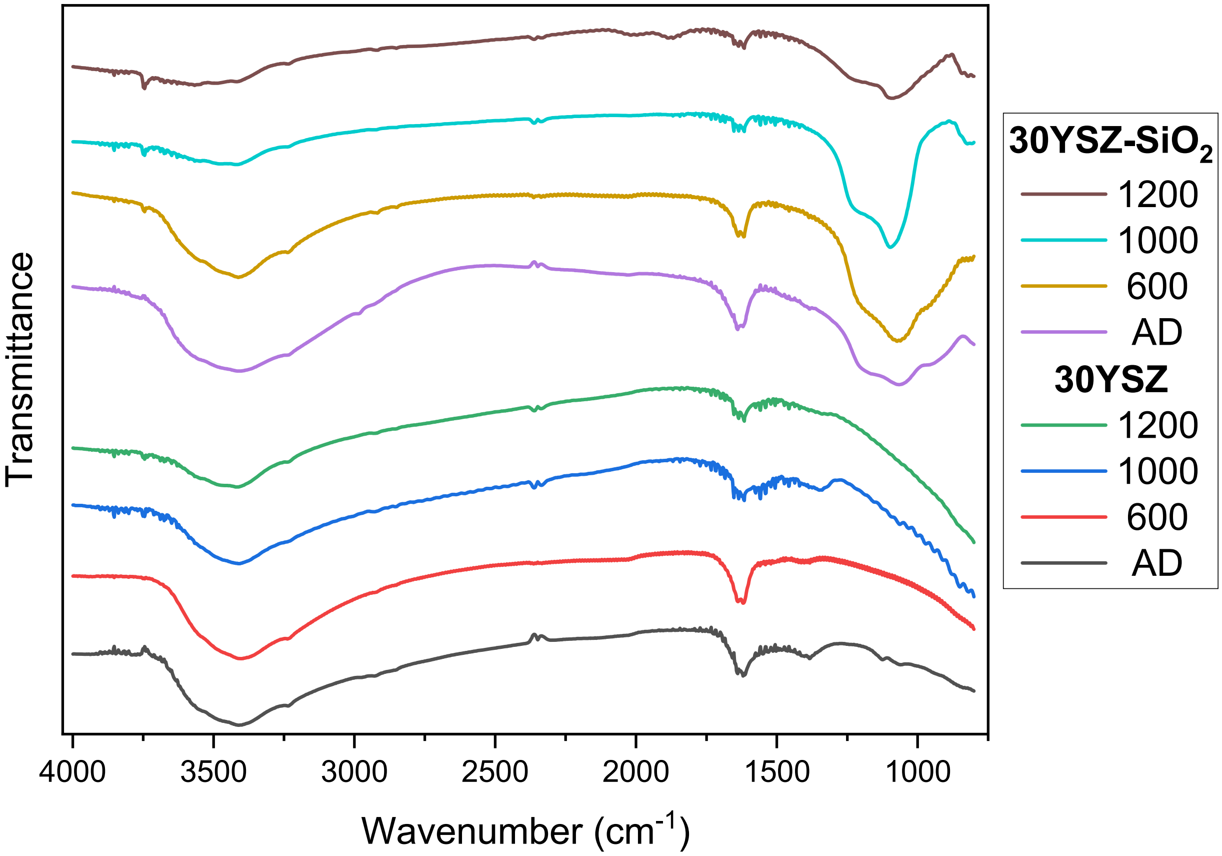

Figure 7.6: FTIR transmittance spectra for 30YSZ (bottom four spectra) and 30YSZ-SiO_2 (top four spectra) from AD to 1200 °C. Hydroxyl content decreases in all samples upon heat treatment but most so in 30YSZ, visible in the reduction in the broad peak from 3750 to 3250 cm^{-1}. The most notable difference between 30YSZ and 30YSZ-SiO_2 is the Si-O-Si at 1150 cm^{-1}.

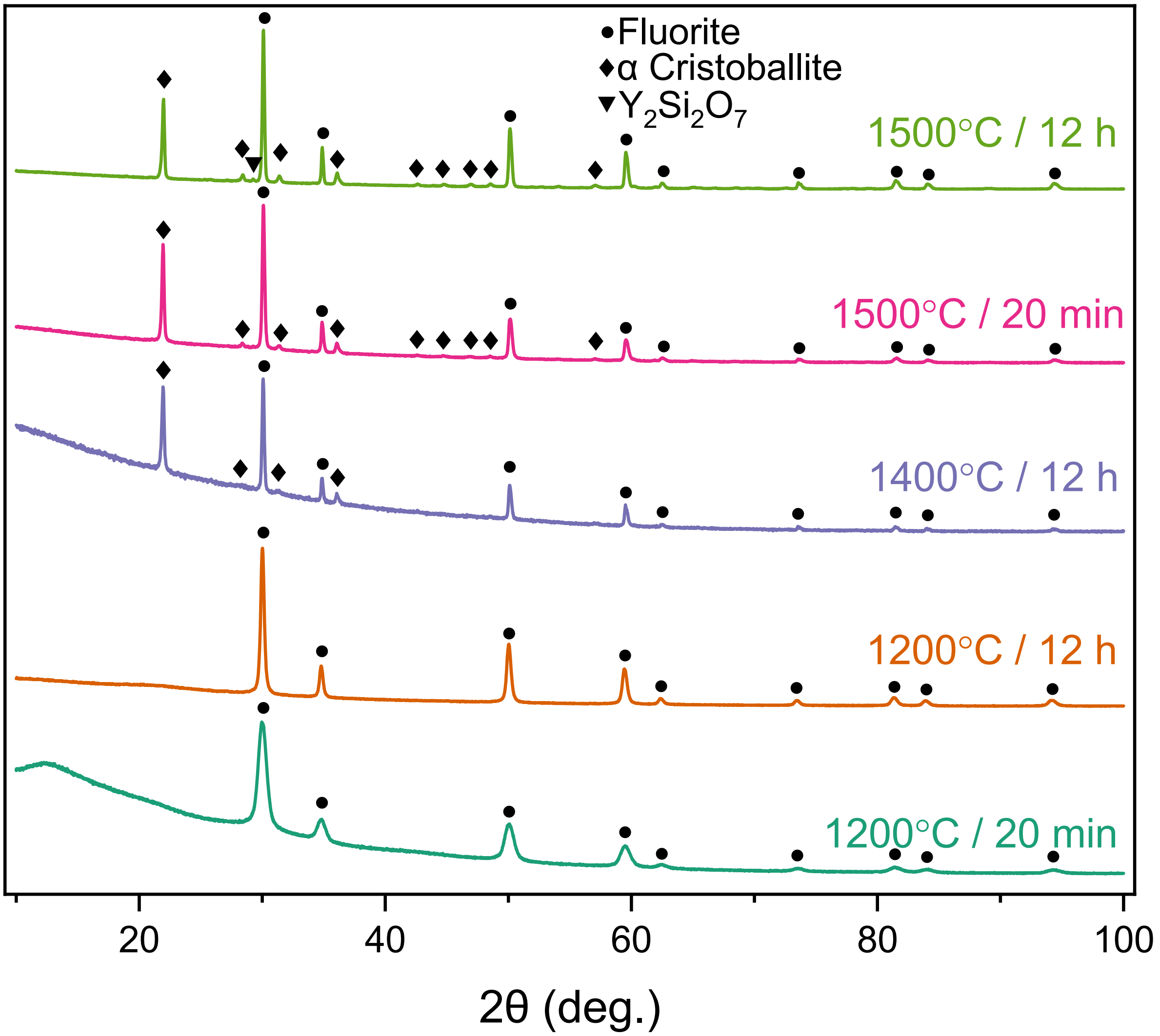

Figure 7.7: XRD patterns for 30YSZ-SiO_2 heat treated under various conditions. At 1200 °C for 20 minutes, an amorphous SiO_2 phase exists indicated by the broad hump at low angles. Only after 12 h at 1400 °C does SiO_2 crystallize into cristobalite. At 1500 °C for 12 h, there was a peak associated with a $Y_2Si_2O_7$ phase.

CHAPTER 8: DEVELOPMENT OF COLLOIDAL SYNTHESES FOR MIXED METAL OXIDE AEROGELS

8.1 Introduction

Previous work demonstrates the improvement in thermal stability of aluminosilicate aerogels when derived from a colloidal boehmite precursor compared to a salt precursor [50,51,70]. The crystalline as dried structure, formed by self-assembly of boehmite crystallites, prevents diffusion and rearrangements upon crystallization that are destructive to the aerogel structure. The particle size of the precursor also allows the aerogel structure to be finely tuned. The larger particles making up the aerogel backbone when derived from a colloidal precursor also may improve thermal stability by delaying the transition from surface to volume diffusion [22,26]. Overall, the structure derived from boehmite was more robust towards resisting densification than the aerogel derived from the aluminum chloride salt.

Though the work on aluminosilicate aerogels derived from boehmite resulted in an aerogel with excellent thermal stability to 1100 °C, questions remain as to the definitive source or mechanism of improved thermal stability of boehmite colloid aerogels compared to those derived from metal salts. Questions remain due to the complexity of evolution in aluminosilicate materials, with key differences arising from the choice of the alumina and silica precursor.

Work over the course of the last 30 years in sol-gel derived aluminosilicates groups these materials into two categories: single phase (formed from solutions of salts and/or alkoxides with mixed Al-O-Si bonding) or diphasic (formed from colloids or colloids with alkoxides with Al-rich and Si-rich regions) [166,174,190–192]. In diphasic gels, the compositional heterogeneity suppresses mullite formation to temperatures exceeding 1250 °C. Critically, this leads to the retention of an amorphous phase that allows the gels to densify via viscous sintering of the silica phase above 1100 °C, but below the crystallization temperature [164,174]. In single phase gels, the temperature at which the mullite forms (near 950 °C) overlaps with temperatures where densification could occur via viscous flow. Overall, densification is enhanced in diphasic systems above 1100 °C. In the context of the work on boehmite-derived aluminosilicate aerogels, the complications that result from the unique phase formation and presence of silica, which can enable viscous sintering, convolutes the effect of precursor structure and starting aerogel morphology on thermal stability.

Therefore, this work seeks to answer the question of how unique structural motifs, and the way these motifs are assembled, influence thermal stability. Furthermore, does the improvement in thermal stability from colloidal precursors extend to aerogel compositions beyond aluminosilicates? The overall purpose is to demonstrate the importance of synthetic precursors and synthetic route on the thermal stability of high porous structures.

In this work, attempts were made to develop a sol-gel route to a YSZ aerogel from colloidal yttria and/or zirconia precursors, adapting the previous work on aluminosilicate aerogels to YSZ. The YSZ aerogels prepared from colloidal precursors were to be compared to salt-derived YSZ aerogels in terms of their structure and thermal stability. Following the procedure performed by Hurwitz *et al.*, three synthesis steps must be developed [50,193]. First, a colloidal precursor must be purchased or synthesized from yttria and/or zirconia. This precursor must be on the scale of 10 to 100 nanometers with surface area in excess of 150 m^2/g to be conducive to formation of a mesoporous aerogel network, as the pore structure of the aerogel has been shown to reflect the size and morphology of the powder precursor [50]. Second, the precursor must be dispersed in solvent and avoid agglomeration to form a stable colloid. Third, a solution of a zirconium alkoxide must be condensed into a coherent gel structure along with the colloidal precursor.

Once these three steps are developed, the gels will be supercritically dried, and work can begin on characterizing the aerogels resulting from this new synthetic procedure. It is expected this procedure will be readily adaptable to other doped zirconias. The thermal stability of this aerogel will be compared to that of the YSZ aerogel prepared in the Gash process from metal salts and propylene oxide.

Though this work did not produce the materials required compared to the salt-derived materials, the efforts to achieve a stable colloid of yttria or zirconia are still informative for future efforts and are detailed in this chapter in Sections 8.3 and 8.4. Future efforts may benefit from the synthesis of colloidal precursors via precipitation for yttria or zirconia or reverse coprecipitation for YSZ to ensure homogeneity of the particles [194–196]. Commercially available yttria, zirconia, or YSZ powders may also prove as a viable alternative starting material and were the focus of efforts covered in this work. Following procurement of a precursor, challenges were faced in the dispersion of this colloidal precursor. In the case of the boehmite precursor, the particles were produced with nitrate functionality via a patented process to enable dispersion in aqueous solution [197]. Functionalization of the surface was attempted to provide a stable dispersion, though the functional groups must be selected as to not inhibit gelation. Functionalization may be avoidable if the crystalline precursors are dispersible over wide enough pH ranges, in which case a suitable acid (e.g., CH_3COOH or HNO_3) or base (e.g., NH_4OH) could stabilize the colloid. Previous work on the colloidal stability of yttria and zirconia suspensions proved useful in this regard, though the colloidal stability of both these systems are notoriously difficult to achieve [198–206].

Given the difficulties faced in achieving a stable colloid for YSZ aerogel synthesis, it may be prudent to identify alternative compositions with improved colloidal stability and the ability to produce an aerogel from a metal salt. Ultimately it is the goal of this segment of the work to not only achieve a thermally stable aerogel, but also advance the field's understanding of aerogel thermal stability in context of aerogel structure and the precursors used to form it. As such, the alumina-zirconia system may prove of interest. Both have readily available metal salts and metal alkoxides. Several stable alumina and AlOOH colloids or dispersible nanopowders are also commercially available. Sol-gel syntheses of these systems have been performed and can be adapted to specifically study the effect of precursor on structure and structure on thermal stability [188,189,207]. Furthermore, alumina and zirconia are thermodynamically stable with each other and do not have any solid solutions [208]. Preliminary work was conducted in this area and will be discussed in Section 8.5.

8.2 Materials & methods

8.2.1 Powders used

Several commercially available powders were utilized for the yttria-zirconia system. For zirconium, zirconium hydroxide nanoparticles ($Zr(OH)_4$, US Research Nanomaterials Inc., 99.9%, 40 nm, Amorphous) were used and are referred to as ZrOH4_NP1. For yttrium, yttrium oxide nanoparticles (Y_2O_3, US Research Nanomaterials Inc., 99.999%, 20-40 nm) referred to as Y2O3_NP1, yttrium oxide nanoparticle 20 wt.% water dispersion (Y_2O_3, US Research Nanomaterials Inc., 99.99%, 10 nm) referred to as Y2O3_NP_D1, yttrium(III) oxide nanopowder (Y_2O_3, Alfa Aesar, 99.995%, 50-70 nm) referred to as Y2O3_NP2, and yttrium(III) oxide nanopowder (Y_2O_3, Alfa Aesar REacton®, 99.995%, 25-50 nm) referred to as Y2O3_NP3 were used.

8.2.2 Powder dispersion

The powders listed above were dispersed in several aqueous and non-aqueous systems via multiple dispersion techniques. The success of each approach will be detailed further in the results, Section 8.3. In the simplest of cases, the powder was added to a liquid slowly under vigorous stirring to disperse the powder. Generally, the next step was to submerge the container in a bath sonicator up to the level of the colloid within. The colloid was sonicated for 10 minutes and then promptly used for further characterization.

More energetic methods were also employed to disperse the powders. Colloidal ball milling was performed on a Fritsch PULVERISETTE 7 Classic planetary micro mill. YSZ milling media of 3 mm diameter were used in 45 mL ZrO_2 grinding bowls. The colloids were prepared at 10 wt.% solids. To each 45 mL bowl, 56.25 g YSZ milling media and 5.625 mL colloid were added. A PFTE gasket was installed followed by the lid. The bowls were mounted into mill holders and secured tightly into the mill. The mill was operated at 800 rpm at 5 min intervals with 30 min rests between milling cycles. The number of cycles varied from one to five. Experiments were also conducted using 0.5 mm YSZ milling media using the same procedure. Ultrasonication was also performed on a Qsonica Q500 Sonicator with a 1/2” probe. It was operated at 60% amplitude, on/off time of 1 s, and run time of 5 min.

Several acid and base systems were used to evaluate the impact of pH and acid/base identity on colloidal stability. Chemicals used include acetic acid (CH_3CO_2H, Sigma Aldrich, glacial, ACS reagent $\geq$ 99.7%), citric acid ($HOC(COOH)(CH_2COOH)_2$, Sigma Aldrich, anhydrous, ACS reagent $\geq$ 99.5%), nitric acid (HNO_3, Sigma Aldrich 70 wt.%), and ammonium hydroxide (NH_4OH, Sigma Aldrich, ACS reagent, 28.0-30.0% NH_3 basis). The target molarity or pH was used to find the amount of acid or base required. The acid or base was slowly added to DI water under vigorous stirring. The nanopowder was then added to the solution and underwent dispersion techniques listed above.

8.2.3 Powder functionalization

This procedure is adapted from a nanoparticle synthesis and functionalization developed by Prof. Markus Niederberger *et al.* [209–212]. The aim is to functionalize nanoparticles with a ligand that increases hydrophilicity and therefore stability of the metal oxide nanoparticles in aqueous colloids. These colloids will then be used to prepare gels that can undergo supercritical drying to form an aerogel. In the work by Niederberger *et al.*, the nanoparticles were formed in the reaction solution via addition of a metal chloride to benzyl alcohol and Trizma® base. In this work, this procedure was adapted with the goal of functionalizing an existing nanopowder with Trimza® by adding the powder to a solution of benzyl alcohol and Trizma®.

First, 20 mL of benzyl alcohol ($C_6H_5CH_2OH$, Sigma Aldrich, anhydrous, 99.8%) was added to a round bottom flask with a stir bar. To the benzyl alcohol, 0.0909 g 2-amino-2-(hydroxymethyl)-1,3-propanediol ($NH_2C(CH_2OH)_3$, Sigma Aldrich, ≥99.9%), also known as Trizma®, is added under stirring. The molar ratio of benzyl alcohol to Trizma® was 240. At this point, a metal oxide nanoparticle is added to the solution and stirred at 80 °C for 24 hours. The molar ratio of metal to Trizma® was 12. During this period, the Trizma is adsorbed to the surface of the particles. The functionalized particles are then centrifuged and washed with ethanol for three cycles, followed by drying at 60 °C. The powder was either used for characterization with SEM or FTIR or for dispersion in water at 10 wt. %.

Though this will be detailed later, the creation of a stable colloid via this approach was never deemed successful. In the case where the powder was successfully functionalized and dispersed with good stability, the solution would be heated to 90 °C to form a gel by desorbing the Trizma off of the particle surface and linking the particles via condensation of newly exposed surface hydroxyl groups.

8.2.4 Characterization of powders & dispersions

Nanopowder morphology was characterized with scanning electron microscopy (SEM) on a Hitachi S4800 at 2 kV accelerating voltage, 10 μA current, and 5 mm working distance. A small amount of powder was applied to carbon tape on an aluminum stub for mounting. The crystalline phase and crystallite size of nanopowders were evaluated with x-ray diffraction (XRD). The powders were deposited via suspension in 200 proof ethanol onto low background holders. XRD was performed using Cu Kα radiation on a Bruker D8 Advance XRD. Scanning conditions were 10 to 100° 2θ, 0.02 degrees per step, and 0.25 seconds per step. Parallel beam geometry was used with a 0.2 mm divergence slit and a panoramic Soller slit. The goniometer has a radius of 280 mm.

The dispersed particle size and stability of the colloid was evaluated using a Malvern Zetasizer Nano ZS via dynamic light scattering (DLS). This technique provides insight to the precursor size and state of agglomeration as a function of pH and ionic strength. Target precursor sizes in solutions are lower than 500 nm at solid loadings of 10 to 20 wt.%. Zeta potential measurements was used to identify regions of colloidal stability and gelation for synthesized precursors. Target zeta potentials are absolute values greater than 30 mV. These methods were used to compare synthesis and dispersion techniques. Colloids were prepared by adding the desired powder into DI water or 200 proof ethanol. Typical target solids loadings were 10 to 20 wt. %. The powder was then further dispersed via bath sonication, ultrasonication, or colloidal ball milling. Immediately following dispersion, a small amount of the colloid was removed and diluted with additional DI water or ethanol to 0.1 g/L. This diluted colloid was added to a Malvern Folded Capillary Zeta Cell (Malvern Panalytical #DTS1070). The cell was held upside down and the colloid was injected to the halfway point of the channel using a syringe, at which point the cell was flipped right-side up and the channel was filled to the full mark. This procedure ensured no air bubbles were trapped. At this point, the cell could be loaded into the instrument for both size distribution and Zeta potential measurements. The index of refraction for yttria was n = 1.9307 and for zirconia was n = 2.1588. Generally, three measurements were taken for size and three for zeta potential with an automatic collection time.

Colloid stability can also be qualitatively evaluated via visual inspection. Following dispersion, an image of the colloid was taken. Time was tracked and additional images of the colloid were collected at various time intervals, ranging from minutes to hours to days. A stable colloid will have a milky appearance that is consistent throughout the height of the solution, generally with a slight blue tint, the result of Rayleigh scattering from the small particle size involved. Signs of instability are gradients in color and/or opaqueness as well as visible settling of powder at the bottom of the container.

8.2.5 Alumina-zirconia gel syntheses

The development of four unique syntheses were planned, each using a unique pair of precursors: (1) aluminum salt and zirconium salt, (2) boehmite colloid and zirconium salt, (3) boehmite colloid and zirconium alkoxide, and (4) aluminum alkoxide and zirconium alkoxide. Only synthesis (3) was attempted in lab using several unique synthetic parameters at a molar ratio of Al:Zr of 3. The synthetic parameters for the test syntheses are shown in Table 8.1.

The boehmite colloid used DISPERAL® P2W (Sasol) as the AlOOH source. In Jar A, the P2W powder was slowly added to DI water at 20 wt.%. In some cases, 200 proof ethanol (Decon Labs) was added to the colloid to reduce the water concentration and improve the stability of the zirconium(IV) butoxide upon combination of Jars A and B. The colloid was stirred until well dispersed and put in a bath sonicator for 10 min. In Jar B, 200 proof ethanol was added followed by the dropwise addition of zirconium(IV) butoxide ($Zr(OC_4H_9)_4$, Sigma Aldrich 80 wt.% in 1-

butanol) while stirring. Several ratios of butoxide to ethanol were used, ranging from 0.07 to 0.30 g zirconium(IV) butoxide per 1 mL ethanol. In attempts to stabilize the zirconium(IV) butoxide and prevent hydrolysis and self-condensation, acetylacetone (AcAc, $CH_3COCH_2COCH_3$, Sigma Aldrich) was added at a molar ratio of acetylacetone to zirconium of 2 or 1 [187]. In one synthesis, a small amount of DI water was added to Jar B dropwise in an attempt to initiate hydrolysis. Jar B stirred for 30 min prior to the addition of Jar A to Jar B, either quickly (indicated by F for fast in Table 8.1) or dropwise (indicated by D). In some syntheses, DI water was added dropwise following combination. For each of the iterations, the stability of the zirconium(IV) butoxide in Jar B was carefully evaluated via visual inspection with precipitation indicating instability. If Jar B remained stable and the two jars could be combined, the behavior of the resulting material was evaluated: precipitation, gelation, or neither.

8.3 Results for yttria-zirconia colloidal stabilization

8.3.1 Powder characterization

The yttria powders were characterized using SEM for particle morphology and XRD for phase and crystallite size. SEM images for Y2O3_NP1, NP2, and NP3 are included in Figure 8.1(a-c). Y2O3_NP1 was specified by the manufacturer to have a particle size of 20 to 40 nm, though SEM revealed a heterogenous population of large agglomerates and many fiber-like structures much larger than the specified size. Y2O3_NP2 was specified to have a particle size of 50 to 70 nm. The images showed a narrow distribution of weakly agglomerated spherical particles on the order of this size. Y2O3_NP3 was specified to have particles of 25 to 50 nm and SEM did not dispute this, though the particles appeared to be highly agglomerated. Some sponge-like structures were also identified in Y2O3_NP3 and their identity or source were not confirmed.

XRD patterns for the yttria powders are shown in Figure 8.2 All powders were identified to be cubic. Y2O3_NP1 has signs of amorphous content, perhaps related to the fiber-like inclusions found in this material. Further elemental analysis may be useful in identifying the purity of this material. Crystallite sizes were calculated in GSASII for all nanopowders. For NP1, NP2, and NP3, the sizes were 28.2, 44.6, and 26.0 nm, respectively. For Y2O3_NP2, the crystallite size is on the order of specified and observed particle size. Therefore, the particles seen in the Figure 8.1(b) may be single crystallites.

8.3.2 Acid/base colloidal stabilization

All nanopowders were evaluated for colloidal stability in water ranging from 0.1 to 10 wt.% solids. None of the powders were stable in water as received and rapidly settled upon the end of mixing or agitation. Y2O3_NP2 offered the most promise, with a z-average particle size of 364 nm and a polydispersity index of 0.361 after bath sonication for 30 minutes. Still, this powder settled over the course of hours.

The nanopowders Y2O3_NP1 and ZrOH4_NP2 were used to study the effect of various acids and pH values on colloidal stability. Nanopowders were added at 1 wt.% solids to the following acids: acetic acid, citric acid, and nitric acid. Solutions were prepared from each acid at a pH of 2 (5800 mM acetic acid, 145 mM citric acid, 10 mM nitric acid) or pH of 4 (0.65 mM acetic acid, 0.11 mM citric acid, 0.1 mM nitric acid). The powder was slowly added to the solution under vigorous stirring, followed by bath sonication.

Following colloid preparation, analysis was performed on a Malvern Zetasizer to quantify zeta potential (measure of colloidal stability, target is an absolute value > 30 mV) and particle size (target is < 500 nm). The results for many of the colloids analyzed are included in Table 8.2. Most of the samples tested were either unstable or had particle sizes much too high. Thus far, the most promising systems have shown to be acetic acid and citric acid, as these two acids could form a clear solution after a few days at a pH of 2. Particularly interesting is the citric acid, as it formed a solid gel at a pH of 2 and solids loading of 10 wt.% after three days. This gel weakened into a viscous sludge after another day or two, but nonetheless provides an interesting area of study and citric acid has been used previously to stabilize yttria colloidal systems [82].

8.3.3 Powder functionalization

Y2O3_NP1 was used in an attempt to functionalize the surface with Trizma® to improve hydrophilicity and colloidal stability in water. The powder was recovered successfully, washed, dried, and analyzed with FTIR for evidence of primary amine (N-H, C-N) bonding. N-H should be a medium peak at 3500 cm^{-1} and C-N a medium peak from 1250 to 1020 cm^{-1}. The broad OH peak from 3750 to 3000 cm^{-1} does present a challenge as it may convolute the N-H peak. Presumably, functionalization should reduce OH content so this peak should change to some degree. Comparing the FTIR spectra in Figure 8.3, there are no major differences between the patterns, though there is a discernable difference at 1120 to 980 cm^{-1}. This could be a sign of C-N bonding, but the change is subtle and could simply be Trizma® that physically adsorbed to the powder and remained after washing. This peak does appear to also exist in the original nanopowder, which should not contain C-N species, so this peak may be the result of an unknown contaminant in the nanopowder itself.

To evaluate the colloidal stability, the functionalized nanopowder was added to DI water at 0.1 and 1.0 wt.% solids. In both cases, the powder settled quickly, at a rate equivalent to the unfunctionalized nanopowder. Performing measurements on the Zetasizer was not deemed necessary. Overall, the powder did not appear to have any improvement in colloidal stability after undergoing the functionalization procedure.

8.3.4 Energetic dispersion via colloidal ball milling and ultrasonication

In this work, colloidal ball milling and ultrasonic dispersion were tested on yttria colloids of Y2O3_NP2 and Y2O3_NP3. The particle size distributions were compared for Y2O3_NP2 and Y2O3_NP3 after bath sonication for 20 min or ultrasonication for 5 min. The results are shown in Figure 8.4(a-d). Y2O3_NP2 had larger average particle size after ultrasonication (2236 nm) than bath sonication (1206 nm), though the distributions were more stable over subsequent runs. This result was surprising as preliminary work with Y2O3_NP2 resulted in promising small particle size distributions that remained stable. Y2O3_NP3 had smaller average particle size after ultrasonication (1233 nm) than bath sonication (3695 nm) but did not have a stable distribution in either case.

To improve the stability of Y2O3_NP2 after ultrasonication, citric acid (CA) solutions were used at either 0.01 mM (pH = 4), 145 mM (pH = 2), or 1.305 mM. This additional concentration was selected as it corresponded to the same molar ratio of metal to citric acid as used in the Y2O3_NP1 colloid that appeared stable and eventually gelled. The three citric acid solutions were prepared, Y2O3_NP2 added at 0.1 wt.%, and the colloids were ultrasonicated for 5 min. The results for size and zeta potential distributions are shown in Figure 8.5(a-f) with size data in (a, c, e) and zeta potential data in (b, d, f). The top row is 145 mM CA, middle row 1.305 mM CA, and bottom row 0.01 mM CA. In terms of size, 145 mM CA had little effect on stabilizing the powder. 0.01 mM had a marginal improvement in reducing particle size and improving the stability of the size distribution between measurements. The 1.305 mM CA was most effective at stabilizing the colloid, with an average particle size of 225 nm and a PDI of 0.185. The data were extremely consistent between runs. Interestingly, 0.01 mM and 145 mM samples had similar zeta potentials of -11.7 and -7.9 mV, as seen in Figure 8(b) and 8(f). 1.305 mM CA had a lower zeta potential than the other samples with an average of -23.5 mV and deviation of 5.37 mV. Figure 8.6 show the stability of 145 mM, 1.305 mM, and 0.01 mM after one hour. 1.305 mM CA was the only colloid that did not visibly settle after this time.

The colloidal stability of Y2O3_NP2 in ethanol was also evaluated following ultrasonication. The colloid was prepared at 1 g Y_2O_3 per 1 L ethanol, ultrasonicated, and diluted to 0.1 g/L for Zetasizer measurements. The particle size distributions for repeated runs are shown in Figure 8.7(a). The distribution showed good stability over subsequent runs and the average particle size of 340 nm with PDI of 0.288 was promising, given no other treatments or stabilization agents were added. The colloid in ethanol did not show settling for upwards of 40 minutes, with the images in Figure 8.7(b) showing the sample 40 minutes after ultrasonication.

Colloidal ball milling was also tested as an option to break up agglomerates and reduce particle size and improve colloidal stability. The particle size distributions for Y2O3_NP1 after bath sonication (to serve as a control), two five-minute cycles with 3 mm media, five five-minute cycles with 3 mm media, and five five-minute cycles with 0.5 mm media are shown in Figure 8.8(a-d). The average particle size was reduced from 1790 nm to 504 nm, comparing bath sonication to two cycles of colloidal ball milling. Five cycles further reduced average particle size to 374 nm. The use of smaller milling media (from 3 mm to 0.5 mm) further reduced average particle size to 251 nm. Overall, colloidal ball milling was effective in reducing average particle size for yttria powders but did result in broad particle size distributions. Furthermore, separation of the colloid from the milling media also posed a challenge, especially with 0.5 mm media.

8.4 Discussion for yttria-zirconia colloidal stabilization

8.4.1 Challenges in stabilization

In this work, several commercially available yttria and zirconium hydroxide powders were sourced for study as precursors to YSZ aerogels. Upon visual inspection with SEM, significant issues with Y2O3_NP1 were found as shown in Figure 8.1(a). The majority of the material was composed of long fibers of unknown composition. There was no sign for particles of the specified size of 20 to 40 nm. Furthermore, XRD revealed the presence of amorphous content in this sample seen in Figure 8.2. These issues demonstrate that careful evaluation of starting materials against manufacturer specifications is critical prior to embarking on the development of new synthesis techniques. Y2O3_NP2 and Y2O3_NP3 were found to be composed of small, spherical particles on the order of specified sizes as seen in Figure 8.1(b-c), but Y2O3_NP3 was more strongly agglomerated. Overall, Y2O3_NP2 offered the best combination of small particle size, homogeneous appearance, and low agglomeration. To form a mesoporous gel with control over the final structure, these features will be important for a precursor to have.

Both zirconia and yttria have relatively poor colloidal stability and have the tendency to rapidly aggregate and settle out of solution [82,199,200,213,214]. Upon addition to DI water under stirring and followed by bath sonication, particle sizes for the powders generally remained above 1000 nm and their size distributions were found to be highly unstable. Visually, the powders rapidly settled out of solution. After studying an array of acids and pH levels, the use of citric acid was determined to be most promising. Furthermore, it even resulted in the gelation of an yttria colloidal sample following a few days’ rest. Citric acid has been successfully employed in the stabilization of yttria, yttrium aluminum garnet, and lutetium aluminum garnet, owing to its ability to both sterically and electrostatically stabilize the particles [82]. Not only does citric acid generate a charge on the particles, but the polar nature of the carboxylic acid also attracts the citric acid to the surface hydroxyl groups on the metal oxide nanopowder, providing a steric stabilization effect. The gelation of the yttria colloid containing citric acid may be its ability to serve as a chelation and complexing agent, which has been used in several sol-gel syntheses with citric acid as the gelation agent [63–65,215]. In this regard, citric acid may be able to serve as both a stabilization and gelation agent. The use of temperature or its conjugate base, sodium citrate, to tune pH may drive the system towards gelation in a controlled manner and warrants further study [82].

To prevent sedimentation and destabilization of colloids, the particle size generally needs to be on the order of 100 nm or smaller to prevent settling. Ultrasonic dispersion [199,213] and colloidal ball milling [82,198] have been applied to reduce particle size in solution to improve stability for yttria and zirconia colloids. Colloidal ball milling was successful in reducing the particle size significantly as demonstrated by the shift in the particle size distribution in Figure 8.8(a-d). Significant challenges were faced when attempting to recover the milled colloid and separate the milling media. The difficulty was exponentially greater when 0.5 mm milling media was used in place of 3 mm media. Various forms of filtration and sieving were attempted but did not lead to success with much of the colloid and powder adhered to the milling media, where the water would eventually evaporate leaving behind an agglomerated powder. The primary restriction is the inability to wash the milling media with DI water to remove the adhered powder. If additional water is added, the solids loading of the colloid will be unknown, which is required for both characterization of the colloid and, especially, for the use of the colloid in subsequent syntheses.

Inputting energy into the colloid via ultrasonication or ball milling does reduce particle size, but the freshly created surface area requires stabilization. Often, the colloids would rapidly flocculate and settle following these dispersion methods. The use of citric acid was successful in sterically and electrostatically stabilizing the new surface area created from ultrasonication , much more than the use of citric acid without ultrasonication. The challenge that exists here is the large experimental space for optimization in terms of amount of citric acid, the use and amount of conjugate base, final pH, and the solids loading of the nanopowder in the colloid. In this work, the identification of 1.305 mM citric acid as a promising concentration was the result of extrapolation from a random colloid sample that had gelled in a previous experiment. As shown in Figure 8.5(c-d), the particle size distribution is narrow and stable with small average particle size and the zeta potential is unique compared to both 145 and 0.01 mM citric acid. At this time, the reason for this result is not clear. It does indicate that much optimization may be possible in the search for stable yttria colloids that will serve as precursors for YSZ aerogel synthesis. Furthermore, the use of ethanol as the solvent for yttria colloids, coupled with ultrasonication, offers promise based upon the small particle size and visually stable colloid that could be prepared in Figure 8.7(a-b).

The Trizma® functionalization procedure was adapted from an approach developed by Niederberger *et al.* with a key difference [209–212]. In their approach, $TiCl_4$ was added to the reaction solution of benzyl alcohol and Trizma® to synthesize and functionalize the nanoparticles in a single step. Here, the nanopowder was added to the solution of benzyl alcohol and Trizma® to functionalize the pre-existing particles. There is no sign that this modification was successful in functionalizing the powder used in this work. Possible modifications that could improve chances of success are dispersing the powder via ultrasonication to expose more surface area and the exploration of other ligands that demonstrate attraction to yttria.

8.4.2 Promising future directions

Ultimately, the development of a colloidal sol-gel synthesis for YSZ aerogels is simply a means to study more fundamental questions on the relationship between structure and thermal stability in metal oxide aerogels. Exploring colloidal stability in yttria and zirconia systems is a complex, involved undertaking. The work described in this chapter points toward several promising directions for the pursuit of yttria colloidal stability. Once a stable yttria colloid is achieved, the next step will be equally as involved: combination of the yttria colloid with a zirconium alkoxide or zirconia colloid and formation of a homogenous gel that can then undergo supercritical drying. At this point, heat treatments and characterization of the structural evolution can commence to understand the structural effects of precursor and synthetic route on the thermal stability of YSZ aerogels.

The directions that deserve more attention are ultrasonication of fine yttria powders in either citric acid solutions in DI water or ethanol. For citric acid, the particle size and stability achieved with 1.305 mM citric acid may prove adequate to pursue combination of this colloid with a zirconia precursor for sol-gel synthesis. If smaller particle size and improved colloidal stability is desired, there exists opportunities to explore the effects of citric acid concentration, sodium citrate concentration, and temperature on colloid properties and gelation characteristics. Furthermore, most work has focused on 1 wt.% solids yttria colloids. This is not adequate for sol-gel synthesis of monolithic materials and was selected to minimize waste of expensive powders during the exploration of stabilization techniques. The solids loading of the colloid will need to be increased to 10 to 20 wt.% and the stability at these loadings will need reassessed.

The use of ethanol is promising for two reasons. One, the particle size achieved simply with ultrasonication was promisingly small. Two, when considering the sol-gel syntheses the colloid will ultimately be employed in, the zirconium alkoxides are extremely water reactive. If zirconium alkoxide is chosen as the zirconia precursor, the combination of these alkoxides with a water-based yttria colloid will result in immediate precipitation of zirconia species and completely preclude the formation of a homogeneous gel. The use of ethanol, and perhaps other alcohols, as the solvent for the yttria will avoid this issue and allow the colloid and zirconium alkoxide to be combined while avoiding the hydrolysis and self-condensation of zirconium alkoxide.

There are two additional routes that are of interest but were not explored due to time constraints. One, the use of yttrium oxyhydroxide (YOOH) powders, analogous to the boehmite (AlOOH) powder used in the work by Hurwitz *et al.* [50,70,71], may prove interesting as a yttria precursor, as well as other rare earth oxyhydroxides for doping zirconia [216,217]. The additional hydroxyl content of such materials should provide higher hydrophilicity or more sites for functionalization or chelation with a stabilizing group. Preliminary work on converting metal hydroxide powders into metal oxyhydroxides via heat treatment and analysis with XRD was conducted but not yet with success.

Two, work by Cheng *et al*. prepared yttria aerogels from yttria nanosheets synthesized under a procedure similar to the Trizma® functionalization approach attempted in this work [212]. The yttria nanosheets are prepared from anhydrous yttrium(III) chloride in benzyl alcohol with octylamine as the stabilizing ligand. The equipment required for the synthesis precluded its study in this work, but further exploration of such systems is of interest in the quest for studying the effect of precursors and sol-gel techniques on aerogel thermal stability.

8.5 Colloidal synthesis in the alumina-zirconia system

8.5.1 Results from preliminary syntheses

The colloidal stability of P2W (boehmite, AlOOH) in water was studied with Zetasizer measurements. The powder was dispersed in DI water and then sonicated in a water bath for 20 minutes. The particle size distribution and zeta potential distribution are shown in Figure 8.9(a-b). The material exhibits excellent colloidal stability in water. The average particle size was 40 nm with a PDI of 0.292. The average zeta potential was +53 mV. The colloid visually appeared stable for several weeks with no sign of settling.

Using the parameters based on previous work by NASA collaborators and those found in literature, test syntheses were performed for Al colloid and Zr alkoxide from a P2W colloid and zirconium(IV) butoxide [50,193]. Eleven unique sets of synthetic parameters and synthesis methods were attempted as included in Table 8.1. Variables included (1) zirconium butoxide with and without small amounts of water, (2) P2W in water, ethanol, or water-ethanol mixture, (3) addition of acetylacetone at one or two times the molar amount of Zr, (4) loading of zirconium butoxide in ethanol ranging from 0.5 to 1.263 mmol Zr / mL ethanol, and (5) dropwise or rapid addition of P2W colloid to zirconium butoxide. The zirconium butoxide is very reactive with water and this poses an issue with the P2W, as it is only dispersible in water. Attempts to add acetylacetone did reduce the reactivity of the zirconium butoxide, but still did not result in the formation of a monolithic gel. In test mixes that included acetylacetone, gels did form, but all were jelly-like and not monolithic. A test synthesis was also performed for the Al colloid and Zr salt from a P2W colloid and zirconyl chloride octahydrate. The acidity of the Zr salt solution did lead to gelation of the colloid, but this occurred rapidly and similarly resulted in the formation of a very weak gel that was not monolithic.

8.5.2 Future directions for alumina-zirconia sol-gel syntheses

The use of alumina-zirconia as a material system for exploring the effects of precursor and sol-gel route on structure and the effects of structure on thermal stability offers great promise. A suite of unique precursors is available for both alumina and zirconia, spanning alkoxides, salts, and colloidally stable nanopowders. There is also a stronger base of literature on which to build new sol-gel syntheses. This is advantageous as it is not the goal of this segment of work to necessarily develop new sol-gel syntheses. Rather, the understanding of effects of precursor and how the precursor is assembled into the aerogel structure on thermal stability *is* the goal. Therefore, readily available precursors and syntheses are beneficial in achieving this aim. To reiterate, there are four syntheses of interest for tackling this question: zirconium salt and aluminum salt, zirconium salt and aluminum colloid, zirconium alkoxide and aluminum colloid, and zirconium alkoxide and aluminum alkoxide. The colloids may be oxides, oxyhydroxides, or hydroxides of the metal. This suite of materials will provide an array of structures to study thermal stability.

Alumina-zirconia sol-gel syntheses were only briefly attempted in this work. The preliminary work that was conducted offers a few lessons learned for future directions. First, this work will benefit from an extensive literature review on alumina, zirconia, and alumina-zirconia sol-gel syntheses. Second, the high reactivity of zirconium alkoxides with water must be overcome. Two potential routes are the use of alumina and/or boehmite colloids without water, such as alcohol-based colloids, or the modulation of zirconium alkoxide reactivity with the choice of alcohol or chelation agents such as acetylacetone [187,188,218,219]. The use of acetylacetone in preliminary work in the aluminum colloid and zirconium alkoxide system proved effective in reducing precipitation and encouraging gelation. Further optimization of synthetic parameters, including concentration of precursors in solvent, amount of water, and amount of acetylacetone, is required to form a monolithic gel from this approach. The other three approaches will require similar optimization which may be informed and quickened by a literature review.

8.6 Summary

An improvement in thermal stability from colloidal precursors for aluminosilicate aerogels has been previously identified, though this system has several complicating factors that convolute the effect of precursor and synthetic route [50,166,174,190–193]. This work sought to answer the question of how unique structural motifs, and the way these motifs are assembled, influence thermal stability. The yttria-stabilized zirconia (YSZ) system was selected to develop a colloidal synthesis to compare against the salt-derived synthesis used throughout this work. To this end, the colloidal stability of yttria was studied with various acids and dispersion methods, including ultrasonication and colloidal ball milling. Improving the notoriously low colloidal stability of yttria proved a challenge, though promising routes are low concentrations of citric acid, which serve as both an electrostatic and steric stabilizer, and the use of ethanol as the solvent, both used in conjunction with ultrasonication. Future work involves the combination of an yttria colloid with a zirconium precursor, such as an alkoxide, to form a homogenous YSZ aerogel.

Though a facile colloidal precursor was not produced, for the final step of condensation of the colloid and/or metal alkoxide into a gel, previous work on sol-gel zirconia will be informative for such efforts [218–227]. Care must be taken to avoid condensation with atmospheric moisture and modifications may have to be made to adapt inclusion of the crystallite precursor. The acid or base content of the colloidal precursor suspension could be employed as a catalyst for the gelation of the zirconium alkoxide. To avoid issues with atmospheric moisture, the use of a glove box may prove necessary to provide an inert, dry environment for the alkoxide.

Given the difficulties faced in the development of a colloidal synthesis for YSZ, attention was turned to the alumina-zirconia system. The literature base and suite of precursors available for this system offer an advantage in achieving the goals of this work in revealing important design considerations based on precursor and synthesis for thermally stable aerogels. Four unique synthetic routes have been proposed and future work encompasses the development of these syntheses, production of four unique aerogels, and study of their structure and evolution after thermal exposure. Detailed characterization of the starting structure and careful evaluation of thermal stability offer the opportunity to understand how structural motifs and their assembly inform structural evolution and thermal stability,

8.7 Figures and tables

Table 8.1: Sample specifications for exploration of a Alumina-zirconia synthesis from P2W bohemite (AlOOH) colloid and zirconium(IV) butoxide.

	A			B				A + B	
Sample	**P2W (g)**	**H_2O (mL)**	**EtOH (mL)**	**EtOH (mL)**	**Zr but. (g)**	**H_2O (mL)**	**AcAc (g)**	**Addition Method**	**H_2O (mL)**
12_03-T1	0.5683	2.278	0	10.0	1.5145	0.086	0	F	0
12_03-T2	0.5683	2.278	0	0	1.5145	0	0	F	0
12_03-T4	0.5683	0	2.880	7.120	1.5145	0	0	D	0.228
12_03-T5	0.5683	2.278	0	10.0	1.5145	0	0	D	0
12_03-T6	0.5683	2.278	5.0	5.0	1.5145	0	0	D	0
12_03-T7	0.5683	2.278	0	10.0	1.5145	0	0.3153	D	0
12_03-T8	0.5683	2.278	0	21.1	1.5145	0	0	D	0
12_03-T9	0.5683	2.278	0	15.0	1.5145	0	0.3153	D	0
12_03-T10	0.5683	2.278	0	15.0	1.5145	0	0.6306	D	0
12_03-T11	0.5683	0	0	15.0	1.5145	0	0.3153	D	0.228

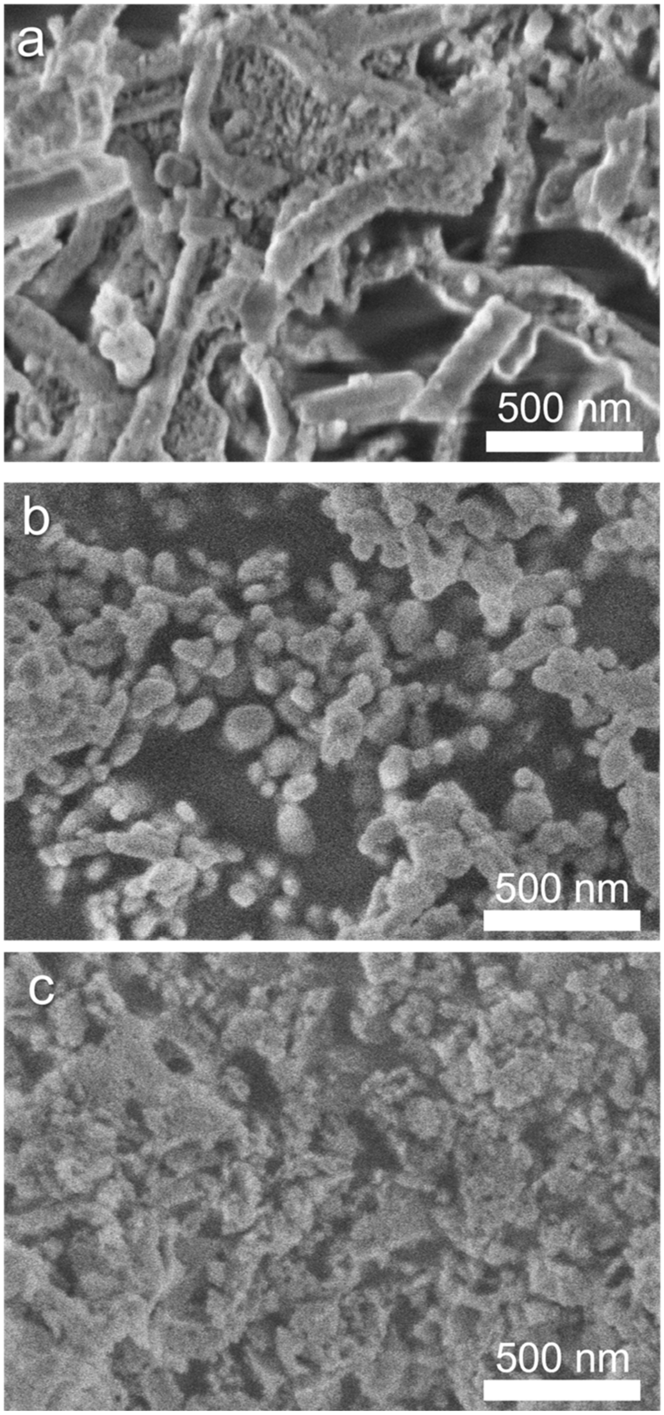

Figure 8.1: SEM images for (a) Y2O3_NP1, (b) Y2O3_NP2, and (c) Y2O3_NP3. The manufacturer specified particle sizes were 20-40 nm, 50-70 nm, and 25-50 nm, respectively. Y2O3_NP1 has many fibrous particles. Y2O3_NP2 shows the best combination of small particle size and low agglomeration.

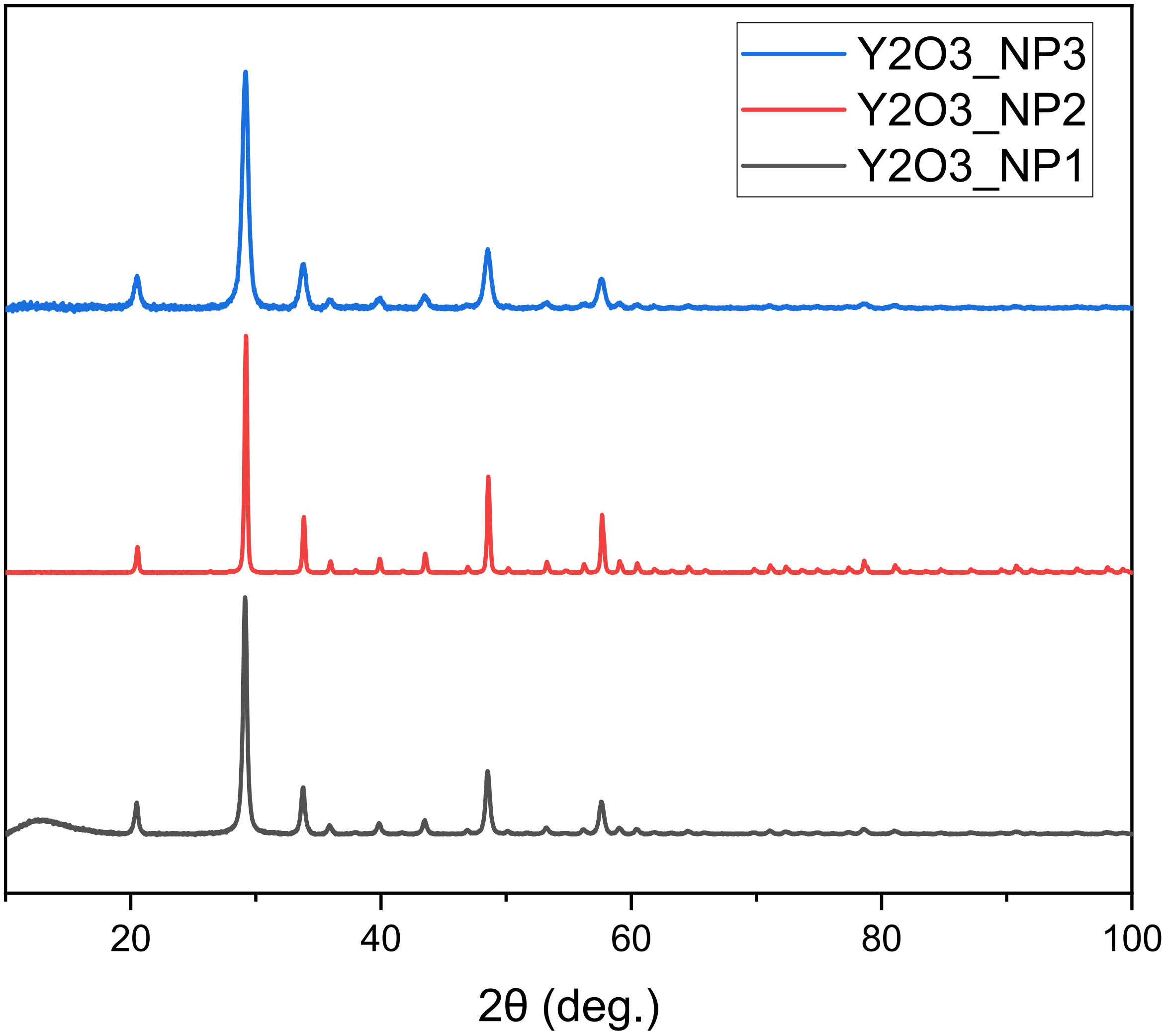

Figure 8.2: XRD patterns for yttria nanopowders. All were identified as the cubic phase. Y2O3_NP1 has some amorphous content, indicated by the broad hump under 20 deg. 2θ. Crystallite size is smallest in Y2O3_NP3, indicated by the broad peaks.

Table 8.2: Data collected for stability of Y2O3_NP1 and ZrOH4_NP1 in citric acid (CA), acetic acid (AA), and nitric acid (NA). The zeta potential (ζ), z-average particle size (z-avg), and polydispersity index (PDI) for particle size are included. All values are the average of three measurements.

Powder	Acid	ζ (mV)	z-avg (nm)	PDI
Y2O3_NP1	-	15.2	807	0.393
Y2O3_NP1	0.11 mM CA	31.1	1446	0.379
Y2O3_NP1	145 mM CA	-3.8	1711	0.228
Y2O3_NP1	5800 mM AA	0	79	0.136
Y2O3_NP1	10 mM NA	16.3	3844	1.000
ZrOH4_NP1	145 mM CA	-21.8	994	0.787
ZrOH4_NP1	5800 mM AA	9.4	1236	0.538
ZrOH4_NP1	10 mM NA	32.8	720	0.563

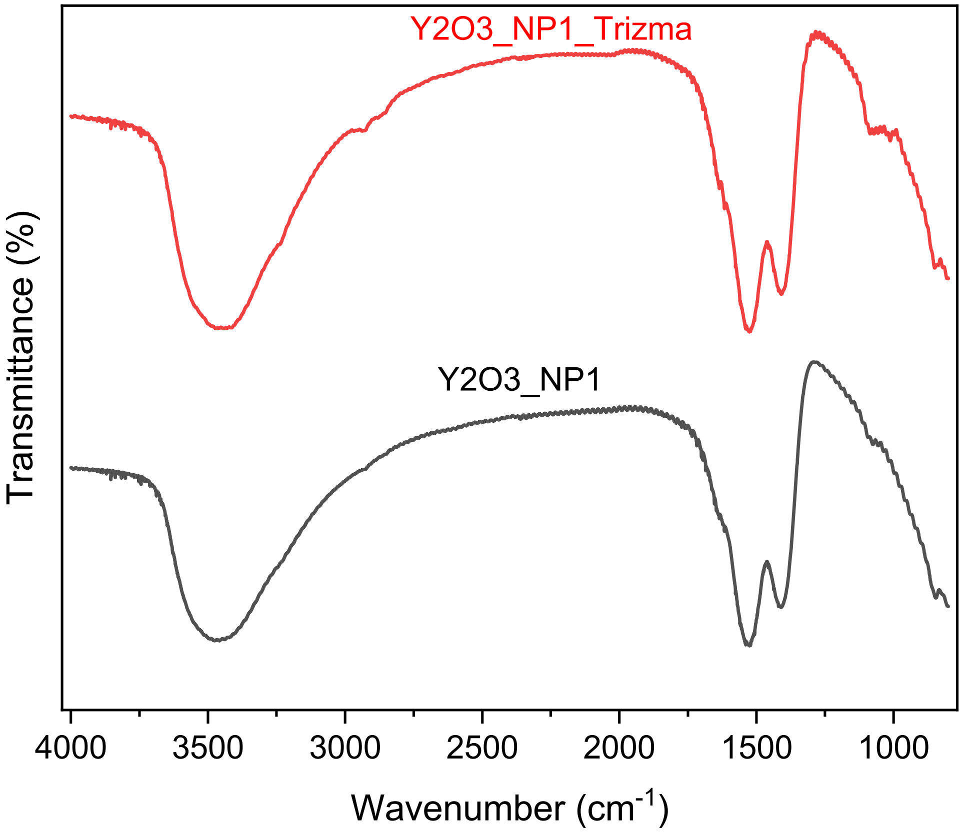

Figure 8.3: FTIR transmittance spectra for Y2O3_NP1 (bottom) and Y2O3_NP1 after attempted functionalization with Trizma® (top). There are no major differences between the patterns, though there is a discernable difference at 1120 to 980 cm^{-1} which could be indicative of C-N, though it also exists in the original nanopowder.

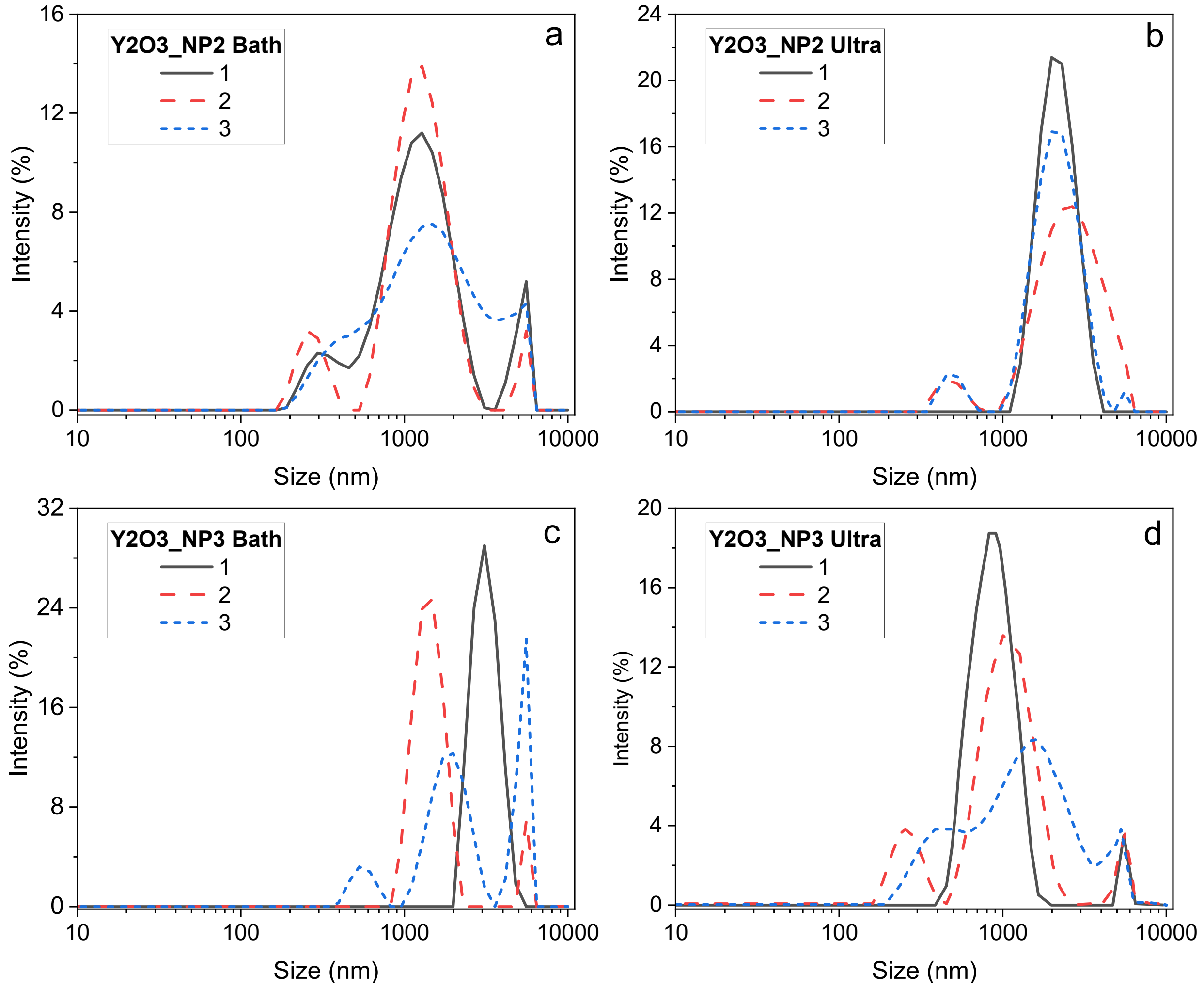

Figure 8.4(a-d): Particle size distributions (Malvern Zetasizer Nano) for Y2O3_NP2 after (a) 20 minutes of bath sonication and (b) 5 minutes of ultrasonication and Y2O3_NP3 after (c) 20 minutes of bath sonication and (d) 5 minutes of ultrasonication. Ultrasonication did not significantly improve colloidal stability for either powder.

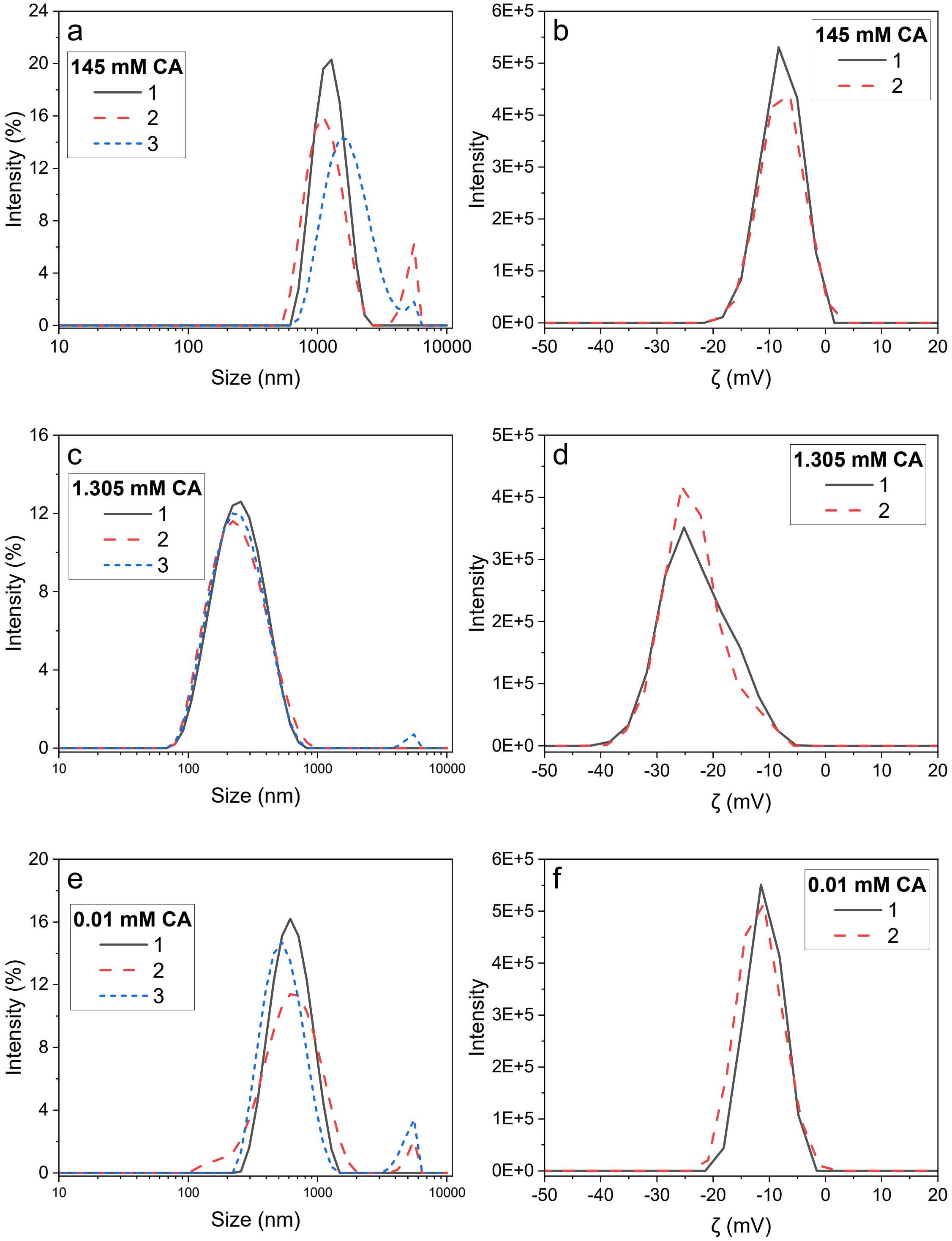

Figure 8.5(a-f): Particle size and zeta potential distributions (Malvern Zetasizer Nano) for Y2O3_NP2 ultrasonicated in a solution of (a, b) 145 mM CA, (c, d) 1.305 mM CA, or (e, f) 0.01 mM CA. 1.305 mM CA exhibited the highest colloidal stability, with the lowest average particle size (225 nm) and stable size distributions over the course of three measurements. The zeta potential distribution shifts to lower values for 1.305 mM CA and is very similar for both 145 and 0.01 mM CA.

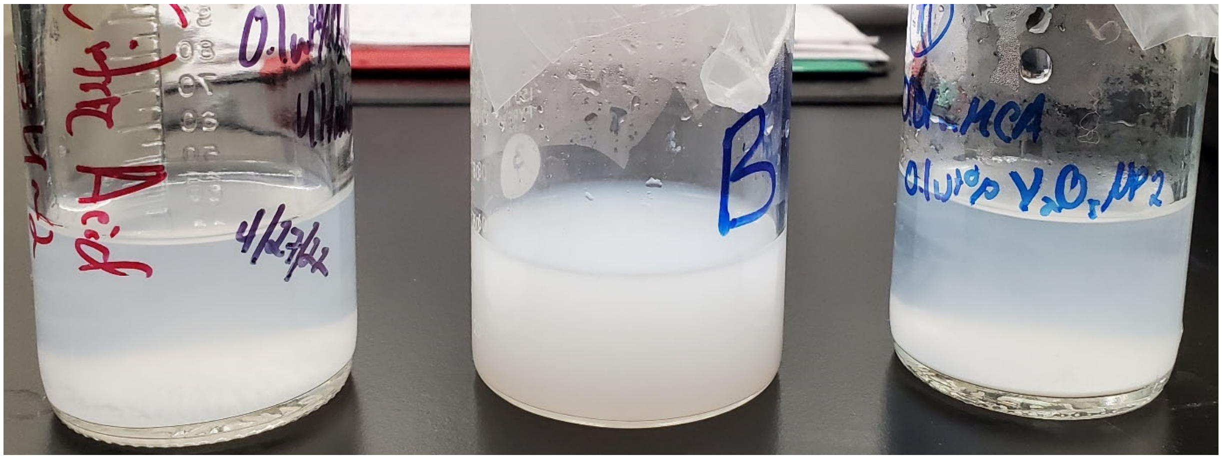

Figure 8.6: 0.1 wt.% Y2O3_NP2 in citric acid solutions, from left to right, of 145 mM, 1.305 mM, and 0.01 mM citric acid (CA). The images were taken 1 hour after ultrasonication of the colloid. After 10 minutes, 145 mM and 0.01 mM CA displayed significant settling and low stability. 1.305 mM CA showed stability and no signs of settling for over an hour.

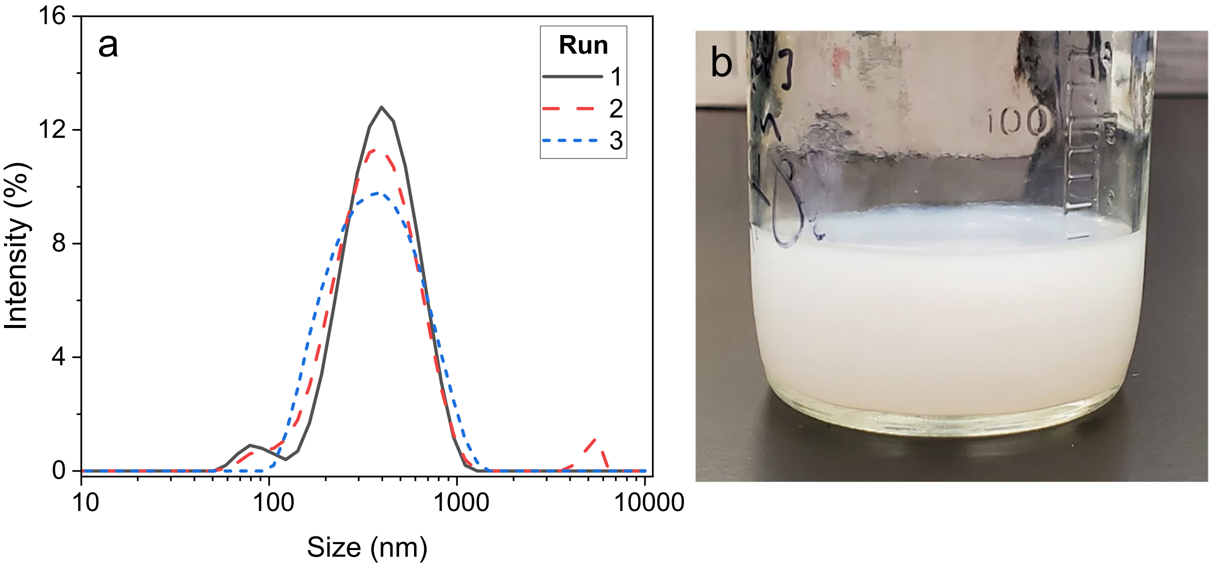

Figure 8.7(a-b): Y2O3_NP2 was dispersed in 200 proof ethanol with ultrasonication for 5 min. The average particle size was 340 nm with relatively low polydispersity seen in the size distribution in (a). After 40 minutes, the colloid, as depicted in (b), showed no sign of settling or destabilization.

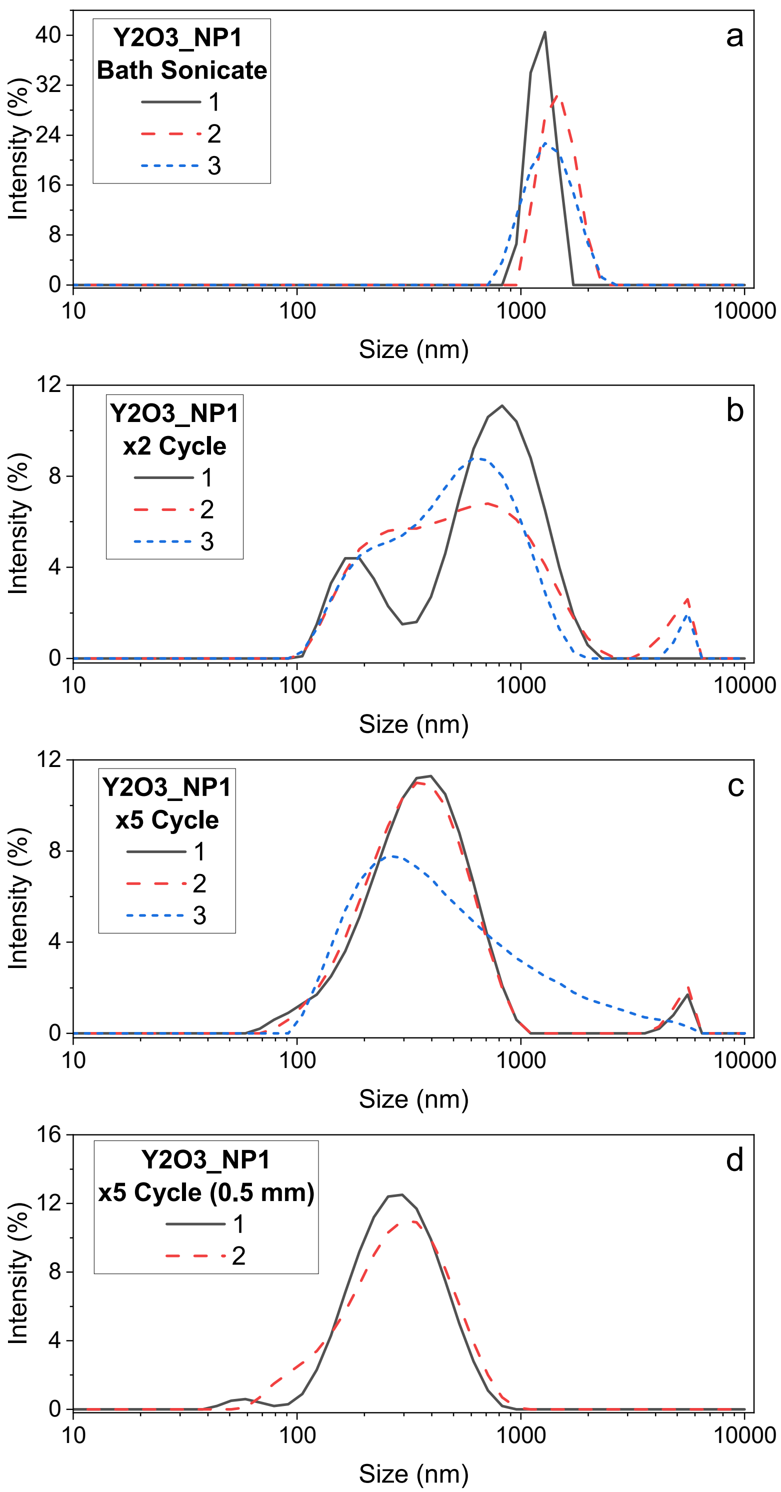

Figure 8.8(a-d): Particle size distributions for Y2O3_NP1 after (a) 20 minutes of bath sonication, (b) two cycles of colloidal ball milling, (c) five cycles, and (d) five cycles with 0.5 mm milling media. Colloidal ball milling reduced particle size and broadened the particle size distribution in all cases. Increased number of cycles reduced particle size further. Reducing the size of milling media from 3.0 to 0.5 mm diameter also reduced particle size.

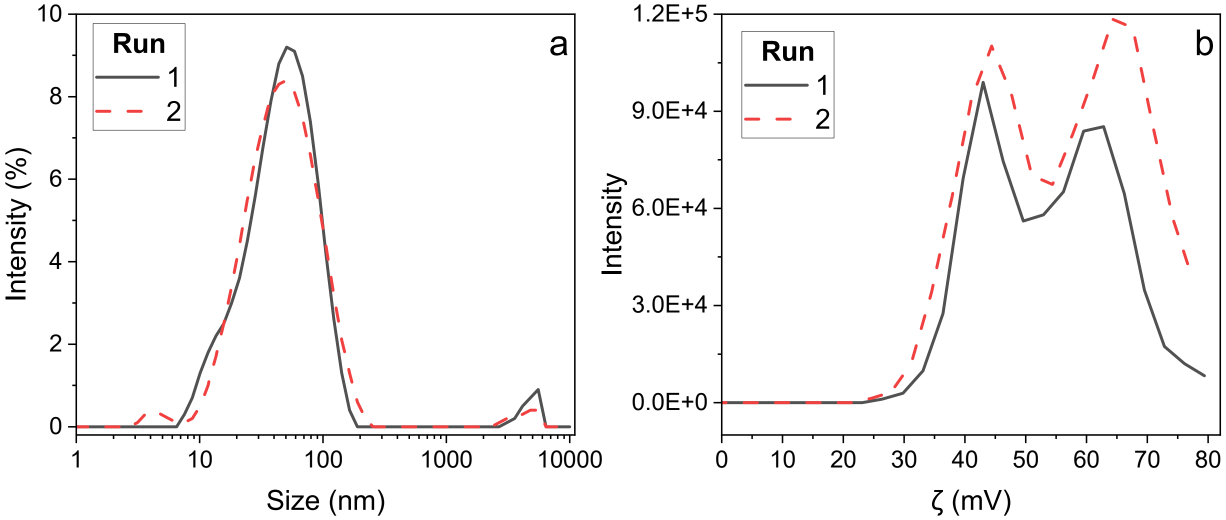

Figure 8.9(a-b): Boehmite powder (Sasol P2W) was dispersed in water with 20 minutes of bath sonication. The (a) particle size distribution is narrow (PDI = 0.292) with average particle size of 40 nm. The (b) zeta potential for the material is very high with an average of 53 mV. This material demonstrates excellent colloidal stability.

CHAPTER 9: SUMMARY AND FUTURE DIRECTIONS

A significant challenge in the field of aerospace materials is the development of lightweight, highly insulating materials that can maintain high performance in extreme environments. Materials with reduced thermal conductivity permit higher operating temperatures and improved insulative performance. Reduced weight mitigates cost and improves payload capacity. A promising class of lightweight, low thermal conductivity materials are aerogels. Aerogels are highly porous, extremely lightweight (densities can be under 0.05 g/cm^3), and display extraordinarily low thermal conductivity (as low as 0.009 W/(m•K) in atmosphere and 0.003 W/(m•K) under vacuum) [3]. The overarching goal of this work is to develop a framework to select compositions and synthetic routes for porous materials with improved thermal stability for use as insulation in aerospace applications.

9.1 Summary of key findings

9.1.1 Improving thermal stability via doped zirconia

Our work demonstrated an improvement in thermal stability of YSZ aerogels with increased yttria content. As measured with nitrogen physisorption, mesoporosity was maintained to 1200 °C for 30 and 50 mol% $YO_{1.5}$, whereas it was eliminated in 0 and 15 mol% $YO_{1.5}$. Increased yttria content was also found to suppress crystallite growth to 1200 °C according to Scherrer analysis of x-ray diffraction data. Inspection of the morphology via SEM corroborated the quantitative techniques in establishing the improved thermal stability of high yttria concentration YSZ aerogels.

These improvements in thermal stability are hypothesized to be the result of favorable tuning of kinetic and thermodynamic parameters. From a thermodynamic perspective, a reduction in specific surface energy with increased yttria content in YSZ has been measured previously

[104]. By reducing surface energy, the driving force for sintering and densification is likewise reduced. From a kinetic perspective, a reduction in cation diffusivity with increased yttria content has been measured previously [105–107]. By reducing cation diffusivity, transport processes that contribute to densification and crystallite growth are slowed. High yttria concentration in YSZ reduces mass transport rates and improves thermodynamic stability, contributing to an aerogel with improved thermal stability. This is an important first step in development of a design framework for thermally stable aerogels to be used as insulation in extreme environments.

The work on composition was expanded to a broader range of dopants, including Y, Yb, Gd, Ce, and Ca at 15 and 30 mol% M/(M+Zr). Differences in performance as a function of composition were observed. 30 mol% Gd and Y maintained the highest SSA and V_{BJH} at 1200 °C. Relative stability, quantified with the percent change of a given property over a temperature range, was introduced as a metric to compare aerogel thermal stability. This served as a useful means of comparing performance when studying a greater number of unique materials. This analysis revealed increased dopant concentration improved thermal stability for all dopants studied. Attempts to derive relationships between thermal stability and weighted cation properties (charge, mass, size) were largely unsuccessful, with only a few statistically significant relationships. A more complete and coherent set of material properties, such as surface energy, cation diffusivity, and more, was deemed necessary as it would lend additional factors to leverage in understanding differences in evolution and thermal stability as a function of composition.

9.1.2 Quantifying the effect of synthetic parameters on structure & stability

A study on the synthetic parameters of water content and solids loading sought to establish additional parameters as effective means of tuning and improving aerogel thermal stability. A full 3^2 factorial set of samples were prepared. Ultimately, large variations were observed in as dried structure properties, but heat treatment to 1000 °C revealed minimal changes in thermal stability. Though the parameters had no effect themselves, this study served as a sort of control for the studies on composition summarized above. Changing dopant identity and concentration modified the starting structure of the aerogel, with increased dopant concentration typically leading to coarser structures. In the work on synthetic parameters, it was established that the changes to the starting structure observed in the composition work would have no measurable effect on thermal stability. Therefore, the changes in thermal stability are in fact the result of changing composition and not changes to the starting structure.

9.1.3 New synthetic routes to thermally stable aerogels

Procedures to post-synthetically coat metal oxide layers on aerogels were adapted from literature [140]. Coatings of silica, zirconia, titania, alumina, and boehmite were applied to thermally stable YSZ compositions developed by this project. The silica-coated 30YSZ aerogels were characterized extensively to elucidate the structure of the material and understand differences in thermal stability between coated and uncoated variants. Silica coatings vastly improved thermal stability to 1000 °C, thought to be the result of grain boundary pinning to reduce crystallite growth, reduced surface energy, and a starting structure composed of larger primary particles and reinforced connections. Beyond 1000 °C, the silica coated materials exhibited very poor thermal stability, hypothesized to result from viscous sintering of the silica beyond 1100 °C. Silica viscous sintering fills mesopores and enhances particle rearrangement and subsequent densification.

Another aim of this project was to compare the effects of structural motif and motif assembly on aerogel thermal stability, ultimately developing links between the starting structure derived from different precursors and the thermal stability of the material. The YSZ system was selected, as it showed promising thermal stability in previous work and eliminated complications present in the aluminosilicate system previously studied in the field. The YSZ system required the development of a colloidal synthesis route. The colloidal stability of yttria was studied as a first step for the new synthesis. Significant challenges were faced given the poor colloidal stability of yttria. The use of citric acid in water as an electrostatic and steric stabilizer as well as the use of ethanol as the solvent for the colloid, both methods coupled with ultrasonication, presented promising results for improving yttria colloidal stability by reducing particle size and increasing settling time.

9.2 Unanswered questions & promising future directions

9.2.1 Composition and aerogel thermal stability

The work described in this thesis has identified several interesting routes for future study in the quest for thermally stable aerogels and a design framework for their development. Through identification of novel materials that demonstrate improved thermal stability, their structure and evolution can be carefully analyzed to understand the fundamental mechanisms that govern their unique stability. Outstanding questions related to these aims and suggested directions to answer the questions are included below.

In the study of dopants in zirconia, differences in behavior were observed as a function of composition. The lack of material property data for the compositions studied impeded the analysis of property – thermal stability relationships for aerogels. Such relationships are critical in developing a design framework for thermally stable metal oxide aerogels. The data collected here on structural evolution of ten unique compositions offers a starting point of identification of these relationships. The missing piece is a material property database, including properties such as surface energy and cation diffusivity, posited to be important in the work on YSZ aerogels, and other properties not yet identified as important. To this end, the study of material properties should be conducted via methods such as water adsorption microcalorimetry and other calorimetric techniques for surface energy [228–230], *in situ* TEM-based single grain boundary creep experiments for grain boundary and surface diffusivity [231], or simulation-based techniques [118,142,232–234]. Once collected, these material properties can be used as dependent variables in statistical analysis of thermal stability of the ten materials prepared here. The takeaways from the statistical analysis can be used to inform the choice of the next generation of doped metal oxide aerogels to synthesize and study.

An alternative approach is to inverse the order of investigation. First, compositions of metal oxide aerogels can be identified that have well-characterized properties, including surface energy, cation diffusivity, thermal conductivity, and more. The compositions of interest will also need to have metal salts available. With these two requirements met, a set of aerogels can be synthesized for these compositions. Their structures can be characterized, and thermal stabilities measured. Then, given the full set of material property data, structure-thermal stability relationships can be tested via statistical methods.

9.2.2 Coatings & colloidal syntheses for metal oxide aerogels

The exploration of new synthetic routes presents an expansive and diverse design space for thermally stably aerogels. This work focused on two possible routes: the use of post-synthetic coatings and the use of colloidal syntheses. The excellent stability of silica-coated YSZ aerogels was demonstrated to 1000 °C, but rapid destabilization beyond this temperature points towards a need to study non-densifying coatings beyond 1000 °C. A strong rationale for the improvement in thermal stability that results from silica coatings is also missing and may be identified through detailed characterization using methods such as TEM and XPS to reveal the distribution and bonding behavior of silica and YSZ throughout the material's evolution.

Coatings of alumina, zirconia, titania, and other metal oxides beyond silica may serve to enhance thermal stability to temperatures beyond 1000 °C by avoiding the viscous sintering experienced with silica coatings. The reactivity of metal alkoxides, apart from those of silicon, must be modulated to effectively coat the YSZ aerogels. The use of chelation agents or alternative solvents may be useful routes to reduce metal alkoxide reactivity. Furthermore, the parameters used in the coating solution must also be optimized, including amount of water, solvent, and modifier per amount of alkoxide. Once YSZ aerogels are prepared with non-densifying coatings, their structure and evolution at high temperatures must be characterized.

Synthesis of aerogels of the same composition, but from different precursors, will provide the basis for study of the connections between structural motifs, the assembly of the motifs, and evolution of the structure at high temperatures. There are two material systems proposed for such a study: yttria-stabilized zirconia or alumina-zirconia. Both systems require a colloidal synthesis which uses one or more precursors in a colloidal form to compare against the salt-derived synthesis used throughout this work. The colloid must be composed of particles on the order of 100 nm or smaller to achieve the mesoporous, high specific surface area structure of an aerogel. For YSZ, additional work is required in achieving a high solids content colloid of yttria with adequate stability. Further study of ethanol as solvent or citric acid in water, both in conjunction with ultrasonication, is warranted given promising initial results for these approaches. With citric acid, citric acid content and the use of sodium citrate both offer parameters to tune yttria colloidal stability. For alumina-zirconia, precursors have been identified, including colloidal precursors for alumina in the form of boehmite. Work should focus on how to integrate these precursors into facile syntheses of mesoporous aerogels. Regardless of whether YSZ or alumina-zirconia aerogels are prepared, the structure and evolution of the colloid-derived and salt-derived aerogel will provide substantial evidence to leverage in understanding the thermal stability of aerogels considering choice of synthetic route and precursor.

9.2.3 Application of thermally stable aerogels in composites for thermal protection systems

In context of all the aims of this work and future directions, the fact remains that aerogels are extremely fragile because of their highly porous structure, but can be reinforced with a variety of weaves, felts, and papers in composite materials. The most promising aerogel formulations should be incorporated into composites and characterized for use in aerospace applications such as thermal protection systems, thermal barriers, and thermoelectric generators. An understanding of how the reinforcement phase (weaves, felts, papers) impact the as dried structure and microstructural evolution will be obtained through characterization of the composites following supercritical drying and thermal exposure. Inspection of the composite morphology with SEM should be conducted and compared to the structure of the aerogel prepared without the reinforcement phase. The gelation and supercritical drying stages may be impacted by the presence of fibers from the reinforcement phase. Furthermore, the structural evolution of the aerogel pore structure upon thermal exposure may follow a different path because of the reinforcement phase. Optimally, this phase would combat shrinkage and densification by acting as a mechanical support for the aerogel. The insulative performance of the overall composite will also be characterized, including the thermal conductivity, gas permeability, and thermal stability of the aerogel composite compared to the reinforcement phase alone.

REFERENCES

[1] Roberts, T. G. *Space Launch to Low Earth Orbit: How Much Does It Cost?* Center for Strategic and International Studies, 2022.

[2] Gordon, M. P. Space Shuttle Orbiter Thermal Protection System Processing Assessment. NASA, May, 1995.

[3] Pierre, A. C., and Pajonk, G. M. “Chemistry of Aerogels and Their Applications.” *Chemical Reviews*, Vol. 102, No. 11, 2002, pp. 4243–4265. https://doi.org/10.1021/cr0101306.

[4] Snapp, C., and Rodriguez, A. Orbiter Thermal Protection System Lessons Learned. Presented at the AIAA SPACE 2011 Conference & Exposition, Long Beach, California, 2011.

[5] Launius, R. D., Krige, J., and Craig, J. I. *Space Shuttle Legacy: How We Did It and What We Learned*. American Institute of Aeronautics and Astronautics, Inc., Reston, VA, 2013.

[6] Chapline, G., Rodriguez, A., Snapp, C., Pessin, M., Bauer, P., Steinetz, B., and Stevenson, C. Thermal Protection Systems. In *Wings in Orbit*, NASA, 2011.

[7] Kistler, S. S. “Coherent Expanded Aerogels and Jellies.” *Nature*, Vol. 127, No. 3211, 1931, p. 741.

[8] Ayers, M. Part 4: The Early Days of Aerogels. Aerogel.org, May, 2000.

[9] Teichner, S. J., and Nicolaon, Gilbert A. Method of Preparing Inorganic Aerogels, 3,672,833Jun 27, 1972.

[10] Steiner, S. The 1980’s: Aerogel Gets Going. Aerogel.org, , 1999.

[11] Tewari, P. H., Hunt, A. J., and Lofftus, K. D. “Ambient-Temperature Supercritical Drying of Transparent Silica Aerogels.” *Materials Letters*, Vol. 3, Nos. 9–10, 1985, pp. 363–367. https://doi.org/10.1016/0167-577X(85)90077-1.

[12] Fricke, J. The Unbeatable Lightness of Aerogels: Take 10 Parts of Metal Oxide, 90 Parts of Air, Mix Well - and Watch Industry Fall upon the Product with Glee. New Scientist, Jan 30, 1993.

[13] Burnett, D. S. “NASA Returns Rocks from a Comet.” *Science*, Vol. 314, No. 5806, 2006, pp. 1709–1710. https://doi.org/10.1126/science.1137084.

[14] Alemán, J. V., Chadwick, A. V., He, J., Hess, M., Horie, K., Jones, R. G., Kratochvíl, P., Meisel, I., Mita, I., Moad, G., Penczek, S., and Stepto, R. F. T. “Definitions of Terms Relating to the Structure and Processing of Sols, Gels, Networks, and Inorganic-Organic

Hybrid Materials (IUPAC Recommendations 2007).” *Pure and Applied Chemistry*, Vol. 79, No. 10, 2007, pp. 1801–1829. https://doi.org/10.1351/pac200779101801.

[15] Schneider, M., and Baiker, A. “Aerogels in Catalysis.” *Catalysis Reviews*, Vol. 37, No. 4, 1995, pp. 515–556. https://doi.org/10.1080/01614949508006450.

[16] Aegerter, M., Leventis, N., and Koebel, M. *Aerogels Handbook (Advances in Sol-Gel Derived Materials and Technologies)*. 2011.

[17] Jullien, R., Olivi-Train, N., Hasmy, A., Woignier, T., Phalippou, J., Bourret, D., and Sempéré, R. “Scaling Theory and Numerical Simulations of Aerogel Sintering.” *Journal of Non-Crystalline Solids*, Vol. 188, Nos. 1–2, 1995, pp. 1–10. https://doi.org/10.1016/0022-3093(95)00023-2.

[18] Olivi-Tran, N., and Jullien, R. “Numerical Simulations of Aerogel Sintering.” *Physical Review B*, Vol. 52, No. 1, 1995, pp. 258–267. https://doi.org/10.1103/PhysRevB.52.258.

[19] Sempéré, R., Bourret, D., Woignier, T., Phalippou, J., and Jullien, R. “Scaling Approach to Sintering of Fractal Matter.” *Physical Review Letters*, Vol. 71, No. 20, 1993, pp. 3307–3310. https://doi.org/10.1103/PhysRevLett.71.3307.

[20] Yang, G., and Biswas, P. “Computer Simulation of the Aggregation and Sintering Restructuring of Fractal-like Clusters Containing Limited Numbers of Primary Particles.” *Journal of Colloid and Interface Science*, Vol. 211, No. 1, 1999, pp. 142–150. https://doi.org/10.1006/jcis.1998.5995.

[21] de la Rosa-Fox, N., Gago-Duport, L., and Esquivias, L. “Aggregation Process in Silica Aerogels on Sintering.” *Journal of Non-Crystalline Solids*, Vols. 192–193, 1995, pp. 534–538. https://doi.org/10.1016/0022-3093(95)00479-3.

[22] Yang, M. Y., Tang, G. H., Sheng, Q., Guo, L., and Zhang, H. “Atomic-Level Sintering Mechanism of Silica Aerogels at High Temperatures: Structure Evolution and Solid Thermal Conductivity.” *International Journal of Heat and Mass Transfer*, Vol. 199, 2022, p. 123456. https://doi.org/10.1016/j.ijheatmasstransfer.2022.123456.

[23] Emmerling, A., Gross, J., Gerlach, R., Goswin, R., Reichenauer, G., Fricke, J., and Haubold, H. G. “Isothermal Sintering of SiO2-Aerogels.” *Journal of Non-Crystalline Solids*, Vol. 125, No. 3, 1990, pp. 230–243. https://doi.org/10.1016/0022-3093(90)90853-E.

[24] Saliger, R., Heinrich, T., Gleissner, T., and Fricke, J. “Sintering Behaviour of Alumina-Modified Silica Aerogels.” *Journal of Non-Crystalline Solids*, Vol. 186, 1995, pp. 113–117. https://doi.org/10.1016/0022-3093(95)00080-1.

[25] Scherer, G. W., Calas, S., and Sempéré, R. “Densification Kinetics and Structural Evolution during Sintering of Silica Aerogel.” *Journal of Non-Crystalline Solids*, Vol. 240, Nos. 1–3, 1998, pp. 118–130. https://doi.org/10.1016/S0022-3093(98)00696-6.

[26] Huang, D., Guo, C., Zhang, M., and Shi, L. “Characteristics of Nanoporous Silica Aerogel under High Temperature from 950 °C to 1200 °C.” *Materials & Design*, Vol. 129, 2017, pp. 82–90. https://doi.org/10.1016/j.matdes.2017.05.024.

[27] Boukenter, A., Champagnon, D., Dumas, J., Duval, E., Quinson, J. F., Rousset, J. L., Serughetti, J., Etienne, S. ., and Mai, C. “A SAXS Study of Silica Aerogels.” *Le Journal de Physique Colloques*, Vol. 24, No. C4, 1989, pp. C4-133-C4-136. https://doi.org/10.1051/jphyscol:1989420.

[28] Emmerling, A., and Fricke, J. “Small Angle Scattering and the Structure of Aerogels.” *Journal of Non-Crystalline Solids*, Vol. 145, 1992, pp. 113–120. https://doi.org/10.1016/S0022-3093(05)80439-9.

[29] Emmerling, A., Petricevic, R., Beck, A., Wang, P., Scheller, H., and Fricke, J. “Relationship between Optical Transparency and Nanostructural Features of Silica Aerogels.” *Journal of Non-Crystalline Solids*, Vol. 185, No. 3, 1995, pp. 240–248. https://doi.org/10.1016/0022-3093(95)00021-6.

[30] Blacher, S., Tihon, P., Pirard, R., Pirard, J. P., Diez, B., Sobry, R., Van den Bosshe, G., Brouers, F., and Sahouli, B. Texture Characterization of SiO2ZrO2 Aerogels by SAXS, Image Analysis of TEM, and N2 Adsorptiondesorption. Presented at the X-Ray Investigations of Polymer Structures, Bielsko-Biala, Poland, 1997.

[31] Barnardo, T., Hoydalsvik, K., Winter, R., Martin, C. M., and Clark, G. F. “In Situ Double Anomalous Small-Angle X-Ray Scattering of the Sintering and Calcination of Sol-Gel Prepared Yttria-Stabilized-Zirconia Ceramics.” *Journal of Physical Chemistry C*, Vol. 113, No. 23, 2009, pp. 10021–10028. https://doi.org/10.1021/jp9012202.

[32] Fenech, J., Viazzi, C., Bonino, J. P., Ansart, F., and Barnabé, A. “Morphology and Structure of YSZ Powders: Comparison between Xerogel and Aerogel.” *Ceramics International*, Vol. 35, No. 8, 2009, pp. 3427–3433. https://doi.org/10.1016/j.ceramint.2009.06.014.

[33] Scherdel, C., and Reichenauer, G. “The Impact of Residual Adsorbate on the Characterization of Microporous Carbons with Small Angle Scattering.” *Carbon*, Vol. 50, No. 8, 2012, pp. 3074–3082. https://doi.org/10.1016/j.carbon.2012.02.093.

[34] Iswar, S., Malfait, W. J., Balog, S., Winnefeld, F., Lattuada, M., and Koebel, M. M. “Effect of Aging on Silica Aerogel Properties.” *Microporous and Mesoporous Materials*, Vol. 241, 2017, pp. 293–302. https://doi.org/10.1016/j.micromeso.2016.11.037.

[35] Zhao, L., Wang, S., Wang, Y., and Li, Z. “Thermal Stability of Anatase TiO2 Aerogels.” *Surface and Interface Analysis*, Vol. 49, No. 3, 2017, pp. 173–176. https://doi.org/10.1002/sia.6103.

[36] Scherdel, C., Miller, E., Reichenauer, G., and Schmitt, J. “Advances in the Development of Sol-Gel Materials Combining Small-Angle X-Ray Scattering (SAXS) and Machine

Learning (ML).” *Processes*, Vol. 9, No. 4, 2021, p. 672. https://doi.org/10.3390/pr9040672.

[37] Castro, R. H. R., and Gouvêa, D. “Sintering and Nanostability: The Thermodynamic Perspective.” *Journal of the American Ceramic Society*, Vol. 99, No. 4, 2016, pp. 1105–1121. https://doi.org/10.1111/jace.14176.

[38] Nafsin, N., Aguiar, J. A., Aoki, T., Thron, A. M., van Benthem, K., and Castro, R. H. R. “Thermodynamics versus Kinetics of Grain Growth Control in Nanocrystalline Zirconia.” *Acta Materialia*, Vol. 136, 2017, pp. 224–234. https://doi.org/10.1016/j.actamat.2017.07.005.

[39] Li, H., Dey, S., and Castro, R. H. R. “Kinetics and Thermodynamics of Densification and Grain Growth: Insights from Lanthanum Doped Zirconia.” *Acta Materialia*, Vol. 150, 2018, pp. 394–402. https://doi.org/10.1016/j.actamat.2018.03.033.

[40] Castro, R. H. R. “On the Thermodynamic Stability of Nanocrystalline Ceramics.” *Materials Letters*, Vol. 96, 2013, pp. 45–56. https://doi.org/10.1016/j.matlet.2013.01.007.

[41] Cao, G. *Nanostructures and Nanomaterials: Synthesis, Properties and Applications*. Imperial College Press, 2004.

[42] Rahaman, M. N. *Ceramic Processing*. CRC Press, Boca Raton, FL, 2017.

[43] Lee, J. K., and Gould, G. “Polyolefin-Based Aerogels.” *NASA Tech*, No. November 2012, 2012, p. 14.

[44] Kim, J., Kwon, J., Kim, S. I., Kim, M., Lee, D., Lee, S., Kim, G., Lee, J., and Han, H. “One-Step Synthesis of Nano-Porous Monolithic Polyimide Aerogel.” *Microporous and Mesoporous Materials*, Vol. 234, 2016, pp. 35–42. https://doi.org/10.1016/j.micromeso.2016.06.037.

[45] Folgar, C., Folz, D., Suchicital, C., and Clark, D. “Microstructural Evolution in Silica Aerogel.” *Journal of Non-Crystalline Solids*, Vol. 353, 2007, pp. 1483–1490. https://doi.org/10.1016/j.jnoncrysol.2007.02.047.

[46] Hench, L. L., and West, J. K. “The Sol-Gel Process.” *Chemical Reviews*, Vol. 90, No. 1, 1990, pp. 33–72. https://doi.org/10.1021/cr00099a003.

[47] Suh, D. J., and Park, T. J. “Sol-Gel Strategies for Pore Size Control of High-Surface-Area Transition-Metal Oxide Aerogels.” *Chemistry of Materials*, Vol. 8, No. 2, 1996, pp. 509–513. https://doi.org/10.1021/cm950407g.

[48] Clapsaddle, B. J., Neumann, B., Wittstock, A., Sprehn, D. W., Gash, A. E., Satcher, J. H., Simpson, R. L., and Bäumer, M. “A Sol-Gel Methodology for the Preparation of Lanthanide-Oxide Aerogels: Preparation and Characterization.” *Journal of Sol-Gel Science and Technology*, Vol. 64, No. 2, 2012, pp. 381–389. https://doi.org/10.1007/s10971-012-2868-6.

[49] Al-Yassir, N., and Le Van Mao, R. "Thermal Stability of Alumina Aerogel Doped with Yttrium Oxide, Used as a Catalyst Support for the Thermocatalytic Cracking (TCC) Process: An Investigation of Its Textural and Structural Properties." *Applied Catalysis A: General*, Vol. 317, No. 2, 2007, pp. 275–283. https://doi.org/10.1016/j.apcata.2006.10.030.

[50] Hurwitz, F. I., Gallagher, M., Olin, T. C., Shave, M. K., Ittes, M. A., Olafson, K. N., Fields, M. G., Guo, H., and Rogers, R. B. "Optimization of Alumina and Aluminosilicate Aerogel Structure for High-Temperature Performance." *International Journal of Applied Glass Science*, Vol. 5, No. 3, 2014, pp. 276–286. https://doi.org/10.1111/ijag.12070.

[51] Hurwitz, F. I., Rogers, R. B., Guo, H., Yu, K., Domanowski, J., Schmid, E., and Fields, M. G. "The Role of Phase Changes in Maintaining Pore Structure on Thermal Exposure of Aluminosilicate Aerogels." *MRS Communications*, Vol. 7, No. 3, 2017, pp. 642–650. https://doi.org/10.1557/mrc.2017.89.

[52] Stöber, W., Fink, A., and Bohn, E. "Controlled Growth of Monodisperse Silica Spheres in the Micron Size Range." *Journal of Colloid and Interface Science*, Vol. 26, No. 1, 1968, pp. 62–69. https://doi.org/10.1016/0021-9797(68)90272-5.

[53] Danks, A. E., Hall, S. R., and Schnepp, Z. "The Evolution of 'sol-Gel' Chemistry as a Technique for Materials Synthesis." *Materials Horizons*, Vol. 3, No. 2, 2016, pp. 91–112. https://doi.org/10.1039/c5mh00260e.

[54] Levy, D., and Zayat, M. *The Sol-Gel Handbook*. John Wiley & Sons, 2015.

[55] Brinker, C. J., and Scherer, G. W. *Sol-Gel Science : The Physics and Chemistry of Sol-Gel Processing*. 1990.

[56] Heinrich, T., Klett, U., and Fricke, J. "Aerogels-Nanoporous Materials Part I: Sol-Gel Process and Drying of Gels." *Journal of Porous Materials*, Vol. 1, No. 1, 1995, pp. 7–17. https://doi.org/10.1007/BF00486520.

[57] Wang, B., Zhang, W., Zhang, W., Mujumdar, A. S., and Huang, L. "Progress in Drying Technology for Nanomaterials." *Drying Technology*, Vol. 23, Nos. 1–2, 2005, pp. 7–32. https://doi.org/10.1081/DRT-200047900.

[58] Prakash, S. S., Brinker, C. J., Hurd, A. J., and Rao, S. M. "Silica Aerogel Films Prepared at Ambient Pressure by Using Surface Derivatization to Induce Reversible Drying Shrinkage." *Nature*, Vol. 374, No. 6521, 1995, pp. 439–443. https://doi.org/10.1038/374439a0.

[59] Gash, A. E., Tillotson, T. M., Satcher, J. H., Hrubesh, L. W., and Simpson, R. L. "New Sol-Gel Synthetic Route to Transition and Main-Group Metal Oxide Aerogels Using Inorganic Salt Precursors." *Journal of Non-Crystalline Solids*, Vol. 285, Nos. 1–3, 2001, pp. 22–28. https://doi.org/10.1016/S0022-3093(01)00427-6.

[60] Clapsaddle, B. J., Sprehn, D. W., Gash, A. E., Satcher, J. H., Simpson, R. L., Jr, J. H. S., and Simpson, R. L. "A Versatile Sol-Gel Synthesis Route to Metal-Silicon Mixed Oxide Nanocomposites That Contain Metal Oxides as the Major Phase." *Journal of Non-Crystalline Solids*, Vol. 350, 2004, pp. 173–181. https://doi.org/10.1016/j.jnoncrysol.2004.06.025.

[61] Chervin, C. N., Clapsaddle, B. J., Chiu, H. W., Gash, A. E., Satcher, J. H., and Kauzlarich, S. M. "Aerogel Synthesis of Yttria-Stabilized Zirconia by a Non-Alkoxide Sol-Gel Route." *Chemistry of Materials*, Vol. 17, No. 13, 2005, pp. 3345–3351. https://doi.org/10.1021/cm0503679.

[62] Gash, A. E., Tillotson, T. M., Satcher, J. H., Poco, J. F., Hrubesh, L. W., and Simpson, R. L. "Use of Epoxides in the Sol-Gel Synthesis of Porous Iron(III) Oxide Monoliths from Fe(III) Salts." *Chemistry of Materials*, Vol. 13, No. 3, 2001, pp. 999–1007. https://doi.org/10.1021/cm0007611.

[63] Vaqueiro, P., and López-Quintela, M. A. "Influence of Complexing Agents and PH on Yttrium-Iron Garnet Synthesized by the Sol-Gel Method." *Chemistry of Materials*, Vol. 9, No. 12, 1997, pp. 2836–2841. https://doi.org/10.1021/cm970165f.

[64] Hwang, B. J., Santhanam, R., and Liu, D. G. Characterization of Nanoparticles of LiMn2O4 Synthesized by Citric Acid Sol-Gel Method. No. 97–98, 2001, pp. 443–446.

[65] Zhang, Z., Gao, Q., Liu, Y., Zhou, C., Zhi, M., Hong, Z., Zhang, F., and Liu, B. "A Facile Citric Acid Assisted Sol-Gel Method for Preparing Monolithic Yttria-Stabilized Zirconia Aerogel." *RSC Advances*, Vol. 5, No. 102, 2015, pp. 84280–84283. https://doi.org/10.1039/c5ra13999f.

[66] Anilkumar, G. M., Mukundan, P., and Warrier, K. G. K. "Low-Temperature Mullitization in Boehmite-Tetraethoxysilane Gel Precursor Containing γ-Alumina and Mullite Nucleating Seeds." *Chemistry of Materials*, Vol. 10, No. 8, 1998, pp. 2217–2220. https://doi.org/10.1021/cm980149y.

[67] Partlow, D. P., and Yoldas, B. E. "COLLOIDAL VERSUS POLYMER GELS AND MONOLITHIC TRANSFORMATION IN GLASS-FORMING SYSTEMS." *Journal of Non-Crystalline Solids*, Vol. 46, 1981, pp. 153–161.

[68] Aravind, P. R., Mukundan, P., Krishna Pillai, P., and Warrier, K. G. K. "Mesoporous Silica-Alumina Aerogels with High Thermal Pore Stability through Hybrid Sol-Gel Route Followed by Subcritical Drying." *Microporous and Mesoporous Materials*, Vol. 96, Nos. 1–3, 2006, pp. 14–20. https://doi.org/10.1016/j.micromeso.2006.06.014.

[69] Matter, F., Luna, A. L., and Niederberger, M. "From Colloidal Dispersions to Aerogels: How to Master Nanoparticle Gelation." *Nano Today*, Vol. 30, 2020, p. 100827. https://doi.org/10.1016/j.nantod.2019.100827.

[70] Hurwitz, F. I., Guo, H., Sheets, E. J., Miller, D. R., and Newlin, K. N. Tailoring of Boehmite-Derived Aluminosilicate Aerogel Structure and Properties: Influence of Ti Addition. In *Materials Research Society Symposium 2011*, No. 1306, 2011, pp. 1–6.

[71] Hurwitz, F. I., Guo, H., Rogers, R. B., Sheets, E. J., Miller, D. R., Newlin, K. N., Shave, M. K., Palczer, A. R., and Cox, M. T. "Influence of Ti Addition on Boehmite-Derived Aluminum Silicate Aerogels: Structure and Properties." *Journal of Sol-Gel Science and Technology*, Vol. 64, No. 2, 2012, pp. 367–374. https://doi.org/10.1007/s10971-012-2866-8.

[72] Rahaman, M. N. *Ceramic Processing and Sintering*. CRC Press, New York, USA, 2003.

[73] Brunauer, S., Emmett, P. H., and Teller, E. "Adsorption of Gases in Multimolecular Layers." *Journal of the American Chemical Society*, Vol. 60, No. 2, 1938, pp. 309–319. https://doi.org/10.1021/ja01269a023.

[74] Barrett, E. P., Joyner, L. G., and Halenda, P. P. "The Determination of Pore Volume and Area Distributions in Porous Substances. 1. Computations from Nitrogen Isotherms." *Journal of the American Chemical Society*, Vol. 73, No. 1, 1951, pp. 373–380.

[75] Thommes, M., Kaneko, K., Neimark, A. V., Olivier, J. P., Rodriguez-Reinoso, F., Rouquerol, J., and Sing, K. S. W. "Physisorption of Gases, with Special Reference to the Evaluation of Surface Area and Pore Size Distribution (IUPAC Technical Report)." *Pure and Applied Chemistry*, Vol. 87, Nos. 9–10, 2015, pp. 1051–1069. https://doi.org/10.1515/pac-2014-1117.

[76] Bardestani, R., Patience, G. S., and Kaliaguine, S. "Experimental Methods in Chemical Engineering: Specific Surface Area and Pore Size Distribution Measurements—BET, BJH, and DFT." *Canadian Journal of Chemical Engineering*, Vol. 97, No. 11, 2019, pp. 2781–2791. https://doi.org/10.1002/cjce.23632.

[77] Juhász, L., Moldován, K., Gurikov, P., Liebner, F., Fábián, I., Kalmár, J., and Cserháti, C. "False Morphology of Aerogels Caused by Gold Coating for SEM Imaging." 2021, pp. 1–12.

[78] Garvie, R. C. "The Occurrence of Metastable Tetragonal Zirconia as a Crystallite Size Effect." *Journal of Physical Chemistry*, Vol. 69, No. 4, 1965, pp. 1238–1243. https://doi.org/10.1021/j100888a024.

[79] Rabiei, M., Palevicius, A., Monshi, A., Nasiri, S., Vilkauskas, A., and Janusas, G. "Comparing Methods for Calculating Nano Crystal Size of Natural Hydroxyapatite Using X-Ray Diffraction." *Nanomaterials*, Vol. 10, No. 9, 2020, pp. 1–21. https://doi.org/10.3390/nano10091627.

[80] Rietveld, H. M. "A Profile Refinement Method for Nuclear and Magnetic Structures." *Journal of Applied Crystallography*, Vol. 2, No. 2, 1969, pp. 65–71. https://doi.org/10.1107/S0021889869006558.

[81] Toby, B. H., and Von Dreele, R. B. "GSAS-II: The Genesis of a Modern Open-Source All Purpose Crystallography Software Package." *Journal of Applied Crystallography*, Vol. 46, No. 2, 2013, pp. 544–549. https://doi.org/10.1107/S0021889813003531.

[82] Bredol, M., and Micior, J. "Preparation and Characterization of Nanodispersions of Yttria, Yttrium Aluminium Garnet and Lutetium Aluminium Garnet." *Journal of Colloid and Interface Science*, Vol. 402, 2013, pp. 27–33. https://doi.org/10.1016/j.jcis.2013.03.060.

[83] Fabrichnaya, O., and Aldinger, F. "Assessment of Thermodynamic Parameters in the System ZrO2-Y2O3-Al2O3." *Zeitschrift für Metallkunde*, Vol. 95, No. 1, 2004, pp. 27–39. https://doi.org/10.3139/146.017909.

[84] Zhu, D., and Miller, R. A. Thermal Conductivity and Sintering Behavior of Advanced Thermal Barrier Coatings. 2002.

[85] Azzopardi, A., Mévrel, R., Saint-Ramond, B., Olson, E., and Stiller, K. "Influence of Aging on Structure and Thermal Conductivity of Y-PSZ and Y-FSZ EB-PVD Coatings." *Surface and Coatings Technology*, Vols. 177–178, 2004, pp. 131–139. https://doi.org/10.1016/j.surfcoat.2003.08.073.

[86] Brandon, J. R., and Taylor, R. "Phase Stability of Zirconia-Based Thermal Barrier Coatings Part I. Zirconia-Yttria Alloys." *Surface and Coatings Technology*, Vol. 46, No. 1, 1991, pp. 75–90. https://doi.org/10.1016/0257-8972(91)90151-L.

[87] Lima, R. S. S., and Marple, B. R. R. "Nanostructured YSZ Thermal Barrier Coatings Engineered to Counteract Sintering Effects." *Materials Science and Engineering A*, Vol. 485, Nos. 1–2, 2008, pp. 182–193. https://doi.org/10.1016/j.msea.2007.07.082.

[88] Winter, M. R., and Clarke, D. R. "Oxide Materials with Low Thermal Conductivity." *Journal of the American Ceramic Society*, Vol. 90, No. 2, 2007, pp. 533–540. https://doi.org/10.1111/j.1551-2916.2006.01410.x.

[89] Winter, M. R., and Clarke, D. R. "Thermal Conductivity of Yttria-Stabilized Zirconia-Hafnia Solid Solutions." *Acta Materialia*, Vol. 54, No. 19, 2006, pp. 5051–5059. https://doi.org/10.1016/j.actamat.2006.06.038.

[90] Clarke, D. R. "Materials Selection Guidelines for Low Thermal Conductivity Thermal Barrier Coatings Temperature Dependence of Thermal Conductivity Models for Thermal Conductivity." *Surface and Coatings Technology*, Vols. 163–164, 2003, pp. 67–74. https://doi.org/dx.doi.org/doi:10.1016/S0257-8972(02)00593-5.

[91] Clarke, D. R., and Levi, C. G. "Materials Design for the Next Generation Thermal Barrier Coatings." *Annual Review of Materials Research*, Vol. 33, No. 1, 2003, pp. 383–417. https://doi.org/10.1146/annurev.matsci.33.011403.113718.

[92] Kakuda, T. R., Limarga, A. M., Bennett, T. D., and Clarke, D. R. "Evolution of Thermal Properties of EB-PVD 7YSZ Thermal Barrier Coatings with Thermal Cycling." *Acta*

Materialia, Vol. 57, No. 8, 2009, pp. 2583–2591. https://doi.org/10.1016/j.actamat.2009.02.019.

[93] Limarga, A. M., Shian, S., Baram, M., and Clarke, D. R. “Effect of High-Temperature Aging on the Thermal Conductivity of Nanocrystalline Tetragonal Yttria-Stabilized Zirconia.” *Acta Materialia*, Vol. 60, No. 15, 2012, pp. 5417–5424. https://doi.org/10.1016/j.actamat.2012.06.054.

[94] Bisson, J.-F., Fournier, D., Poulain, M., Lavigne, O., and Mévrel, R. “Thermal Conductivity of Yttria-Zirconia Single Crystals, Determined with Spatially Resolved Infrared Thermography.” *Journal of the American Ceramic Society*, Vol. 83, No. 8, 2004, pp. 1993–1998. https://doi.org/10.1111/j.1151-2916.2000.tb01502.x.

[95] Rumble, J. R., Ed. *CRC Handbook of Chemistry and Physics*. Taylor & Francis, Boca Raton, FL, 2020.

[96] Hostaša, J., Pabst, W., and Matějíček, J. “Thermal Conductivity of Al2O3-ZrO2 Composite Ceramics.” *Journal of the American Ceramic Society*, Vol. 94, No. 12, 2011, pp. 4404–4409. https://doi.org/10.1111/j.1551-2916.2011.04875.x.

[97] Schlichting, K. W., Padture, N. P., and Klemens, P. G. “Thermal Conductivity of Dense and Porous Yttria-Stabilized Zirconia.” *Journal of Materials Science*, Vol. 36, No. 12, 2001, pp. 3003–3010. https://doi.org/10.1023/A:1017970924312.

[98] Živcová, Z., Gregorová, E., Pabst, W., Smith, D. S., Michot, A., and Poulier, C. “Thermal Conductivity of Porous Alumina Ceramics Prepared Using Starch as a Pore-Forming Agent.” *Journal of the European Ceramic Society*, Vol. 29, No. 3, 2009, pp. 347–353. https://doi.org/10.1016/j.jeurceramsoc.2008.06.018.

[99] Raghavan, S., Wang, H., Dinwiddie, R. B., Porter, W. D., and Mayo, M. J. “The Effect of Grain Size, Porosity and Yttria Content on the Thermal Conductivity of Nanocrystalline Zirconia.” *Scripta Materialia*, Vol. 39, No. 8, 1998, pp. 1119–1125. https://doi.org/10.1016/S1359-6462(98)00290-5.

[100] Chervin, C. N., Clapsaddle, B. J., Chiu, H. W., Gash, A. E., Satcher, J. H., and Kauzlarich, S. M. “Role of Cyclic Ether and Solvent in a Non-Alkoxide Sol-Gel Synthesis of Yttria-Stabilized Zirconia Nanoparticles.” *Chemistry of Materials*, Vol. 18, No. 20, 2006, pp. 4865–4874. https://doi.org/10.1021/cm061258c.

[101] Chao, X., Yuan, W., Shi, Q., and Zhu, Z. “Improvement of Thermal Stability of Zirconia Aerogel by Addition of Yttrium.” *Journal of Sol-Gel Science and Technology*, Vol. 80, No. 3, 2016, pp. 667–674. https://doi.org/10.1007/s10971-016-4158-1.

[102] Zhao, Z., Chen, D., and Jiao, X. “Zirconia Aerogels with High Surface Area Derived from Sols Prepared by Electrolyzing Zirconium Oxychloride Solution: Comparison of Aerogels Prepared by Freeze-Drying and Supercritical CO2(l) Extraction.” *Journal of Physical Chemistry C*, Vol. 111, No. 50, 2007, pp. 18738–18743. https://doi.org/10.1021/jp075150b.

[103] Hurwitz, F. I., Rogers, R. B., Guo, H., Garg, A., Olson, N. S., Phan, D., and Cashman, J. L. “Phase Development and Pore Stability of Yttria- and Ytterbia-Stabilized Zirconia Aerogels.” *Journal of the American Ceramic Society*, Vol. 103, No. 12, 2020, pp. 6700–6711. https://doi.org/10.1111/jace.17376.

[104] Drazin, J. W., and Castro, R. H. R. “Phase Stability in Nanocrystals: A Predictive Diagram for Yttria-Zirconia.” *Journal of the American Ceramic Society*, Vol. 98, No. 4, 2015, pp. 1377–1384. https://doi.org/10.1111/jace.13504.

[105] Kilo, M., Taylor, M. A., Argirusis, C., Borchardt, G., Lesage, B., Weber, S., Scherrer, S., Scherrer, H., Schroeder, M., and Martin, M. “Cation Self-Diffusion of 44Ca, 88Y, and 96Zr in Single-Crystalline Calcia- and Yttria-Doped Zirconia.” *Journal of Applied Physics*, Vol. 94, No. 12, 2003, pp. 7547–7552. https://doi.org/10.1063/1.1628379.

[106] Kilo, M., Borchardt, G., Lesage, B., Katasov, O., Weber, S., and Scherrer, S. “Cation Transport in Yttria Stabilized Cubic Zirconia: 96Zr Tracer Diffusion in (ZrxY1-x)O2-x/2 Single Crystals with 0.15≤x≤0.48.” *Journal of the European Ceramic Society*, Vol. 20, No. 12, 2000, pp. 2069–2077. https://doi.org/10.1016/S0955-2219(00)00072-8.

[107] Kilo, M., Borchardt, G., Lesage, B., Weber, S., Scherrer, S., Schroeder, M., and Martin, M. “Y and Zr Tracer Diffusion in Yttria-Stabilized Zirconia at Temperatures between 1250 K and 2000 K.” *Key Engineering Materials*, Vols. 206–213, No. I, 2001, pp. 601–604. https://doi.org/10.4028/www.scientific.net/kem.206-213.601.

[108] Shi, J. L., Lin, Z. X., and Yen, T. S. “Effect of Dopants on the Crystallite Growth of Superfine Zirconia Powder.” *Journal of the European Ceramic Society*, Vol. 8, No. 2, 1991, pp. 117–122. https://doi.org/10.1016/0955-2219(91)90117-I.

[109] Shi, J. L., Ruan, M. L., and Yen, T. S. “Crystallite Growth in Yttria-Doped Superfine Zirconia Powders and Their Compacts: A Comparison between Y-TZP and YSZ.” *Ceramics International*, Vol. 22, No. 2, 1996, pp. 137–142. https://doi.org/10.1016/0272-8842(95)00069-0.

[110] Matsui, K., Yoshida, H., and Ikuhara, Y. “Grain-Boundary Structure and Microstructure Development Mechanism in 2-8 Mol% Yttria-Stabilized Zirconia Polycrystals.” *Acta Materialia*, Vol. 56, No. 6, 2008, pp. 1315–1325. https://doi.org/10.1016/j.actamat.2007.11.026.

[111] Scherer, G. W. “Theory of Drying.” *Journal of the American Ceramic Society*, Vol. 73, No. 1, 1990, pp. 3–14. https://doi.org/10.1111/j.1151-2916.1990.tb05082.x.

[112] Schindelin, J., Arganda-Carreras, I., Frise, E., Kaynig, V., Longair, M., Pietzsch, T., Preibisch, S., Rueden, C., Saalfeld, S., Schmid, B., Tinevez, J. Y., White, D. J., Hartenstein, V., Eliceiri, K., Tomancak, P., and Cardona, A. “Fiji: An Open-Source Platform for Biological-Image Analysis.” *Nature Methods*, Vol. 9, No. 7, 2012, pp. 676–682. https://doi.org/10.1038/nmeth.2019.

[113] Arganda-Carreras, I., Kaynig, V., Rueden, C., Eliceiri, K. W., Schindelin, J., Cardona, A., and Seung, H. S. “Trainable Weka Segmentation: A Machine Learning Tool for Microscopy Pixel Classification.” *Bioinformatics*, Vol. 33, No. 15, 2017, pp. 2424–2426. https://doi.org/10.1093/bioinformatics/btx180.

[114] Krogstad, J. A., Lepple, M., Gao, Y., Lipkin, D. M., and Levi, C. G. “Effect of Yttria Content on the Zirconia Unit Cell Parameters.” *Journal of the American Ceramic Society*, Vol. 94, No. 12, 2011, pp. 4548–4555. https://doi.org/10.1111/j.1551-2916.2011.04862.x.

[115] Baes, C. F., and Mesmer, R. E. *The Hydrolysis of Cations*. Wiley, 1976.

[116] Shannon, R. D. “Revised Effective Ionic Radii and Systematic Studies of Interatomic Distances in Halides and Chalcogenides.” *Acta Crystallographica Section A*, Vol. 32, No. 5, 1976, pp. 751–767. https://doi.org/10.1107/S0567739476001551.

[117] Huang, D., Venkatachari, K. R., and Stangle, G. C. “Influence of Yttria Content on the Preparation of Nanocrystalline Yttria-Doped Zirconia.” *Journal of Materials Research*, Vol. 10, No. 3, 1995, pp. 762–773. https://doi.org/10.1557/JMR.1995.0762.

[118] González-Romero, R. L., Meléndez, J. J., Gómez-García, D., Cumbrera, F. L., and Domínguez-Rodríguez, A. “A Molecular Dynamics Study of Grain Boundaries in YSZ: Structure, Energetics and Diffusion of Oxygen.” *Solid State Ionics*, Vol. 219, 2012, pp. 1–10. https://doi.org/10.1016/j.ssi.2012.05.004.

[119] Chen, I.-W. “Mobility Control of Ceramic Grain Boundaries and Interfaces.” *Materials Science and Engineering: A*, Vol. 166, Nos. 1–2, 1993, pp. 51–58. https://doi.org/10.1016/0921-5093(93)90309-3.

[120] Hwang, S. -L, and Chen, I. -W. “Grain Size Control of Tetragonal Zirconia Polycrystals Using the Space Charge Concept.” *Journal of the American Ceramic Society*, Vol. 73, No. 11, 1990, pp. 3269–3277. https://doi.org/10.1111/j.1151-2916.1990.tb06449.x.

[121] Lee, H. B., Prinz, F. B., and Cai, W. “Atomistic Simulations of Surface Segregation of Defects in Solid Oxide Electrolytes.” *Acta Materialia*, Vol. 58, No. 6, 2010, pp. 2197–2206. https://doi.org/10.1016/j.actamat.2009.12.005.

[122] Nafsin, N., and Castro, R. H. R. *Effect of Grain Boundary Segregation on the Thermodynamic Stability of Nano-Crystalline Yttria Stabilized Zirconia (YSZ)*. PhD Thesis. 2013.

[123] Mazaheri, M., Zahedi, A. M., Haghighatzadeh, M., and Sadrnezhaad, S. K. “Sintering of Titania Nanoceramic: Densification and Grain Growth.” *Ceramics International*, Vol. 35, No. 2, 2009, pp. 685–691. https://doi.org/10.1016/j.ceramint.2008.02.005.

[124] Li, J., and Ye, Y. “Densification and Grain Growth of Al2O3 Nanoceramics during Pressureless Sintering.” *Journal of the American Ceramic Society*, Vol. 89, No. 1, 2006, pp. 139–143. https://doi.org/10.1111/j.1551-2916.2005.00654.x.

[125] Coble, R. L. “Sintering Crystalline Solids. I. Intermediate and Final State Diffusion Models.” *Journal of Applied Physics*, Vol. 32, No. 5, 1961, pp. 787–792. https://doi.org/10.1063/1.1736107.

[126] Olson, N. S., Hurwitz, F. I., Guo, H., Madden, N. J., Stokes, J. L., Rogers, R. B., and Krogstad, J. A. “Enhanced Thermal Stability of High Yttria Concentration YSZ Aerogels.” *Journal of the American Ceramic Society*, No. February, 2021, pp. 1–13. https://doi.org/10.1111/jace.17792.

[127] Clarke, D. R., and Phillpot, S. R. Thermal Barrier Coating Materials. *Materials Today*. 6. Volume 8, 22–29.

[128] Levi, C. G. “Emerging Materials and Processes for Thermal Barrier Systems.” *Current Opinion in Solid State and Materials Science*, Vol. 8, No. 1, 2004, pp. 77–91. https://doi.org/10.1016/j.cossms.2004.03.009.

[129] Boulc’h, F., Dessemond, L., and Djurado, E. “Dopant Size Effect on Structural and Transport Properties of Nanometric and Single-Phased TZP.” *Solid State Ionics*, Vols. 154–155, 2002, pp. 143–150. https://doi.org/10.1016/S0167-2738(02)00422-8.

[130] Yi, H., Che, J., Liang, G., and Liu, Z. “Effect of Rare Earth Elements on Stability and Sintering Resistance of Tetragonal Zirconia for Advanced Thermal Barrier Coatings.” *Crystals*, Vol. 11, No. 287, 2021.

[131] Quach, D. V., and Castro, R. H. R. “Direct Measurement of Grain Boundary Enthalpy of Cubic Yttria-Stabilized Zirconia by Differential Scanning Calorimetry.” *Journal of Applied Physics*, Vol. 112, No. 8, 2012, pp. 3–8. https://doi.org/10.1063/1.4761992.

[132] Nafsin, N., Li, H., Leib, E. W., Vossmeyer, T., Stroeve, P., and Castro, R. H. R. “Stability of Rare-Earth-Doped Spherical Yttria-Stabilized Zirconia Synthesized by Ultrasonic Spray Pyrolysis.” *Journal of the American Ceramic Society*, Vol. 100, No. 10, 2017, pp. 4425–4434. https://doi.org/10.1111/jace.14971.

[133] Toby, B. H., and Von Dreele, R. B. “GSAS-II: The Genesis of a Modern Open-Source All Purpose Crystallography Software Package.” *Journal of Applied Crystallography*, Vol. 46, No. 2, 2013, pp. 544–549. https://doi.org/10.1107/S0021889813003531.

[134] Yashima, M., Morimoto, K., Ishizawa, N., and Yoshimura, M. “Diffusionless Tetragonal–Cubic Transformation Temperature in Zirconia–Ceria Solid Solutions.” *Journal of the American Ceramic Society*, Vol. 76, No. 11, 1993, pp. 2865–2868. https://doi.org/10.1111/j.1151-2916.1993.tb04028.x.

[135] Li, L., Van Der Biest, O., Wang, P. L., Vleugels, J., Chen, W. W., and Huang, S. G. “Estimation of the Phase Diagram for the ZrO2-Y2O3-CeO2 System.” *Journal of the European Ceramic Society*, Vol. 21, No. 16, 2001, pp. 2903–2910. https://doi.org/10.1016/S0955-2219(01)00218-7.

[136] Holzwarth, U., and Gibson, N. “The Scherrer Equation versus the ‘Debye-Scherrer Equation.’” *Nature Nanotechnology*, Vol. 6, No. 9, 2011, pp. 534–534. https://doi.org/10.1038/nnano.2011.145.

[137] Matter, F., Luna, A. L., and Niederberger, M. “From Colloidal Dispersions to Aerogels: How to Master Nanoparticle Gelation.” *Nano Today*, Vol. 30, 2020, p. 100827. https://doi.org/10.1016/j.nantod.2019.100827.

[138] Rechberger, F., and Niederberger, M. “Synthesis of Aerogels: From Molecular Routes to 3-Dimensional Nanoparticle Assembly.” *Nanoscale Horizons*, Vol. 2, No. 1, 2017, pp. 6–30. https://doi.org/10.1039/c6nh00077k.

[139] Wu, N. L., Wang, S. Y., and Rusakova, I. A. “Inhibition of Crystallite Growth in the Sol-Gel Synthesis of Nanocrystalline Metal Oxides.” *Science*, Vol. 285, No. 5432, 1999, pp. 1375–1377. https://doi.org/10.1126/science.285.5432.1375.

[140] Zu, G., Shen, J., Wang, W., Zou, L., Lian, Y., Zhang, Z., Liu, B., and Zhang, F. “Robust, Highly Thermally Stable, Core-Shell Nanostructured Metal Oxide Aerogels as High-Temperature Thermal Superinsulators, Adsorbents, and Catalysts.” *Chemistry of Materials*, Vol. 26, No. 19, 2014, pp. 5761–5772. https://doi.org/10.1021/cm502886t.

[141] Pedregosa, F., Varoquaux, G., Gramfort, A., Michel, V., Thirion, B., Grisel, O., Blondel, M., Prettenhofer, P., Weiss, R., Dubourg, V., Vanderplas, J., Passos, A., and Cournapeau, D. “Scikit-Learn: Machine Learning in Python.” *MACHINE LEARNING IN PYTHON.*

[142] Jain, A., Ong, S. P., Hautier, G., Chen, W., Richards, W. D., Dacek, S., Cholia, S., Gunter, D., Skinner, D., Ceder, G., and Persson, K. A. “Commentary: The Materials Project: A Materials Genome Approach to Accelerating Materials Innovation.” *APL Materials*, Vol. 1, No. 1, 2013, p. 011002. https://doi.org/10.1063/1.4812323.

[143] Shannon, R. D., and Prewitt, C. T. “Effective Ionic Radii in Oxides and Fluorides.” *Acta Crystallographica Section B Structural Crystallography and Crystal Chemistry*, Vol. 25, No. 5, 1969, pp. 925–946. https://doi.org/10.1107/S0567740869003220.

[144] Al-Yassir, N., and Le Van Mao, R. “Thermal Stability of Alumina Aerogel Doped with Yttrium Oxide, Used as a Catalyst Support for the Thermocatalytic Cracking (TCC) Process: An Investigation of Its Textural and Structural Properties.” *Applied Catalysis A: General*, Vol. 317, No. 2, 2007, pp. 275–283. https://doi.org/10.1016/j.apcata.2006.10.030.

[145] Stöcker, C., and Baiker, A. “Zirconia Aerogels: Effect of Acid-to-Alkoxide Ratio, Alcoholic Solvent and Supercritical Drying Method on Structural Properties.” *Journal of Non-Crystalline Solids*, Vol. 223, No. 3, 1998, pp. 165–178. https://doi.org/10.1016/S0022-3093(97)00340-2.

[146] Lebedev, A. E., Menshutina, N. V., Khudeev, I. I., and Kamyshinsky, R. A. “Investigation of Alumina Aerogel Structural Characteristics at Different «precursor-

Water-Ethanol» Ratio.” *Journal of Non-Crystalline Solids*, No. July, 2020. https://doi.org/10.1016/j.jnoncrysol.2020.120475.

[147] Clapsaddle, B. J., Sprehn, D. W., Gash, A. E., Jr, J. H. S., and Simpson, R. L. “A Versatile Sol – Gel Synthesis Route to Metal – Silicon Mixed Oxide Nanocomposites That Contain Metal Oxides as the Major Phase.” *Journal of Non-Crystalline Solids*, Vol. 350, 2004, pp. 173–181. https://doi.org/10.1016/j.jnoncrysol.2004.06.025.

[148] Brinker, C. J., and Scherer, G. W. *Sol-Gel Science : The Physics and Chemistry of Sol-Gel Processing*. 1990.

[149] Krogstad, J. A., Lepple, M., Gao, Y., Lipkin, D. M., and Levi, C. G. “Effect of Yttria Content on the Zirconia Unit Cell Parameters.” *Journal of the American Ceramic Society*, Vol. 94, No. 12, 2011, pp. 4548–4555. https://doi.org/10.1111/j.1551-2916.2011.04862.x.

[150] Franzel, L., Wingfield, C., Bertino, M. F., Mahadik-Khanolkar, S., and Leventis, N. “Regioselective Cross-Linking of Silica Aerogels with Magnesium Silicate Ceramics.” *Journal of Materials Chemistry A*, Vol. 1, No. 19, 2013, p. 6021. https://doi.org/10.1039/c3ta90165c.

[151] Sanli, D., and Erkey, C. “Monolithic Composites of Silica Aerogels by Reactive Supercritical Deposition of Hydroxy-Terminated Poly(Dimethylsiloxane).” *ACS Applied Materials & Interfaces*, Vol. 5, No. 22, 2013, pp. 11708–11717. https://doi.org/10.1021/am403200d.

[152] Randall, J. P., Meador, M. A. B., and Jana, S. C. “Tailoring Mechanical Properties of Aerogels for Aerospace Applications.” *ACS Applied Materials & Interfaces*, Vol. 3, No. 3, 2011, pp. 613–626. https://doi.org/10.1021/am200007n.

[153] Leventis, N. “Three-Dimensional Core-Shell Superstructures: Mechanically Strong Aerogels.” *Accounts of Chemical Research*, Vol. 40, No. 9, 2007, pp. 874–884. https://doi.org/10.1021/ar600033s.

[154] Leventis, N., Sotiriou-Leventis, C., Zhang, G., and Rawashdeh, A.-M. M. “Nanoengineering Strong Silica Aerogels.” *Nano Letters*, Vol. 2, No. 9, 2002, pp. 957–960. https://doi.org/10.1021/nl025690e.

[155] Mohite, D. P., Larimore, Z. J., Lu, H., Mang, J. T., Sotiriou-Leventis, C., and Leventis, N. “Monolithic Hierarchical Fractal Assemblies of Silica Nanoparticles Cross-Linked with Polynorbornene via ROMP: A Structure–Property Correlation from Molecular to Bulk through Nano.” *Chemistry of Materials*, Vol. 24, No. 17, 2012, pp. 3434–3448. https://doi.org/10.1021/cm3017648.

[156] Wu, N. L., Wang, S. Y., and Rusakova, I. A. “Inhibition of Crystallite Growth in the Sol-Gel Synthesis of Nanocrystalline Metal Oxides.” *Science*, Vol. 285, No. 5432, 1999, pp. 1375–1377. https://doi.org/10.1126/science.285.5432.1375.

[157] Wang, Q., Li, X., Fen, W., Ji, H., Sun, X., and Xiong, R. "Synthesis of Crack-Free Monolithic ZrO2 Aerogel Modified by SiO2." *Journal of Porous Materials*, Vol. 21, No. 2, 2014, pp. 127–130. https://doi.org/10.1007/s10934-013-9756-5.

[158] Ingel, R. P., and Lewis III, D. "Lattice Parameters and Density for Y2O3-Stabilized ZrO2." *Journal of the American Ceramic Society*, Vol. 69, No. 4, 1986, pp. 325–332. https://doi.org/10.1111/j.1151-2916.1986.tb04741.x.

[159] Chen, I.-W., and Wang, X.-H. "Sintering Dense Nanocrystalline Ceramics without Final-Stage Grain Growth." *Nature*, Vol. 404, 2000, pp. 168–171.

[160] Lange, F. F. "Transformation-Toughened ZrO2: Correlations between Grain Size Control and Composition in the System." *Journal of the American Ceramic Society*, Vol. 69, No. 3, 1985, pp. 240–242.

[161] De Souza, D. P. F., and De Souza, M. F. "Liquid Phase Sintering of RE2O3: YSZ Ceramics - Part I. Grain Growth and Expelling of the Grain Boundary Glass Phase." *Journal of Materials Science*, Vol. 34, No. 16, 1999, pp. 4023–4030. https://doi.org/10.1023/A:1004659832382.

[162] Clarke, D. R. "On the Equilibrium Thickness of Intergranular Glass Phases in Ceramic Materials." *Journal of the American Ceramic Society*, Vol. 70, No. 1, 1987, pp. 15–22. https://doi.org/10.1111/j.1151-2916.1987.tb04846.x.

[163] Brunauer, S., Kantro, D. L., and Weise, C. H. "THE SURFACE ENERGIES OF AMORPHOUS SILICA AND HYDROUS AMORPHOUS SILICA." *Canadian Journal of Chemistry*, Vol. 34, No. 10, 1956, pp. 1483–1496. https://doi.org/10.1139/v56-190.

[164] Scherer, G. W. "Viscous Sintering of Particle-Filled Composites." Vol. 70, No. 6, 1991.

[165] Zhuravlev, L. T. "The Surface Chemistry of Amorphous Silica. Zhuravlev Model." *Colloids and Surfaces A: Physicochemical and Engineering Aspects*, Vol. 173, Nos. 1–3, 2000, pp. 1–38. https://doi.org/10.1016/S0927-7757(00)00556-2.

[166] Ivankovic, H., Tkalcec, E., Nass, R., and Schmidt, H. "Correlation of the Precursor Type with Densification Behavior and Microstructure of Sintered Mullite Ceramics." *Journal of the European Ceramic Society*, Vol. 23, No. 2, 2003, pp. 283–292. https://doi.org/10.1016/S0955-2219(02)00176-0.

[167] Sacks, M. D., Bozkurt, N., and Scheiffele, G. W. "Fabrication of Mullite and Mullite-Matrix Composites by Transient Viscous Sintering of Composite Powders." *Journal of the American Ceramic Society*, Vol. 74, No. 10, 1991, pp. 2428–2437. https://doi.org/10.1111/j.1151-2916.1991.tb06780.x.

[168] Kobata, A., Kusakabe, K., and Morooka, S. "Growth and Transformation of TiO2 Crystallites in Aerosol Reactor." *AIChE Journal*, Vol. 37, No. 3, 1991, pp. 347–359. https://doi.org/10.1002/aic.690370305.

[169] Xiong, Y., and Pratsinis, S. E. “Formation of Agglomerate Particles by Coagulation and Sintering—Part I. A Two-Dimensional Solution of the Population Balance Equation.” *Journal of Aerosol Science*, Vol. 24, No. 3, 1993, pp. 283–300. https://doi.org/10.1016/0021-8502(93)90003-R.

[170] Xiong, Y., Kamal Akhtar, M., and Pratsinis, S. E. “Formation of Agglomerate Particles by Coagulation and Sintering—Part II. The Evolution of the Morphology of Aerosol-Made Titania, Silica and Silica-Doped Titania Powders.” *Journal of Aerosol Science*, Vol. 24, No. 3, 1993, pp. 301–313. https://doi.org/10.1016/0021-8502(93)90004-S.

[171] Seto, T., Hirota, A., Fujimoto, T., Shimada, M., and Okuyama, K. “Sintering of Polydisperse Nanometer-Sized Agglomerates.” *Aerosol Science and Technology*, Vol. 27, No. 3, 1997, pp. 422–438. https://doi.org/10.1080/02786829708965482.

[172] Tsantilis, S., Pratsinis, S. E., and Briesen, H. “Sintering Time for Silica Particle Growth.” *Aerosol Science and Technology*, Vol. 34, No. 3, 2001, pp. 237–246. https://doi.org/10.1080/02786820119149.

[173] Ojovan, M. I., and Tournier, R. F. “On Structural Rearrangements Near the Glass Transition Temperature in Amorphous Silica.” *Materials*, Vol. 14, No. 18, 2021, p. 5235. https://doi.org/10.3390/ma14185235.

[174] Fahrenholtz, W. G., Smith, D. M., and Iii, J. C. “Effect of Precursor Particle Size on the Densification and Crystallization Behavior of Mullite.” *Journal of the American Ceramic Society*, Vol. 76, No. 2, 1993, pp. 433–437. https://doi.org/10.1111/j.1151-2916.1993.tb03802.x.

[175] Ramamoorthy, R., and Chaim, R. “Microstructural Evolution in Nanocrystalline Y-TZP Containing a Silicate Glass.” *Journal of the European Ceramic Society*, Vol. 21, No. 16, 2001, pp. 2895–2902. https://doi.org/10.1016/S0955-2219(01)00215-1.

[176] Aguilar, D. H., Torres-Gonzalez, L. C., Torres-Martinez, L. M., Lopez, T., and Quintana, P. “A Study of the Crystallization of ZrO2 in the Sol-Gel System: ZrO2-SiO2.” *Journal of Solid State Chemistry*, Vol. 158, No. 2, 2001, pp. 349–357. https://doi.org/10.1006/jssc.2001.9126.

[177] Li, X., Yin, X., Zhang, L., and He, S. “The Devitrification Kinetics of Silica Powder Heat-Treated in Different Conditions.” *Journal of Non-Crystalline Solids*, Vol. 354, No. 28, 2008, pp. 3254–3259. https://doi.org/10.1016/j.jnoncrysol.2008.02.016.

[178] Fabrichnaya, O., Seifert, H. J., Weiland, R., Ludwig, T., Aldinger, F., and Navrotsky, A. “Phase Equilibria and Thermodynamics in the Y2O3–Al2O3–SiO2 System.” *International Journal of Materials Research*, Vol. 92, No. 9, 2001, pp. 1083–1097. https://doi.org/10.3139/ijmr-2001-0197.

[179] Mao, H., Selleby, M., and Fabrichnaya, O. “Thermodynamic Reassessment of the Y 2O3–Al2O3–SiO2 System and Its Subsystems.” *Calphad*, Vol. 32, No. 2, 2008, pp. 399–412. https://doi.org/10.1016/j.calphad.2008.03.003.

[180] Schubert, U. Sol – Gel Chemistry and Methods. In *The Sol-Gel Handbook: Synthesis, Characterization and Applications*, 2015, pp. 1–28.

[181] Gawel, B., Gawel, K., and Øye, G. "Sol-Gel Synthesis of Non-Silica Monolithic Materials." *Materials*, Vol. 3, No. 4, 2010, pp. 2815–2833. https://doi.org/10.3390/ma3042815.

[182] Livage, J. "The Gel Route to Transition Metal Oxides." *Journal of Solid State Chemistry*, Vol. 64, No. 3, 1986, pp. 322–330. https://doi.org/10.1016/0022-4596(86)90076-9.

[183] Livage, J., and Sanchez, C. "Sol-Gel Chemistry." *Journal of Non-Crystalline Solids*, Vol. 145, 1992, pp. 11–19. https://doi.org/10.1016/S0022-3093(05)80422-3.

[184] Livage, J., Henry, M., and Sanchez, C. "Sol-Gel Chemistry of Transition Metal Oxides." *Prog. Solid St. Chem*, Vol. 18, 1988, pp. 259–341. https://doi.org/10.1016/0079-6786(88)90005-2.

[185] Kessler, V. G., Spijksma, G. I., Seisenbaeva, G. A., Håkansson, S., Blank, D. H. A., and Bouwmeester, H. J. M. "New Insight in the Role of Modifying Ligands in the Sol-Gel Processing of Metal Alkoxide Precursors: A Possibility to Approach New Classes of Materials." *Journal of Sol-Gel Science and Technology*, Vol. 40, Nos. 2–3, 2006, pp. 163–179. https://doi.org/10.1007/s10971-006-9209-6.

[186] Pfeiffer, H., Bosch, P., and Bulbulian, S. "Zr Alkoxide Chain Effect on the Sol-Gel Synthesis of Lithium Metazirconate." *Materials Chemistry and Physics*, Vol. 78, No. 2, 2003, pp. 558–561. https://doi.org/10.1016/S0254-0584(02)00382-6.

[187] Changrong, X., Huaqiang, C., Hong, W., Pinghua, Y., Guangyao, M., and Dingkun, P. "Sol–Gel Synthesis of Yttria Stabilized Zirconia Membranes through Controlled Hydrolysis of Zirconium Alkoxide." *Journal of Membrane Science*, Vol. 162, Nos. 1–2, 1999, pp. 181–188. https://doi.org/10.1016/S0376-7388(99)00137-4.

[188] Pérez, L. L., Perdriau, S., Brink, G. T., Kooi, B. J., Heeres, H. J., and Melián-Cabrera, I. "Stabilization of Self-Assembled Alumina Mesophases." *Chemistry of Materials*, Vol. 25, No. 6, 2013, pp. 848–855. https://doi.org/10.1021/cm303174r.

[189] Poco, J. F., Satcher, J. H., and Hrubesh, L. W. "Synthesis of High Porosity, Monolithic Alumina Aerogels." *Journal of Non-Crystalline Solids*, Vol. 285, Nos. 1–3, 2001, pp. 57–63. https://doi.org/10.1016/S0022-3093(01)00432-X.

[190] Komarneni, S., Suwa, Y., and Roy, R. "Application of Compositionally Diphasic Xerogels for Enhanced Densification: The System Al2O3-SiO2." *Journal of the American Ceramic Society*, Vol. 69, No. 7, 1986, p. C-155-C–156. https://doi.org/10.1111/j.1151-2916.1986.tb04808.x.

[191] Komarneni, S., and Rutiser, C. "Single-Phase and Diphasic Aerogels and Xerogels of Mullite: Preparation and Characterization." *Journal of the European Ceramic Society*, Vol. 16, No. 2, 1996, pp. 143–147. https://doi.org/10.1016/0955-2219(95)00141-7.

[192] Hoffman, D. W., Roy, R., and Komarneni, S. “Diphasic Xerogels, A New Class of Materials: Phases in the System Al2o3-Sio2.” *Journal of the American Ceramic Society*, Vol. 67, No. 7, 2006, pp. 468–471. https://doi.org/10.1111/j.1151-2916.1984.tb19636.x.

[193] Hurwitz, F. I., Guo, H., and Newlin, K. N. “Influence of Boehmite Precursor on Aluminosilicate Aerogel Pore Structure, Phase Stability and Resistance to Densification at High Temperatures.” *Polymer Preprints*, Vol. 52, No. 1, 2011, pp. 16–17.

[194] Fokema, M. D., Chiu, E., and Ying, J. Y. “Synthesis and Characterization of Nanocrystalline Yttrium Oxide Prepared with Tetraalkylammonium Hydroxides.” *Langmuir*, Vol. 16, No. 7, 2000, pp. 3154–3159. https://doi.org/10.1021/la991156j.

[195] Kuo, C. W., Shen, Y. H., Hung, I. M., Wen, S. B., Lee, H. E., and Wang, M. C. “Effect of Y2O3 Addition on the Crystal Growth and Sintering Behavior of YSZ Nanopowders Prepared by a Sol-Gel Process.” *Journal of Alloys and Compounds*, Vol. 472, Nos. 1–2, 2009, pp. 186–193. https://doi.org/10.1016/j.jallcom.2008.05.027.

[196] Bangi, U. K. H., Park, C. S., Baek, S., and Park, H. H. “Sol-Gel Synthesis of High Surface Area Nanostructured Zirconia Powder by Surface Chemical Modification.” *Powder Technology*, Vol. 239, 2013, pp. 314–318. https://doi.org/10.1016/j.powtec.2013.02.014.

[197] Sasol Performance Chemicals. DISPERAL and DISPAL High-Purity Dispersible Alumina Hydrates. Sasol Chemicals North America LLC.

[198] Bell, N. S., Monson, T. C., Diantonio, C., and Wu, Y. “Practical Colloidal Processing of Multication Ceramics.” *Journal of Ceramic Science and Technology*, Vol. 7, No. 1, 2016, pp. 1–28. https://doi.org/10.4416/JCST2015-00025.

[199] Rami, M. L., Meireles, M., Cabane, B., and Guizard, C. “Colloidal Stability for Concentrated Zirconia Aqueous Suspensions.” *Journal of the American Ceramic Society*, Vol. 92, No. SUPPL. 1, 2009, pp. 50–56. https://doi.org/10.1111/j.1551-2916.2008.02681.x.

[200] Santos, S. C., Setz, L. F. G., Yamagata, C., and Mello-Castanho, S. R. H. “Rheological Study of Yttrium Oxide Aqueous Suspensions.” *Materials Science Forum*, Vols. 660–661, 2010, pp. 712–717. https://doi.org/10.4028/www.scientific.net/MSF.660-661.712.

[201] Sprycha, R., Jablonski, J., and Matijević, E. “Zeta Potential and Surface Charge of Monodispersed Colloidal Yttrium(III) Oxide and Basic Carbonate.” *Journal of Colloid And Interface Science*, Vol. 149, No. 2, 1992, pp. 561–568. https://doi.org/10.1016/0021-9797(92)90443-P.

[202] Voigt, J. A. *An Integrated Study of the Ceramic Processing of Yttria*. Iowa State University, 1986.

[203] Winkler, R., Ré, E., Arrachart, G., and Pellet-Rostaing, S. “Impact of Solvent Structuring in Water/Tert-Butanol Mixtures on the Assembly of Silica Nanoparticles to Aerogels.”

Langmuir, Vol. 35, No. 24, 2019, pp. 7905–7915. https://doi.org/10.1021/acs.langmuir.9b00655.

[204] Xing, X., Sun, G., Li, Z., and Ngai, T. "Stabilization of Colloidal Suspensions: Competing Effects of Nanoparticle Halos and Depletion Mechanism." *Langmuir*, Vol. 28, No. 46, 2012, pp. 16022–16028. https://doi.org/10.1021/la303547m.

[205] Zachariah, Z., Espinosa-Marzal, R. M., Spencer, N. D., and Heuberger, M. P. "Stepwise Collapse of Highly Overlapping Electrical Double Layers." *Physical Chemistry Chemical Physics*, Vol. 18, No. 35, 2016, pp. 24417–24427. https://doi.org/10.1039/c6cp04222h.

[206] Kosmulski, M. "Compilation of PZC and IEP of Sparingly Soluble Metal Oxides and Hydroxides from Literature." *Advances in Colloid and Interface Science*, Vol. 152, Nos. 1–2, 2009, pp. 14–25. https://doi.org/10.1016/j.cis.2009.08.003.

[207] Wang, X., Tian, Y., Yu, C., Liu, L., Zhang, Z., Wu, Y., and Shen, J. "Organic/Inorganic Double-Precursor Cross-Linked Alumina Aerogel with High Specific Surface Area and High-Temperature Resistance." *Ceramics International*, Vol. 48, No. 12, 2022, pp. 17261–17269. https://doi.org/10.1016/j.ceramint.2022.02.287.

[208] Jerebtsov, D. A., Mikhailov, G. G., and Sverdina, S. V. "Phase Diagram of the System: Al2O3–ZrO2." *Ceramics International*, Vol. 26, No. 8, 2000, pp. 821–823. https://doi.org/10.1016/S0272-8842(00)00023-7.

[209] Niederberger, M., Bartl, M. H., and Stucky, G. D. "Benzyl Alcohol and Transition Metal Chlorides as a Versatile Reaction System for the Nonaqueous and Low-Temperature Synthesis of Crystalline Nano-Objects with Controlled Dimensionality." *Journal of the American Chemical Society*, Vol. 124, No. 46, 2002, pp. 13642–13643. https://doi.org/10.1021/ja027115i.

[210] Heiligtag, F. J., Rossell, M. D., Süess, M. J., and Niederberger, M. "Template-Free Co-Assembly of Preformed Au and TiO2 Nanoparticles into Multicomponent 3D Aerogels." *Journal of Materials Chemistry*, Vol. 21, No. 42, 2011, pp. 16893–16899. https://doi.org/10.1039/c1jm11740h.

[211] Niederberger, M., and Cölfen, H. "Oriented Attachment and Mesocrystals: Non-Classical Crystallization Mechanisms Based on Nanoparticle Assembly." *Physical Chemistry Chemical Physics*, Vol. 8, No. 28, 2006, pp. 3271–3287. https://doi.org/10.1039/b604589h.

[212] Cheng, W., Rechberger, F., and Niederberger, M. "Three-Dimensional Assembly of Yttrium Oxide Nanosheets into Luminescent Aerogel Monoliths with Outstanding Adsorption Properties." *ACS Nano*, Vol. 10, No. 2, 2016, pp. 2467–2475. https://doi.org/10.1021/acsnano.5b07301.

[213] Santos, S. C., Acchar, W., Yamagata, C., and Mello-Castanho, S. “Yttria Nettings by Colloidal Processing.” *Journal of the European Ceramic Society*, Vol. 34, No. 10, 2014, pp. 2509–2517. https://doi.org/10.1016/j.jeurceramsoc.2014.03.006.

[214] Yasrebi, M., Springgate, M. E., Nikolas, D. G., Kemp, W., Sturgis, D. H., and McCarthy, J. M. “Colloidal Stability of Zirconia-Doped Yttria-Silica Binary Aqueous Suspensions.” *Journal of the American Ceramic Society*, Vol. 80, No. 6, 1997, pp. 1615–1618. https://doi.org/10.1111/j.1151-2916.1997.tb03028.x.

[215] Wang, X., Li, C., Shi, Z., Zhi, M., and Hong, Z. “The Investigation of an Organic Acid Assisted Sol-Gel Method for Preparing Monolithic Zirconia Aerogels.” *RSC Advances*, Vol. 8, No. 15, 2018, pp. 8011–8020. https://doi.org/10.1039/c7ra13041d.

[216] Holsa, J., Chateau, C., Leskela, T., and Leskela, M. “Optical Study of Phase Transformations in Rare Earth Oxyhydroxides.” *Acta Chemica Scandinavica A*, Vol. 39, 1985, pp. 415–421.

[217] Yang, S., Powell, M., Kolis, J. W., and Navrotsky, A. “Thermochemistry of Rare Earth Oxyhydroxides, REOOH (RE = Eu to Lu).” *Journal of Solid State Chemistry*, Vol. 287, No. February, 2020, p. 121344. https://doi.org/10.1016/j.jssc.2020.121344.

[218] López, T., Tzompantzi, F., Hernández-Ventura, J., Gómez, R., Bokhimi, X., Pecchi, G., and Reyes, P. “Effect of Zirconia Precursor on the Properties of ZrO2-SiO2 Sol-Gel Oxides.” *Journal of Sol-Gel Science and Technology*, Vol. 24, No. 3, 2002, pp. 207–219. https://doi.org/10.1023/A:1015380523481.

[219] Schäfer, H., Brandt, S., Milow, B., Ichilmann, S., Steinhart, M., and Ratke, L. “Zirconia-Based Aerogels via Hydrolysis of Salts and Alkoxides: The Influence of the Synthesis Procedures on the Properties of the Aerogels.” *Chemistry - An Asian Journal*, Vol. 8, No. 9, 2013, pp. 2211–2219. https://doi.org/10.1002/asia.201300488.

[220] Ward, D. A., and Ko, E. I. “Synthesis and Structural Transformation of Zirconia Aerogels.” *Chemistry of Materials*, Vol. 5, No. 7, 1993, pp. 956–969. https://doi.org/10.1021/cm00031a014.

[221] Debsikdar, J. C. “Transparent Zirconia Gel-Monolith from Zirconium Alkoxide.” *Journal of Non-Crystalline Solids*, Vol. 86, Nos. 1–2, 1986, pp. 231–240. https://doi.org/10.1016/0022-3093(86)90491-6.

[222] Bangi, U. K. H., Ali, T., and Park, H. “Ambient Pressure-Dried Zirconia Xerogels and Aerogels Using Various Catalysts.” *Macromolecular Symposia*, Vol. 400, No. 1, 2021, p. 2100013. https://doi.org/10.1002/masy.202100013.

[223] Suh, D. J., Park, T. J., Han, H. Y., and Lim, J. C. “Synthesis of High-Surface-Area Zirconia Aerogels with a Well-Developed Mesoporous Texture Using CO2 Supercritical Drying.” *Chemistry of Materials*, Vol. 14, No. 4, 2002, pp. 1452–1454. https://doi.org/10.1021/cm025516r.

[224] Okubo, T., and Nagamoto, H. "Low-Temperature Preparation of Nanostructured Zirconia and YSZ by Sol-Gel Processing." *Journal of Materials Science*, Vol. 30, No. 3, 1995, pp. 749–757. https://doi.org/10.1007/BF00356338.

[225] Kim, S. G., Nam, S. W., Yoon, S. P., Hyun, S. H., Han, J., Lim, T. H., and Hong, S. A. "Sol-Gel Processing of Yttria-Stabilized Zirconia Films Derived from the Zirconium n-Butoxide-Acetic Acid-Nitric Acid-Water-Isopropanol System." *Journal of Materials Science*, Vol. 39, No. 8, 2004, pp. 2683–2688. https://doi.org/10.1023/B:JMSC.0000021442.30015.3c.

[226] Kim, S. G., Yoon, S. P., Nam, S. W., Hyun, S. H., and Hong, S. A. "Fabrication and Characterization of a YSZ/YDC Composite Electrolyte by a Sol-Gel Coating Method." *Journal of Power Sources*, Vol. 110, No. 1, 2002, pp. 222–228. https://doi.org/10.1016/S0378-7753(02)00270-7.

[227] Zu, G., Shen, J., Zou, L., Zou, W., Guan, D., Wu, Y., and Zhang, Y. "Highly Thermally Stable Zirconia/Silica Composite Aerogels Prepared by Supercritical Deposition." *Microporous and Mesoporous Materials*, Vol. 238, 2017, pp. 90–96. https://doi.org/10.1016/j.micromeso.2016.03.005.

[228] Drazin, J. W., and Castro, R. H. R. "Water Adsorption Microcalorimetry Model: Deciphering Surface Energies and Water Chemical Potentials of Nanocrystalline Oxides." *Journal of Physical Chemistry C*, Vol. 118, No. 19, 2014, pp. 10131–10142. https://doi.org/10.1021/jp5016356.

[229] Chen, S., Avila-Paredes, H. J., Kim, S., Zhao, J., Munir, Z. A., and Navrotsky, A. "Direct Calorimetric Measurement of Grain Boundary and Surface Enthalpies in Yttria-Stabilized Zirconia." *Physical Chemistry Chemical Physics*, Vol. 11, No. 17, 2009, pp. 3039–3042. https://doi.org/10.1039/b905911n.

[230] Quach, D. V., and Castro, R. H. R. "Direct Measurement of Grain Boundary Enthalpy of Cubic Yttria-Stabilized Zirconia by Differential Scanning Calorimetry." *Journal of Applied Physics*, Vol. 112, No. 8, 2012, pp. 3–8. https://doi.org/10.1063/1.4761992.

[231] Vikrant, K. S. N., Grosso, R. L., Feng, L., Muccillo, E. N. S., Muche, D. N. F., Jawaharram, G. S., Barr, C. M., Monterrosa, A. M., Castro, R. H. R., García, R. E., Hattar, K., and Dillon, S. J. "Ultrahigh Temperature in Situ Transmission Electron Microscopy Based Bicrystal Coble Creep in Zirconia I: Nanowire Growth and Interfacial Diffusivity." *Acta Materialia*, Vol. 199, 2020, pp. 530–541. https://doi.org/10.1016/j.actamat.2020.08.069.

[232] González-Romero, R. L., Meléndez, J. J., Gómez-García, D., Cumbrera, F. L., Domínguez-Rodríguez, A., and Wakai, F. "Cation Diffusion in Yttria-Zirconia by Molecular Dynamics." *Solid State Ionics*, Vols. 204–205, No. 1, 2011, pp. 1–6. https://doi.org/10.1016/j.ssi.2011.10.006.

[233] Zhao, S., Shao, C., Zahiri, S., Zhao, C., and Bao, H. "Thermal Transport in Nanoporous Yttria-Stabilized Zirconia by Molecular Dynamics Simulation." *Journal of Shanghai*

Jiaotong University (Science), Vol. 23, No. 1, 2018, pp. 38–44. https://doi.org/10.1007/s12204-018-1907-z.

[234] Ballabio, G., Bernasconi, M., Pietrucci, F., and Serra, S. “Ab Initio Study of Yttria-Stabilized Cubic Zirconia Surfaces.” *Physical Review B - Condensed Matter and Materials Physics*, Vol. 70, No. 7, 2004, pp. 1–6. https://doi.org/10.1103/PhysRevB.70.075417.